Technical Physics, Vol. 45, No. 8, 2000, pp. 1001–1008. Translated from Zhurnal Tekhnicheskoĭ Fiziki, Vol. 70, No. 8, 2000, pp. 45–52.

GASES AND LIQUIDS

Nonlinear Capillary Oscillation of a Charged Drop

D. F. Belonozhko and A. I. Grigor'ev

Yaroslavl State University, Sovetskaya ul. 14, Yaroslavl, 150000 Russia

E-mail: rectorat@uniyar.ac.ru

Received May 18, 1999; in final form October 14, 1999

Abstract—In the quadratic approximation with respect to the amplitudes of capillary oscillation and velocity field of the liquid moving inside a charged drop of a perfectly conducting fluid, it is shown that the liquid drop oscillates about a weakly prolate form. This refines the result obtained in the linear theory developed by Lord Rayleigh, who predicted oscillation about a spherical form. The extent of elongation is proportional to the initial amplitude of the principal mode and increases with the intrinsic charge carried by the drop. An estimate is obtained for the characteristic time of instability development for a critically charged drop. © *2000 MAIK "Nauka/Interperiodica".*

Studies of capillary oscillation and stability of a charged drop are motivated by numerous applications [1]. The problem was reviewed in [1–7] and references therein. However, most theoretical analyses are based on the linearized system of fluid-dynamics equations. Only recent studies have captured the nonlinear nature of the phenomenon and provided essentially new information about the mechanism of instability of a highly charged drop and its capillary oscillation [2–7].

1. A charged spherical drop with an intrinsic charge Q greater than a certain critical value becomes unstable, because the electrical repulsive forces exceed the surface tension forces. At the close of the nineteenth century, Lord Rayleigh developed a linear model of this instability [8]. Since then, studies of the instability of a highly charged drop and its generalizations have grown into a broad area of research having important technical applications.

From the perspective of classical physics, the thermal motion of molecules gives rise to drop oscillations of amplitude $\sim\sqrt{kT/\gamma}$ about the equilibrium spherical form, where k is Boltzmann's constant, T is the absolute temperature, and γ is the surface tension of the liquid. Each mode is characterized by a specific critical value of surface charge, and a supercritical charge leads to the onset of instability. The stability of the drop with respect to its intrinsic charge Q is generally characterized by the so-called Rayleigh parameter $W \equiv Q^2/4\pi\gamma R^3$, where R is the drop radius. The second mode is the most unstable, and the corresponding critical value of the Rayleigh parameter is $W_c = 4$.

In this paper, we solve Rayleigh's problem in the quadratic approximation with respect to the amplitudes of the velocity field and surface perturbation and determine the geometric form about which a subcritically charged liquid drop oscillates.

2. Consider a drop of an inviscid, perfectly conducting liquid of density ρ characterized by the surface tension γ and carrying a charge Q. The linear theory of capillary oscillation postulates that there exists a time moment that can be treated as $t = 0$, when the drop geometry is described by the second mode of linear capillary oscillation of a small finite amplitude ε and the velocity field is zero. The initial drop volume is equal to that of a spherical drop of radius R. The problem is to determine the axially symmetric oscillations of the drop in the case of an axially symmetric potential velocity field in the drop.

We use the dimensionless variables in which $\rho \equiv 1$, $\gamma \equiv 1$, and $R \equiv 1$. The mathematical model of the problem is then written in spherical coordinates with the origin at the center of the drop as follows:

$$\Delta\psi = 0; \quad \mathbf{U} = \nabla \cdot \psi, \tag{1}$$

$$\Delta\Phi = 0; \quad \mathbf{E} = -\nabla \cdot \Phi, \tag{2}$$

$$r \longrightarrow \infty: |\nabla\Phi| \longrightarrow 0, \tag{3}$$

$$r = 0: |\nabla\psi| < \infty, \tag{4}$$

$$-\frac{1}{4\pi}\oint\frac{\partial\Phi}{\partial n}dS = Q; \quad S(r, \Theta, \varphi) \equiv \begin{cases} r = 1 + \xi(\Theta, t) \\ 0 \le \Theta \le \pi \\ 0 \le \varphi < 2\pi, \end{cases} \tag{5}$$

$$r = 1 + \xi(\Theta, t): \Phi = \text{const}, \tag{6}$$

$$\frac{\partial\psi}{\partial r} = \frac{\partial\xi}{\partial t} + \frac{1}{r^2}\frac{\partial\xi}{\partial\Theta}\frac{\partial\psi}{\partial\Theta}, \tag{7}$$

$$\Delta\mathfrak{F} - \frac{\partial\psi}{\partial t} - \frac{1}{2}(\nabla \cdot \psi)^2 + \mathfrak{F}_E = \mathfrak{F}_\gamma; \quad \mathfrak{F}_E = \frac{E^2}{8\pi}, \tag{8}$$

$$t = 0: r = 1 + \xi_* + \varepsilon P_2(\cos\Theta), \tag{9}$$

$$P_2(\mu) = \frac{1}{2}(3\mu^2 - 1), \quad \int_V dV = \frac{4}{3}\pi;$$

$$V(r, \Theta, t) \equiv \begin{cases} 0 \le r \le 1 + \varepsilon_* + \varepsilon P_2(\cos(\Theta)), \\ 0 \le \Theta \le \pi, \quad 0 \le \varphi < 2\pi, \end{cases} \tag{10}$$

$$\psi = 0. \tag{11}$$

This is a boundary value problem with the free surface $r = 1 + \xi(\Theta, t)$ and three unknown functions: the potential $\Phi = \Phi(r, \Theta, t)$ of the electric field outside the drop, the potential $\psi = \psi(r, \Theta, t)$ of the velocity field inside the drop, and the surface deviation $\xi = \xi(\Theta, t)$ from a regular sphere with $r = 1$.

The potentials Φ and ψ satisfy the Laplace equations (1) and (2) under the boundary and initial conditions (3)–(8) and (9)–(11), respectively.

Both kinematic and dynamic boundary conditions for the velocity field **U**, (7) and (8), contain nonlinear terms. Condition (4) implies that **U** is bounded at the center of the drop. In (8), $\Delta\mathfrak{F}$ is the difference between the constant pressure components inside and outside the drop, $\mathfrak{F}_E$ is the electric pressure on the drop surface [9, 10], and $\mathfrak{F}_\gamma$ is the capillary pressure under the curved drop surface [11].

It follows from (3) that the electric field **E** must be bounded at infinity. The continuity of the tangential components of $\mathbf{E}(\mathbf{r}, t)$ at the charged surface of a conductor means that the surface is equipotential (see (6)) [10]. The condition for the normal components of $\mathbf{E}(\mathbf{r}, t)$ at the interface is written in (5) in an integral form, where **n** is the outward unit normal to the drop surface. The quantity ξ_* in (9) is determined by (10), which means that the volumes of the initial drop and a spherical drop of unit radius are equal.

3. In dimensionless variables, the amplitude ε of an initial deviation from spherical form is measured in units of the spherical drop radius. We treat ε as a small parameter and seek a solution to the problem as a series expansion in integer powers of ε, omitting the terms of order higher than two:

$$\Phi = \Phi_0 + \Phi_1 + \Phi_2 + O(\varepsilon^3), \tag{12}$$

$$\psi = \psi_1 + \psi_2 + O(\varepsilon^3), \tag{13}$$

$$r = 1 + \xi, \quad \xi = \xi_1 + \xi_2 + O(\varepsilon^3), \tag{14}$$

$$\Phi_m \sim \psi_m \sim \xi_m \sim O(\varepsilon^m); \ m = 1, 2; \ \Phi_0 = O(1). \tag{15}$$

The functions Φ, ψ, and ξ are assumed to be of the same order as their partial derivatives. Under these assumptions, since the Laplace operator is linear, we can use the expansions obtained in the Appendices to split the problem (1)–(11) into problems of zeroth, first, and second order [11] for the seven functions Φ_0, Φ_m, ψ_m, and ξ_m, where $m = 1$ and 2.

In the zeroth approximation, the nontrivial relations are (2), (3), (5), and (8). They contain the electric potential, the capillary pressure, and the constant component of the difference of pressures inside and outside the drop. Problem (1)–(11) reduces to one for the static field $\Phi_0(r)$, with the known functions $\psi_0 \equiv 0$ and $\xi_0 \equiv 0$:

$$\frac{d^2\Phi_0}{dr^2} = 0, \quad \mathbf{E}_1 = -\frac{d\Phi_0}{dr}\mathbf{e}_r,$$

$$-\frac{1}{4\pi}\int_0^{2\pi}\int_0^{\pi}\left(\frac{d\Phi_0}{dr}\right)_{r=1}\sin(\Theta)\,d\Theta\,d\varphi = Q, \tag{16}$$

$$r \longrightarrow \infty: \left|\frac{d\Phi_0}{dr}\right| \longrightarrow 0,$$

where $\mathbf{e}_r$ is the unit radial vector.

The solution of the problem is $\Phi_0 = Q/r$. Using this solution and formulas (1B), (2C), and (5D)–(10D) from the Appendices, the first- and second order problems are easily formulated. The first order problem is written as

$$\Delta\psi_1 = 0, \quad \mathbf{U}_1 = \nabla \cdot \psi_1, \tag{17}$$

$$\Delta\Phi_1 = 0, \quad \mathbf{E}_1 = -\nabla \cdot \Phi_1, \tag{18}$$

$$r \longrightarrow \infty: |\nabla\Phi_1| \longrightarrow 0, \tag{19}$$

$$r = 0: |\nabla\psi_1| < \infty, \tag{20}$$

$$r = 1: -\frac{1}{4\pi}\int_0^{2\pi}\int_0^{\pi}\left(\frac{d\Phi_1}{dr}\right)\sin(\Theta)\,d\Theta\,d\varphi = 0, \tag{21}$$

$$\Phi_1 - \xi_1 Q = 0, \tag{22}$$

$$\frac{\partial\psi_1}{\partial r} = \frac{\partial\xi_1}{\partial t}, \tag{23}$$

$$\frac{\partial\psi_1}{\partial t} + \frac{Q}{4\pi}\left[\frac{\partial\Phi_1}{\partial r} + 2\xi_1 Q\right] = 2\xi_1 + \Delta_\Omega\xi_1, \tag{24}$$

$$t = 0: \xi_1 = \varepsilon P_2(\cos(\Theta));$$
$$P_2(\cos(\Theta)) = \frac{1}{2}(3\cos^2(\Theta) - 1), \tag{25}$$

$$\psi_1 = 0. \tag{26}$$

The problem for the second-order quantities is written as follows:

$$\Delta\psi_2 = 0, \quad \mathbf{U}_2 = \nabla \cdot \psi_2, \tag{27}$$

$$\Delta\Phi_2 = 0, \quad \mathbf{E}_2 = -\nabla \cdot \Phi_2, \tag{28}$$

$$r \longrightarrow \infty: |\nabla \cdot \Phi_2| \longrightarrow 0, \tag{29}$$

$$r = 0: |\nabla \cdot \psi_2| < \infty, \tag{30}$$

$$r = 1: -\frac{1}{4\pi}\int_0^{2\pi}\int_0^{\pi}\left(\frac{d\Phi_2}{dr} + 2\xi_1\frac{\partial\Phi_1}{\partial r} + \xi_1\frac{\partial\Phi_1^2}{\partial r^2} - \frac{\partial\xi_1}{\partial\Theta}\frac{\partial\Phi_1}{\partial\Theta}\right)\sin\Theta d\Theta d\varphi = 0, \tag{31}$$

$$\Phi_2 - \xi_2 Q = -\xi_1\frac{\partial\Phi_1}{\partial r} + \xi_1^2 Q, \tag{32}$$

$$\frac{\partial\psi_2}{\partial r} + \xi_1\frac{\partial^2\psi_1}{\partial r^2} = \frac{\partial\xi_2}{\partial t} + \frac{\partial\xi_1}{\partial\Theta}\frac{\partial\psi_1}{\partial\Theta}, \tag{33}$$

$$\frac{\partial\psi_2}{\partial t} + \frac{Q}{4\pi}\left[\frac{\partial\Phi_2}{\partial r} + 2\xi_2 Q\right] = 2\xi_2 + \Delta_\Omega\xi_2 - \frac{1}{2}\left(\frac{\partial\psi_1}{\partial r}\right)^2 - \frac{1}{2}\left(\frac{\partial\psi_1}{\partial\Theta}\right)^2 - \xi_1\frac{\partial}{\partial r}\left(\frac{\partial\psi_1}{\partial t}\right) - 2\xi_1^2 - 2\xi_1\Delta_\Omega\xi_1 + 5\xi_1\frac{Q^2}{4\pi} + 2\xi_1\frac{Q}{4\pi}\frac{\partial\Phi_1}{\partial r} - \xi_1\frac{Q}{4\pi}\frac{\partial^2\Phi_1}{\partial r^2} + \frac{1}{8\pi}\left(\frac{\partial\Phi_1}{\partial r}\right)^2 - \frac{1}{8\pi}\left(\frac{\partial\Phi_1}{\partial\Theta}\right)^2, \tag{34}$$

$$t = 0: \xi_2 = -\frac{\varepsilon^2}{5}, \tag{35}$$

$$\psi_2 = 0, \tag{36}$$

where Δ_Ω is the angular part of the Laplace operator, with $r = 1$. The functions ψ_1 and Φ_1 are determined from (17)–(20) in the following general form:

$$\psi_1 = \sum_{m=0}^{\infty} C_m r^m P_m(\cos\Theta), \quad C_m = C_m(t), \tag{37}$$

$$\Phi_1 = F + \sum_{m=0}^{\infty}\frac{F_m}{r^{m+1}}P_m(\cos\Theta), \quad F_m = F_m(t), \quad F = F(t). \tag{38}$$

At any moment, the deviation $\xi_1 = \xi_1(\Theta, t)$ of the drop surface is a single-valued continuous function of $\cos\Theta$; therefore, it can be represented as a series in terms of the orthogonal Legendre polynomials $\{P_m(\cos\Theta)\}$:

$$\xi_2 = \sum_{m=0}^{\infty} Z_m(t)P_m(\cos\Theta). \tag{39}$$

To solve problem (17)–(26), we have to substitute (37)–(39) into (17)–(26); use the orthogonality of the Legendre polynomials, i.e., the fact that $\{P_m(\cos\Theta)\}$ are the eigenfunctions of the angular part of the Laplace operator in spherical coordinates ($\Delta_\Omega P_m(\cos\Theta) = -m(m+1)P_m(\cos\Theta)$); and formulate the Cauchy problem for a homogeneous system of ordinary differential equations for the unknown functions $C_m(t)$, $F_m(t)$, and $Z_m(t)$. By finding these unknowns and substituting them into (37)–(39), we can write the stable solutions to the first-order problem as

$$\xi_1 = \varepsilon\cos(\omega_2 t)P_2(\cos\Theta), \tag{40}$$

$$\psi_1 = -\frac{\varepsilon\omega_2}{2}\sin(\omega_2 t)P_2(\cos\Theta), \tag{41}$$

$$\Phi_1 = \varepsilon Q\cos(\omega_2 t)P_2(\cos\Theta), \tag{42}$$

$$\omega_2 = 8 - 2W, \quad W = \frac{Q^2}{4\pi} < 4. \tag{43}$$

Substituting (40)–(43) and the obvious equalities

$$P_2^2(\cos\Theta) = \frac{1}{5} + \frac{2}{7}P_2(\cos\Theta) + \frac{18}{35}P_4(\cos\Theta),$$

$$\left(\frac{\partial P_2(\cos\Theta)}{\partial\Theta}\right)^2 = \frac{6}{5} + \frac{6}{7}P_2(\cos\Theta) - \frac{72}{35}P_4(\cos\Theta)$$

into (31)–(34), we obtain

$$r = 1: -\frac{1}{4\pi}\int_0^{2\pi}\int_0^{\pi}\left(\frac{d\Phi_2}{dr}\right)\sin\Theta d\Theta d\varphi = 0, \tag{31'}$$

$$\Phi_2 + \xi_2 Q = 2\varepsilon^2 Q\cos^2(\omega_2 t) \times\left[\frac{1}{5} + \frac{2P_2(\cos\Theta)}{7} + \frac{18P_4(\cos\Theta)}{35}\right], \tag{32'}$$

$$\frac{\partial\psi_2}{\partial r} - \frac{\partial\xi_2}{\partial t} = \varepsilon^2\omega_2\sin(2\omega_2 t) \times\left[-\frac{1}{5} - \frac{P_2(\cos\Theta)}{14} + \frac{27P_4(\cos\Theta)}{35}\right], \tag{33'}$$

$$\frac{\partial\psi_2}{\partial t} + \frac{Q}{4\pi}\left[\frac{\partial\Phi_2}{\partial r} + 2\xi_2 Q\right] - 2\xi_2 - \Delta_\Omega\xi_2 = \varepsilon^2\left[\cos^2(\omega_2 t)\frac{9\omega_2^2 - 22W + 40}{20} - \frac{\omega_2^2}{4} + \left(\cos^2(\omega_2 t)\frac{15\omega_2^2 - 56W + 80}{28} - \frac{\omega_2^2}{4}\right)P_2(\cos\Theta) + \left(\cos^2(\omega_2 t)\frac{9(2\omega_2^2 - 21W + 20)}{28} - \frac{\omega_2^2}{4}\right)P_4(\cos\Theta)\right]. \tag{34'}$$

The system including (27)–(30), (31')–(34'), (35), and (36) is the reformulated second-order problem. It can be solved in the same way as the first-order one.

4. The solution obtained by substituting the resulting first- and second-order terms into (12)–(14) is

$$r = 1 - \frac{\varepsilon^2}{5}\cos^2(\omega_2 t) + \varepsilon\cos(\omega_2 t)P_2(\cos\Theta)$$
$$+ \frac{\varepsilon^2}{\omega_2^2}(\chi_1 - (\chi_1 + \chi_2)\cos(\omega_2 t) + \chi_2\cos(2\omega_2 t))$$
$$\times P_2(\cos\Theta) + \frac{18}{35}\varepsilon^2(\chi_3 - (\chi_3 + \chi_4)\cos(\omega_4 t) \quad (44)$$
$$+ \chi_4\cos(2\omega_2 t))P_4(\cos\Theta),$$

$$\Phi = \pm 2\sqrt{\pi W}\left[\frac{1}{r} + \varepsilon\cos(\omega_2 t)\frac{P_2(\cos\Theta)}{r^3}\right.$$
$$+ \frac{\varepsilon^2}{\omega_2^2}(\chi_1 + K - (\chi_1 + \chi_2)\cos(\omega_2 t)$$
$$+ (\chi_2 + K)\cos(2\omega_2 t))\frac{P_2(\cos\Theta)}{r^3} \quad (45)$$
$$+ \frac{18}{35}\varepsilon^2(\chi_3 + 1 - (\chi_3 + \chi_4)\cos(\omega_4 t)$$
$$\left. + (\chi_4 + 1)\cos(2\omega_2 t))\frac{P_4(\cos\Theta)}{r^5}\right],$$

$$\psi = -\frac{\varepsilon\omega_2}{2}\sin(\omega_2 t)r^2 P_2(\cos\Theta) + \frac{\varepsilon^2}{\omega_2^2}\left(\frac{\chi_1 + \chi_2}{2}\sin(\omega_2 t)\right.$$
$$\left. + G\sin(2\omega_2 t)\right)r^2 P_2(\cos\Theta) \quad (46)$$
$$+ \frac{18}{35}\varepsilon^2\left(\frac{\chi_3 + \chi_4}{\omega_4}\sin(\omega_4 t) + L\sin(2\omega_2 t)\right)r^4 P_4(\cos\Theta),$$

$$\chi_1 \equiv \frac{44 - 5W}{14}, \quad \chi_2 \equiv \frac{23W - 116}{42}, \quad \chi_3 \equiv \frac{36 - 5W}{\omega_4^2},$$

$$\chi_4 \equiv \frac{12 + W}{4(10 - W)}, \quad W \equiv \frac{Q^2}{4\pi}, \quad 0 \le W \ll 4,$$

$$G \equiv \frac{2(26 - 5W)}{21}, \quad L \equiv \frac{(9 - 2W)\sqrt{2(4 - W)}}{2(10 - W)},$$

$$K \equiv \frac{2\omega_2^2}{7}, \quad \omega_2^2 \equiv 2(4 - W), \quad \omega_4^2 \equiv 12(6 - W).$$

The sign of the potential in (45) corresponds to the sign of the drop charge. In the expressions for Φ and ψ, the terms that depend on time only are omitted.

The solution given by (44)–(46) is uniformly valid for $W \ll 4$, because it does not contain any secular terms or terms with small denominators. When the Rayleigh parameter W approaches the critical value $W_c = 4$ for the principal-mode instability, $\omega_2^2 \longrightarrow 0$ in (44)–(46) and the asymptotic character of the solution is violated. This fact determines the domain of uniform validity of the solutions written out here. The case of a highly charged drop with $W \longrightarrow 4$ was considered in [2]. Formula (44) is identical with the solutions found by using the Lindstedt–Poincaré and multiple-scales methods [11].

5. Solution (44) has some interesting features that have not been noted in [2–6].

Equation (44) of the oscillating surface contains terms nonperiodic in time. The surface associated with these terms is written as

$$r_* = 1 + \varepsilon^2 A P_2(\cos\Theta) + \varepsilon^4 B P_4(\cos\Theta),$$
$$A = \frac{44 - 5W}{28(4 - W)}, \quad B = \frac{18}{35}\frac{36 - 5W}{12(6 - W)} \quad (47)$$

and can be considered as the surface about which the drop oscillates.

The equation of the surface of a prolate spheroid with a small eccentricity β can be approximated by a series in $\{P_m(\cos\Theta)\}$. In the quadratic approximation with respect to β, this equation has the form

$$r = b\left(1 + \frac{1}{6}\beta^2\right) + \frac{b\beta^2}{3}P_2(\cos(\Theta)),$$

where b is the semiminor axis of the spheroid. Such a spheroid is the best approximation of the surface r_* if

$$b\left(1 + \frac{1}{6}\beta^2\right) = 1, \quad \frac{b\beta}{3} = \varepsilon^2 A.$$

These equations can be used to find the eccentricity and semiaxes of the spheroid approximating the surface defined by (47). Denoting the semimajor axis of this spheroid by a, we have

$$\beta = \varepsilon(\sqrt{3A} + O(\varepsilon^3)), \quad b = 1 + O(\varepsilon^3),$$
$$a = 1 + \varepsilon^2\frac{3A}{2} + O(\varepsilon^2), \quad A = \frac{44 - 5W}{28(4 - W)}. \quad (48)$$

According to (48), even an uncharged drop with the initial disturbance $\sim P_2(\cos\Theta)$ oscillates about a spheroid of eccentricity $\beta = 1.1\varepsilon$, which is close to the dimensionless amplitude ε of the initial disturbance. It is clear that the eccentricity of a spheroid about which a drop of a viscous liquid oscillates must exponentially decrease as the energy of the initial deformation dissipates. In the case of a perfect liquid drop, the energy of an initial deformation is merely distributed between the interacting modes.

Curves *1* and *2* in Fig. 1 represent the surfaces (47) and (48) with $\varepsilon = 0.3$ for a charged drop at $W = 3$. Numerical calculations reveal that when $\varepsilon < 0.3$, the

ellipsoid described by (48) well approximates the surface defined by (47) about which the drop oscillates. The accuracy of the approximation improves with decreasing ε. The influence of W on the accuracy of the approximation of a nonoscillating drop surface (47) by the spheroid defined by (48) with ε = 0.3 becomes noticeable starting from $W \approx 3$. As ε decreases, the value of W above which the approximation in (48) fails increases, approaching the limit $W = 4$.

Curves *3* and *4* in Fig. 1 show the contours of the limit deformations of an oscillating drop. The contour that is the most prolate along the polar axis (curve *3*) represents the geometry of the drop at $t = T_2 m$ (with $m = 0, 1, 2, \ldots$), where $T_2 \approx 2.22$ is the period of the second mode of capillary oscillation. At the moments $T_2/2 + T_2 m$, the drop has the most oblate geometry, represented by curve *4*.

The relative elongation of the semimajor axis of the spheroid defined by (48) is described by the function

$$\delta(\varepsilon, W) = 1.5\varepsilon^2(44 - 5W)/28(4 - W).$$

The graphs of this function are shown in Fig. 2 for various values of ε. It is clear from this figure that the eccentricity of the spheroid defined by (48), i.e., the extent of elongation about which the drop oscillates, rapidly increases with W.

6. Even though solution (44) has a nonasymptotic character when $W \approx 4$, it is interesting to compare its behavior to that of the first-order solution for $W \longrightarrow 4$ as W approaches the critical value. Indeed, in the linear approximation with respect to ε, the surface equation

$$r_s(\varepsilon, W, \Theta, t) = 1 + \varepsilon\cos(\omega_2 t)P_2(\cos(\Theta))$$

has the following limit form as $W \longrightarrow 4$:

$$\lim_{W \to 4} r_s(\varepsilon, W, \Theta, t) = 1 + \varepsilon P_2(\cos\Theta), \qquad (49)$$

where r_s represents the equation of the drop surface in the first approximation with respect to ε.

In this approximation, the drop has a prolate nonoscillating form when $W = 4$. When the Rayleigh parameter W slightly exceeds the critical value $W_c = 4$, this form elongates exponentially in time; when $W < 4$, the drop oscillates stably.

When the second-order terms are taken into account in (44), we have the limit

$$\lim_{W \to 4} r_s(\varepsilon, W, \Theta, t) = 1 + \varepsilon P_2(\cos(\Theta)) - \frac{\varepsilon^2}{5} + \varepsilon^2\frac{18}{35}\sin^2(t\sqrt{6})P_4(\cos\Theta) + \frac{12}{7}\varepsilon^2 t^2 P_2(\cos\Theta). \qquad (50)$$

In the first approximation, a small left neighborhood of $W = 4$ is a domain of stability; in the second-order approximation, it is a domain where the asymptotic expansion is not valid. At nearly critical $W \longrightarrow 4$, the second term in (44) grows with time, becoming comparable to the preceding term in a characteristic time $t \sim O(\varepsilon^{-1/2})$ and exceeding it as t increases further, as indicated by the last term in (50).

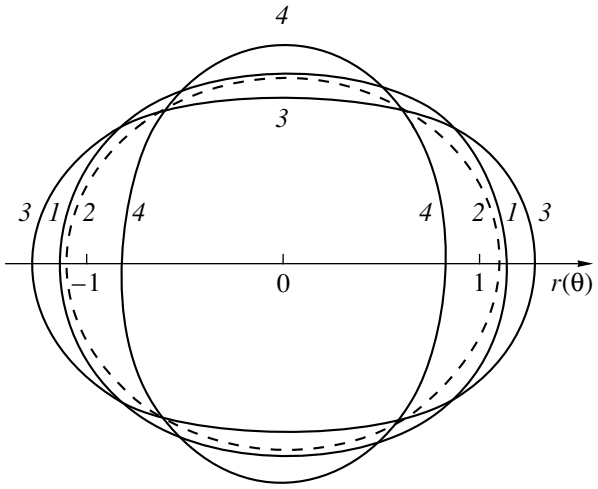

Fig. 1. Contours of possible forms taken by the drop.

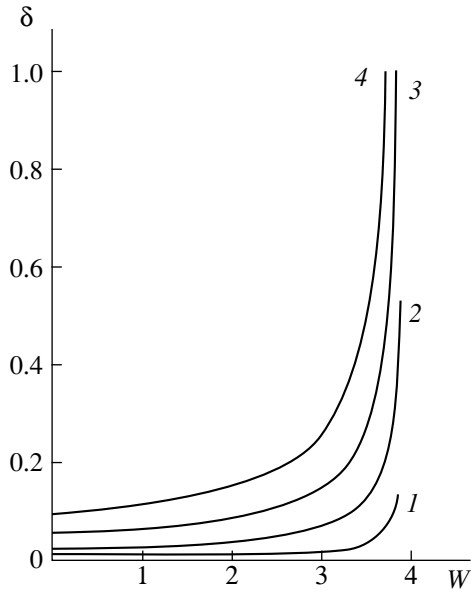

Fig. 2. Dependence of the relative elongation $\delta(\varepsilon, W)$ of the semimajor axis of the spheroid (48) on W at ε = (*1*) 0.1, (*2*) 0.2, (*3*) 0.03, and (*4*) 0.4.

Water drops of about a millimeter in diameter can be treated as low-viscous and well conducting [1]. For a water drop ($\rho = 1$ g/cm^3) of radius $R \sim 10^{-1}$ cm, capillary oscillations with an amplitude ~10^{-8} cm are characterized by a dimensionless amplitude $\varepsilon \sim 10^{-7}$. Accordingly, the dimensionless time $t \sim \varepsilon^{-1/2} \sim 3 \times 10^3$. In the dimensionless variables used here, the time unit is $t_* = ((\rho R^3)/\gamma)^{1/2} \sim 4 \times 10^{-3}$ s. The corresponding physical time equals $t_1 = tt_* \sim 10$ s, which agrees with an estimate obtained in [12] by using another method in

the spheroidal approximation for an unstable drop. This is the time interval within which the expansion (50) can be used to describe the evolution of the surface geometry after the drop is critically charged. From physical considerations, a critically charged drop must be unstable. Therefore, the value t_f obtained can be interpreted as an estimate for the time interval from the moment when the drop is charged to the moment when the drop becomes stable by losing a part of its charge.

7. The nonlinear analysis of capillary oscillations of a charged drop performed to the second-order terms inclusive reveals that the time-averaged surface form of an oscillating, subcritically charged drop of a perfectly conducting liquid is well approximated by the spheroidal surface defined by (48). The eccentricity of the approximating spheroid is proportional to the initial deviation amplitude and considerably increases the intrinsic charge of the drop. The relative elongation of the spheroid compared to the radius of an equivalent perfectly spherical drop is proportional to the amplitude squared of the initial deviation, increasing with the intrinsic charge.

A water drop one millimeter in diameter carrying the critical charge changes its form according to (50) within an interval of about ten seconds, which is easy to observe experimentally; therefore, the effect can be detected.

APPENDIX

A. Asymptotic Expansions of the Components of the Normal to the Drop Free Surface and Their Derivatives

At a moment t, the geometry of an oscillating drop surface obeys the following equation written in spherical coordinates with unit basis vectors $\mathbf{e}_r$, $\mathbf{e}_\Theta$, and $\mathbf{e}_\varphi$:

$$F(r, \Theta, t) = 0, \quad f(r, \Theta, t) = r - 1 - \xi(r, \Theta, t).$$

Using the well-known relation

$$\mathbf{n} = \frac{\nabla F(r, \Theta, t)}{|\nabla F(r, \Theta, t)|},$$

we obtain the components of the normal vector $\mathbf{n}$ to this surface and their derivatives with respect to the spherical coordinates:

$$r = 1\colon n_r = \left[1 + \frac{1}{r^2}\left(\frac{\partial \xi}{\partial \Theta}\right)^2\right]^{-1/2}, \quad n_\varphi \equiv 0, \tag{1A}$$

$$n_\Theta = -\frac{1}{r}\left[1 + \frac{1}{r^2}\left(\frac{\partial \xi}{\partial \Theta}\right)^2\right]\frac{\partial \xi}{\partial \Theta}, \tag{2A}$$

$$\frac{\partial n_r}{\partial r} = \frac{1}{r^3}\left[1 + \frac{1}{r^2}\left(\frac{\partial \xi}{\partial \Theta}\right)^2\right]^{-3/2}\left(\frac{\partial \xi}{\partial \Theta}\right)^2, \tag{3A}$$

$$\begin{aligned}\frac{\partial n_\Theta}{\partial \Theta} &= -\frac{1}{r}\frac{\partial^2 \xi}{\partial \Theta^2}\left[1 + \frac{1}{r^2}\left(\frac{\partial \xi}{\partial \Theta}\right)^2\right]^{-1/2} \\ &+ \frac{1}{r^3}\left(\frac{\partial \xi}{\partial \Theta}\right)^2\frac{\partial^2 \xi}{\partial \Theta^2}\left[1 + \frac{1}{r^2}\left(\frac{\partial \xi}{\partial \Theta}\right)^2\right]^{-3/2}.\end{aligned} \tag{4A}$$

The problem under consideration is solved in the approximation in which the following asymptotic estimates and expansions with respect to the small dimensionless amplitude ε of the initial drop deformation are valid:

$$\begin{aligned}&\xi \sim \frac{\partial \xi}{\partial \Theta} \sim \frac{\partial^2 \xi}{\partial \Theta^2} \sim O\varepsilon, \quad r = 1 + \xi, \\ &\frac{1}{r} = 1 - \xi + \xi^2 + O(\varepsilon^3), \ \frac{1}{r^2} = 1 - 2\xi + 3\xi^2 + O(\varepsilon^3), \\ &\frac{1}{r^3} = 1 - 3\xi + 6\xi^2 + O(\varepsilon^3).\end{aligned} \tag{5A}$$

By virtue of (5A), (1A)–(4A) can be rewritten as follows:

$$n_r = 1 - \frac{1}{2}\left(\frac{\partial \xi}{\partial \Theta}\right)^2 + O(\varepsilon^3), \tag{6A}$$

$$n_\Theta = -\frac{\partial \xi}{\partial \Theta} + \xi\frac{\partial \xi}{\partial \Theta} + O(\varepsilon^3), \tag{7A}$$

$$\frac{\partial n_r}{\partial r} = \left(\frac{\partial \xi}{\partial \Theta}\right)^2 + O(\varepsilon^3), \tag{8A}$$

$$\frac{\partial n_\Theta}{\partial \Theta} = -\frac{\partial^2 \xi}{\partial \Theta^2} + \xi\frac{\partial^2 \xi}{\partial \Theta^2} + O(\varepsilon^3). \tag{9A}$$

B. The Asymptotic Form of the Capillary Pressure under the Curved Drop Surface

For a given mean liquid surface curvature H and surface tension coefficient γ, the Laplace pressure distribution at the surface is determined as $\mathfrak{S}_\gamma = 2H_\gamma$. The value of H can be calculated as $2H = \operatorname{div}\mathbf{n}$. In dimensionless variables such that $\gamma \equiv 1$, we have $\mathfrak{S}_\gamma = \operatorname{div}\mathbf{n}$ and

$$\operatorname{div}\mathbf{A} = \frac{1}{r^2}\frac{\partial (r^2 A_r)}{\partial r} + \frac{1}{r\sin\Theta}\frac{(\partial A_\Theta \sin\Theta)}{\partial \Theta} + \frac{1}{r\sin\Theta}\frac{\partial A_\varphi}{\partial \varphi}.$$

Since the problem is axially symmetric ($n_\varphi \equiv 0$), it holds that

$$\mathfrak{S}_\gamma = \frac{2n_r}{r} + \frac{\partial n_r}{\partial r} + \frac{1}{r}\frac{\partial n_\Theta}{\partial \Theta} + \frac{n_\Theta}{r}\cot\Theta.$$

Substituting (5A)–(9A) into the last expression, we

have

$$\mathfrak{F}_\gamma = 2 - 2\xi - \frac{\partial^2\xi}{\partial\Theta^2} - \frac{\partial\xi}{\partial\theta}\cot\Theta + 2\xi\left[\xi + \frac{\partial^2\xi}{\partial\Theta^2} + \frac{\partial\xi}{\partial\theta}\cot\Theta\right] + O(\varepsilon^3).$$

The unknown function ξ is sought in the form $\xi = \xi_1 + \xi_2 + O(\varepsilon^3)$, $\xi_1 \sim O(\varepsilon)$, $\xi_2 \sim O(\varepsilon^2)$. Hence,

$$\mathfrak{F}_\gamma = 2 - 2\xi_1 - \Delta_\Omega\xi_1 + 2\xi_1(\xi_1 + \Delta_\Omega\xi_1) + O(\varepsilon^3), \quad \Delta_\Omega = \frac{\partial^2}{\partial\Theta^2} + \frac{\partial}{\partial\Theta}\cot\Theta, \tag{1B}$$

where Δ_Ω is the angular part of the Laplace operator in spherical coordinates with $r = 1$.

C. Asymptotic Expansion of Initial Conditions

Let us derive the asymptotic expansion of integral (10) over the drop volume at the initial moment. We have

$$r = 1 + \xi_* + \varepsilon P_2(\cos\Theta),$$

$$\frac{4}{3}\pi = \int_V dv = \int_0^{2\pi}\int_0^{\pi}\int_0^{r} r^2\sin\Theta\,dr\,d\Theta\,d\varphi = \frac{2\pi}{3}\int_0^{\pi} r^3\sin\Theta\,d\Theta$$

$$= \frac{2\pi}{3}\int_{-1}^{1} r^3\,d\mu = \frac{2\pi}{3}\int_{-1}^{1}[1 + \xi_* + \varepsilon P_2(\mu)]^3\,d\mu,$$

$$2 = (1 + \xi_*)^3\int_{-1}^{1}\left[1 + \frac{\varepsilon}{1 + \xi_*}P_2(\mu)\right]^3 d\mu, \tag{1C}$$

$$2 = (1 + \xi_*)^3\int_{-1}^{1}\left[1 + \frac{3\varepsilon}{1 + \xi_*}P_2(\mu) + \frac{3\varepsilon^2}{(1 + \xi_*)^2}P_2^2(\mu) + O(\varepsilon^3)\right]^3 d\mu$$

or

$$2 = 2(1 + \xi_*)^3\left[1 + \frac{3}{5}\frac{\varepsilon^2}{(1 + \xi_*)^2}\right] + O(\varepsilon^3),$$

$$1 = (1 + \xi_*)\left(\left[1 + \frac{3}{5}\frac{\varepsilon^2}{(1 + \xi_*)^2}\right] + O(\varepsilon^3)\right)^{1/3}$$

$$\approx (1 + \xi_*)\left[1 + \frac{\varepsilon^2}{5(1 + \xi_*)^2}\right].$$

The resulting equation for ξ_* has the roots $-\varepsilon^2/5$ and $\varepsilon^2/5 - 1$. Setting ξ_* equal to the one for which the initial condition (9) can be written as an asymptotic expansion in ε, we rewrite (9) and (10) in a simpler form:

$$t = 0: r = 1 + \varepsilon P_2(\cos\Theta) - \frac{\varepsilon^2}{5}. \tag{2C}$$

D. Expansions of Potentials and Related Quantities in the Vicinity of an Unperturbed Drop Surface

The electrostatic potential Φ on the surface $r = 1 + \xi$ can be expressed in terms of Φ and its partial derivatives on the unit sphere surface with the required accuracy as

$$r = 1 + \xi:$$
$$\Phi = \Phi(r, \Theta, t) = \Phi(1 + \xi, \Theta, t) = \Phi(1, \Theta, t) + \frac{\partial\Phi}{\partial r}(1, \Theta, t)\xi + \frac{1}{2}\frac{\partial^2\Phi}{\partial r^2}(1, \Theta, t)\xi^2 + O(\varepsilon^3).$$

Using (12), (14), and (15), we rewrite this expression as

$$r = 1 + \xi:$$
$$\Phi = \Phi_0|_{r=1} + \left(\Phi_1 + \xi_1\frac{\partial\Phi_0}{\partial r}\right)_{r=1} + \left[\Phi_2 + \xi_2\frac{\partial\Phi_0}{\partial r} + \xi_1\frac{\partial\Phi_1}{\partial r} + \frac{1}{2}\xi_1^2\frac{\partial^2\Phi_0}{\partial r^2}\right]_{r=1} + O(\varepsilon^3). \tag{1D}$$

Now, the value of Φ on the surface $r = 1 + \xi$ equals the sum of terms defined on the surface $r = 1$ with the required accuracy.

Applying a similar method and using (6A) and (7A), we find

$$r = 1 + \xi:$$
$$\nabla\Phi = \nabla\Phi_0|_{r=1} + \left(\nabla\Phi_1 + \xi_1\frac{\partial\nabla\Phi_0}{\partial r}\right)_{r=1} + \left[\nabla\Phi_2 + \xi_2\frac{\partial\nabla\Phi_0}{\partial r} + \xi_1\frac{\partial\nabla\Phi_1}{\partial r} + \frac{1}{2}\xi_1^2\frac{\partial^2\nabla\Phi_0}{\partial r^2}\right]_{r=1} + \mathbf{e}_r O(\varepsilon^3) + \mathbf{e}_\Theta O(\varepsilon^3), \tag{2D}$$

$$\frac{\partial\Phi}{\partial n} = n_r\frac{\partial\Phi}{\partial r} + \frac{n_\Theta}{r}\frac{\partial\Phi}{\partial\Theta} = \left[1 - \frac{1}{2}\left(\frac{\partial\xi}{\partial\Theta}\right)^2\right] \times \left[\frac{\partial\Phi}{\partial r} + \xi\frac{\partial^2\Phi}{\partial r^2} + \frac{\xi^2}{2}\frac{\partial^3\Phi}{\partial r^3}\right]_{r=1} + (1 - \xi + \xi^2)\left[-\frac{\partial\xi}{\partial\Theta} + \xi\frac{\partial\xi}{\partial\Theta}\right]$$

$$\times\left[\frac{\partial\Phi}{\partial\Theta}+\xi\frac{\partial^2\Phi}{\partial d\partial\Theta}+\frac{\xi^2}{2}\frac{\partial^3\Phi}{\partial r^2\partial\Theta}\right]+O(\varepsilon^3),$$

$$\frac{\partial\Phi}{\partial n}=\left[\frac{\partial\Phi_0}{\partial r}+\frac{\partial\Phi_1}{\partial r}+\xi_1\frac{\partial^2\Phi_0}{\partial r^2}-\frac{\partial\xi_1}{\partial\Theta}\frac{\partial\Phi_0}{\partial\Theta}\right.$$

$$+\xi_2\frac{\partial^2\Phi_0}{\partial r^2}-\frac{\partial^2\xi_2}{\partial\Theta}\frac{\partial\Phi_0}{\partial\Theta}+\frac{\partial\Phi_2}{\partial r}$$

$$+\xi_1\frac{\partial^2\Phi_1}{\partial r^2}+\frac{\xi_1^2}{2}\frac{\partial^3\Phi_0}{\partial r^3}+\frac{1}{2}\left(\frac{\partial\xi_1}{\partial\Theta}\right)^2\frac{\partial\Phi_0}{\partial\Theta}$$

$$\left.-\frac{\partial\xi_1}{\partial\Theta}\frac{\partial\Phi_1}{\partial\Theta}-\xi_1\frac{\partial\xi_1}{\partial\Theta}\frac{\partial^2\Phi_0}{\partial r\partial\Theta}+2\xi_1\frac{\partial\xi_1}{\partial\Theta}\frac{\partial\Phi_0}{\partial\Theta}\right]_{r=1}+O(\varepsilon^3). \quad (3D)$$

For $S\{(r, \Theta, \varphi) \equiv r = 1 + \xi(\Theta, t); 0 \le \Theta < \pi; 0 \le \varphi < 2\pi\}$, we have

$$dS=\frac{r^2\sin\Theta}{\cos\gamma}d\Theta d\varphi=\frac{r^2\sin\Theta}{(\mathbf{e}_r\cdot\mathbf{n})}d\Theta d\varphi$$

$$=\frac{(1+2\xi+\xi^2)\sin\Theta}{1-\frac{1}{2}\left(\frac{\partial\xi}{\partial\Theta}\right)^2+O(\varepsilon^3)}d\Theta d\varphi, \quad (4D)$$

$$dS=\left(1+2\xi_1+2\xi_2+\xi_1^2+\frac{1}{2}\left(\frac{\partial\xi}{\partial\Theta}\right)^2\right)\sin\Theta d\Theta d\varphi,$$

where $\cos\gamma$ is the cosine of the angle between the radial unit vector $\mathbf{e}_r$ and the normal $\mathbf{n}$ to the drop surface. The zeroth-order terms in (1)–(11) are easily determined by using (1D)–(4D), (1B), and (12)–(15). The complete mathematical formulation of the zeroth-order problem is given by (16). Using its solution, $\Phi_0 = Q/r$, we can simplify (1D)–(4D) and write out the following approximations:

$$r=1+\xi:$$

$$\Phi=Q+(\Phi_1-Q\xi_1)_{r=1}$$

$$+\left[\Phi_2-Q\xi_2+\xi_1\frac{\partial\Phi_1}{\partial r}+\xi_1^2Q\right]_{r=1}+O(\xi^3), \quad (5D)$$

$$\mathfrak{F}_E=\frac{E^2}{8\pi}=\frac{(\nabla\Phi)^2}{8\pi}=\frac{Q^2}{4\pi}-\frac{Q}{4\pi}\left(\frac{\partial\Phi_1}{\partial r}+2\xi_1Q\right)_{r=1}$$

$$-\frac{Q}{4\pi}\left[\frac{\partial\Phi_2}{\partial r}+2\xi_2Q+\xi_1Q\frac{\partial^2\Phi_1}{\partial r^2}-2\xi_1\frac{\partial\Phi_1}{\partial r}-5\xi_1^2\right]_{r=1} \quad (6D)$$

$$+\frac{1}{8\pi}\left[\frac{\partial\Phi_1}{\partial r}\right]_{r=1}^2+\frac{1}{8\pi}\left[\frac{\partial\Phi_1}{\partial\Theta}\right]_{r=1}^2+O(\varepsilon^3),$$

$$\frac{\partial\Phi}{\partial n}dS=\left\{-Q+\left[\frac{\partial\Phi_1}{\partial r}+\frac{\partial\Phi_2}{\partial r}+2\xi_1\frac{\partial\Phi_1}{\partial r}\right.\right.$$

$$\left.\left.+\xi_1\frac{\partial\Phi_1^2}{\partial r^2}-\frac{\partial\xi_1}{\partial\Theta}\frac{\partial\Phi_1}{\partial\Theta}\right]_{r=1}\right\}d\Theta d\varphi. \quad (7D)$$

The expansions of the velocity potential ψ and its partial derivatives on the drop surface are constructed by analogy with (1D), and we have

$$r=1+\xi:\ \psi=\left[\psi_1+\psi_2+\xi_1\frac{\partial\psi_1}{\partial r}\right]_{r=1}+O(\varepsilon^3), \quad (8D)$$

$$\frac{\partial\psi}{\partial r}=\left[\frac{\partial\psi_1}{\partial r}+\frac{\partial\psi_2}{\partial r}+\xi_1\frac{\partial^2\psi_1}{\partial r^2}\right]_{r=1}+O(\varepsilon^3), \quad (9D)$$

$$\frac{\partial\xi}{\partial\Theta}\frac{\partial\psi}{\partial\Theta}=\left[\frac{\partial\xi_1}{\partial\Theta}\frac{\partial\psi_1}{\partial\Theta}\right]_{r=1}+O(\varepsilon^3),$$

$$(\nabla\cdot\psi)^2=\left(\frac{\partial\psi_1}{\partial r}\right)_{r=1}+\left(\frac{\partial\psi_1}{\partial\Theta}\right)_{r=1}+O(\varepsilon^3). \quad (10D)$$

REFERENCES

1. A. I. Grigor'ev and S. O. Shiryaeva, Izv. Akad. Nauk, Mekh. Zhidk. Gaza, No. 3, 3 (1994).
2. J. A. Tsamopoulos and R. A. Brawn, J. Fluid Mech. **147**, 373 (1984).
3. R. Natarayan and R. A. Brawn, Proc. R. Soc. London, Ser. A **410**, 209 (1987).
4. W. A. Pelecasis and J. A. Tsamopoulos, Phys. Fluids A **2**, 1328 (1990).
5. J. Q. Feng and K. V. Beard, J. Fluid Mech. **227**, 429 (1991).
6. T. G. Wong, A. V. Anilkumar, and C. P. Lee, J. Fluid Mech. **308**, 1 (1996).
7. Z. C. Feng, J. Fluid Mech. **333**, 1 (1997).
8. Lord Rayleigh (J. W. Strett), Philos. Mag. **14**, 184 (1882).
9. L. D. Landau and E. M. Lifshitz, *Course of Theoretical Physics*, Vol. 8: *Electrodynamics of Continuous Media* (Nauka, Moscow, 1982; Pergamon, New York, 1984).
10. L. D. Landau and E. M. Lifshitz, *Hydrodynamics* (Nauka, Moscow, 1986).
11. A. Nayfeh, *Introduction to Perturbation Techniques* (Wiley, New York, 1981; Mir, Moscow, 1984).
12. S. O. Shiryaeva, A. I. Grigor'ev, and I. D. Grigor'eva, Zh. Tekh. Fiz. **65** (9), 39 (1995) [Tech. Phys. **40**, 885 (1995)].

Translated by V. Gursky

Technical Physics, Vol. 45, No. 8, 2000, pp. 1009–1013. Translated from Zhurnal Tekhnicheskoĭ Fiziki, Vol. 70, No. 8, 2000, pp. 53–57.

Electron Heat Transport in the Magnetic Filter of a Volume Plasma-Based Source of H^-/D^- Ions

O. L. Veresov, S. V. Grigorenko, and S. Yu. Udovichenko

Efremov Research Institute of Electrophysical Apparatus, St. Petersburg, 189631 Russia

Received June 22, 1999

Abstract—A time-independent one-dimensional model of the electron energy balance in the region of the magnetic filter of a volume plasma-based ion source is justified. The local electron energy balance equation and the steady density profiles of the plasma components are used to determine the transverse (with respect to the magnetic field) electron temperature profile, which is found to agree well with the experimental profile. The temperature profile obtained analytically is then used to refine the particle balance in a plasma with two ion species and, accordingly, to find the optimum conditions for the formation of an H^-/D^- beam and for extracting the beam from the source. © *2000 MAIK "Nauka/Interperiodica".*

INTRODUCTION

In [1], we proposed a model describing the transport of a plasma with two ion species across the magnetic field in a steady volume plasma-based source of negative ions which is intended to inject ion beams into cyclotron accelerators from the outside. Profiles of the electric field and of the densities of the plasma components obtained with this model allowed us to determine the optimum conditions for the formation of an H^-/D^- beam. The calculated plasma parameters were found to agree qualitatively with the experimental data obtained in multipole two-chamber ion sources with a magnetic filter adjacent to the plasma electrode [1, 2]. However, a qualitative comparison between the numerical and experimental results turned out to be incorrect, because, in simulations, we specified the experimentally measured mean electron temperature in the first chamber (where the plasma is created) and neglected the electron temperature variations in the second chamber (in the region of the magnetic filter), whereas the experimental data show that the electron temperature depends on the magnetic and electric fields, as well as on some other plasma parameters in the magnetic filter region. The plasma electrons along the magnetic filter may be cooled markedly, which leads to a more efficient generation of negative ions via the dissociative attachment of slow electrons to the excited gas molecules.

The cooling of plasma electrons in the transverse magnetic field of a volume plasma-based ion source was studied in [3, 4]. However, the formula derived in those papers to describe the electron temperature variations is semiempirical, because the authors assumed that the electron heat flux through the magnetic filter is proportional to the electron flux itself. The proportionality coefficient was varied over a broad range and was determined by bringing the calculated profile of the electron temperature as a function of the magnetic flux into coincidence with the relevant experimental profile. The profile derived by Haas *et al.* [5] to describe the spatial variation of the electron temperature along the magnetic filter is also semiempirical. The constants characterizing this profile were found from the corresponding experimental profiles of the electron density, electron temperature, and plasma potential. In the theoretical model proposed in [5], the steady-state electron plasma density across the magnetic field was described by an exponentially decreasing one-dimensional profile and the electron temperature was assumed to be a two-dimensional function of the coordinates. However, a comparison between the electron-energy relaxation length and the sizes of the chamber of the ion source under consideration shows that electron heat conduction equalizes the electron temperature along the magnetic field. Consequently, the electron temperature should be treated as a one-dimensional function of the coordinate transverse to the magnetic field.

In this paper, we apply the electron energy balance equation and the density profiles of the plasma components [1] in order to derive a steady-state transverse (with respect to the magnetic field) electron temperature profile in a multipole two-chamber ion source. Then, we use the temperature profile obtained analytically in order to refine the particle balance in a plasma with two ion species and, accordingly, to find the optimum condition for the formation of an H^-/D^- beam and for extracting the beam from the source.

1063-7842/00/4508-1009$20.00

JUSTIFICATION FOR THE USE OF A ONE-DIMENSIONAL ELECTRON ENERGY BALANCE EQUATION

We analyze electron heat transport in a magnetic field using the classical scheme of a multicusp two-chamber ion source described in [1, 2] as an example. The second chamber (the region of the magnetic filter) is a cylinder of radius R and length L_f. A plasma electrode with an exit hole is positioned at the end of the second chamber and is aimed at extracting ion beams from the source. The longitudinal profile of the magnetic field, which is directed along the z-axis of a cylinder, is bell-shaped. We neglect the magnetic field nonuniformity and set the magnetic field B equal to its mean value along a magnetic filter of length L_f in order for the magnetic flux $\int_0^{L_f} B dz$ to be conserved. We put the origin of the coordinates at the entrance to the second chamber, so that the region where the plasma is created (the first chamber) corresponds to the negative values of the ordinate z.

The time-independent electron energy balance equation in the second chamber is generally three-dimensional. Under the condition that the energy of the directed motion is much lower than the thermal energy, $m_e u_e^2/2 \ll T_e$, the energy balance equation has the form [6]

$$\frac{2}{3}\operatorname{div}\mathbf{q}_e + (n_e\mathbf{u}_e)\nabla T_e + \frac{2}{3}n_e T_e \operatorname{div}\mathbf{u}_e + \frac{2m_e}{m_0}n_e T_e \nu_{e0} = 0, \quad (1)$$

where $\mathbf{q}_e$ is the electron heat flux, $\mathbf{u}_e$ is the directed electron velocity, n_e is the electron density, T_e is the electron temperature, m_e is the mass of an electron, m_0 is the mass of a gas molecule, and ν_{e0} is the averaged (over the relative velocities) rate of elastic collisions between electrons and molecules.

Let us show that the electron temperature is a one-dimensional function of the coordinates $T_e(z)$. In a weakly ionized plasma, the electron-energy relaxation lengths along and across the magnetic field are equal to [7]

$$\lambda_\parallel = \left(\frac{10}{3}\frac{T_e}{m_e^2}\frac{m_0}{\nu_{e0}}\right)^{1/2}, \quad \lambda_\perp = \lambda_\parallel\frac{\nu_{e0}}{\omega_{Be}}, \quad (2)$$

where $\omega_{Be} = eB/m_e c$ is the electron gyrofrequency.

Estimates made for sources of the type under consideration suggest that $\lambda_\parallel \gg R$ and $\lambda_\perp < L_f$. Consequently, electron heat conduction equalizes the electron temperature along the magnetic field, and the local energy balance across the magnetic field can be described by equation (1).

In equation (1), the directed electron velocity is defined as

$$\begin{aligned}\mathbf{u}_e &= \mathbf{u}_{e\parallel} + \mathbf{u}_{ed} + \mathbf{u}_{et},\\ \mathbf{u}_{e\parallel} &= b_{e\parallel}\mathbf{E}_{e\parallel} - D_{e\parallel}\frac{\nabla_\parallel(n_e T_e)}{n_e T_e},\\ \mathbf{u}_{et} &= b_{e\perp}\mathbf{E}_\perp - D_{e\perp}\frac{\nabla_\perp(n_e T_e)}{n_e T_e},\\ \mathbf{u}_{ed} &= b_{ed}[\mathbf{E}\times\mathbf{h}] + D_{ed}\frac{[\mathbf{h}\times\nabla(n_e T_e)]}{n_e T_e},\end{aligned} \quad (3)$$

where $\mathbf{h}$ is the unit vector along the magnetic field and $\mathbf{u}_{e\parallel}$, $\mathbf{u}_{et}$, and $\mathbf{u}_{ed}$ are the directed-velocity components along and across the magnetic field, respectively.

In a strong magnetic field, the electron transport coefficients have the form $b_{e\parallel} = e/m_e\nu_{e0}$, $D_{e\parallel} = T_e b_{e\parallel}/e$, $b_{ed} = e/m_e\omega_{Be}$, $D_{ed} = T_e b_{ed}/e$, $b_{e\perp} = e\nu_{e0}/m_e\omega_{Be}^2$, and $D_{e\perp} = b_{e\perp}T_e/e$.

The electric field $E_\perp$ is driven by a current flowing through the magnetic filter when the plasma electrode is held at a positive bias potential relative to the walls of both the first and second chambers of the source. In the central region of the second chamber, the conditions $\mathbf{E}_\perp \gg \mathbf{E}_\parallel$ and $\nabla_\perp n_e \gg \nabla_\parallel n_e$ are satisfied for a plasma with two ion species such that the density of negative ions is comparable with the electron density. The electric field causes negative ions with the temperature $T_i \ll T_e$ to accumulate near the chamber axis, thereby creating an ion–ion plasma with a weak field $E_\parallel \sim T_i/e$ in the axial region [7]. Since this field is not strong enough to confine the electrons, the radial electron density $n_e(r)$ is nearly constant. An electron–ion plasma with a strong ambipolar field $E_\parallel \sim T_e/e$ occupies the region near the chamber wall; moreover, the plasma potential drops preferentially in a narrow charged sheath in the immediate vicinity of the wall. Consequently, far from the wall of the second chamber, we can neglect the contribution to equation (1) of the velocity component $\mathbf{u}_{e\parallel}$ in comparison with the contribution of $\mathbf{u}_{et}$.

In (1), the electron heat flux has the form

$$\begin{aligned}\mathbf{q}_e &= \mathbf{q}_{e\parallel} + \mathbf{q}_{et} + \mathbf{q}_{ed},\\ \mathbf{q}_{e\parallel} &= n_e T_e b_{e\parallel}\mathbf{E}_\parallel - \frac{5}{2}n_e D_{e\parallel}\nabla_\parallel T_e,\\ \mathbf{q}_{et} &= -g_{Te}[n_e T_e b_{e\perp}\mathbf{E}_\perp + \nabla_\perp(n_e T_e D_{e\perp})]\\ -\frac{5}{2}n_e D_{e\perp}\nabla_\perp T_e &= -g_{Te}n_e T_e\mathbf{u}_{et} - \left(\frac{5}{2}+g_{Te}\right)n_e D_{e\perp}\nabla_\perp T_e,\\ \mathbf{q}_{ed} &= -n_e T_e b_{ed}[\mathbf{h}\times\mathbf{E}] + \frac{5}{2}D_{ed}[\mathbf{h}\times\nabla_\perp(n_e T_e)],\end{aligned} \quad (4)$$

where $g_{Te} = (T_e/\nu_{e0})(\partial\nu_{e0}/\partial T_e)$ is the thermal diffusivity.

For $T_e \le 3$ eV, the cross section σ_{e0} for elastic electron–molecule collisions is independent of the electron temperature [8]. In this case, the collision frequency is proportional to the electron velocity, and, under the assumption that the electrons obey a Maxwellian velocity distribution, the effective collision frequency has the form [6] $\nu_{e0} = (4/3)\sigma_{e0} n_{H_2} v_{Te}$, where $v_{Te} = (8T_e/\pi m_e)^{1/2}$ is the electron thermal velocity and n_{H_2} is the density of the gas molecules. Accordingly, the thermal diffusivity is equal to $g_{Te} = 1/2$.

Repeating the arguments regarding the longitudinal and transverse components of the directed velocity, we can also neglect the electron heat flux $\mathbf{q}_{e\|}$ along the magnetic field in comparison with the cross-field flux $\mathbf{q}_{e\perp}$. The components $\mathbf{u}_{ed}$ and $\mathbf{q}_{ed}$ of the electron velocity and electron heat flux do not contribute to equation (1), because, for a uniform magnetic field, we have $\nabla[\mathbf{h} \times \mathbf{E}]$, $\nabla[\mathbf{h} \times \nabla(n_e T_e)] = 0$. Hence, far from the wall of the second chamber of the ion source, the electron energy balance equation (1) is one-dimensional and the directed electron velocity and electron heat flux are described by the above expressions for $\mathbf{u}_{et}(z)$ and $\mathbf{q}_{et}(z)$, respectively.

PROFILES OF THE ELECTRON TEMPERATURE AND OF THE DENSITIES OF THE PLASMA COMPONENTS ALONG THE MAGNETIC FILTER

To determine the electron temperature from equation (1) requires a knowledge of the steady profiles of the electron density and electric field in a current-carrying plasma. Plasma transport across a strong magnetic field is governed by heavy plasma ions rather than by plasma electrons. Using the one-dimensional model developed in [1] to describe the transport of a plasma with two ion species across the magnetic field and taking into account the condition that the plasma is quasineutral, we can obtain the following equations for the densities of negative ions $n_-(x)$ and electrons $n_e(x)$ in a source of H^-/D^- ions:

$$\frac{dn_-^*}{dx} + \alpha_2 n_-^{*2} - \alpha_1 n_-^* = 0, \quad (5)$$

$$n_e = \frac{\beta}{\gamma} n_-. \quad (6)$$

Here, $x = z/L_f$, $n_-^* = n_-/n_{-0}$, $n_{-0} = n_-(x = 0)$,

$$\alpha_2 = \left(1 + \frac{\beta}{\gamma}\right)\frac{\gamma^2}{\beta}\frac{S_{MN}}{S_{ED}}\frac{L_f}{b_+ E_0}\left[1 + \frac{b_+}{b_-}\left(1 + \frac{\beta}{\gamma}\right)\right],$$

$$\alpha_1 = \gamma\frac{S_{IZ}}{S_{ED}}\frac{n_H}{n_{-0}}\frac{L_f}{b_+ E_0}\left[1 + \frac{b_+}{b_-}\left(1 + \frac{\beta}{\gamma}\right)\right],$$

$\beta = S_{AD} n_H$, $\gamma = S_{DA} n_{H_2(v'')}$, n_H is the atomic density, $n_{H_2(v'')}$ is the density of the excited gas molecules, $S_{AD} = \langle\sigma v\rangle_{AD}$ is the rate of associative detachment of electrons from negative ions in their collisions with H atoms, $S_{DA} = \langle\sigma v\rangle_{DA}$ is the rate of dissociative attachment of electrons to the excited molecules $H_2(v'')$, $S_{MN} = \langle\sigma v\rangle_{MN}$ is the ion–ion recombination rate, $S_{ED} = \langle\sigma v\rangle_{ED}$ is the rate of electron detachment from negative ions in electron–negative-ion collisions, $S_{IZ} = \langle\sigma v\rangle_{IZ}$ is the rate of ionization of H atoms by electrons, E_0 is the electric field of a current-carrying plasma at the entrance to the filter, and $b_\pm = e\nu_{\pm 0}/2m_\pm\omega_{B\pm}^2$ are the mobilities of positive and negative ions.

Equation (5) was derived in the approximation $d\gamma/dx \ll S_{ED} dn_-/dx$ and $d\ln(S_{ED})/dx \ll d\ln(n_-)/dx$. The density of the excited molecules is determined from the balance between their production and losses:

$$n_{H_2} n_{ef} S_{EV} = n_{H_2(v'')}\nu_{H_2}/bR, \quad (7)$$

where n_{ef} is the density of fast electrons emitted from the heated cathode into the first chamber, S_{EV} and ν_{H_2} are the production rate of the excited molecules and their mean directed velocity, and $b = 5$–10 is the number of collisions of the excited molecule with the wall that still do not change the excited state of the molecule.

Estimates show that the loss rates of the excited gas molecules on the walls of both the first and second chambers are higher than the rates of their quenching in the processes of dissociative attachment (S_{DA}) and ionization (S_{IZ}) in the source plasma.

In a first approximation, we assume that α_1 and α_2 are independent of both the electron temperature and the x-coordinate. Then, we obtain from (5) and (6) the steady profile of the electron plasma density:

$$n_e^*(x) = \exp(\alpha_1 x)\left[1 - \frac{\alpha_2}{\alpha_1}(1 - \exp(\alpha_1 x))\right]^{-1}, \quad (8)$$

where we introduce the notation $n_e^*(x) = n_e(x)/n_{e0}$ and $n_{e0} = n_e(x = 0)$.

Accordingly, for $\alpha_1 x \ll 1$, the electric field profile in a current-carrying plasma is given by the expression

$$E_\perp(x) = E_0/n_-^*(x) \approx E_0[1 + (\alpha_2 - \alpha_1)x]. \quad (9)$$

Here, $E_0 = 2(\varphi_0 - \varphi_e)/(2 + \alpha_2)L_f$, where φ_0 is the plasma potential in the first chamber and φ_e is the potential of the plasma electrode.

In the model proposed here to describe the electron heat transport in the second chamber of a volume

plasma-based ion source, equation (1) reduces to the following equation for the electron temperature:

$$\frac{d^2y}{dx^2} + \frac{A}{y}\left(\frac{dy}{dx}\right)^2 - D + 0.33E_\perp^*\frac{dy}{ydx} + 0.29\frac{dE_\perp^*}{dx}$$
$$+\left(0.11E_\perp^* + 1.52\frac{dy}{dx}\right)\frac{d\ln(n_e^*)}{dx} + 0.29y\frac{d^2\ln(n_e^*)}{dx^2} \quad (10)$$
$$+ 0.11y\left(\frac{d\ln(n_e^*)}{dx}\right)^2 = 0,$$

where $y = T_e(x)/T_{e0}$, $T_{e0} = T_e(x = 0)$, $E_\perp^* = E_\perp eL_f/T_{e0}$, $A = 1.64$, and $D = 0.57\omega_{Be}^2 m_e^2 L_f^2/m_0 T_{e0}$.

Ignoring the electric field $E_\perp^*$ and the derivative dn_e^*/dx, we obtain the following solution to equation (10):

$$y_0(x) = \frac{T_e(x)}{T_{e0}} = \left[1 - \frac{1}{2}\left[\frac{2D}{2A+1}\right]^{1/2} x\right]^{1/2}. \quad (11)$$

An analysis of equation (10) shows that, for $x \le 1$, the electric field of a current-carrying plasma contributes to the electron temperature only in the region where this field is maximum. At small values of the argument $x \ge 0$, it is important to take into account the electron density profile.

For $\alpha_1 x \ll 1$, we can use expression (8) to obtain from (10) the following equation for T_e at $x \ge 0$:

$$y\frac{d^2y}{dx^2} + A\left(\frac{dy}{dx}\right)^2 - Dy + Cy^2(1 + \alpha_2 x)^{-2} = 0, \quad (12)$$

where $C = 0.38(\alpha_2 - \alpha_1)\alpha_2$.

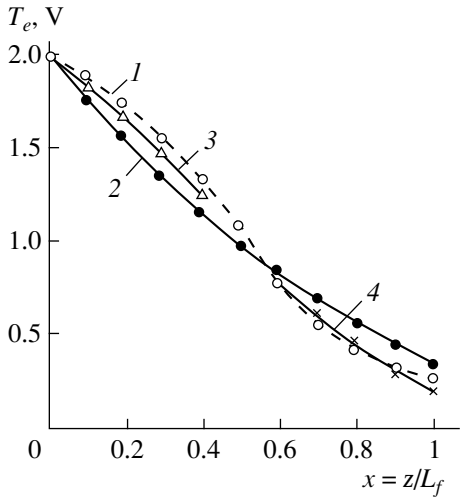

Fig. 1. Electron temperature profiles along the source axis in the region of the magnetic filter: (*1*) experimental profile, (*2*) profile calculated from (11), (*3*) corrected profile (14), and (*4*) corrected profile (16).

This equation can be transformed into the first-order differential equation

$$\left(\frac{dy}{dx}\right)^2 = \frac{2D}{2A+1}y - \frac{Cy^2}{(1 + \alpha_2 x)^2(A+1)}, \quad (13)$$

in which the second term on the right-hand side is a small correction to the first term. Solving equation (13) by the method of successive approximations yields

$$y(x \ge 0) = y_0(x) + C_1\frac{x}{1 + \alpha_2 x}, \quad (14)$$

where $y_0(x)$ is defined in (11) and $C_1 = C[(2D/(2A + 1))^{-1/2} + 3/2\alpha_2]/2(A + 1)$.

For $x \le 1$, we can neglect the second derivative of the function y in comparison with the leading-order term D_1 in equation (10) and apply the method of successive approximations to solve the equation

$$A\left(\frac{dy}{dx}\right)^2 + 0.33\frac{eE_0L_f}{T_{e0}}[1 + (\alpha_2 - \alpha_1)x]\frac{dy}{dx} - D_1 y = 0, \quad (15)$$

where $D_1 = D - 0.29(\alpha_2 - \alpha_1)eE_0L_f/T_{e0}$.

In this case, the electron temperature profile has the form

$$y(x \le 1) = \left[1 - \frac{1}{2}\left(\frac{D_1}{A}\right)^{1/2} x\right]^{1/2} - \frac{0.08eE_0L_f}{A(\alpha_2 - \alpha_1)T_{e0}}[1 + (\alpha_2 - \alpha_1)x]^2. \quad (16)$$

We compared the calculated and experimental profiles $T_e(x)$ for the following parameters of the plasma and of the ion source [2]: $B = 100$ G, $L_f \approx 5$ cm, $R = 5$ cm, $n_{H_2} = 10^{14}$ cm^{-3}, $n_H = 10^{13}$ cm^{-3}, $n_{e0} \approx 9 \times 10^{12}$ cm^{-3}, $T_{e0} \approx 2$ eV, $\varphi_0 \approx 4$ eV, and $\varphi_e \approx 1.25$ eV. Figure 1 shows the experimental (curve *1*) electron temperature profile and the analytic (curve *2*) profile $T_e(x)$ calculated from (11). In a first approximation, we assume that the parameters α_1 and α_2 are independent of both the electron temperature and the x-coordinate. We bring the profile $n_e(x)$ calculated from (8) into coincidence with the experimental electron density profile (see Fig. 2) to obtain $\alpha_2 \approx 3.3$ and $\alpha_1 \approx 0.3$. Substituting these parameter values into formulas (14) and (16), we determine the corrections to the electron temperature profile (11), which are represented in Fig. 1 by curves *3* and *4*, respectively.

Note that, for the above parameters of the ion-source plasma, the conditions for the electron energy relaxation $\lambda_\parallel \gg R$ and $\lambda_1 < L_f$ and the condition $m_e u_e^2/2 \ll T_e$ are all well satisfied. The directed electron

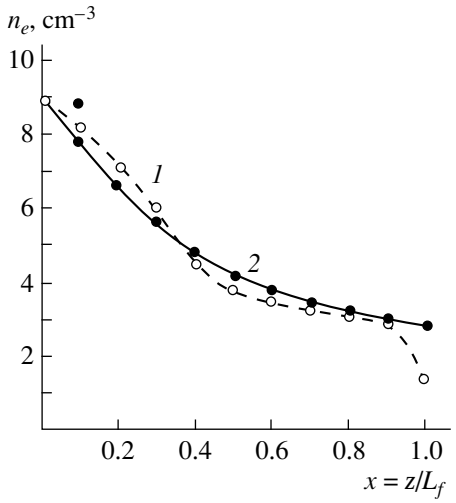

Fig. 2. Electron density profiles in the magnetic filter: (*1*) experimental profile and (*2*) profile calculated from (8).

velocity should be estimated from the maximum component $\mathbf{u}_{ed}$ in expression (3).

By virtue of the relationship $\beta/\gamma \approx 1.5$, our model of the electron heat transport across the magnetic field far from the wall of the second chamber is one-dimensional with a fairly high degree of confidence. When the associative detachment of electrons from negative ions is enhanced (i.e., when $\beta/\gamma \gg 1$ and $n_e \gg n_-$), the electron–ion plasma expands from the wall toward the chamber axis and occupies most of the volume of the ion source [7]. In this case, the electron density becomes two-dimensional and the one-dimensional approach used here fails.

CONCLUSION

The one-dimensional model proposed here to describe the electron energy balance in the region of the magnetic filter of a volume plasma-based ion source allowed us to determine the electron temperature profile along the source axis. The analytic profile agrees well with the experimental one and makes it possible to refine the rates of the elementary processes that are sensitive to the electron temperature and govern the equilibrium density profiles (6) and (8) of the plasma components.

In a second approximation, equation (5) for the density of negative ions should be solved with the coordinate-dependent coefficients $\alpha_2(x)$ and $\alpha_1(x)$. The solution to this equation,

$$n_-^* = F(x)\left(\int_0^x \alpha_2(x)F(x)dx + 1\right)^{-1},$$

where $F(x) = \exp\int_0^x \alpha_1(x)dx$, then enables us to refine the density profile of negative ions in the magnetic filter region adjacent to the plasma electrode. By controlling this profile, it is possible to form ion beams with the maximum current and to extract them from the source.

The above plasma parameters are representative of ion sources of the type under consideration. Under the conditions prevailing in these sources, taking into account the electron-density and electric-field profiles yields a small correction to the electron temperature profile in the region of the magnetic filter. Specifically, the variables $n_e(x)$ and $T_e(x)$ in the electron energy balance equation become independent of each other. The electron density is determined from the model of the transport of heavy plasma components across the magnetic field, under the assumption that the plasma is quasi-neutral. In this case, electron temperature variations may substantially change the plasma density profile.

If the plasma electric field is strong (with an increased potential φ_0 in the first chamber and a decreased potential φ_e of the plasma electrode), then the relation between the electron-density and electron-temperature profiles becomes closer. An increase in the plasma electric field raises the intensity of the electron heat flux q_{et} (4), which is directed toward the first chamber (where the plasma is created) and is governed by the directed electron velocity. As a result, the plasma electrons are cooled more efficiently in the magnetic filter region adjacent to the plasma electrode.

REFERENCES

1. O. L. Veresov, S. V. Grigorenko, and S. Yu. Udovichenko, Zh. Tekh. Fiz. **70** (4), 111 (2000) [Tech. Phys. **45**, 236 (2000)].
2. K. Jayamanna, M. McDonald, D. H. Yuan, and P. W. Schmor, in *Proceedings of the European Particle Accelerator Conference, EPAC-90, Nice, 1990*, p. 647.
3. M. Ogasawara, T. Yamakawa, F. Sato, and Y. Okumura, in *Proceedings of the International Symposium on the Production and Neutralization of Negative Ion Beams, Brookhaven, 1990*, p. 596.
4. A. J. T. Holmes in *Proceedings of the International Symposium on the Production and Neutralization of Negative Ion, Brookhaven, 1992*, p. 101.
5. F. A. Haas, L. M. Lea, and A. J. T. Holmes, J. Phys. D **24**, 1541 (1991).
6. V. E. Golant, A. P. Zhilinskii, and I. E. Sakharov, *Fundamentals of Plasma Physics* (Atomizdat, Moscow, 1977; Wiley, New York, 1980).
7. V. A. Rozhanskiĭ and L. D. Tsendin, *Collision Transfer in a Partially Ionized Plasma* (Énergoatomizdat, Moscow, 1988).
8. J. P. Shkarofsky, T. W. Johnston, and M. P. Bachynski, *The Particle Kinetics of Plasmas* (Addison-Wesley, Reading, 1966; Atomizdat, Moscow, 1969).

Translated by O. E. Khadin

Technical Physics, Vol. 45, No. 8, 2000, pp. 1014–1018. Translated from Zhurnal Tekhnicheskoĭ Fiziki, Vol. 70, No. 8, 2000, pp. 58–62.

SOLIDS

Simulation of the Melting and Crystallization Processes in Monocrystalline Silicon Exposed to Nanosecond Laser Radiation

S. P. Zhvavyĭ

Institute of Electronics, Belarussian Academy of Sciences, Minsk, 220090 Belarus

Received October 12, 1998; in final form, July 26, 1999.

Abstract—Numerical simulation of the melting and crystallization processes of monocrystalline silicon exposed to the nanosecond radiation of a ruby laser was carried out with the kinetics of the phase transformations accounted for on the basis of Kolmogorov equations. A two-dimensional mechanism of nucleation and growth of the new phase was invoked to describe the phase transitions. It was shown that the temporal dependences of monocrystal overheating and liquid phase supercooling in the melting and crystallization stages, respectively, are nonmonotonic and determined by the kinetics of the phase transitions. The maximum values of the overheating and supercooling were ~100 K. © *2000 MAIK "Nauka/Interperiodica".*

The melting and recrystallization processes of monocrystalline silicon initiated by nanosecond laser pulses have been studied in many papers (see, for example, [1–4]). Generally, the Stephan problem is solved to clarify the main relationships of the effect of laser irradiation. This approach is warranted for processes deviating only slightly from equilibrium conditions. However, as follows from experimental studies [5–7] on irradiation of semiconductor surfaces by nano- and picosecond laser pulses, phase transitions occur far from equilibrium. In [8, 9], the simulation of laser annealing of amorphous silicon layers takes into account the nonequilibrium character of the processes and is based on a consideration of the phase state of the irradiated sample cell as a function of enthalpy and the elapsed time before nucleation of the new phase. Another approach [10] is based on solving the Stephan problem for the nonlinear dependence of the phase boundary velocity on temperature. However, problems involving the kinetics of the new phase formation have rarely been dealt with in these studies.

This paper presents a model of melting and crystallization of monocrystalline silicon irradiated by a nanosecond ruby laser, which takes into account the kinetics of the phase transformations using Kolmogorov equations [11–13]. We previously used a similar approach in a numerical simulation of laser annealing of amorphous silicon [14, 15], in which the crystallization process of a highly supercooled melt is controlled by a three-dimensional growth mechanism of already available nuclei. Here, it is assumed that both melting and crystallization occur as a result of homogeneous nucleation through two-dimensional layer-by-layer growth [11, 12, 16–18].

Variation of the temperature of monocrystalline silicon irradiated by nanosecond laser pulses is described on the basis of the one-dimensional thermal conductivity equation

$$\rho c(T)\frac{\partial T}{\partial t} = \frac{\partial}{\partial x}\left[k(x, T)\frac{\partial T}{\partial x}\right] + S(x, T) - \rho L\left(\frac{\partial \varphi}{\partial t} - \frac{\partial \Psi}{\partial t}\right) \quad (1)$$

with the boundary and initial conditions

$$\left.\frac{\partial T}{\partial x}\right|_{x = 0} = 0, \quad T(x \longrightarrow \infty, t) = T_0, \quad T(x, t = 0) = T_0, \quad (2)$$

where ρ is the density, $c(T)$ is the specific heat capacity, $k(x, T)$ is the coefficient of thermal conductivity, L is the latent heat of phase transition, and T_0 is the initial temperature.

The heat source term $S(x, t)$ in (1) describes the heat evolved due to absorption of the laser radiation:

$$S(x, t) = (1 - R)\alpha(x, T)\frac{W(T)}{\tau_i} \times \exp\left[-\int_0^x \alpha(x', T)dx'\right], \quad (3)$$

where R and $\alpha(x, T)$ are the reflection and absorption coefficients, respectively, and W and τ_1 are the energy density and duration of the laser pulse, respectively.

The two last terms on the right-hand side of Eq. (1) describe the capacities of heat sinks and sources in melting and crystallization of silicon. Here, $\varphi(x, t)$ is the fraction of the melt formed at point x by the time t after melting begins and $\Psi(x, t)$ is the fraction of crys-

tallized melt at point x by the time t after crystallization begins; in this case, the condition $\varphi(x, t) + \Psi(x, t) + \gamma(x, t) = 1$ should be fulfilled, where $\gamma(x, t)$ is the fraction of monocrystal not melted at point x by the time t. In the theory of phase transitions, the fraction of new phase formed is expressed in terms of the nucleation rate $J(t)$ and the growth rate $V(t)$ [11, 12]:

$$\varphi(x, t) = 1 - \exp\left\{-\beta\int_{t_1}^{t} J(\tau)\left[\int_{\tau}^{t} V(t')dt'\right]^n d\tau\right\}, \quad (4)$$

where t_1 is the time of the start of nucleation at point x and β is the form factor. The function $J(t)$ is determined by the nucleation mechanism. In this study, the kinetics of melting and crystallization is considered in the framework of the layer-by-layer growth model [11, 13]; i. e., it is assumed that the growth of the new phase proceeds as ongrowth of successive layers. The formation of each layer proceeds by two-dimensional growth of nuclei (the exponent $n = 2$ in (4)), and the nuclei of a new ith layer can emerge only in the crystallized regions of the preceding $(i + 1)$th layer. In this case, the expression for the nucleation rate has the form [11, 12]

$$J(t) = N\frac{kT}{h}\exp\left(-\frac{U}{kT}\right)\exp\left(-\frac{\pi a\sigma^2 T_m}{kT\Delta T}\right), \quad (5)$$

where $N = N_0 f(x, t)$, N_0 is the density of atoms per cm^2 at the interface, and $f(x, t) = \Psi(x + a, t) + \gamma(x + a, t) = 1 - \varphi(x + a, t)$ is the fraction of monocrystalline phase of the preceding layer where crystallization centers of the next layer can be formed.

During melting, centers of the liquid phase can arise only in the crystalline regions of the layer and, in this case, $f(x, t) = 1 - \varphi(x, t)$ [12]; U is the activation energy for the transition of an atom through the phase boundary; a is the interatomic distance (the monolayer height); σ is the surface energy of the phase boundary; $\Delta T = T - T_m$ for melting; and $\Delta T = T_m - T$ for crystallization.

The expression used for the growth rate has the form [13]

$$V(t) = a\frac{kT}{h}\exp\left(-\frac{U}{kT}\right)\left[1 - \exp\left(-\frac{L^*}{kT_m}\frac{\Delta T}{T}\right)\right], \quad (6)$$

where L^* is the melting heat per atom.

In the two-phase (transition) region, which includes molten and crystalline silicon, the parameters of the problem are defined as follows [14]:

$$a(x, t) = \varphi(x, t)a_l(x, t) + [1 - \varphi(x, t)]a_s(x, t), \quad (7)$$

where the indices l and s refer to the liquid and crystalline phases, respectively.

Equation (1), in combination with (2)–(7), was solved numerically by a sweep method. The shape of the laser pulse was specified by the function $\sin^2(\pi t/2\tau_i)$ with $\tau_i = 70$ ns. The values of the silicon parameters used in solving the problem are listed in the table.

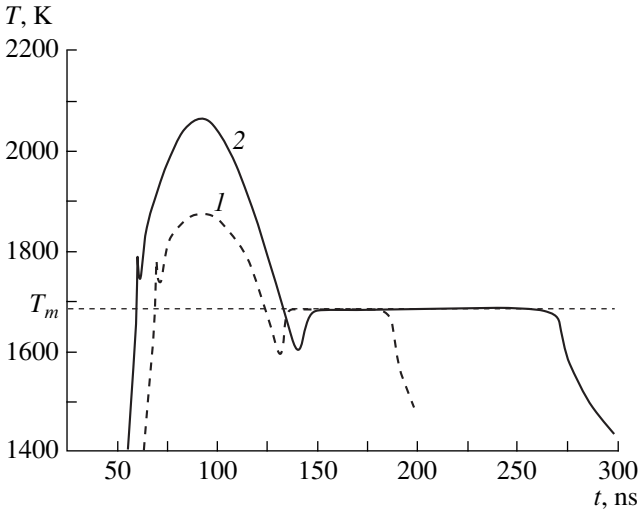

Fig. 1. Temporal dependence of the temperature of silicon surface at a radiation power density of W = (*1*) 1.5 and (*2*) 2 J/cm^2.

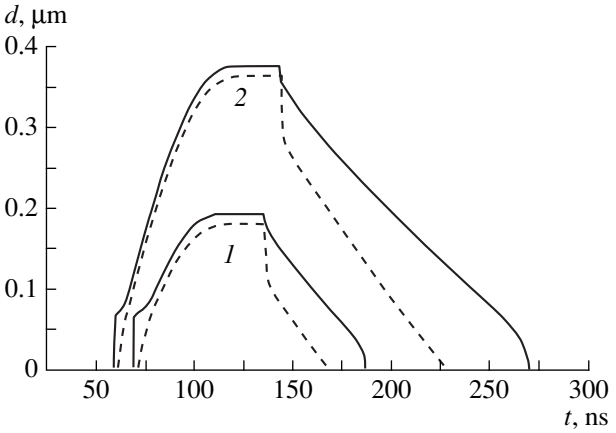

Fig. 2. Temporal dependence of the silicon melting depth. $\varphi = 0.01$ (solid curve), $\varphi = 0.99$ (dashed curve); (*1*, *2*) same as in Fig. 1.

In Fig. 1, the temporal dependences of the temperature of a monocrystalline silicon surface are shown for two values of the energy density, $W = 1.5$ and 2 J/cm^2. It is seen that at the early stage of heating, a narrow peak is observed on the temperature curve. As follows from the calculations, this peak appears as the silicon begins to melt and corresponds to overheating of the surface layer. The overheating before melting starts is as high as $\Delta T \approx 100$ K (Fig. 3), both at $W = 2$ J/cm^2 and $W = 1.5$ J/cm^2. In the time interval $\Delta t < 1$ ns in a near-surface layer $\Delta x \approx 0.075$ μm thick (Figs. 2, 5), nuclei of the liquid phase arise, which at $\Delta T \approx 100$ K start to grow at a high rate (Fig. 4). Because of the large latent heat L of the phase transition in silicon, formation of the melt-

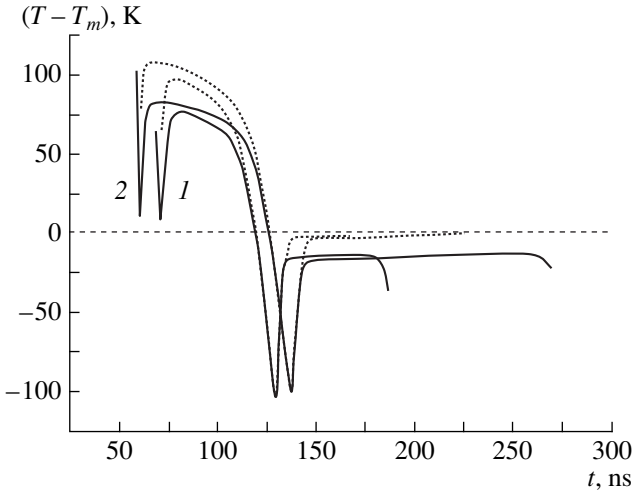

Fig. 3. Temporal dependence of overheating and supercooling of silicon at the boundaries of the two-phase region φ = 0.01 (solid curve) and φ = 0.99 (dashed curve) ((*1*, *2*) same as in Fig. 1).

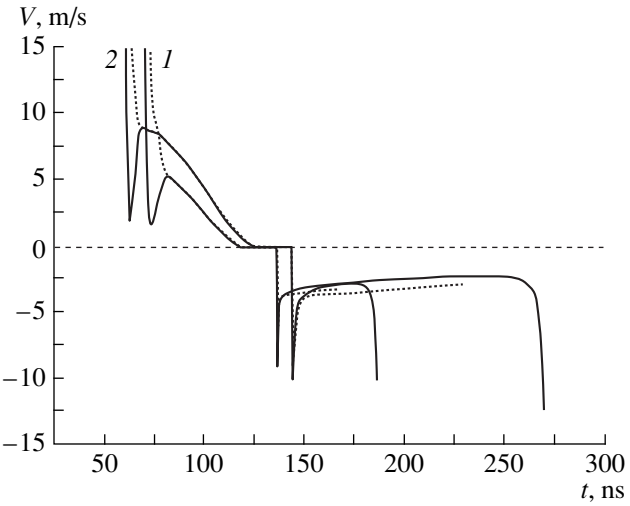

Fig. 4. Temporal dependence of the velocity of advance of the boundaries φ = 0.01 (solid curve) and φ = 0.99 (dashed curve) of the two-phase region at W = (*1*) 1.5 and (*2*) 2 J/cm^2.

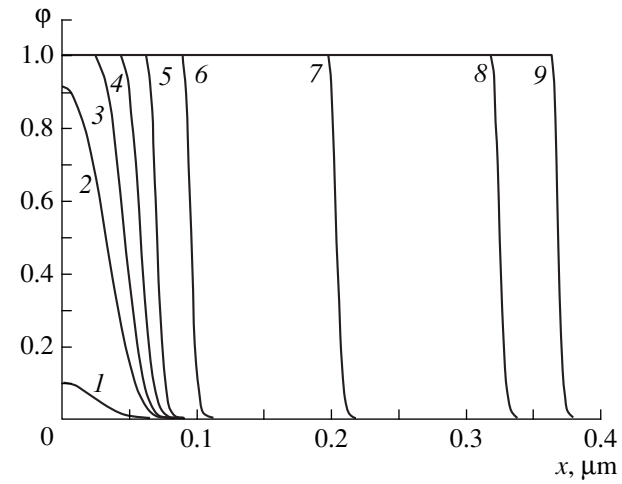

Fig. 5. Depth variation of the silicon liquid phase fraction at W = 2 J/cm^2 at various times t = (*1*) 59, (*2*) 61, (*3*) 62, (*4*) 64, (*5*) 65, (*6*) 68, (*7*) 80, (*8*) 100, and (*9*) 133 ns.

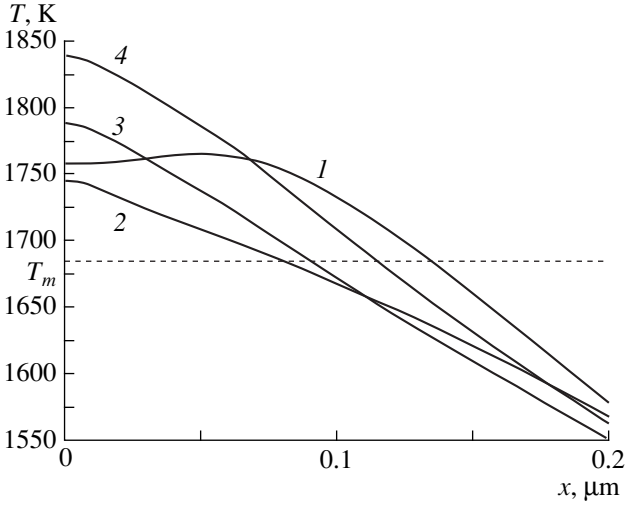

Fig. 6. Calculated temperature profiles at W = 2 J/cm^2 for time t = (*1*) 59, (*2*) 61, (*3*) 62, (*4*) 64 ns.

ing nuclei and their growth causes a reduction in overheating at the forward boundary of the two-phase region down to $\Delta T \approx 10$ K (Fig. 3), cooling of the adjacent crystalline regions (Figs. 5, 6), and a significant reduction in the propagation velocity of the forward boundary down to $V \approx 2$ m/s (Fig. 4).[1] As the forward boundary slowly propagates into the sample bulk (Fig. 5, curves *1*–*5*), an increase in the melt fraction at the surface and formation of the rear boundary of the transition region occur; i.e., a continuous liquid phase layer forms. Thus, at the initial stage of melting of monocrystalline silicon, in time $\Delta t \approx$ 5–6 ns, a molten layer $\Delta x \approx$ 0.07–0.08 μm thick with a fairly narrow transition region $\Delta x \approx 0.015$ μm is formed at the surface (Figs. 2, 5).

Further heating of silicon by laser radiation results in renewed increases in overheating and the velocity of forward boundary movement, both of which attain their maximum values at this stage (Figs. 3, 4). Thus, at W = 2 J/cm^2, $\Delta T|_{\varphi = 0.01} \approx 80$ K and $V|_{\varphi = 0.01} \approx 9$ m/s. At the rear boundary, the overheating is somewhat higher, $\Delta T|_{\varphi = 0.99} \approx 105$ K, and the velocity of the boundary movement $V|_{\varphi = 0.99}$ becomes equal to $V|_{\varphi = 0.01}$, remaining so until completion of the melting process. As the

[1] The condition used to define the position of the rear boundary of the two-phase (transition) region is that the melting (crystallization) process is considered finished if φ = 0.99 (Ψ = 0.99) [8]. The position of the forward boundary is defined by the condition φ = 0.01 (Ψ = 0.01).

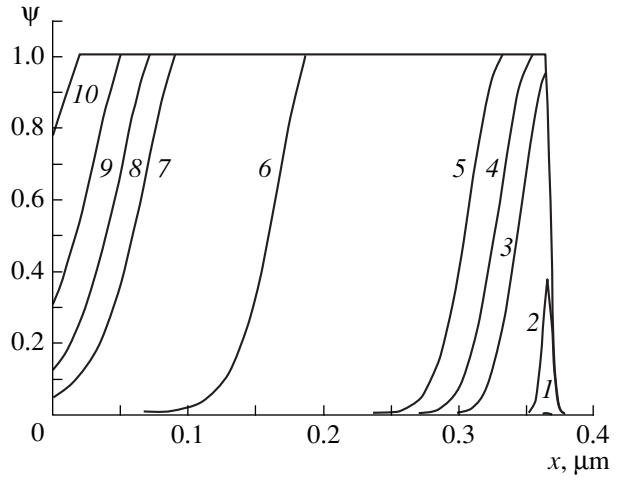

Fig. 7. Depth variation of the fraction of crystallized silicon at $W = 2$ J/cm^2 for time t = (*1*) 136, (*2*) 139, (*3*) 142, (*4*) 145, (*5*) 150, (*6*) 201, (*7*) 243, (*8*) 251, (*9*) 259, and (*10*) 268 ns.

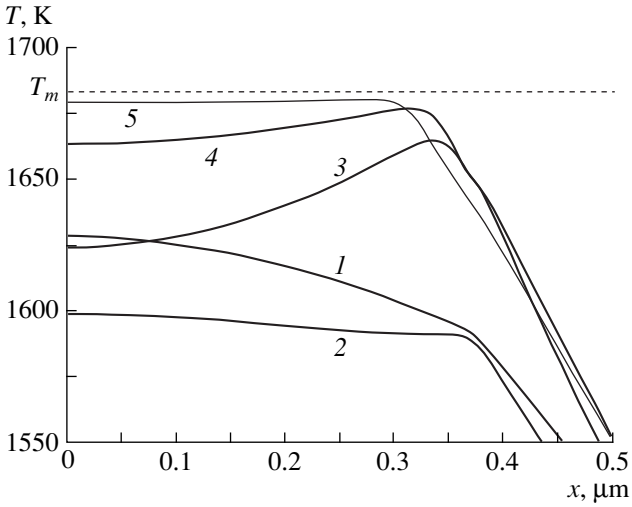

Fig. 8. Calculated temperature profiles at $W = 2$ J/cm^2 for time t = (*1*) 136, (*2*) 139, (*3*) 142, (*4*) 145, and (*5*) 150 ns.

melt moves deeper into the sample bulk and the influx of light energy decreases, the overheating and the propagation rate gradually decrease and, by the time the laser radiation is ended, the ingress of melt into the semiconductor bulk ceases and the two-phase region remains immobile for $\Delta t \approx 20$ ns (Figs. 2, 4). For this period of time, as a result of heat drain to the sample volume, which is no longer compensated by the laser radiation, the overheating vanishes completely and the melt becomes supercooled by $\Delta T \approx 100$ K (Fig. 3) in the vicinity of the transition region and by 80 K (Fig. 1) at the surface. With the onset of, and increase in, supercooling, the formation and growth of the nuclei of the crystalline phase begins (Fig. 7, curve *8*). The heat release in the silicon crystallization process causes an increase in temperature and the emergence of a peak in the temperature profile within the two-phase region (Fig. 8, curves *2–4*). The temperature gradient produced in the melt at the forward boundary of the two-phase region ($\Psi = 0.01$) causes spreading of the transition region toward the surface, increasing its thickness to $\Delta x \approx 0.075$ μm (Fig. 2), since the emerging nuclei of the new layer are subjected to greater supercooling and, consequently, their nucleation and growth rates are higher than in the preceding layer. As more heat is released from growth of the crystalline phase, the temperature distribution becomes uniform (Fig. 8) and supercooling at the forward boundary ($\Psi = 0.01$) and the rear boundary ($\Psi = 0.99$) of the transition region drops to ~4 K and ~18 K, respectively. The velocity of advance of the boundaries decreases to 3–4 m/s. The advance of the crystallization region toward the sample surface is accompanied by a minor temperature increase (of ~2 K); and the velocities $V|_{\Psi = 0.99}$ and $V|_{\Psi = 0.01}$ drop from ~3 to 2.2 m/s and from 4 to 3 m/s, respectively. Only at the final stage, when the thickness of the transition layer becomes less than 0.05 μm (Fig. 2), do the supercooling at the rear boundary and the velocity $V|_{\Psi = 0.99}$ increase sharply (Figs. 3, 4). The reason is that the heat sources contained in a narrow layer with $\psi > 0.5$ are insufficient to offset the heat which is being removed to the sample bulk.

Silicon parameter values

Parameters	Crystalline Si	Molten Si
ρ, g/cm^3	2.328	$2.53–0.152 \times 10^{-3}(T–T_m)$ [19]
c, J/g K	$0.844 + 1.18 \times 10^{-4}T – 1.55 \times 10^4 T^{-2}$ [19]	1.04
L, J/g	1787 [19]	
k, W/cm K	$\frac{1521}{T^{1.226}}$, $T < 1200$ K, $\frac{8.97}{T^{0.5}}$, $T \geq 1200$ K [20]	0.585 [19]
R	0.35	0.72
α, cm^{-1}	$1578\exp(T/493)$ [21]	10^6 [20]
U, eV	1.22 [22]	
σ, erg/cm^2	300	

Thus, the temporal variations of the overheating of crystalline silicon and supercooling of the melt proceed nonmonotonically and depend on the phase transformation kinetics. Maximum overheating and supercooling values, both equal to ~100 K, are attained at the early stages of melting and crystallization, respectively. Formation of a continuous film of melt at the surface of monocrystalline silicon takes 5–6 ns. The average velocity of advance of the two-phase region is ~8–9 m/s for melting and ~3–4 m/s for crystallization.

REFERENCES

1. R. F. Wood and G. E. Giles, Phys. Rev. B **23**, 2923 (1981).
2. D. H. Lowndes, R. F. Wood, and J. Narayan, Phys. Rev. Lett. **52**, 561 (1984).
3. V. A. Pilipovich, V. L. Malevich, G. D. Ivlev, and V. V. Zhidkov, Inzh.-Fiz. Zh. **48**, 306 (1985).
4. G. M. Gusakov, A. A. Komarnitskii, and A. S. Em, Phys. Status Solidi A **107**, 261 (1988).
5. G. E. Jellison, Jr., D. H. Lowndes, D. N. Mashburn, and R. F. Wood, Phys. Rev. B **34**, 2407 (1986).
6. M. Yu. Aver'yanova, S. Yu. Karpov, Yu. V. Koval'chuk, *et al.*, Pis'ma Zh. Tekh. Fiz. **12** (18), 1119 (1986) [Sov. Tech. Phys. Lett. **12**, 462 (1986)].
7. A. G. Cullis, H. C. Weber, N. G. Chew, *et al.*, Phys. Rev. Lett. **49**, 219 (1982).
8. R. F. Wood and G. A. Geist, Phys. Rev. B **34**, 2606 (1986).
9. V. Yu. Balandin, A. V. Dvurechenskiĭ, and L. N. Aleksandrov, Poverkhnost, No. 1, 53 (1986).
10. R. Černy, R. Šašik, I. Lukes, and V. Chab, Phys. Rev. B **44**, 4097 (1991).
11. L. N. Aleksandrov, *Crystallization and Recrystallization Kinetics of Semiconductor Films* (Nauka, Novosibirsk, 1985).
12. V. Z. Belen'kiĭ, *Geometric–Probabilistic Models of Crystallization* (Nauka, Moscow, 1989).
13. V. P. Skripov and V. P. Koverda, *Spontaneous Crystallization of Supercooled Liquids* (Nauka, Moscow, 1984).
14. S. P. Zhvavyĭ, Zh. Prikl. Spektrosk. **50**, 589 (1989).
15. S. P. Zhvavyĭ and O. L. Sadovskaya, Poverkhnost, No. 11, 101 (1990).
16. Ya. I. Frenkel', *Kinetic Theory of Liquids* (Nauka, Leningrad, 1975; Clarendon, Oxford, 1946).
17. M. Vollmer, *Kinetik der Phasenbildung* (Steinkopff, Dresden, 1939; Nauka, Moscow, 1986).
18. L. N. Aleksandrov, *Formation Kinetics and Structures of Solid Layers* (Nauka, Novosibirsk, 1972).
19. A. R. Regel' and V. M. Glazov, *Physical Properties of Electronic Melts* (Nauka, Moscow, 1980).
20. A. E. Bell, RCA Rev. **40**, 295 (1979).
21. M. Toulemonde, S. Unamuno, R. Heddache, *et al.*, Appl. Phys. A **36**, 31 (1985).
22. G. Andra, H.-D. Geiler, G. Gotz, *et al.*, Phys. Status Solidi A **74**, 511 (1982).

Translated by M. Lebedev

Technical Physics, Vol. 45, No. 8, 2000, pp. 1019–1024. Translated from Zhurnal Tekhnicheskoĭ Fiziki, Vol. 70, No. 8, 2000, pp. 63–68.

SOLIDS

The Determination of the Model Interaction Potential Parameters from a Comparison of Experimental and Calculated Ion Ranges in an Amorphous Substance

E. G. Sheĭkin

Research Enterprise for Hypersonic Systems, St. Petersburg, 196066 Russia

Received November 13, 1998

Abstract—Parameters of the model atomic interaction potential are suggested to be determined by comparing the experimental and analytical values of projective ion ranges. The parameters were found for the interaction of Bi, Pb, Au, Yb, Er, Eu, Cs, Xe, Sn, Rb, Kr, Ga, and Cu ions with carbon and boron atoms. © *2000 MAIK "Nauka/Interperiodica".*

The proper selection of atomic interaction potential is of great importance in analysis and numerical simulation of low- and medium-energy ion motion in a substance. The interaction potential must adequately characterize elastic scattering while being easy to apply. In [1], a model interaction potential that basically satisfies these requirements was proposed. It is written in the form of screened Coulomb potential

$$V(r) = \frac{Z_1 Z_2 e^2}{r}\begin{cases}1 - r/a, & r \le a,\\ 0, & r > a,\end{cases} \qquad (1)$$

where Z_1 and Z_2 are the charges of an ion nucleus and target atom, respectively; r is the distance between colliding particles; and a is the screening radius.

It is assumed that the screening radius depends on the ion energy as

$$a = a_{TF}\varepsilon^{-1/4}/\beta. \qquad (2)$$

This relationship provides an adequate description of the experimentally found stopping power of ions in elastic collisions throughout the energy range. Here, $a_{TF} = 0.8853a_0/(Z_1^{2/3} + Z_2^{2/3})^{1/2}$, e is the charge of an electron, and a_0 is the Bohr radius. The reduced energy ε is related to the ion energy E as $\varepsilon = Em_2a_{TF}/(Z_1Z_2e^2(m_1 + m_2))$, where m_1 and m_2 are the masses of an ion and target atom, respectively. The parameter β appearing in (2) is viewed as an adjusting parameter.

In this work, we will try to estimate β for specific ion–target pairs by comparing theoretical and experimental values of projective ion ranges in a substance.

For interaction potential (1) with screening radius (2), the stopping power of ions is given by [1]

$$s_n(\varepsilon) = \frac{\sqrt{\varepsilon}}{\beta^2} f(X(\varepsilon)), \qquad (3)$$

where $f(X) = X[(1 + X)\ln(1 + 1/X) - 1]$ and

$$X(\varepsilon) = \frac{\beta^2}{4(\varepsilon^{3/2} + \beta\varepsilon^{3/4})}.$$

Figure 1 shows the stopping powers of ions $s_n(\varepsilon)$ calculated from (3) for three values of β. It follows that the stopping power depends on β only slightly for $\varepsilon > 2$. Hence, results for ion energies $\varepsilon \le 2$ are the most appropriate if β is determined by comparing the theory and experiment.

Projective ranges will be estimated using results obtained in [2]. In that work, elastic scattering of ions is treated in terms of potential (1) and inelastic scattering is considered within the approximation of continu-

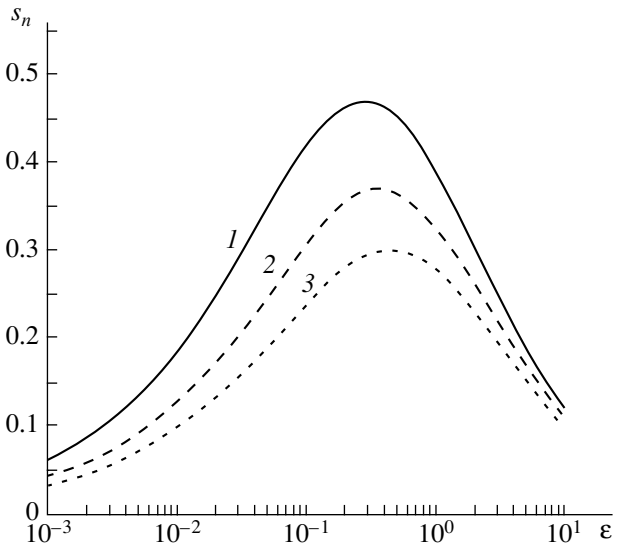

Fig. 1. Stopping power vs. energy for model potential (*1*) with screening radius (*2*) at β = (*1*) 0.5, (*2*) 0.6, and (*3*) 0.7.

1063-7842/00/4508-1019$20.00

ous deceleration with stopping power $s_n(\varepsilon) = k\sqrt{\varepsilon}$, where k is a dimensionless parameter. In the calculations, we will take into account the threshold character of ion deceleration. This means that an ion will stop if its energy ε becomes less than the threshold energy ε_{th}. The latter is related to the energy of atom displacement E_d [3]. In view of these assumptions, the projective ion range $R_p(\varepsilon)$ can be represented in the form [2]

$$R_p(\varepsilon) = \tilde{R}_p(\varepsilon) - \mu_{th}(\varepsilon)\tilde{R}_p(\varepsilon_{th}),$$
$$\tilde{R}_p(\varepsilon) = \lambda_0(\varepsilon)\sum_{i=0}^{N} b_i\varepsilon^{i/2}, \quad (4)$$

where

$$\lambda_0(\varepsilon) = \frac{\beta^2\sqrt{\varepsilon}}{n\pi a_{TH}^2(1+Q/2)},$$

n is the target atom density, $Q = \gamma k\beta^2$, $\gamma = 4m_1m_2/(m_1 + m_2)^2$, and μ_{th} is the mean direction cosine of ion motion at the instant its energy becomes less than ε_{th}.

At $\varepsilon \le 2$, we can put $N = 6$ in representation (4); in this case, the relative error of the ion range calculation will not exceed 0.5%, according to [2]. In [2], μ_{th} was calculated by the Monte Carlo method. In this work, we suggest an expression approximating the results of [2]:

$$\mu_{th}(\varepsilon) = \left[1 + \left(0.16 + 1.6\frac{m_2}{m_1} + 3.65\left(\frac{m_2}{m_1}\right)^2\right)\varepsilon^{0.25}\right]^{-1}. \quad (5)$$

The use of (5) instead of the Monte Carlo expression for μ_{th} introduces additional relative and absolute errors into the projective ranges of no more than 0.1% and 0.5 Å, respectively, throughout the energy range.

The coefficients b_i in (4) are found by solving the set of linear equations with N variables

$$F_j + \sum_{i=1}^{N} b_i\psi_{i,j} = 0, \quad j = 1\ldots N, \quad (6)$$

where

$$F_i = \int_0^{\varepsilon_{max}} (\lambda_0 + b_0(L(\lambda_0) - \lambda_0))(L(\lambda_0\varepsilon^{i/2}) - \lambda_0\varepsilon^{i/2})d\varepsilon,$$

$$\psi_{i,j} = \int_0^{\varepsilon_{max}} (L(\lambda_0\varepsilon^{i/2}) - \lambda_0\varepsilon^{i/2})(L(\lambda_0\varepsilon^{j/2}) - \lambda_0\varepsilon^{j/2})d\varepsilon,$$

$$L(f) = \int_0^{\varepsilon} p_e(\varepsilon \longrightarrow \varepsilon'')\int_0^{\varepsilon''} f(\varepsilon')\mu(\varepsilon'', \varepsilon') \times p_n(\varepsilon'' \longrightarrow \varepsilon')d\varepsilon'd\varepsilon'',$$

$$b_0 = \frac{2+Q}{Q + \gamma(1 + m_2/m_1)/2},$$

$$\mu(\varepsilon'', \varepsilon') = \frac{1}{2}\left[\left(1 - \frac{m_2}{m_1}\right)\sqrt{\frac{\varepsilon''}{\varepsilon'}} + \left(1 + \frac{m_2}{m_1}\right)\sqrt{\frac{\varepsilon'}{\varepsilon''}}\right],$$

$$p_e(\varepsilon \longrightarrow \varepsilon'') = \frac{1}{\varepsilon Q}\left(\frac{\varepsilon''}{\varepsilon}\right)^{\frac{1}{Q}-1}, \quad \varepsilon'' \le \varepsilon,$$

$$p_n(\varepsilon'' \longrightarrow \varepsilon') = \frac{\gamma X(\varepsilon'')[X(\varepsilon'') + 1]}{\varepsilon''[\gamma X(\varepsilon'') + (1 - \varepsilon'/\varepsilon'')]^2} \times \begin{cases} 1 & \text{at } (1-\gamma)\varepsilon'' \le \varepsilon' \le \varepsilon'', \\ 0 & \text{at } \varepsilon > \varepsilon'', \quad \varepsilon' < (1-\gamma)\varepsilon''. \end{cases}$$

Let us briefly explain the physical meaning of the functions involved in (6). The function $p_e(\varepsilon \longrightarrow \varepsilon'')$ defines the probability density of the ion energy being changed from ε to ε'' under inelastic deceleration, $p_n(\varepsilon'' \longrightarrow \varepsilon')$ defines that of the ion energy being changed from ε'' to ε' under elastic collision, and $\mu(\varepsilon'', \varepsilon')$ is the scattering angle cosine of an elastically colliding ion when its energy changes from ε'' to ε'. The value of ε_{max} is the extreme of the energy interval in which projective ranges are calculated.

According to (4)–(6), for an ion–target pair, the projective range depends on β, which characterizes elastic scattering of ions, and k, which describes inelastic deceleration of ions. Assuming these parameters to be unknown, we will try to find them by contrasting experimental and theoretical values of the projective ranges. As a measure of discrepancy, we will take residue $S(\beta, k)$:

$$S(\beta, k) = \sum_{i=1}^{N_{exp}}\left[\frac{R_p^{exp}(\varepsilon_i) - R_p(\beta, k, \varepsilon_i)}{\sigma_i}\right]^2, \quad (7)$$

where $R_p^{exp}(\varepsilon_i)$ is an experimental projective range, σ_i is the standard deviation of the measured projective ranges at an energy ε_i, N_{exp} is the number of data points, and $R_p(\beta, k, \varepsilon_i)$ is a theoretical projective range [unlike (4), the parameters β and k enter in explicit form].

The parameters β and k will be found from the minimum condition for the residue $S(\beta, k)$. Experimental values of projective ranges will be taken from [4]. The value of σ_i in [4] is defined as $\sigma_i = \max(14\ \text{Å}; 0.05R_p^{exp}(\varepsilon_i))$.

In order that the errors involved in β and k be determined simultaneously with the calculation of these parameters, we will make the following assumptions. Let the discrepancy between calculated and experimental results be random. Also, let random discrepancies between experimental and theoretical ranges of ions with an energy ε_i be distributed by the normal law with

the zero expectation and a dispersion σ_i^2. Then [5], S in (7) is a random quantity obeying the chi-square (χ^2) distribution with the number of degrees of freedom ($N_{\exp} - 1$). The probability density for this distribution is

$$p(S) = \frac{1}{2^{(N_{\exp}-1)/2}\Gamma((N_{\exp}-1)/2)} S^{(N_{\exp}-3)/2} e^{-S/2}, \quad (8)$$

where $\Gamma(x)$ is gamma function.

The expectation of the random quantity S is $(N_{\exp} - 1)$. The probability that the random quantity S lies in the interval $0 \le S \le S_P$ is given by

$$\int_0^{S_P} p(S)dS = P. \quad (9)$$

The tolerance ranges for β and k are determined from the inequality $S(\beta, k)/S_P \le 1$. Given P, S_P is found from (9).

Figure 2 shows $S(\beta_{opt}, k)/S_P$ vs. k curves for different ion–target pairs at $P = 0.95$. The value of β_{opt} is found from the residue minimum for a given k and also depends on k. β_{opt} vs. k curves for the pairs in Fig. 2 are displayed in Fig. 3.

From Fig. 2, it follows that $S(\beta_{opt}, k)$ for Cu–C, Au–C, and Rb–B pairs is within the tolerance range $S_{0.95}$ for k in the interval of $0 \le k \le 0.1$. For Au–C, the projective ranges were measured for $0.0127 \le \varepsilon \le 0.127$. In this energy interval, ions are decelerated largely because of elastic collisions with target atoms; inelastic deceleration can be ignored. As a result, $S(\beta_{opt}, k)/S_P$ is virtually k-independent for this pair. For Ga–C, $S(\beta_{opt}, k)/S_P$ has a minimum, which is more distinct here than in the other pairs. For this pair, experimental data were obtained for energies $0.142 \le \varepsilon \le 2.12$, which are larger than for the other pairs. Accordingly, inelastic scattering processes are most significant in this case. As follows from Fig. 3, β_{opt} grows with k almost linearly. The weakest $\beta_{opt}(k)$ dependence is observed for Au–C. Hence, it can be expected that β for this pair will be determined with the greatest accuracy.

The k values obtained from the experimental data in Figs. 2 and 3 ($\varepsilon \le 2$) are rough estimates. The exact evaluation of β from these results thus requires that k be calculated with independent experimental or theoretical data. The inequality $S(\beta_{opt}, k)/S_P < 1$ holds in a wide range of k. Hence, k can be determined with a not too high accuracy. Therefore, we will take advantage of the frequently used Lindhard's expression (see, e.g., [6, 7])

$$k = \xi \frac{0.0793 Z_1^{1/2} Z_2^{1/2}}{(Z_1^{2/3} + Z_2^{2/3})^{3/4}} \frac{(m_1 + m_2)^{3/2}}{m_1^{3/2} m_2^{1/2}}. \quad (10)$$

It is assumed that ξ varies in the [1, 2] interval. In (10), m_1 and m_2 are expressed in atomic mass units.

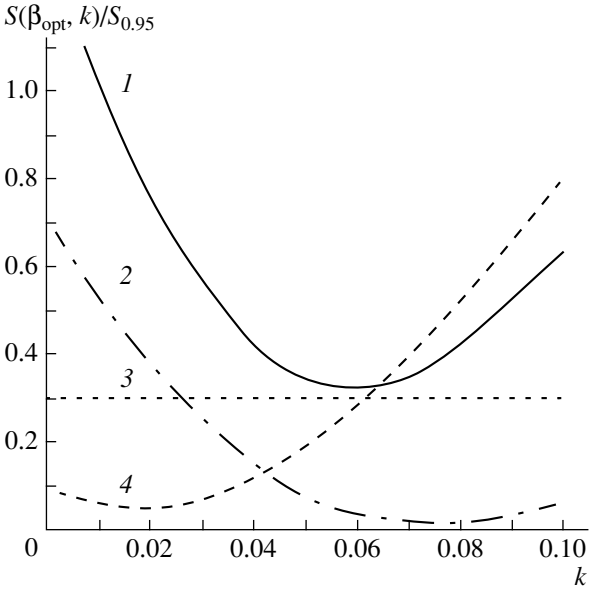

Fig. 2. Normalized residue vs. k. Ion–target pairs are (*1*) Ga–C, (*2*) Rb–B, (*3*) Au–C, and (*4*) Cu–C.

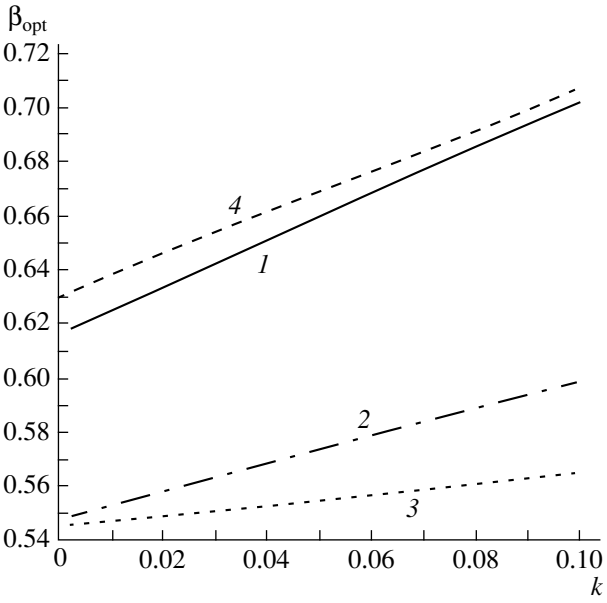

Fig. 3. β_{opt} vs. k. Ion–target pairs are (*1*) Ga–C, (*2*) Rb–B, (*3*) Au–C, and (*4*) Cu–C.

Analysis [4] of 19 ion–target pairs similar to that illustrated in Figs. 2 and 3 showed that, under such conditions, (10) provides the best estimate of k at $\xi = 1$. The associated value of k will be designated as k^*. For example, $k^* = 0.0573$ and 0.0541 for the Ga–C and Rb–B pairs (Fig. 2), respectively. The corresponding values of $S(\beta_{opt}, k^*)/S_P$, as follows from Fig. 2, deviate from the smallest ones insignificantly. Hereafter, the parameter β will be found from the minimum condition for $S(\beta, k^*)/S_P$. The inequality $S(\beta, k^*)/S_P \le 1$ will be used

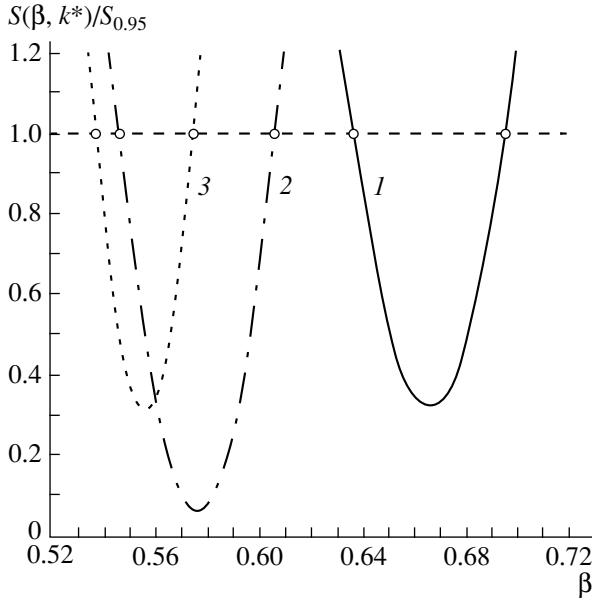

Fig. 4. Normalized residue vs. β. Ion–target pairs are (*1*) Ga–C, (*2*) Rb–B, and (*3*) Au–C. Circles denote the confidence interval for β.

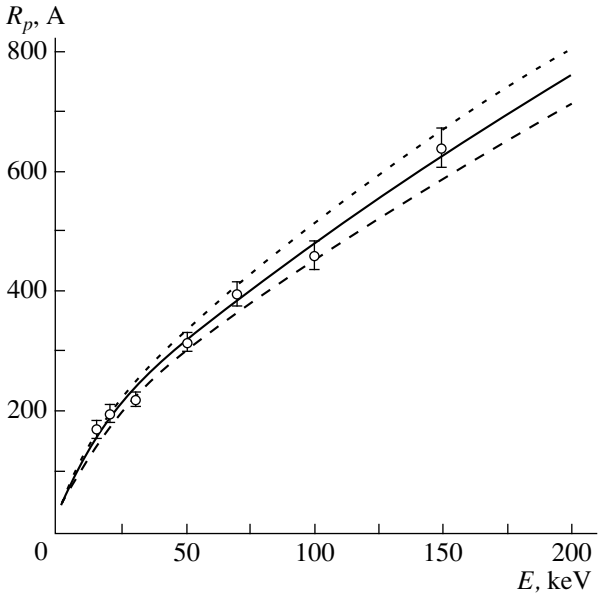

Fig. 5. Energy dependence of the projective range of Au ions in carbon. Error bars, experiment [4]. Calculation by (4)–(6) at β = 0.556, 0.537, and 0.575 is represented by continuous, dashed, and dotted curves, respectively.

to estimate the tolerance range of β. Figure 4 depicts normalized residue $S(\beta, k^*)/S_P$ vs. β curves for three ion–target pairs at $P = 0.95$. They look like quadratic parabolas and have distinct minima whose positions specify the desired parameter β. The intersections of the curves with the $S(\beta, k^*)/S_P = 1$ level are treated as extremes of the tolerance ranges of β for the corresponding pair. For example, for Ga–C and Au–C, the allowable values of β fall into the ranges $0.637 \le \beta \le 0.696$ and $0.537 \le \beta \le 0.575$, respectively, with a probability $P = 0.95$. The relative error thus determined in β for the different ion–target pairs varies from 3.5 to 5.5%. Since this error is estimated approximately, we will set it equal to 5% on average. Figure 5 compares the experimental projective ranges of Au ions in carbon and theoretical values calculated by (4)–(6) for three β's. It is seen that all data points fall into the interval bounded by the extreme curves for β. At β = 0.556, which corresponds to the minimum of $S(\beta, k^*)/S_P$, the calculation and experiment coincide within the experimental error.

The table lists the values of β for 19 ion–target pairs. With regard for the estimated error, they are rounded off to two significant digits. As follows from the table, the values of β are close to each other and lie in the interval $0.53 \le \beta \le 0.59$, except for Ga and Cu ions. These values were employed to calculate ion ranges by the Monte Carlo method using the algorithm described in [1]. In these calculations, the projective ion ranges R_p and their standard deviations ΔR_p were determined. The number of histories was 10^5. According to [1], the relative error in this case is no more than 0.3%. The calculated values of R_p and ΔR_p listed in the table are in good agreement with the experimental data. The maximum absolute discrepancy ΔR_p between them is 61 Å (300-keV Cs ions in B). The associated relative error is 23% for this case. Recall that β was estimated using the experimental data for projective ranges R_p alone. The coincidence of the calculated and experimental ΔR_p values supports the validity of β's for the ion–target pairs considered. In addition, this fact strengthens the selection of potential (1) for simulating ion motion in a substance.

The calculated results are well approximated by the relationship

$$\frac{\Delta R_p}{R_p} = \sqrt{\frac{m_2}{m_1}}\frac{0.846}{1 + 0.473\sqrt{\varepsilon}}. \qquad (11)$$

From (11), the relative error $\Delta R_p/R_p$ is no more than 2% for ions with $m_1/m_2 > 5$ and energies between $0.01 < \varepsilon < 2.5$. This relationship can be used for estimating ΔR_p when R_p is calculated [for example, with (4)–(6)] or known from experiment.

To conclude, a method for determining the parameters of the model interaction potential is suggested. It is based on comparing experimental and calculated projective ion ranges in amorphous substances. The potential parameters estimated for 19 ion–target pairs were applied to calculate ion ranges by the Monte Carlo method. Both the projective ranges R_p and standard deviations ΔR_p are in good agreement with the experi-

Experimental ion ranges vs. those calculated by the Monte Carlo method

Ion	Target	β	E, keV	Experiment [4]		Monte Carlo calculation		Ion	Target	β	E, keV	Experiment [4]		Monte Carlo calculation	
				R_p, Å	ΔR_p, Å	R_p, Å	ΔR_p, Å					R_p, Å	ΔR_p, Å	R_p, Å	ΔR_p, Å
Bi	B	0.54	20	180	30	177	32	Cs	B	0.55	20	165	45	164	36
			50	285	60	302	53				50	285	65	290	61
			100	440	90	459	78				100	450	110	465	93
			300	1050	170	965	153				300	1180	262	1126	201
	C	0.53	15	140	27	146	28		C	0.57	20	170	43	176	41
			40	245	37	256	48				50	290	69	309	68
			80	390	60	386	70				100	490	105	491	104
			150	615	115	573	101				200	820	152	824	164
Pb	B	0.55	20	175	30	183	33	Xe	C	0.55	20	150	30	165	38
			50	310	70	312	55				50	290	60	290	64
			100	450	100	474	81				100	480	100	464	99
			300	1050	200	997	157				300	1200	230	1108	210
	C	0.56	20	205	44	190	37	Sn	C	0.58	30	235	45	228	54
			50	315	60	322	60				50	310	65	316	73
			100	495	91	488	88				100	515	100	509	112
			200	790	137	763	132				300	1300	260	1241	241
Au	B	0.57	20	200	50	193	36	Rb	B	0.58	20	170	45	172	44
			50	330	70	328	59				50	325	80	325	79
			100	470	90	501	87				100	565	150	564	127
			300	1100	172	1056	171				300	1550	320	1607	311
	C	0.56	20	197	25	187	37		C	0.59	30	210	70	233	62
			50	315	47	318	61				50	330	90	332	85
			100	460	80	484	89				100	590	160	568	136
			150	640	121	627	112				200	1077	270	1057	230
Yb	B	0.56	20	180	40	180	36	Kr	C	0.58	30	206	60	227	61
			50	310	60	310	59				50	320	90	326	84
			100	480	90	479	88				100	610	155	562	135
			300	1100	190	1053	176				150	870	220	805	183
	C	0.55	20	176	35	175	36	Ga	C	0.67	20	216	52	222	65
			50	295	59	300	60				50	415	110	423	115
			100	490	95	463	89				100	730	200	740	185
			200	800	150	742	137				300	2000	500	2111	442
Er	C	0.58	10	135	48	129	28	Cu	C	0.68	30	280	90	301	88
			50	310	90	329	67				50	430	130	440	122
			75	421	95	421	84				100	785	215	783	200
			100	500	105	506	99				200	1547	400	1509	342
Eu	C	0.55	30	220	45	215	46								
			50	320	64	293	62								
			100	458	90	458	93								
			200	729	140	752	144								

mental data. This counts in favor of the selected model potential and supports the validity of its parameters.

REFERENCES

1. E. G. Sheĭkin, Zh. Tekh. Fiz. **69** (5), 1 (1999) [Tech. Phys. **44**, 481 (1999)].
2. E. G. Sheĭkin, Zh. Tekh. Fiz. **69** (2), 93 (1999) [Tech. Phys. **44**, 218 (1999)].
3. E. G. Sheĭkin, Zh. Tekh. Fiz. **67** (10), 16 (1997) [Tech. Phys. **42**, 1128 (1997)].
4. M. Grande, F. C. Zawislak, D. Fink, and M. Behar, Nucl. Instrum. Methods Phys. Res., Sect. B **61**, 282 (1991).
5. D. J. Hudson, *Statistics. Lectures on Elementary Statistics and Probability* (Geneva, 1964; Mir, Moscow, 1967).
6. M. A. Kumakhov and F. F. Komarov, *Energy Loss and Ranges of Ions in Solids* (Belarus. Gos. Univ., Minsk, 1979).
7. H. Muramatsu, H. Ishii, E. Tanaka, *et al.*, Nucl. Instrum. Methods Phys. Res., Sect. B **134**, 126 (1998).

Translated by V. Isaakyan

Technical Physics, Vol. 45, No. 8, 2000, pp. 1025–1031. Translated from Zhurnal Tekhnicheskoĭ Fiziki, Vol. 70, No. 8, 2000, pp. 69–76.

SOLIDS

Theoretical and Experimental Study of Photoacoustic and Electron–Acoustic Effects in Solids with Internal Stresses

K. L. Muratikov and A. L. Glazov

Ioffe Physicotechnical Institute, Russian Academy of Sciences, Politekhnicheskaya ul. 26, St. Petersburg, 194021 Russia

Received August 27, 1999

Abstract—Results of a theoretical and experimental study of photoacoustic and electron–acoustic effects in solids with internal stresses are presented. In the theoretical part, an approach to describing these effects on the basis of a generalized concept of thermoelastic energy of a solid with internal stresses and the nonlinear Murnaghan model for the elastic part of its energy is developed. The results of studying objects with internal stresses in the context of an integrated experimental approach incorporating the techniques of photodeflection and thermal-wave and photoacoustic microscopy with piezoelectric recording of the signal are reported. It is shown that a similar approach allows one to detect the arrangement of the strained surface areas of the object and to evaluate the extent to which its thermal and thermoelastic parameters are affected by internal stresses. The results of applying this approach to a study of Vickers indentations in silicon nitride ceramics are reported. © *2000 MAIK "Nauka/Interperiodica".*

Internal stresses can radically change the properties of materials [1]. In this connection, the development of methods for detecting them in different materials has received considerable attention. At present, a number of methods are being used to tackle this problem. Among these are primarily the optical method [2], the ultrasonic technique [3], X-ray [4] and neutron [5, 6] diffraction, magnetic measurements [7, 8], Raman spectroscopy [9, 10], mechanoluminescence [11], detection of thermal radiation from the absorption of ultrasonic oscillations by the object being studied [12], and the methods based on holographic interferometry [13–15]. These methods have shown their high efficiency in solving problems of detecting internal stresses in different types of objects. At the same time, serious restrictions are inherent in most of these methods due to the origin of the corresponding physical processes. The only exceptions are the last two methods, which are based on fairly general physical principles and can be applied to a wide range of objects. However, relatively moderate spatial resolution is inherent in these methods. In this connection, much attention has recently been given to studying the possibility of using the photoacoustic [16–26] and electron–acoustic [27–30] effects to detect mechanical stresses in solids. An important point to note when using either of these methods is the conversion of the optical-radiation or electron-beam energy to thermal energy with its subsequent transformation into acoustic energy owing to the thermoelastic effect. Therefore, when considering the photoacoustic and electron–acoustic effects, we may disregard the details of the interaction of the optical radiation and the electron beam with the material. In fact, we may restrict ourselves in both cases to consideration of the thermoelastic mechanism of generating acoustic vibrations in solid-state objects. An important advantage of thermoelastic generation of sound is its versatility [31]. In this connection, the photoacoustic and electron–acoustic methods for detecting internal stresses may basically be regarded as belonging to a small group of general-purpose methods that make it possible to detect internal mechanical stresses in objects of different origin.

A body of experimental data in support of this possibility has been already obtained. The experimental results obtained so far support the possibility of using the photoacoustic and electron–acoustic effects to detect internal stresses in metals [16, 17, 20, 21, 28, 30] and in ceramics [17–19, 22–25, 27]. Theoretical models of the possible influence of internal stresses on photoacoustic and electron–acoustic signals have also been suggested. A model for generating photoacoustic and electron–acoustic signals was proposed [20]; this model explicitly relates the dependence of these signals on stresses to the dependence of thermal material parameters on these stresses. The photoacoustic and the electron acoustic effects were analyzed [26, 32] in the context of a nonlinear mechanical model of a solid with regard for the possible influence of internal stresses on the thermoelastic component of the energy of the solid. This model yields correct estimates for the nonlinear mechanical and acoustic parameters of solids and makes it possible to explain the photoacoustic and electron–acoustic effects in ceramics with internal stresses, in which a profound influence of internal stresses on thermal parameters has not been observed [22–25]. In this connection, the prime objective of this work is the further theoretical and experimental study of photoa-

1063-7842/00/4508-1025$20.00

coustic and electron–acoustic effects in solids with internal stresses.

An experimental investigation of the influence of internal stresses on the photoacoustic and electron–acoustic effects presents serious difficulties. They are mainly related to the need to monitor a large number of different object characteristics during the experiments. This includes, first of all, independent monitoring of the thermal, elastic, and thermoelastic parameters of the object. Furthermore, in these experiments, information about the surface relief of the object is found to be extremely useful, since it allows detection of strained areas of the sample and, thereby, monitoring of the arrangement of areas with internal stresses.

We turn to a more detailed consideration of the subject. We begin by analyzing the theory of the phenomena being considered. In [20, 26, 32, 33], the basic concepts of the theory of photoacoustic and electron–acoustic effects in solids with internal stresses were generally formulated. In addition, the possible dependence of the thermoelastic energy of the solid on strain was taken into account [26, 32, 33]. This dependence was chosen on the basis of theoretical analysis of the influence of strain on the thermal expansion coefficient of the solids [34]. At the same time, from general considerations, the dependence of the thermoelastic energy on strain can be represented in a somewhat more general form taking into account the possible influence of a change in the volume of the body under strain on this energy. Such general representation of the thermoelastic energy is used in this study. According to this approach, the density of the thermoelastic energy of the body can be represented as (correct to first order terms of the strain tensor stemming from the influence of optical radiation or an electron beam)

$$W_T = -\gamma_{ik}(u_{ik} - U_{ik})\Delta T, \tag{1}$$

where $\gamma_{ik} = \gamma_0[(1 + \beta_0 U_{ll})\delta_{ik} + \beta_1 U_{ik}]$, γ_0 is the coefficient of thermoelastic coupling for an unstrained body, β_0 and β_1 are coefficients determining the dependence of thermoelastic coupling on the initial distortion,

$$u_{ik} = \frac{1}{2}\left(\frac{\partial u_i}{\partial x_k} + \frac{\partial u_k}{\partial x_i} + \frac{\partial u_l}{\partial x_i}\frac{\partial u_l}{\partial x_k}\right)$$

is the tensor of overall strain in the body, U_{ik} is the tensor of initial strain in the body, $\Delta T = T - T_0$, and T_0 is the ambient temperature.

Note that, for $\beta_0 = 0$, Eq. (1) transforms into the expression for the thermoelastic energy density used in [26, 32, 33] while, for $\beta_0 = \beta_1 = 0$, it transforms into the expression for the thermoelastic energy density of an isotropic solid without internal stresses [35].

The Murnaghan model can be used to determine the thermoelastic energy density of a strained solid, taking into account nonlinear effects under deformation [36]. In this model, the thermoelastic energy density is determined by the expression

$$W_E = (\lambda + 2\mu)\frac{I_1^2}{2} - 2\mu I_2 + (l + 2m)\frac{I_1^3}{3} - 2mI_1I_2 + nI_3, \tag{2}$$

where λ and μ are Lamé coefficients; l, m, and n are the Murnaghan constants; $I_1 = u_{kk}$;

$$I_2 = \frac{1}{2}[(u_{kk})^2 - u_{lm}u_{lm}];$$

and

$$I_3 = \frac{1}{3}\left[u_{ik}u_{il}u_{kl} - \frac{3}{2}u_{ik}u_{ik}u_{ll} + \frac{1}{2}(u_{ll})^3\right].$$

Knowledge of the energy densities of a solid makes it possible to set up the equation of motion for the components of the body. In the context of nonlinear mechanics [37], this equation can be written as

$$\frac{\partial P_{ik}}{\partial x_k} = \rho_0 \Delta \ddot{u}_i, \tag{3}$$

where $P_{ik} = \dfrac{\partial X_i}{\partial x_m} t_{km}$ is the Piola–Kirchhoff tensor; t_{km} is the stress tensor related to the internal energy of the body $W = W_E + W_T$ by the relation $t_{km} = \partial W/\partial u_{km}$; X_i are coordinates of points of the strained body; x_i are coordinates of points of the body in the initial unstrained state; and ρ_0 is the density of the body in the initial state.

Note that the coordinates of points of the strained and unstrained body are related by the equation

$$X_i(x_1, x_2, x_3, t) = x_i + U_i(x_1, x_2, x_3) + \Delta u_i(x_1, x_2, x_3, t), \tag{4}$$

where U_i are components of the vector of the initial strain in the body; Δu_i are components of the vector of the strain caused by the effect of optical radiation or an electron beam on the body and superimposed on the initial strain.

Further description of the problem depends on the chosen system of coordinates x_i or X_i, which are referred to as the Lagrangian and Eulerian coordinates, respectively [38]. In the context of the current problem, Eq. (3) is written in the Lagrangian representation; therefore, further consideration will be carried out in this representation. Further solution of the problem depends on the mutual arrangement of the optical radiation or electron beam and the object. In this study, for the sake of definiteness, the geometry of the problem will be considered as shown in Fig. 1.

In its general formulation, the problem of acoustic-vibration generation by a non-steady-state optical or electron beam in the context of thermoelasticity theory goes beyond the above-formulated statements, which

should be supplemented with an equation for nonsteady-state thermal-flux propagation in a solid. Basically, such an equation can be derived by the method used, for instance, in [35]. However, in [35], this equation was derived in the context of linear elastic theory. In nonlinear elastic theory, the difference between the parameters of strained and unstrained objects should be taken into account more precisely. Therefore, we will dwell briefly on deducing the thermal conductivity equation in the context of nonlinear elastic theory.

According to [35], the rate of heat generation or absorption in a unit volume is connected with the entropy density S by the relationship $T\partial S/\partial t$. Therefore, for an arbitrary volume element of the strained body, the following equation is valid:

$$\int dVT\frac{\partial S}{\partial t} = -\int dV \operatorname{div}\mathbf{Q} + \int dVw, \tag{5}$$

where $\mathbf{Q}$ is the vector of the thermal-flux density in the solid with initial strains; w is the energy density released in the body owing to the effect of external sources (optical radiation or electron beam).

The entropy density of a strained body with regard to the impact of optical or electron-beam excitation can be written as

$$S(\mathbf{R}, T, t) = S_0(\mathbf{U}, T) + \Delta S(\mathbf{R}, T, t), \tag{6}$$

where the vectors $\mathbf{R}$ and $\mathbf{U}$ are defined by the components (X_1, X_2, X_3) and (U_1, U_2, U_3), respectively; $S_0(\mathbf{U}, T)$ is the entropy density of the body with initial strain; and $\Delta S(\mathbf{R}, T, t)$ is the variation of the entropy density of the body as a result of an external excitation.

In its thermodynamic sense, the density of thermoelastic energy of the body (1) represents the variation of the free energy density ΔF of the body. Therefore, the entropy variation ΔS is given by

$$\Delta S = -\frac{\partial \Delta F}{\partial T} = -\frac{\partial W_T}{\partial T} = \gamma_{ik}\Delta u_{ik}, \tag{7}$$

where $\Delta u_{ik} = u_{ik} - U_{ik}$.

The entropy density S_0 of the body with initial strain and given volume is related to temperature by the expression

$$S_0 = \rho C_v \ln T, \tag{8}$$

where C_v is heat capacity of the body with initial strain.

To transform the coordinates in equation (5) into those of an unstrained body, we can use the relationship $\rho dV = \rho_0 dV_0$ [38], where dV_0 is a volume element of the body in the unstrained state. In addition, it is necessary to use the relation [39] between integrals over the volume for thermal fluxes in strained and unstrained bodies

$$\int dV \operatorname{div}\mathbf{Q} = \int dV_0 \operatorname{div}\mathbf{q}, \tag{9}$$

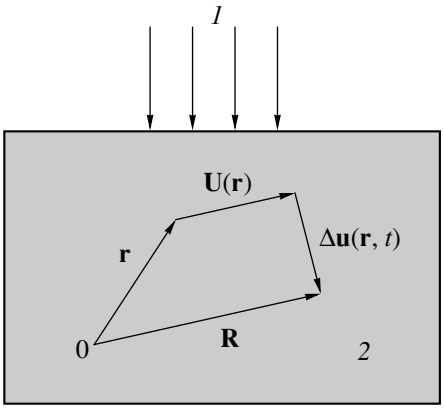

Fig. 1. Geometry of sample arrangement: (*1*) is the exciting radiation or electron beam; (*2*) is the sample.

where $\mathbf{q}$ is the vector of thermal-flux density per unit area of the unstrained body.

The components of the heat flux $\mathbf{q}$ in a solid with initial strains can be specified in the form [39]

$$q_i = -K_{ik}\frac{\partial T}{\partial x_k}, \tag{10}$$

where K_{ik} is thermal-conductivity tensor of the body with initial strains.

It should be noted that, according to the field theories of nonlinear mechanics [20, 39], the thermal-conductivity tensor K_{ik} generally has the structure

$$K_{ik} = (K_0\delta_{ik} + K_1U_{ik} + K_2I_{il}U_{lk}), \tag{11}$$

where the quantities K_0, K_1, and K_2 should be considered as scalar functions of the three invariants of the initial strain tensor, temperature, and convolution of its first derivatives with respect to coordinates with the initial strain tensor [20, 39].

Using equations (5)–(10), as well as the outlined rules, we can derive the thermal conductivity equation for a body with initial strain in the starting coordinate system, i.e., in the Lagrangian representation. On the basis of the stated results, this equation can be obtained from (5) in the form

$$\rho_0 c_v\frac{\partial \Delta T}{\partial t} + \gamma_0 T\frac{\rho_0}{\rho}[(1 + \beta_0 U_{pp})\delta_{ik} + \beta_1 U_{ik}]\frac{\partial \Delta u_{ik}}{\partial t} = \frac{\partial}{\partial x_i}\left(K_{ik}\frac{\partial \Delta T}{\partial x_k}\right) + \frac{\rho_0}{\rho}W. \tag{12}$$

Note that all quantities in Eq. (12) are assumed to be expressed in the Lagrangian coordinates corresponding to the position of points in the unstrained body. The influence of strains on the heat capacity of the body is usually insignificant and is discussed elsewhere [40]. In the second term on the left-hand side of equation (12), the strains Δu_i in this study are considered to be small. Therefore, restricting ourselves to quantities of the first

order of smallness in (12), we may assume that $T \cong T_0$. Density ρ in Eq. (12) can be determined (correct to the terms of the first order of smallness in the initial strains in the body) from the relationship $\rho \cong (1 - U_{ll})\rho_0$. If, in Eq. (12), we set $\beta_0 = \beta_1 = 0$, $\rho = \rho_0$, and $K_{ik} = K\delta_{ik}$, this equation transforms into the well-known equation of thermal conductivity for isotropic bodies [35].

The second term on the left-hand side of Eq. (12) describes dilatation processes in a solid during deformation. They are vital in the process of emission of infrared radiation by solids under deformation [12] but usually exert little influence on photoacoustic and electron–acoustic effects in solids. Therefore, when considering the photoacoustic and electron–acoustic processes in solids, this term is usually ignored.

According to the formulated conditions, the determination of heat fluxes is generally an intricate mathematical problem. A further simplification can be carried out on the basis of additional experimental data concerning the behavior of thermal properties of a material subjected to mechanical stresses. In [22–25], several photothermal methods were used to show that residual stresses only slightly affect the thermophysical properties of silicon nitride ceramics.

In this study, investigations of the influence of internal stresses on the photoacoustic effect are restricted solely to silicon nitride ceramics. Therefore, according to experimental results obtained in [22–25], we assume that the appearance of internal stresses in the sample does not result in a noticeable variation of the thermal parameters. In addition, we assume that the exciting radiation is time-modulated by a harmonic law and the sample surface is irradiated uniformly. Then, if radiation is absorbed in the near-surface region of the sample, the non-steady-state component of temperature inside the sample will be defined by the expression

$$\Delta T(z, t) = \Delta T_s e^{-\sigma z + i\omega t}, \qquad (13)$$

where $\sigma = (1 + i)\sqrt{\omega/2\kappa}$, κ is thermal diffusivity of the sample, ΔT_s is amplitude of the temperature oscillations at the sample surface, and ω is the circular frequency of modulation of the exciting radiation.

Knowledge of the temperature distribution in the sample allows displacements of the sample surface under the action of exciting radiation to be determined from Eq. (3) and the photoacoustic signal to be found with a piezoelectric recording method. A detailed scheme for these calculations was described elsewhere [26, 32, 33]. Therefore, passing over the details of the calculations, we immediately present the net result for a photoacoustic signal with piezoelectric signal recording for the case when the thermoelastic energy of the sample is defined by Eq. (1). Then, for the photoacoustic signal $V(\omega)$ in a sample with uniform initial strains $U_i = A^{(i)}x_i$ ($A^{(i)}$ are arbitrary coefficients characterizing the strain in different directions), we obtain the following result:

$$V(\omega) = V_0(\omega)\frac{1 + \beta_0 U_{pp} + \beta_1 U_{33}}{\sqrt{1 + A^3}[1 + 2lU_{pp} + (4m' + n')U_{33}]^{3/2}}, \qquad (14)$$

where $V_0(\omega)$ is the photoacoustic piezoelectric signal from the sample in the absence of initial strains [41],

$$l' = \frac{l}{\rho_0 c_l^2}, \quad m' = \frac{m}{\rho_0 c_l^2}, \quad n' = \frac{n}{\rho_0 c_l^2},$$

$$\text{and } c_l = \sqrt{\frac{3K = 4\mu}{3\rho_0}}.$$

Equation (14) shows that the dependence of the photoacoustic piezoelectric signal on internal stresses stems from the nonlinear elastic and inelastic properties of the medium. In deducing Eq. (14), no special assumptions were made about the nature of the interaction of radiation with the material and, hence, this result is also valid for an electron–acoustic signal, provided it is due to the thermoelastic mechanism. Note that, for $\beta_1 = 0$, expression (14) transforms into the corresponding result for a photoacoustic signal obtained in [26, 32, 33].

In the experimental part of this work, silicon nitride ceramics were studied. The key feature of the experimental approach is the use of several photothermal and photoacoustic techniques in combination with the optical deflection method [42]. This approach makes it possible to measure independently the thermal, elastic, and thermoelastic parameters of the sample. In turn, the optical deflection method is very useful for determining the surface relief of the sample, in particular, the positions of plastically deformed areas.

We studied experimentally the influence of internal strains on the thermal and elastic parameters of samples of silicon nitride ceramics that were indented using the Vickers method. The Vickers indentation method is one of the most reliable and reproducible methods for inducing stresses and cracks in samples [43]. The general structure of the region formed in the ceramics in the vicinity of the Vickers indentation site is shown in Fig. 2. Results of the photodeflection and photoreflection measurements, as well as the obtained thermal-wave images of Vickers indentations in silicon nitride ceramics were considered in detail previously [22–25]. Therefore, in this paper, only the optical deflection images of regions in the vicinity of Vickers indentations are presented. A representative example of such images is shown in Fig. 3. According to these images, the maximum surface deformation was attained in the immediate region of plastic deformation in the vicinity of an indentation site. For instance, the surface deformation amounted to 3–4 μm for an indentation load of 196 N. As for the surface-relief changes in the ceramics away from the indentation site, they are related to surface strain resulting from the formation of lateral surface cracks in the ceramics during Vickers indentation [43].

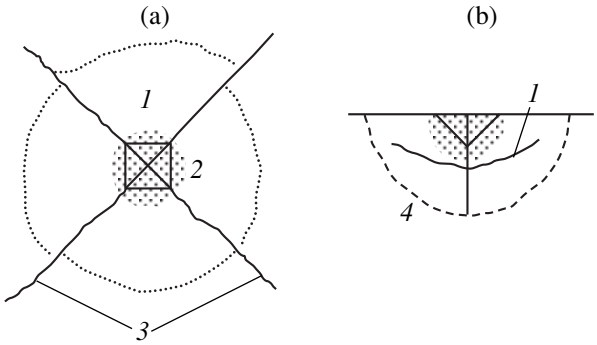

Fig. 2. Schematic representation of the impression and crack system in ceramics: (*1*) are subsurface horizontal cracks, (*2*) is the region of plastic deformation, (*3*) are radial cracks, (*4*) are subsurface medial cracks; (a) is the top view and (b) is the cross section.

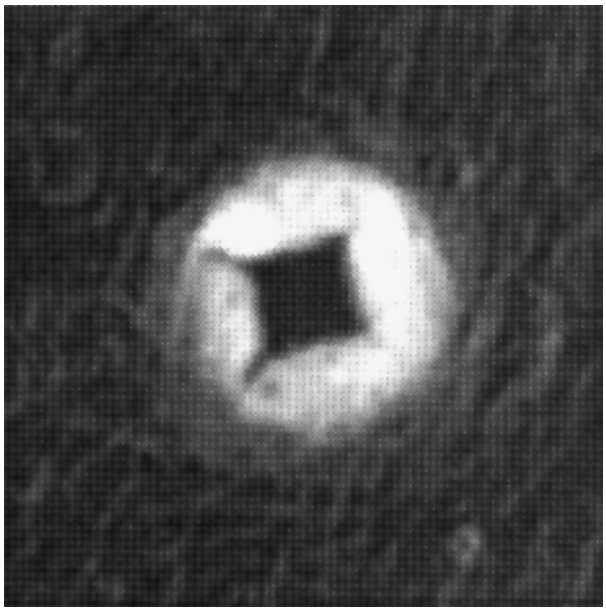

Fig. 3. Optical deflection image of the region of silicon nitride ceramics near a Vickers indentation. Load is 98 N. The image size is 500×500 μm.

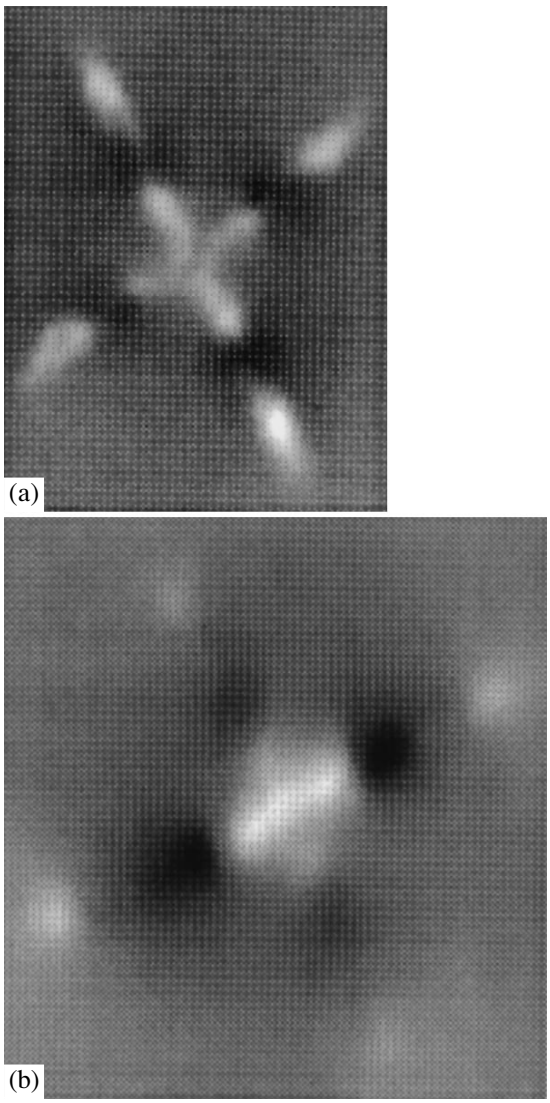

Fig. 4. Region of silicon nitride ceramics near a Vickers indentation. The image was obtained by the photoacoustic method with a piezoelectric recording of the signal. Load is 98 N. Modulation frequency of exciting radiation is 113 kHz. (a) is an old indentation; the image size is 240×320 μm. (b) is a new indentation; the image size is 380×400 μm.

In this study, comprehensive investigations of the indentations were carried out by the photoacoustic technique with a piezoelectric signal recording method. In particular, we studied both old indentations about five years of age and new ones that were made several days before the measurements. In Fig. 4, images of both old and new indentations obtained by the photoacoustic technique are presented. First, we note that these images are very similar in structure to those obtained for Vickers-indented ceramics by the electron–acoustic method [27]. This result supports the theoretical conclusion that the photoacoustic and electron–acoustic signals are formed by the same mechanisms.

At the same time, a noticeable difference in the structures of the old and new indentations should be noted. This difference becomes especially pronounced if we superpose corresponding photoacoustic and optical deflection images represented in the form of contour plots. Examples of such superposed images are shown in Fig. 5. It can be seen that, for new indentations, the regions with maximum values of photoacoustic signals are positioned near the tips of radial cracks. For old indentations, the regions with maximum values of photoacoustic signals are appreciably closer to their centers and correspond approximately to the intersection site of radial and subsurface lateral cracks. We also

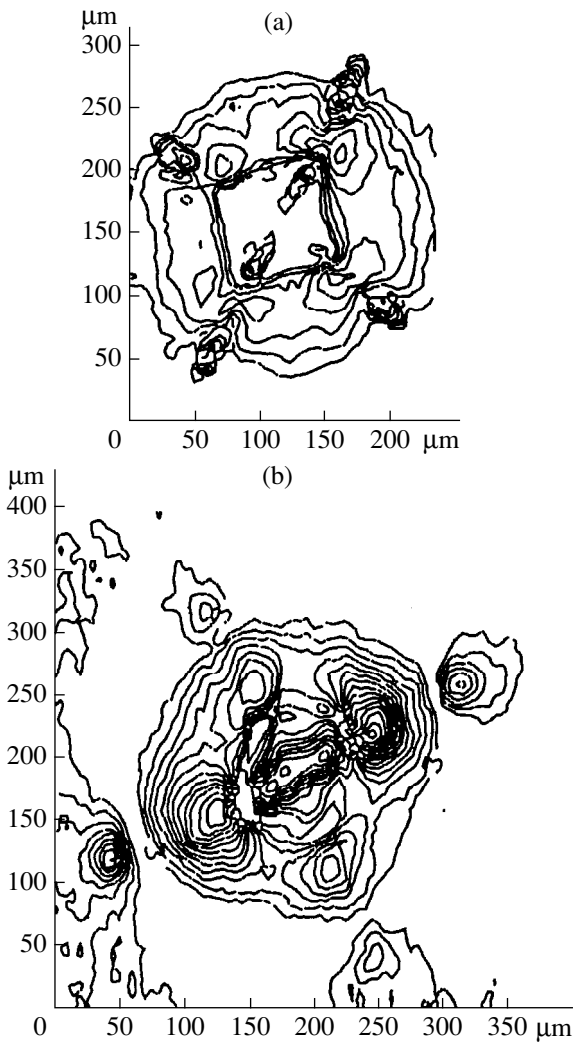

Fig. 5. Superposition of two images of a silicon nitride ceramic region in the vicinity of a Vickers indentation; the images were obtained by the photoacoustic and optical techniques and are shown as contour plots. (a) and (b) are the same as in Fig. 4.

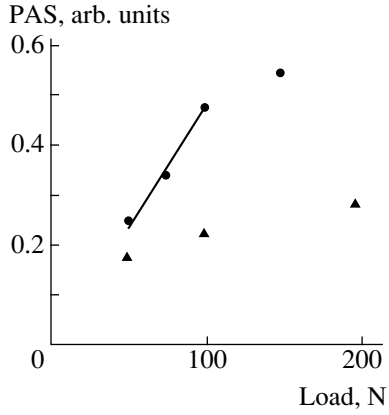

Fig. 6. Dependence of the maximum value of the photoacoustic signal (PAS) obtained by a piezoelectric recording on the load value. Modulation frequency of exciting radiation is 98 kHz. (●) correspond to old Vickers indentations. (▲) correspond to new Vickers indentations.

note that the maximum values of photoacoustic signals are somewhat higher in the latter case.

These features are presumably explained by the fact that gradual stress relaxation occurs with time in the vicinity of radial cracks. At the same time, near the intersection site of radial and subsurface lateral cracks, the latter gradually develop and approach the surface. This is consistent with the well-known result for silicon nitride ceramics: under the effect of stresses, the motion of dislocations does not occur in its volume; at the same time, a noticeable motion of the dislocations over the fracture surfaces can be observed [44].

To analyze this subject in greater detail, we studied the dependence of the maximum value of the photoacoustic signal (PAS) near the tips of both types of cracks on the indentation load. The results of these measurements are shown in Fig. 6. They show that, as the load increases, the photoacoustic signal at first grows and then gradually levels off. This dependence of the photoacoustic signal may be related to the fact that an increase in the crack length promotes an increase in stresses at its tips [45]. Therefore, under a certain indentation load, the stress at the tips of the cracks reaches a limiting value corresponding to the ultimate strength of the material. After that, a further increase in stresses becomes impossible and the photoacoustic signal levels off.

Expression (14) and the data shown in Fig. 6 allow estimation of the upper limit values of the parameters β_0, β_l, l, m, and n. It should be taken into account that the maximum possible strains in present-day ceramics that do not result in their failure meet the condition $U_{\max} \leq 1\%$ [46]. Then, in order to explain the variation in the photoacoustic signal at a level of 10% according to Eq. (14), we should assume that $\beta_0 \cong \beta_1 \cong 10$ and l, m, and $n \leq 10\rho_0 c_l^2$. Theoretical estimation of the coefficient β [34] yielded a value on the order of unity. However, only metals were considered [34]. As for the quantities l, m, and n, the values obtained from estimations with Eq. (14) are in the correct range of the Murnaghan parameters [36]. At the same time, Eq. (14) makes it possible to explain qualitatively the difference in the magnitudes of photoacoustic signals observed near the tips of the radial and subsurface lateral cracks. For subsurface lateral cracks, the principal component of the strain tensor that contributes to the photoacoustic signal is the component U_{33}. For radial cracks, the principal strains near the crack tips are related to U_{11} and U_{22}. The strains U_{11} and U_{22} also result in strains of the U_{33} type, but they are related by the Poisson ratio. The Poisson ratio for silicon nitride ceramics is approximately equal to 0.26 [44]. Therefore, according to expression (14), the strains near the tips of radial cracks exert somewhat less influence on the photoacoustic signal compared with the case of the subsurface lateral cracks.

Thus, the theoretical and experimental results reported here show that the photoacoustic and electron–acoustic effects in solids with internal stresses can be described in the context of the nonlinear theory of elasticity and thermoelasticity. An important advantage of the photoacoustic and electron–acoustic methods for detecting internal stresses is their versatility, since, according to the presented theory, their internal-stress sensitivity is based on the general linear elastic properties of solids.

REFERENCES

1. I. A. Birger, *Residual Stresses* (MAShGIZ, Moscow, 1963).
2. A. Ya. Aleksandrov and M. Kh. Akhmetayanov, *Polarization Optical Methods in the Mechanics of Deformable Bodies* (Nauka, Moscow, 1974).
3. Y. H. Pao and W. Sachse, Phys. Acoust. **17**, 61 (1984).
4. B. Eigenmann, B. Scholtes, and E. Macherauch, Mater. Sci. Eng. A **118**, 1 (1989).
5. M. R. Daymond, M. A. M. Bourke, R. B. von Dreele, *et al.*, J. Appl. Phys. **82**, 1554 (1997).
6. M. Ceretti, C. Braham, J. L. Lebrun, *et al.*, Exp. Tech. **20** (3), 14 (1996).
7. É. S. Gorkunov and M. V. Tartachnaya, Zavod. Lab. **59** (7), 22 (1993).
8. C. C. H. Lo, F. Tang, Y. Shi, *et al.*, J. Appl. Phys. **85**, Part 2A, 4595 (1999).
9. T. Iwaoka, S. Yokogama, and Y. Osaka, Jpn. J. Appl. Phys. **24**, 112 (1984).
10. M. Bowden and D. J. Gardiner, Appl. Spectrosc. **51**, 1405 (1997).
11. C. N. Xu, T. Watanabe, M. Akiyama, and X. G. Zheng, Appl. Phys. Lett. **74**, 2414 (1999).
12. A. K. Wong, R. Jones, and J. G. Sparrow, J. Phys. Chem. Solids **48**, 749 (1987).
13. G. N. Cheryshev, A. L. Popov, V. M. Kozintsev, and I. I. Ponomarev, *Residual Stresses in Deformable Solids* (Nauka, Moscow, 1996).
14. M. J. Pechersky, R. F. Miller, and C. S. Vikram, Opt. Eng. **34**, 2964 (1995).
15. C. S. Vikram, M. J. Pechersky, C. Feng, and D. Engelhaupt, Exp. Tech. **20** (6), 27 (1996).
16. M. Kasai and T. Sawada, Springer Ser. Opt. Sci. **62**, 33 (1990).
17. R. M. Burbelo, A. L. Gulyaev, L. I. Robur, *et al.*, J. Phys. (Paris) **4**, C7-311 (1994).
18. D. N. Rose, D. C. Bryk, G. Arutunian, *et al.*, J. Phys. (Paris) **4**, C7-599 (1994).
19. H. Zhang, S. Gissinger, G. Weides, and U. Netzekmann, J. Phys. (Paris) **4**, C7-603 (1994).
20. M. Qian, Chin. J. Acoust. **14** (2), 97 (1995).
21. R. M. Burbelo and M. K. Zhabitenko, Prog. Nat. Sci., Suppl. **6**, 720 (1996).
22. K. L. Muratikov, A. L. Glazov, D. N. Rose, *et al.*, Pis'ma Zh. Tekh. Fiz. **23** (5), 44 (1997) [Tech. Phys. Lett. **23**, 188 (1997)].
23. K. L. Muratikov, A. L. Glazov, D. N. Rose, and J. E. Dumar, Pis'ma Zh. Tekh. Fiz. **24** (21), 40 (1998) [Tech. Phys. Lett. **24**, 846 (1998)].
24. K. L. Muratikov, A. L. Glazov, D. N. Rose, and J. E. Dumar, in *Proceedings of the 10th International Conference "Photoacoustic and Photothermal Phenomena," 10 ICPPP, Rome, 1998*; AIP Conf. Proc. **463**, 187 (1998).
25. K. L. Muratikov, A. L. Glazov, D. N. Rose, and J. E. Dumar, in *Proceedings of the 3rd International Congress on Thermal Stresses, Thermal Stresses'99, Cracow, 1999*, p. 669.
26. K. L. Muratikov, Pis'ma Zh. Tekh. Fiz. **24** (13), 82 (1998) [Tech. Phys. Lett. **24**, 536 (1998)].
27. J. H. Cantrell, M. Qian, M. V. Ravichandran, and K. W. Knowles, Appl. Phys. Lett. **57**, 1870 (1990).
28. Q. R. Yin, B. Y. Zhang, Y. Yang, *et al.*, Prog. Nat. Sci., Suppl. **6**, 115 (1996).
29. F. Jiang, S. Kojima, B. Zhang, and Q. Yin, Jpn. J. Appl. Phys., Part 1 **37**, 3128 (1998).
30. Y. Gillet and C. Bissieux, in *Proceedings of the 10th International Conference "Photoacoustic and Photothermal Phenomena," 10 CPPP, Rome, 1998*, p. 131.
31. L. M. Lyamshev, *Radiation Acoustics* (Nauka, Moscow, 1996).
32. K. L. Muratikov, in *Proceedings of the 10th International Conference "Photoacoustic and Photothermal Phenomena," 10 CPPP, Rome, 1998*, pp. 478–480.
33. K. L. Muratikov, Zh. Tekh. Fiz. **69** (7), 59 (1999) [Tech. Phys. **44**, 792 (1999)].
34. R. I. Garber and I. A. Gindin, Fiz. Tverd. Tela (Leningrad) **3**, 176 (1961) [Sov. Phys. Solid State **3**, 127 (1961)].
35. L. D. Landau and E. M. Lifshitz, *The Theory of Elasticity* (Nauka, Moscow, 1987).
36. A. I. Lur'e, *Nonlinear Theory of Elasticity* (Nauka, Moscow, 1980).
37. T. Tokuoka and M. Saito, J. Acoust. Soc. Am. **45**, 1241 (1969).
38. G. I. Petrashen', *Propagation of Waves in Anisotropic Elastic Media* (Nauka, Leningrad, 1980).
39. A. Green and J. Adkins, *Large Elastic Deformation and Non-Linear Continuum Mechanics* (Clarendon, Oxford, 1960; Mir, Moscow, 1965).
40. K. Y. Kim, Phys. Rev. B **54**, 6245 (1996).
41. W. Jackson and N. M. Amer, J. Appl. Phys. **51**, 3343 (1980).
42. M. Rosete-Aquilar and R. Díaz-Uribe, Appl. Opt. **32**, 4690 (1993).
43. R. F. Cook and G. M. Pharr, J. Am. Ceram. Soc. **73**, 787 (1990).
44. D. G. Miller, C. A. Andersson, S. C. Singhal, *et al.*, AMMRC CTR 76-32 (Watertown, Mass., 1976), Vol. IV.
45. L. I. Sedov, *A Course in Continuum Mechanics* (Nauka, Moscow, 1970; Wolters-Noordhoff, Groningen, 1971–1972), Vol. 2.
46. T. J. Mackin and T. E. Purcell, Exp. Tech. **20** (2), 15 (1996).

Translated by M. Lebedev

Technical Physics, Vol. 45, No. 8, 2000, pp. 1032–1041. Translated from Zhurnal Tekhnicheskoĭ Fiziki, Vol. 70, No. 8, 2000, pp. 77–86.

SOLID-STATE ELECTRONICS

Special Features of the Growth of Hydrogenated Amorphous Silicon in PECVD Reactors

Yu. E. Gorbachev, M. A. Zatevakhin, V. V. Krzhizhanovskaya, and V. A. Shveĭgert

Institute for High-Performance Computing & Data Bases, St. Petersburg, 198005 Russia

E-mail: gorbachev@hm.csa.ru

Received February 10, 1999;
in final form, October 27, 1999.

Abstract—A model has been developed to calculate the growth parameters of silicon films in diode- and triode-type PECVD reactors and to analyze the factors affecting the deposition of silicon-containing radicals. Mechanisms of the effect of diluting silane with molecular hydrogen on the film growth process have been explained.

INTRODUCTION

One of the most widespread methods of growing hydrogenated amorphous silicon films is the technology based on deposition from the gas phase of silicon-containing radicals produced by the decomposition of silane by an RF discharge plasma in PECVD reactors. At present, various types of such systems are used. In one of these, the diode system, the substrate serves as one of the electrodes. In another system, belonging to a numerous class of systems with remote plasma and usually called a triode system, the substrate is placed outside the plasma discharge (PECVD reactors). This system was proposed and thoroughly investigated in [1]. By increasing the growth rate and film quality through optimizing the parameters of PECVD reactors, significant technological advantages can be attained. Therefore, various models are being proposed, which, with differing degrees of detail, describe the processes in the growth chamber and allow improvements to be made in the reactor design.

The first comprehensive model of the growth process of hydrogenated amorphous silicon film was proposed in [2].

A rather simple and effective model developed later [3] is suitable for making prompt estimates of all basic process parameters with sufficient accuracy. Apart from silane (SiH_4), 12 major chemical components of the mixture are included in this model: SiH_n, n = 1–3; H; H_2; Si_2H_n, n = 3–6; Si_3H_8; $Si_2H_6^*$; and $Si_2H_6^{**}$ (asterisks denote the excited electronic state). Recently, a similar model but with a different set of chemical components and a much more elaborate presentation of the electronic subsystem was proposed [4]. The authors carried out quite detailed measurements of the system parameters and provided the experimental data necessary for verifying the models.

In the framework of the model proposed in [3], the authors carried out a computational investigation of the physical and chemical processes occurring in a purely silane plasma of a diode reactor and performed a detailed analysis of the role of various components and the effect of the system parameters on film growth for major operating regimes. It was found that, at low pressures, molecular hydrogen accumulates in the chamber, so that silane ceases to be the only carrier component. In addition, in practice, a technology based on diluting silane with hydrogen is often used, which saves silane and makes the production of silicon films ecologically cleaner. Under these conditions, the model of [3] is inadequate.

In this study, a model that takes into account the changes in silane concentration during film growth is presented. Transport due to diffusion was determined using, instead of fixed coefficients, those calculated by Wilke's formula representing a first approximation of diffusion in a multicomponent medium. It has been shown that further elaboration of the description of diffusion processes does not improve the accuracy of the calculations of the component fluxes onto the film surface. Calculations of the plasma discharge were carried out using a fluidic model [5] affording a means of calculating electron densities. Expressions have also been obtained for the rate constants of reactions initiated by electron impact in silane–hydrogen mixtures. Hence, the processes in reactors could be studied in a wider range of parameters and the processes taking place in silane diluted with molecular hydrogen could be simulated. The proposed model describes the processes in triode-type reactors with the discharge zone some distance away from the substrate. Finally, in this work, the effect of the reactor volume, which in almost every real installation does not coincide with the discharge zone volume, has been accounted for in a correct manner.

1063-7842/00/4508-1032$20.00

MATHEMATICAL MODEL

In the proposed model of a PECVD reactor, the gas-phase processes in its chamber are described by one-dimensional equations of chemical kinetics, in which, as estimated in [3], only transfer processes by diffusion are taken into account:

$$\frac{\partial n_i}{\partial t} = \frac{\partial}{\partial x}\left(D_i\frac{\partial n_i}{\partial x}\right) + F_i. \quad (1)$$

Here, n_i is the number density of the ith component and F_i is the source term describing chemical transformations (for more detail, refer to [3]). The effective diffusion coefficient of the ith component D_i is calculated by Wilke's formula [6], commonly used in practical calculations of multicomponent gas mixtures:

$$D_i = (n - n_i)\left[\sum_{\substack{k=1,\\ k\neq 1}}^{N_k} n_k/D_{ki}\right]^{-1}, \quad (2)$$

where n is the total number density of the mixture.

The ambipolar diffusion coefficient D_{ki} is calculated by the formula of the molecular kinetic theory of gases [7] with use of the Lennard–Jones 6–12 potential

$$D_{ki} = 0.002628\frac{\sqrt{T^3/2\mu_{ki}}}{p\sigma_{ki}^2\Omega_{ki}^{(1.1)^*}(T_{ki}^*)}\ \frac{\text{cm}^2}{\text{s}}. \quad (3)$$

Here, $\mu_{ki} = m_k m_i/(m_k + m_i)$ is the effective mass of the kth and ith species, m_i is the molecular weight of the ith species, $\sigma_{ki} = (\sigma_k + \sigma_i)/2$ is the effective collision diameter, $T_{ki}^* = kT/\varepsilon_{ki}$ is the characteristic temperature, $\varepsilon_{ki} = \sqrt{\varepsilon_k\varepsilon_i}$ is a parameter of the potential for intermolecular interaction (potential well depth), k is the Boltzmann constant, and $\Omega_{ki}^{(1.1)^*}(T_{ki}^*)$ is a reduced Ω-integral of collisions for mass transfer normalized by the Ω-integral of the model of hard spheres. Values of the T_{ki}^* function for a wide range of characteristic temperatures T_{ki}^* can be found in monograph [7]; in the calculations, approximate formulas given in [8] were used. Values of the Lennard–Jones potential parameters σ_i and ε_i borrowed from [9] are given in Table 1.

In [10], experimental determinations of the ambipolar diffusion coefficients of silyl in silane and molecular hydrogen were carried out and found to be equal to 140 ± 30 and 580 ± 140 cm^2/s, respectively, at the temperature 320 K and pressure 1 torr. Under these conditions, formula (3) gives the values of 111 and 536 cm^2/s, respectively, in good agreement with measured data.

To finalize the formulation of the problem, we need to know the dependence of the rate constants of chemical reactions initiated by an electron beam on pressure p and the interelectrode separation l. To define this dependence in such a way as to circumvent calculations of the corresponding electron temperatures, it was suggested in [3] to use the following relation between the reaction constants k_r and the ionization constants k_i:

$$k_r/k_r^0 = (k_i/k_i^0)^{\varepsilon_r/\varepsilon_i}, \quad (4)$$

where ε_r and ε_i are the thresholds for the chemical reaction and ionization, respectively [11], and the superscript "0" refers to certain conditions for which the values of the constants are known (below, these conditions are called "basic").

Then, assuming that the plasma as a whole is neutral, that the withdrawal rate of electrons is equal to the withdrawal rate of ions (mainly SiH_2^+ ions), and that the carrier mixture consists of silane and molecular hydrogen, the following expression can be obtained using formula (2):

$$\frac{k_i}{k_i^0} = \frac{n_t}{n_t^0}\frac{n_{\text{SiH}_4}^0}{n_{\text{SiH}_4}} \times \frac{(n_{\text{SiH}_4}^0/D_{\text{SiH}_4\,\text{SiH}_2}^0 + n_{\text{H}_2}^0/D_{\text{H}_2\,\text{SiH}_2}^0)}{(n_{\text{SiH}_4}/D_{\text{SiH}_4\,\text{SiH}_2} + n_{\text{H}_2}/D_{\text{H}_2\,\text{SiH}_2})}\left(\frac{l^0}{l}\right)^2. \quad (5)$$

Here, n_t and n_t^0 are the numerical densities of the mixture under present and basic conditions, respectively. For the basic conditions, a silane–hydrogen mixture is chosen with partial hydrogen and silane pressures $p_{\text{H}_2}^0 = p_{\text{SiH}_4}^0 = 0.125$ torr at the temperature $T^0 = 520$ K and the interelectrode separation $l^0 = 2.5$ cm, the reason being that the constants for these conditions were determined in [2].

Table 1. Parameters of the Lennard–Jones potential

Component	σ_i, Å	ε_i/k, K
SiH_4	4.084	207.6
SiH_3	3.943	170.3
SiH_2	3.803	133.1
SiH	3.662	95.8
H	2.5	30.0
H_2	2.915	59.7
Si_2H_6	4.828	301.3
$Si_2H_6^*$	4.828	301.3
$Si_2H_6^{**}$	4.828	301.3
Si_2H_5	4.717	306.9
Si_2H_4	4.601	312.6
Si_2H_3	4.494	318.2
Si_3H_8	5.562	331.2

Table 2. List of chemical reactions and reaction constants

Reaction no.	Reactions	Constants*, cm^3/s
R1	$SiH_4 + e \longrightarrow SiH_3 + H$	3.000×10^{-11}
R2	$SiH_4 + e \longrightarrow SiH_2 + 2H$	1.500×10^{-10}
R3	$SiH_4 + e \longrightarrow SiH + H + H_2$	9.340×10^{-12}
R4	$SiH_4 + e \longrightarrow SiH_2 + H_2$	7.190×10^{-12}
R5	$H_2 + e \longrightarrow 2H$	4.490×10^{-12}
R6	$Si_2H_6 + e \longrightarrow SiH_3 + SiH_2 + H$	3.720×10^{-10}
R7	$Si_2H_6 + e \longrightarrow Si_2H_4 + 2H$	3.700×10^{-11}
R8	$SiH_4 + H \longrightarrow SiH_3 + H_2$	2.530×10^{-12}
R9	$SiH_4 + SiH_2 \longrightarrow Si_2H_6^*$	1.000×10^{-11}
R10	$SiH_4 + SiH \longrightarrow Si_2H_3 + H_2$	1.700×10^{-12}
R11	$SiH_4 + SiH \longrightarrow Si_2H_5$	2.500×10^{-12}
R12	$SiH_4 + Si_2H_5 \longrightarrow SiH_3 + Si_2H_6$	5.000×10^{-13}
R13	$SiH_4 + Si_2H_4 \longrightarrow Si_3H_8$	1.000×10^{-10}
R14	$SiH_3 + H \longrightarrow SiH_2 + H_2$	1.000×10^{-10}
R15	$SiH_3 + SiH_3 \longrightarrow SiH_4 + SiH_2$	1.500×10^{-10}
R16	$SiH_3 + SiH_3 \longrightarrow Si_2H_6^{**}$	1.000×10^{-11}
R17	$SiH_3 + Si_2H_5 \longrightarrow SiH_4 + Si_2H_4$	1.000×10^{-10}
R18	$SiH_3 + Si_2H_5 \longrightarrow Si_3H_8$	1.000×10^{-11}
R19	$SiH_3 + Si_2H_6 \longrightarrow SiH_4 + Si_2H_5$	3.270×10^{-12}
R20	$SiH_2 + H \longrightarrow SiH + H_2$	7.960×10^{-13}
R21	$SiH_2 + Si_2H_6 \longrightarrow Si_3H_8$	1.200×10^{-10}
R22	$Si_2H_3 + H_2 \longrightarrow Si_2H_5$	1.700×10^{-12}
R23	$Si_2H_4 + H_2 + SiH_4 + SiH_2$	1.000×10^{-10}
R24	$Si_2H_5 + H \longrightarrow Si_2H_4 + H_2$	1.000×10^{-10}
R25	$Si_2H_6 + H \longrightarrow SiH_4 + SiH_3$	7.160×10^{-12}
R26	$Si_2H_6 + H \longrightarrow Si_2H_5 + H_2$	1.430×10^{-11}
R27	$Si_2H_6^* \longrightarrow Si_2H_4 + H_2$	$5.000 \times 10^6\ s^{-1}$
R28	$Si_2H_6^* + M \longrightarrow Si_2H_6 + M$ (M, a species colliding with $Si_2H_6^*$)	1.000×10^{-10}
R29	$Si_2H_6^{**} \longrightarrow SiH_4 + SiH_2$	$2.300 \times 10^7\ s^{-1}$
R30	$Si_2H_6^{**} \longrightarrow SiH_4 + H_2$	$2.300 \times 10^7\ s^{-1}$
R31	$Si_3H_8 + H \longrightarrow Si_2H_5 + SiH_4$	2.170×10^{-11}
R32	$Si_3H_8 + SiH_3 \longrightarrow Si_4H_9 + H_2$	1.000×10^{-11}

* Data are given for the interelectrode separation $l^0 = 2.5$ cm, partial pressures of molecular hydrogen and silane $p^0 = 0.125$ torr, and temperature $T^0 = 520$ K.

Other finalizing relationships for system (1) are boundary conditions (3) accounting for a concentration jump near the deposition surface, which, under the conditions specified above, can be of considerable magnitude:

$$-D_i \frac{\partial n_i}{\partial x} = \frac{s_i c_i}{2(2 - s_i)} n_i. \quad (6)$$

Here, $\partial/\partial x$ is a normal derivative at the outside of the surface, $c_i = 2\sqrt{2kT/\pi m_i}$ is the thermal velocity, and s_i is the deposition coefficient of the ith species. Values of these coefficients are given in [2]: $s_i = 0.15$ for SiH_3 and Si_2H_5; $s_i = 1$ for SiH, SiH_2, Si_2H_3, and Si_2H_4; and $s_i = 0$ for all other components. The electron density in the interelectrode gap is calculated in the fluidic approximation using a model described in detail in [5]. In the simulations, it is assumed that the hot electrons causing dissociation are available only in the interelectrode gap. Away from the gap, the energy of electrons diffusing from the discharge zone drops exponentially and becomes insufficient for initiating chemical reactions. In this sense, a technological system in which the substrate is outside the discharge zone can be considered as a system with remote plasma.

For numerical solution of this problem, a method described in [3] was employed.

Basic chemical reactions and their rate constants are listed in Table 2. In addition, silane and disilane pyrolysis reactions are taken into consideration, which, as is proved by the calculations, make an insignificant contribution to the total chemical balance.

2. ANALYTICAL RESULTS

Asymptotic analysis based on the difference of scale of different processes gave some analytical formulas and an explanation of the interrelationship between conditions in the chamber and various process parameters. In [3], such relationships are given only for the diode system, whereas in this work, such an analysis has been made for the triode system as well. The entire calculation area $0 < x < L$ was divided into two zones: $0 < x < l$, where the density n_e of electrons initiating the chemical reactions was taken equal to that in the interelectrode gap, and $l < x < L$, where plasma is penetrating, but the energy of its electrons is not enough to initiate the reactions. It is assumed that in the latter zone of size $d = L - l$, only monomolecular reactions or reactions involving molecular collisions are proceeding.

Estimates of basic processes similar to those in [3] produced the following simplified equation for the behavior of silyl:

$$D_{SiH_3} d^2 n_{SiH_3}/dx^2 = 2k_8 n_H n_{SiH_4} - k_{32} n_{SiH_3} n_{Si_3H_8}, \quad (7)$$

where k_i is the constant of the ith reaction (i is the reaction number in Table 2); condition (6) with a deposition coefficient $s_{SiH_3} = 0.15$ is taken as the boundary conditions for this equation.

A corresponding analysis for atomic hydrogen, which is the major initiator of silyl production, leads to

the following balance equation in the discharge region $0 < x < l$:

$$-D_H d^2 n_H/dx^2 = 2k_2 n_e n_{SiH_4} - k_8 n_{SiH_4} n_H. \quad (8)$$

Outside the discharge region at $l < x < L$ the behavior of atomic hydrogen is described by the same equation, except that the first term on the right-hand side should be omitted ($n_e = 0$); i.e., hydrogen gets outside the discharge zone only due to diffusion. Solving these equations with boundary conditions (6) in the absence of deposition ($s_H = 0$) and with the condition of smooth joining of solutions at the boundary of the zones (at $x = l$), we get an analytical expression for the atomic hydrogen concentration profile:

$$n_H = \frac{2k_2 n_e}{k_8}\left(1 - \frac{\sinh(d/L_H)}{\sinh(L/L_H)}\cosh\frac{x}{L_H}\right), \quad 0 < x < l, \quad (9)$$

$$n_H = \frac{2k_2 n_e}{k_8}\frac{\sinh(l/L_H)}{\sinh(L/L_H)}\cosh\frac{L-x}{L_H}, \quad l < x < L. \quad (10)$$

Substitution of expressions (9) and (10) into equation (7) yields an analytical dependence on the system parameters of the flow of silyl towards the surface:

$$\Gamma_{SiH_3} = \frac{2k_2 n_e n_{SiH_4} L_3}{\sinh(L/L_3)}\left[2\sinh^2\frac{l}{2L_3} + \frac{L_H^2}{L_3^2 - L_H^2}\frac{1}{\sinh(L/L_H)} \times\left(\cosh\frac{l}{L_3}\sinh\frac{L}{L_H} - \cosh\frac{L}{L_3}\sinh\frac{l}{L_H} - \sinh\frac{d}{L_H}\right)\right], \quad (11)$$

$$L_H = \sqrt{D_H/(k_8 n_{SiH_4})}, \quad L_3 = \sqrt{D_{SiH_3}/(k_{32} n_{Si_3H_8})}.$$

Here, L_H and L_3 are reaction-diffusion lengths for atomic hydrogen and silyl, respectively, introduced in [3] and defined as the distance which a diffusing species will travel before entering into a chemical reaction. For $l \longrightarrow L$ ($d \longrightarrow 0$), expression (11) describes a diode system.

To conclude this section, we consider the behavior of silylyl. In the discharge zone, silylyl is produced mainly via the decomposition of silane by electron impact, reaction R2, and through reaction R23, whereas, outside this zone, it is produced in reactions R15 and, again, R23. Withdrawal of silylyl through reactions in both cases depends on its reaction with silane (R9). The Si_2H_4 radical is an intermediate product of the cycle of fast chemical reactions R9, R27, and R23; therefore, its concentration is close to the equilibrium value $n^e_{Si_2H_4} = k_9 n_{SiH_2} n_{SiH_4}/(k_{23} n_{H_2} + k_{13} n_{SiH_4})$ [3]. If it were not for reaction R13 diverting part of the silicon atoms to higher silanes, reactions R23 and R9 would compensate one another and the only mechanism for silylyl to escape from the zone would be its diffusion to the surface for deposition and pumping out. Because the cycle in not closed, silylyl is withdrawn through a reaction with an effective constant $k_{eff} = k_9 k_{13} n_{SiH_4}/(k_{23} n_{H_2} + k_{13} n_{SiH_4}) \cong k_9/(n_{H_2}/n_{SiH_4} + 1)$. The last approximate equality is a consequence of $k_{13} \cong k_{23}$. Therefore, the behavior of silylyl can be described by the equations

$$-D_{SiH_2} d^2 n_{SiH_2}/dx^2 = k_2 n_e n_{SiH_4} - k_{ef} n_{SiH_2} n_{SiH_4}, \quad 0 < x < l, \quad (12)$$

$$-D_{SiH_2} d^2 n_{SiH_2}/dx^2 = k_{15} n^2_{SiH_3} - k_{ef} n_{SiH_2} n_{SiH_4}, \quad l < x < L. \quad (13)$$

By solving these equations with corresponding boundary conditions, an analytical expression for the flux of silylyl to the surface has been obtained, but, in view of its clumsiness, we do not present it here.

3. RESULTS AND DISCUSSION

(1) *Comparison with experiment.* Comparison with experimental data in the literature is difficult, because the set of parameters describing the system available there is far from complete. For this reason, we chose the results given in [4] for comparison. In this work, exhaustive information on the experimental conditions and results of numerical calculations are described.

The experimental installation was a chamber with a volume of 10 l and contained two electrodes of radius 8 cm located 2.7 cm apart. For this configuration, the ratio of the reaction volume to the total volume of the chamber is $R_v = 0.054$ (for more details, see Section 3.5). The experiments were carried out with a mixture of silane and hydrogen in equal molar concentrations with a flow rate equal to 3.6 l/h under normal atmospheric conditions; the temperature in the reactor was 400 K. A program for computing parameters of the RF discharge between two plane-parallel electrodes was used to calculate the electron densities [5]. The main problem was to obtain a good estimate of the discharge power. In [4], from a comparison of the self-bias potential computed in simulations of argon plasma based on corresponding experiments, it was determined that the power directed to the discharge amounted to 50% of the total power. The same conclusion was made from a comparison of the calculated concentrations of H_2 and SiH_4 in the hydrogen–silane plasma with experimental data. Therefore, in calculations performed for the suggested model, we used the power value of 0.05 W/cm^2 proposed in [4].

Figure 1 shows the dependence of the film growth rate on the discharge frequency at a constant pressure of 16 Pa in the reactor. It is seen that the results are in good agreement with experimental data up to a frequency of 30 MHz. At frequencies higher than 30 MHz, the calculated curve tends to level off. The same tendency, although more gradual, was noted in [4]. At the same

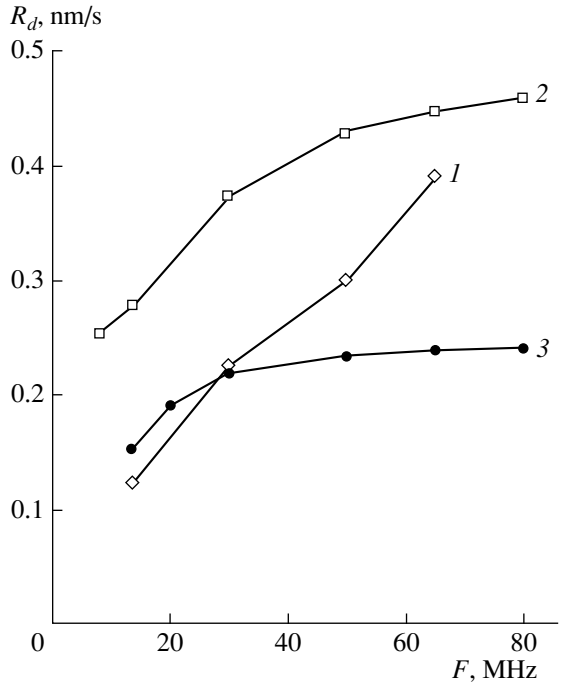

Fig. 1. Film growth rate as a function of discharge frequency at a constant pressure in the chamber p = 16 Pa. (*1*) Experiment [4], (*2*) calculation [4], and (*3*) this work.

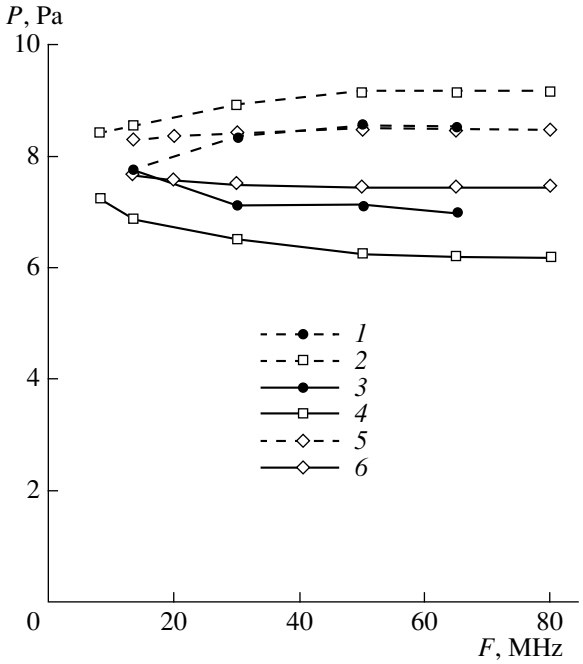

Fig. 2. Partial pressures of molecular hydrogen (*1*, *3*, *5*) and silane (*2*, *4*, *6*) as a function of discharge frequency. (*1*, *3*) Experiment [4], (*2*, *4*) calculation [4], and (*5*, *6*) this work.

time, in [4], the experimental dependence of the growth rate on frequency was approximately linear. To explain this effect, additional investigations are needed; their possible directions have been proposed in [4].

From the calculations of the partial pressures of molecular hydrogen and silane as functions of the discharge frequency given in Fig. 2, it is seen that the data obtained using the approach developed in this study are in better agreement with experiment than the calculation results obtained in [4].

(2) *Specific features of chemical kinetics at low pressures.* With the model described in Section 1, calculations are possible of the processes at low pressures, at which silane decomposition becomes noticeable and the concentration of molecular hydrogen can no longer be considered small. Below, we discuss in detail the qualitative differences of these processes from those taking place at high pressures.

Dependence of the electron density in the discharge zone on the process parameters was described by a formula [3] derived for the case of constant discharge power

$$n_e(p_{SiH_4}l) = n_e^0 p_{SiH_4}^0 l^0 / p_{SiH_4} l, \qquad (14)$$

where n_e^0 is the electron density under basic conditions, taken equal to 5×10^8 cm^{-3}. This formula is true for pressures that are not very low, but it was used for the qualitative analysis in the entire range of pressures. For other key parameters of the problem, values characteristic of real experimental setups were chosen [1, 2]: the temperature in the reaction chamber was taken equal to 520 K, the pressure was 0.25 torr, and the interelectrode distance was $l = L$ = 2.5 cm. Under these conditions, the reactor parameters corresponded to a characteristic pumping time of τ = 1s at a pressure of 1 torr (for more details on this characteristic, see Section 3.4). The calculations were carried out for the pressure range $0.02 < p < 1$ torr. All the results given in this section refer to the case of pure silane as the carrier.

One of main distinctions of the considered processes is a considerable rise in the concentration of atomic hydrogen with decreasing pressure. There are a number of reasons for this. First of all, as seen from formula (9), the concentration of atomic hydrogen in the particular case of homogeneous discharge is given by formula

$$n_H = 2k_2 n_e / k_8; \qquad (15)$$

i.e., it depends only on the electron density. This formula is also in good agreement with the calculation results. At the same time, as seen from formulas (4), (5), and (14), the electron density and the constant k_2 rise rapidly with decreasing silane pressure, so that the concentration of atomic hydrogen increases by nearly five orders of magnitude as the pressure in the chamber decreases from 1 to 0.02 torr and the relative silane concentration decreases to 0.3 as a result of its decomposition. The increase in atomic hydrogen concentration causes qualitative changes in various processes.

The behavior of other components with variations in pressure does not change compared with the description in [3], except for the fact that the concentration of Si_2H_6 drops at pressures below 0.1 torr. The same effect is observed for Si_3H_8. This is due to the appreciable drop in silane concentration and the increase in atomic hydrogen concentration, the main reactants determining the formation and decomposition of these components. The increase in atomic hydrogen concentration also affects the balance and role of different reactions in silyl decomposition. Thus, at low pressures, a noticeable growth in the role of the decomposition process in the silyl balance is observed; at 0.02 torr, it becomes dominant and prevails over deposition. Note, however, that this result is entirely a property of the model, because the use of formula (14) at very low pressures gives values of the electron density that are too high.

At pressures below about 0.08 torr in silyl decomposition, the reaction $SiH_4 + Si_3H_8 \longrightarrow Si_4H_9 + H_2$ gives way as the dominant process to reaction $SiH_3 + SiH_3 \longrightarrow SiH_4 + SiH_2$; and at pressures of about 0.02 torr, to the reaction between silyl and atomic hydrogen, which begins to make a noticeable contribution to the production of silyl. As before, silyl formation is completely dominated by the reaction between silane and atomic hydrogen.

Contributions of individual reactions to the silylyl balance remain largely unchanged, but its production at low pressures increases so much that most of the silylyl is deposited instead of being decomposed. Because of all these changes, the contribution of silylyl to film growth, which, with decreasing pressure, increases at a greater rate than that of silyl, becomes dominant at a pressure of 0.02 torr. This should cause appreciable modifications in the film structure.

Taking into account silane decomposition at low pressures revealed further details of the division [3] of all components into three groups: stationary, nonstationary, and quasi-stationary. It was found that SiH can be considered strictly stationary only at high pressures. In addition, at high pressures, stationary components also include silylyl, the balance of which is maintained by two reactions with silane: $SiH_4 + e \longrightarrow SiH_2 + 2H + e$ and $SiH_4 + SiH_2 \longrightarrow Si_2H_6^*$, with the latter reaction keeping the concentrations of $Si_2H_6^*$ and Si_2H_4 (which is produced via decomposition of $Si_2H_6^*$) stationary. At low pressures, these last two components go over to the quasi-stationary group because of the appreciable decomposition of silane, resulting in an increase in electron density and reaction rate constants. This is especially noticeable in the behavior of atomic hydrogen, whose concentration at high pressure is stationary and adequately described by formula (15). At low pressures, the deviation from stationarity caused by these processes makes atomic hydrogen nonstationary and appreciable accumulation of this component in the reaction chamber begins. Other parts of this classification remain qualitatively unchanged (see details in [3]).

(3) *Effect of diffusion coefficients.* The use of formula (2) in calculating the diffusion coefficients does not significantly change the main results (such as the growth rate and film composition) compared with calculations in which these coefficients were assumed to be equal to the coefficients of ambipolar diffusion of the respective components in silane, as was done in [3]. This result appears to be quite evident at high pressures, where the concentration of molecular hydrogen is rather low and the diffusion coefficients calculated by formula (2) are close to the corresponding ambipolar coefficients. However, at low pressures, these values are distinctly different.

This fact suggests that the concentration profiles of the depositing components adjust in such a way as to maintain the production–deposition balance, irrespective of the particular values of the diffusion coefficients (the rate of chemical decomposition of silyl and silylyl at low pressures is small).

For a more detailed investigation of this issue, calculations using the above approach were carried out for a mixture of silane and molecular hydrogen at equal partial pressures and constant electron density $5 \times 10^8\,\mathrm{cm}^{-3}$. In this case, the influence of the diffusion coefficients is more pronounced. For the same purpose, a simplified formula was used to calculate reaction rate constants as functions of pressure [3]:

$$\frac{k_r}{k_r^0} = \left(\frac{l^0 p^0}{lp}\right)^{2\epsilon_r/\epsilon_i}.$$

Under these conditions, the diffusion coefficients calculated by Wilke's formula differ from the ambipolar diffusion coefficients by a factor of 1.6–1.7. Still, at low pressures where the silyl–silylyl balance is dominated by deposition, the fluxes of these components to the substrate are practically coincident in the two cases, despite distinctly different concentration profiles. At high pressures, silylyl is spent mainly through reactions in the bulk and the values of fluxes obtained with the use of constant ambipolar diffusion coefficients are somewhat less than those given by Wilke's formula; however, this difference is a mere 10% for silyl and 20% for silylyl, which is much less than the difference in the coefficients, and the contribution of silylyl to film growth under these pressures is insignificant.

To check this, a series of calculations was carried out for varying values of the diffusion coefficients. In one of these, the diffusion coefficient for silyl was assumed to be twice as large. The film growth rate was almost unchanged, although at a pressure of 1 torr, the silyl concentration dropped by a factor of 1.5.

This fact is explained as follows. Because the dominant contribution to film growth comes from the flux of silyl, the growth rate can be analyzed using expression (11). At $d = 0$, this expression is significantly simpli-

fied, reducing to $\Gamma_{SiH_3} = 2k_2 n_e n_{SiH_4} L_3 \tanh(L/2L_3)$. For real values of the diffusion coefficient, $L/2L_3 < 0.7$ throughout the range of pressures studied and, therefore, the dependence of Γ_{SiH_3} on L_3 is weak. An increase in the diffusion coefficient only reduces the dependence of the flux of silyl on its value. Thus, silyl deposition is virtually unaffected by diffusion processes.

A similar result was also obtained for silylyl. The twofold increase in the silylyl diffusion coefficient did not produce any significant changes. At low pressures, the silylyl concentration decreased, but the modified profiles ensured exactly the same value of its flux. At higher pressures, the silylyl balance is completely controlled by chemical reactions; therefore, its concentration (as well as concentrations of all other components) remained the same, but the flux increased somewhat (by 37% at $p = 1$ torr). However, at this pressure, the contribution from SiH_2 to film growth is quite small and cannot change the final result.

It can be concluded from the above that further specifying the description of diffusion transport cannot significantly change the results, especially in the case of a pure silane plasma.

(4) *Effect of the flow rate.* The flow rate of the mixture through the working reactor volume is one of the important factors affecting the film growth parameters, and, at the same time, it can be easily varied. In [3], an approach that allows one to take into account the effect of the flow rate using a simple one-dimensional model was suggested. In this approach, the initial steady-state problem is replaced with a nonstationary problem, which is to be solved for a time period τ equal to the characteristic time of transit of the mixture in the reactor working volume. Decomposition of a considerable part of silane occurring at low flow rates and a significant increase in the molecular hydrogen concentration render the model suggested in [3] inapplicable for studying the role of the flow rate in a relatively wide range of this parameter.

Using the model presented in this study, the effect of the flow rate has been analyzed for the example of pure silane for τ ranging from 0.13 to 2.6 s, which, at a pressure of 0.25 torr, corresponds to a change in the chamber volume from 1 to 20 l for the fixed flow rate of silane of 5 l/h at atmospheric pressure. Values of the other parameters were the same as in the previous sections, and the electron density was calculated by formula (14).

As in [3], variation of the flow rate was found to affect, first of all, the concentration of Si_2H_6: it increased by an order of magnitude as the flow rate was reduced by the same factor. At the same time, the concentration of Si_3H_8 increased by a factor of about 5. On the whole, variation of the flow rate corresponding to the considered range of τ caused only insignificant variations of the characteristics of the growing film. Thus, with a decreasing flow rate, the film growth rate increased by 30%. This was due to an increase in both the electron density and the reaction rate constants with a decreasing partial concentration of silane. The relative contribution of silylyl increased by about the same amount. This was caused by an increase in the concentration of molecular hydrogen and, subsequently, a greater contribution to the recovery of the silylyl concentration from the cyclic reaction $SiH_4 + SiH_2 \longrightarrow Si_2H_6^* \longrightarrow Si_2H_4 + H_2 \longrightarrow SiH_4 + SiH_2$.

(5) *The effect of chamber volume.* The problem considered above is closely related to the effect of the ratio of the reaction volume to the entire chamber volume, because circulation of the components throughout the volume can change the course of the processes.

To investigate this aspect in a one-dimensional case, the following approach was suggested: the area under study was expanded by adding a region R such that the ratio R_v would have been equal to the total chamber volume. The calculations for a fixed parameter τ and variable R_v gave estimates of the effect of circulation. The results described below were obtained for a total chamber volume of 2 l and $\tau = 0.26$ s; other parameters were the same as before.

Changing the parameter R_v from 1 to 0.2 resulted in an insignificant (about 25%) increase in the rates of film growth and silyl deposition. This increase was caused by increased concentrations of silane and silyl in the reaction volume because of the influx of SiH_4 from the chamber volume. At the same time, silylyl deposition remained nearly constant, because some increase in its production due to the reaction of silylyl decomposition (R15) was offset by reaction $SiH_4 + SiH_2$ and deposition occurs only from a thin near-wall layer, where the concentration of silyl is low. Figures 3–5 illustrate some distinctive features of these processes.

In Fig. 3, profiles of typical representatives of the three classes of components are shown: nondepositing and slowly reacting (H_2), nondepositing and rapidly reacting (H), and depositing and rapidly reacting (SiH_2). It is seen that the concentrations of the latter two components in the reaction volume are practically independent of the chamber volume. They are determined by reactions proceeding in the discharge zone, and circulation has little effect on them. The concentration of molecular hydrogen, on the contrary, is constant throughout the chamber volume and is appreciably reduced by circulation.

The small reaction-diffusion length for silylyl with respect to the chamber dimensions is the reason for the weak influence of the chamber volume on the balance and flows of this radical (Figs. 4, 5). Only some increase in its production due to a higher silane concentration can be noted; this increase is compensated by its more intensive (for the same reason) decomposition, so that flows onto the substrate turn out to be about the same.

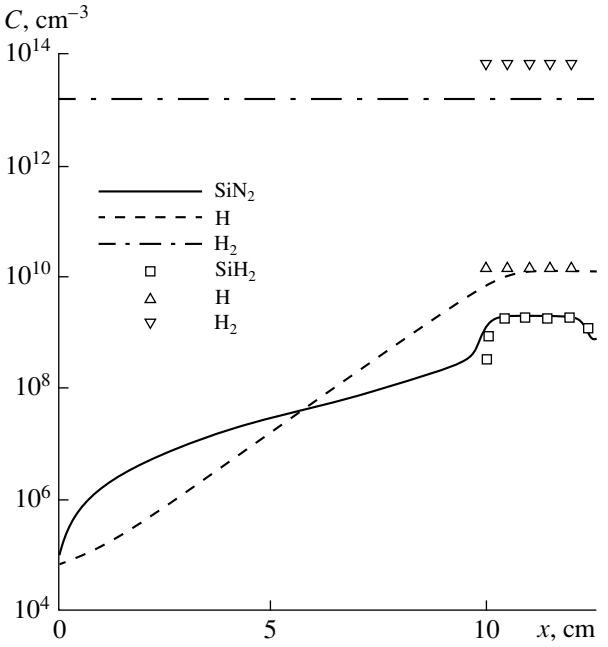

Fig. 3. Concentration profiles of silylyl and molecular and atomic hydrogen at different values of the ratio of reaction volume to the total chamber volume R_v equal to 0.2 (curves) and 1 (dots).

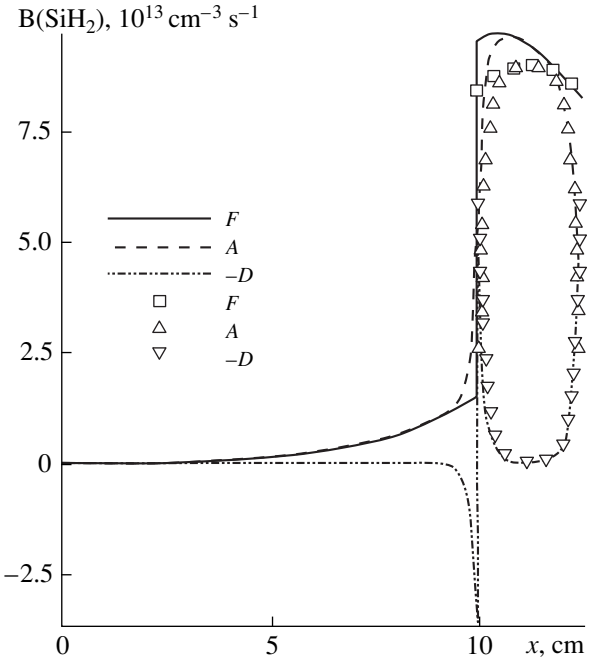

Fig. 4. Silylyl balance at different values of the ratio of reaction volume to the total chamber volume R_V: *F*, production; *A*, decomposition; *D*, diffusion; R_V = 0.2 (curves) and 1 (dots).

(6) *The effect of diluting silane with molecular hydrogen.* In real equipment, a mixture of silane and molecular hydrogen is widely used. To evaluate the effect of silane dilution, calculations have been carried out for a silane content in this mixture varying from 100 to 20%, the other parameters having the same values as before. The electron density was determined using an RF discharge model [5]. Calculations for a discharge power of 0.025 W/cm^2 have shown that, in these conditions, the average electron density rises nearly linearly from 4.3×10^8 to 6.7×10^8 cm^{-3} as the silane content in the mixture is reduced.

As the silane content at constant pressure is reduced, the diffusion coefficients of the components, with the exception of H_2, increase by a factor of 2–3. Variation of the concentrations of all reaction products under these conditions is shown in Fig. 6. The film growth rate rises, and the relative contribution of silylyl to overall deposition becomes larger (Fig. 7). The growth rate rises, despite falling silane concentration, because of an increase in the total production of depositing components due to higher rate constants of reactions initiated by electron impact (see expressions (4) and (5)) and increased electron density. In addition, the net result of lowering the concentration and the simultaneous increase in the diffusion coefficients is that the greater part of the produced silyl is deposited; this is true for other depositing components, except Si_2H_3 and Si_2H_4, which are effectively decomposed by molecular hydrogen. The behavior of silylyl is explained by the fact that with an increasing concentration of H_2 and a decreasing concentration of silane, the fraction of silylyl being deposited rises significantly. At the same time, the intensity of the above-mentioned cyclic reaction rises, leading to the recovery of the SiH_2 concentration.

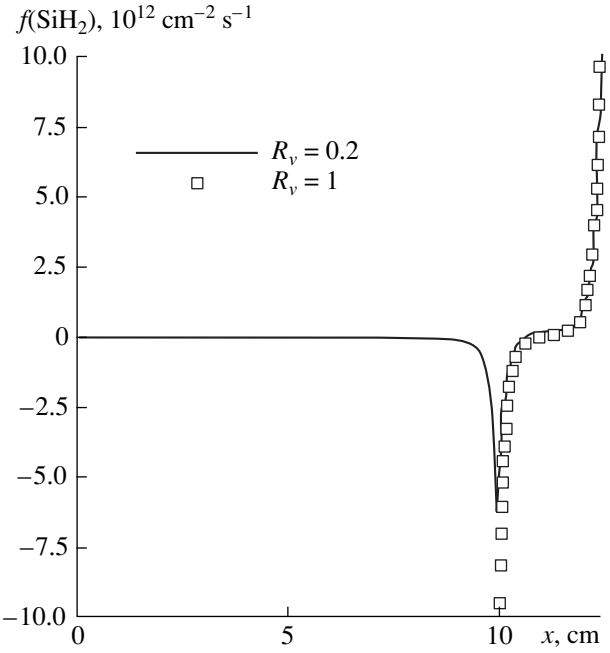

Fig. 5. Silylyl fluxes at different values of the ratio of the reaction volume to the total chamber volume R_V.

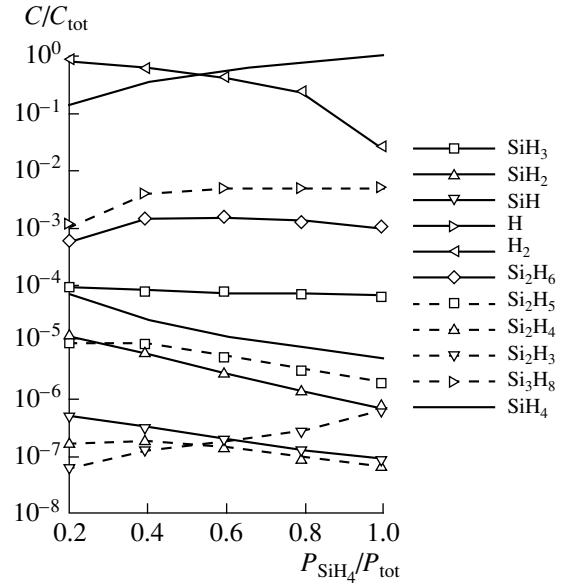

Fig. 6. Concentrations of components as a function of the silane fraction in the initial silane–hydrogen mixture at constant pressure.

Also worth noting is the considerable reduction in the Si_3H_8 concentration with dilution (Fig. 6). The reason is that alongside the drop in production by the reaction $SiH_4 + Si_2H_4$, it is decomposed via the reaction with atomic hydrogen, whose concentration rises at a high rate. The result is a drastic drop in Si_4H_9 production, and the greater part of the silicon produced in the reaction is deposited.

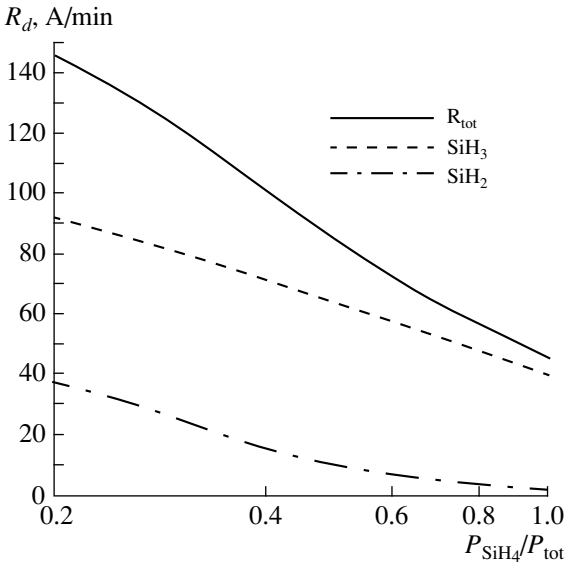

Fig. 7. Film growth rate and contributions of silyl and silylyl to it as a function of the fraction of silane in the initial silane–hydrogen mixture at constant pressure.

(7) *Specific features of the triode system.* All the results described above were obtained for a diode system in which the discharge zone is located between two electrodes, one of which serves as a substrate for the growing film. One alternative technology is the so-called triode system, in which the discharge zone is separated from the substrate. Formulation of the respective problem has been described in Sections 1 and 2.

In order to investigate the effect of the separation of electrodes from the substrate, calculations of film growth from a pure silane plasma were carried out for the same problem parameters as previously used (with the exception of parameter $L = 5$ cm, with parameter l/L varying from 0.4 to 1). The electron densities determined using the RF discharge model [5] were varied from 6.8×10^8 to 4.9×10^8 cm^{-3}. The calculation results obtained using the above analytical expressions for the silyl flux (11) and the concentration profile of atomic hydrogen (9), (10) are in good agreement with numerical simulation results, as seen in Figs. 8 and 9, respectively.

As a result of varying the parameter l/L in the range specified above, the film growth rate (at a constant discharge power) decreased by only half. The cause of the slow decrease in the growth rate with increasing separation between the electrode and the substrate is the increase in electron densities and rate constants of reactions initiated by electron impact as the interelectrode separation l is reduced, which partially compensates decomposition of silicon-containing components outside the discharge zone. In addition, a drastic reduction in the contribution to the film growth from silylyl

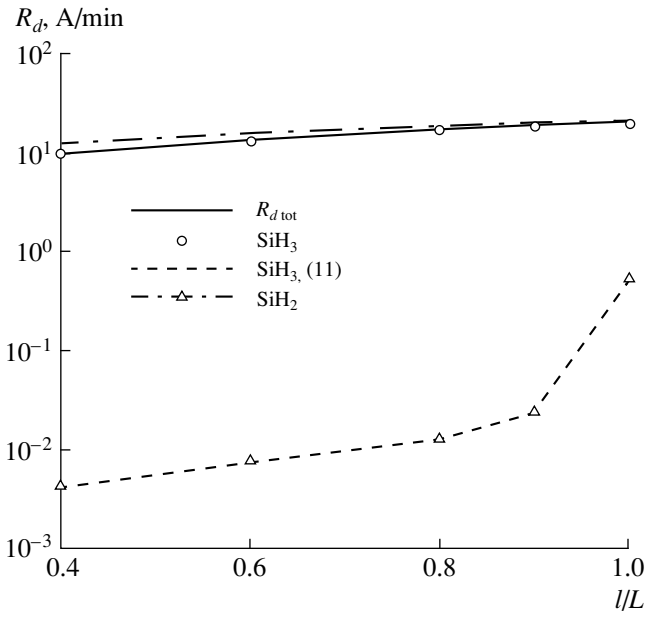

Fig. 8. Film growth rate and contributions of silyl and silylyl as a function of the ratio of discharge zone to the total reactor zone. Numerical and analytical solutions (formula (11)).

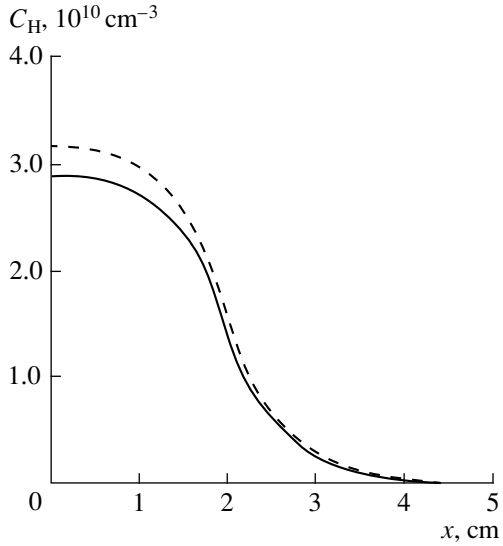

Fig. 9. Atomic hydrogen profiles for the triode reactor system (l/L = 0.4): solid curve, analytical solution; dashed curve, numerical solution.

should be noted, starting as soon as the electrode is moved away from the substrate (Fig. 8). This is especially remarkable in view of the fact that at the same time, its concentration and total production are rising. Two main reasons for this effect can be indicated. The first is that the reaction-diffusion length of silylyl is much less compared with silyl; therefore, the bulk decomposition of silylyl is more efficient. The second reason is the very different mechanisms of their production. The major source of silyl is the reaction between silane and atomic hydrogen, which, as seen in Fig. 9, diffuses quite intensively beyond the discharge zone. On the other hand, the main contribution to silylyl production comes from the reaction between silane molecules themselves; therefore, production of SiH_2 outside the discharge is small.

CONCLUSIONS

In this work, numerical investigations of the growth of hydrogenated amorphous silicon films have been carried out under various conditions in the growth chamber.

Comparison with experimental data has demonstrated the ability of the model to predict the film growth rate and concentrations of individual components with reasonable accuracy.

It has been shown that the widely used technique of diluting silane with molecular hydrogen both increases the growth rate and reduces production of higher silanes, making this technology more economical and ecologically clean. Moreover, dilution increases the contribution of silylyl to film growth, appreciably affecting its properties.

Analysis of a widely used reactor system has been carried out. Numerical simulation has shown that the effective decomposition of silylyl outside the discharge zone reduces its contribution to film growth as the substrate is displaced away from the discharge.

The analytical expressions obtained for silyl and silylyl fluxes and for the profile of atomic hydrogen closely approximate the results of numerical computations and can be used for making the corresponding estimations.

ACKNOWLEDGMENTS

This work was partly supported by the Russian Foundation for Basic Research, project no. 97-01-00233 and INTAS, project no. 96-0235.

REFERENCES

1. O. A. Golikova, Fiz. Tekh. Poluprovodn. (Leningrad) **25**, 1517 (1991) [Sov. Phys. Semicond. **25**, 915 (1991)].
2. M. J. Kushner, J. Appl. Phys. **63**, 2532 (1988).
3. Yu. E. Gorbachev, M. A. Zatevakhin, and I. D. Kaganovich, Zh. Tekh. Fiz. **66** (12), 89 (1996) [Tech. Phys. **41**, 1247 (1996)].
4. G. J. Nienhuis, W. J. Goedheer, *et al.*, J. Appl. Phys. **82**, 2060 (1997).
5. M. I. Zhilyaev, V. A. Shveĭgert, and I. V. Shveĭgert, Prikl. Mekh. Tekh. Fiz. **35** (1), 13 (1994).
6. C. R. Wilke, Chem. Eng. Prog. **46** (2), 95 (1950).
7. J. O. Hirschfelder, C. F. Curtiss, and R. B. Bird, *Molecular Theory of Gases and Liquids* (Wiley, New York, 1954; Inostrannaya Literatura, Moscow, 1961).
8. I. P. Ginzburg, *Friction and Heat Transfer in Moving Gas Mixtures* (Leningrad. Univ., Leningrad, 1975).
9. J. Perrin and O. Leroy, Contrib. Plasma Phys. **36** (3), 3 (1996).
10. N. Itabashi, K. Kamo, and N. Nishawaki, Jpn. J. Appl. Phys. **28**, 325 (1989).
11. J. Perrin, J. Phys. D **26**, 1662 (1993).

Translated by B. Kalinin

Technical Physics, Vol. 45, No. 8, 2000, pp. 1042–1044. Translated from Zhurnal Tekhnicheskoĭ Fiziki, Vol. 70, No. 8, 2000, pp. 87–90.

OPTICS, QUANTUM ELECTRONICS

Electroluminescence of Ion-Implanted Si–SiO_2 Structures

A. P. Baraban, P. P. Konorov, L. V. Malyavka, and A. G. Troshikhin

St. Petersburg State University, Institute of Physics, Universitetskaya nab., St. Petersburg, 198904 Russia

Received October 6, 1999

Abstract—Specific features of the electroluminescence of ion-implanted (Ar ion implantation in oxide layer bulk) and ion-synthesized (SIMOX technology) Si–SiO_2 structures were studied. The electroluminescence from the electrolyte-insulator-semiconductor system was registered in the 250–800 nm range at room temperature. It has been found that implantation increases the concentration of centers already present in the oxide layer bulk and creates new luminescent centers. The nature and the models of the centers are discussed. © *2000 MAIK "Nauka/Interperiodica".*

Lately, ion implantation in solid-state structures has been widely used both in fundamental and applied research. This is due to a range of opportunities offered by implantation, which produces controllable transformations of both the structure and atomic and electronic properties of solids by way of introducing selected ions to a specified depth (depending on the impinging ion energy). This allows the type and level of doping in the semiconductor near-surface region to change, to form submerged oxide layers in the bulk of silicon (SIMOX technology), and to significantly modify the electrophysical properties of dielectric layers at the semiconductors surface [1]. One of the main problems involved in the utilization of ion implantation is to determine the properties and nature of the defects introduced in the process. The development of a fast, nondestructive process control method is an important fundamental and practical task. Electroluminescence (EL) is a highly reliable method of studying Si–SiO_2 structures. It detects the presence and identifies the types of defects in the oxide layer, as well as their concentration and spatial distribution, by measuring the spectral distribution and intensity of characteristic bands [2].

The purpose of this work is to study the specific features of EL in ion-implanted and ion-synthesized Si–SiO_2 structures and apply EL to the study of defects produced by implantation.

The EL in the 250–800 nm range was registered from an electrolyte–insulator–semiconductor system [2], with the sensitivity significantly enhanced due to utilization of a field electrode transparent in this spectral range (1 pH water solution of Na_2SO_4). The measurements were carried out in a photon-counting regime at 293 K.

In this paper, three types of Si–SiO_2 structures were investigated. Type 1 structures were produced by the thermal oxidation of silicon (grade KDB-10 (100)) in accordance with the usual technologies. Type 2 structures were made by SIMOX technology. Oxygen ions of energy 190 keV and dose 1.8×10^{18} cm^{-2} were implanted into the silicon bulk at 650°C, followed by annealing for 6 hours at 1320°C and the etching away of the outer silicon layer, which resulted in the formation of a 390-nm-thick silicon dioxide layer. Type 3 structures were prepared by the thermal oxidation of KÉF-5 (100) silicon in a humid oxygen ambient at 950°C and the subsequent implantation of argon ions. The ion energy, 130 keV, was chosen with a view to having the maximum density of implanted ions in the middle of the oxide layer, and the doses were in the 10^{13}–3.2×10^{17} cm^{-2} range. Some of these structures were subjected to a fast thermal (radiative) annealing (FTA) at temperatures of 500–1100°C for 10 s.

Figure 1 shows EL spectra of type 1 structures prepared with the use of different technologies. Earlier, characteristic emission bands at energies 1.9, 2.3, 2.7, 3.3, 3.8, and 4.6 eV, corresponding to various types of defects located in the oxide layer and at the Si–SiO_2 interface, were identified in this spectrum [2]. It has

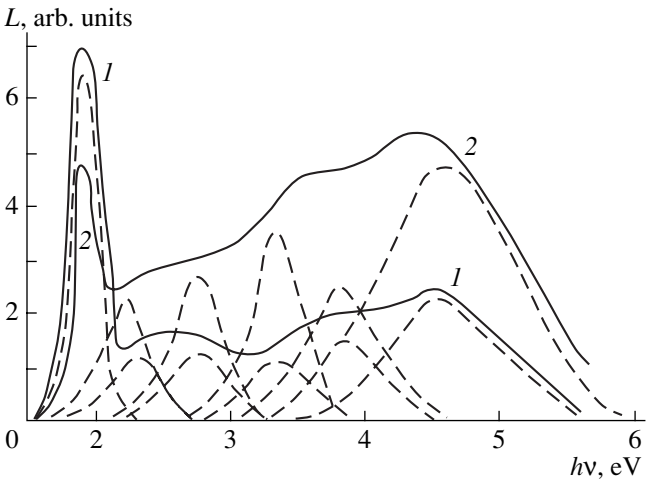

Fig. 1. EL spectra of standard Si–SiO_2 structures produced by thermal oxidation of KDB-10 (100) silicon: (*1*) in water vapor at 950°C; (*2*) in dried oxygen at 1100°C.

1063-7842/00/4508-1042$20.00 © 2000 MAIK "Nauka/Interperiodica"

been shown that the luminescence centers responsible for the red EL band at 1.9 eV are silanol groups localized in the outer SiO_2 layer and that their concentration and spatial distribution correlate with those of the electron capture centers [2]. Three-coordinated silicon localized near the Si–SiO_2 interface is the center responsible for the EL band at 2.3 eV, which is due to intracenter electron transitions in silicon atoms induced by hot electrons created in the oxide layer [2]. Luminescence centers responsible for emission in the ultraviolet (UV) spectral range are localized near the Si–SiO_2 interface [2], but the nature of these centers in these particular structures has not yet been conclusively ascertained.

The EL band at 2.7 eV is the most interesting. In nonimplanted structures, it is observed only in the range of electric fields producing impact ionization of the SiO_2 matrix. Its localization is not fixed, being coincident with the position of the impact ionization probability maximum in SiO_2 (determined by the electric field strength in the oxide layer), where the concentration of dangling Si–O bonds is a maximum.

The EL spectrum of type 2 structures is presented in Fig. 2. The band at 1.9 eV is not observed in this spectrum, indicating the absence of silanol groups in the oxide layer. This is explained by the specific technology of these structures, which eliminates penetration of the fragments of water molecules (hydrogen, hydroxyl groups) into the oxide layer.

At the same time, an intense band at 2.7 eV is observed in the EL spectrum for electric fields not causing impact ionization. Its intensity is practically not affected by etching half the oxide layer away. This means that the centers that are responsible for this band are mainly localized near the Si–SiO_2 interface. The energy position and the root-mean-square variance of this band (0.35 ± 0.05 eV) are the same as in nonimplanted structures. An emission band at 4.4 ± 0.1 eV occurs in the UV range of the spectrum, which is well fitted by the Gaussian distribution function with a root-mean-square variance of 0.4 ± 0.1 eV.

EL spectra of type 3 structures are presented in Fig. 3. There are three well-resolved EL bands in the spectrum. Two of the bands have the same energy positions at 1.9 and 2.7 eV and fit the same Gaussian distributions as in the initial structures, but the EL band at 2.7 eV is excited by fields lower than those causing the impact ionization in the oxide layer. As in type 2 structures, one EL band in the UV range is observed at energy 4.4 eV. It fits the Gaussian function with the same variance.

It has been found that the intensity of the EL band at 1.9 eV grows with an increase in the implantation dose for doses up to 10^{14} cm^{-2}, levels off at 10^{15} cm^{-2}, and drops down as the dose is further increased. The EL bands at 2.7 and 4.4 eV are seen in spectra of the structures implanted with doses 10^{13} cm^{-2} and higher. A further increase of the dose to 10^{17} cm^{-2} causes a drop in the intensity of these bands, which is succeeded by rapid growth at a dose of 3.2×10^{17} cm^{-2}. The ratio of intensities of the bands at 2.7 and 4.4 eV stays constant.

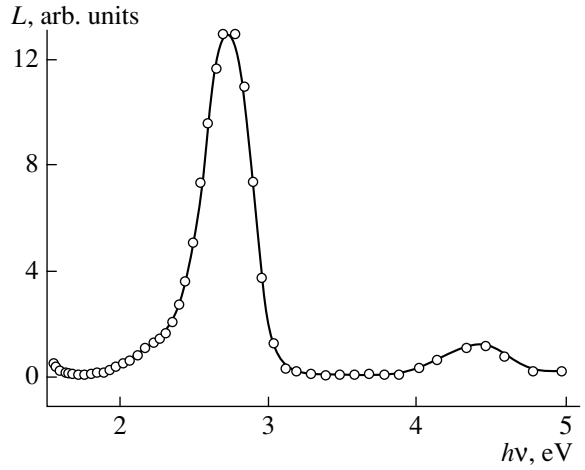

Fig. 2. EL spectra of Si–SiO_2 structures formed using SIMOX technology.

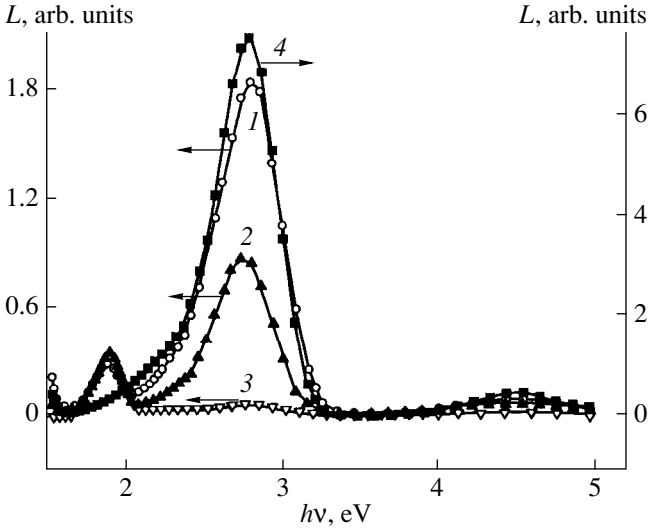

Fig. 3. EL spectra of argon-implanted Si–SiO_2 structures. D = (*1*) 10^{13}; (*2*) 10^{14}; (*3*) 10^{16}; (*4*) 3.2×10^{17} cm^{-2}.

To determine the localization area of the luminescence centers, we monitored the intensity variations of the bands at 1.9, 2.7, and 4.4 eV resulting from the progressive etching away of the oxide layer. It has been found that the centers emitting at 1.9 eV are localized in the outer region of the oxide layers, as in the nonimplanted structures. The localization area of the centers broadens with the implantation dose. Centers emitting at 2.7 and 4.4 eV are located mainly in the 30–140 nm region from the Si–SiO_2 interphase boundary. Their distribution maximum is closer to the Si boundary than that of the implanted argon ions. Increase of the dose

causes the smearing of the spatial distribution of luminescence centers and the shifting of its maximum towards the Si boundary. The intensities of all EL bands observed decrease as a result of FTA as the anneal temperature is increased.

To reveal the nature of the defects responsible for the EL at 2.7 and 4.4 eV, let us discuss the processes occurring in the silicon oxide layers during argon ion implantation. The bombarding argon ions lose their energy in the oxide layer through interactions with its atomic and electronic subsystems, thereby generating the structural defects of the SiO_2 matrix and electron-hole pairs, respectively.

In the outer region of the oxide layer, approximately equal amounts of energy are dissipated due to interactions with the atomic and electronic subsystems. In the bulk of the oxide layer, the more probable channel of energy dissipation for the bombarding argon atoms is the interaction with the atomic subsystem. Therefore, the greatest amount of dangling Si–O bonds occurs near the maximum of the distribution of implanted argon ions, and the Si and O atoms are found displaced deeper into the oxide layer. The estimated displacement from the distribution maximum of implanted argon ions is 80–170 nm for oxygen atoms and 30–70 nm for Si atoms. As a consequence, two nonstoichiometric regions of SiO_x with $x > 2$ and $x < 2$ are formed in the bulk of the oxide layer [3]. The region rich in oxygen ($x > 2$) is located closer to the boundary with silicon due to the larger displacement of oxygen atoms compared with that of Si atoms.

In the oxygen-deficient region of SiO_2, defects of the two-coordinated silicon atom (O_2 = Si:) type are formed; these we consider to be the EL centers responsible for the 2.7- and 4.4-eV bands. Such defects are generated in ion implantation as two of the Si–O bonds in a silicon-oxygen tetrahedron become broken and the broken bonds spatially separated because of the greater inward displacements of oxygen atoms in the oxide layer. According to data in the literature [4], in defects of this type, two radiative transitions are possible with energies 2.7 and 4.4 eV, their excitation energy being equal to approximately 5 eV. These luminescence centers are excited due to interaction with hot electrons whose mean kinetic energy in the electric fields of the range used for exciting EL in SiO_2 is just around 5 eV. The decrease in the intensity of the 2.7- and 4.4-eV bands caused by exposure to external factors (FTA) is explained by the partial restoration of the broken bonds in the oxide layer bulk and a decrease in the concentration of two-coordinated silicon. The nonmonotonic behavior of the intensity of 2.7- and 4.4-eV EL bands with an implantation dose is of special interest. This fact indicates that the variation of the concentration of =Si-type defects is nonmonotonic. The lowering of the concentration of these defects with an increasing dose is apparently due to the partial restoration of the broken bonds because of the considerable reduction of the average distance between neighboring implantation-induced defects accompanied by structural changes in the oxide layer due to the change in the silicon-oxygen bond angle, the formation of =Si=Si=-type defects in the SiO_2 bulk, and so on. The drastic enhancement of these EL bands at the highest doses suggests the renewed generation of defects like two-coordinated silicon, which this time takes place in a dielectric layer whose structure and properties differ from those of the initial SiO_2 matrix. This argumentation is supported by the nonmonotonic behavior of the intensity of a photoluminescence band at 2.7 eV with an increasing dose of silicon implanted in the oxide layer, as well as with an increasing concentration of excess silicon in SiO_2 films [5, 6].

The abovementioned peculiarities of the EL band at 1.9 eV (due to silanol groups in the oxide layer) display the considerable transformation of the atomic structure in the outer portion of the oxide layer as a result of ion implantation. The growth of the concentration and localization area of the silanol groups is attributed to the generation of these defects in the retardation tracks of bombarding argon ions due to the breaking of the Si–O bonds and their subsequent capture by hydrogen and/or by hydroxyl groups localized in the oxide layer or diffusing from the ambient. This process results in the growth of the concentration of electron traps in the outer region of the oxide layer and depends on the argon implantation dose.

In the case of the Si–SiO_2 structures produced by SIMOX technology, the EL bands at 2.7 eV and 4.4 eV are also attributed to defects of the two-coordinated silicon (=S :) type. However, these defects in such structures are due to the formation of silicon clusters near the Si–SiO_2 interface during the fabrication process.

Thus, EL provides a quick and efficient (a spectrum can be taken in less than 10 minutes) means of studying ion-implanted Si–SiO_2 structures and getting information about their structural and electrophysical properties.

REFERENCES

1. H. Ryssel and I. Ruge, *Ionenimplantation* (Teubner, Stuttgart, 1978; Nauka, Moscow, 1983).
2. A. P. Baraban, V. V. Bulavinov, and P. P. Konorov, *Electronics of SiO_2 Layers on Silicon* (Leningrad. Gos. Univ., Leningrad, 1988).
3. B. Garido, J. Samitier, S. Bota, *et al.*, J. Non-Cryst. Solids **187**, 101 (1995).
4. L. N. Skuja, A. N. Streletsky, and A. B. Pakovich, Solid State Commun. **50**, 1069 (1984).
5. W. Skorupa, R. A. Yankov, *et al.*, Appl. Phys. Lett. **68**, 2410 (1996).
6. D. J. DiMaria, J. R. Kirtley, *et al.*, J. Appl. Phys. **56**, 401 (1984).

Translated by S. Egorov

Technical Physics, Vol. 45, No. 8, 2000, pp. 1045–1050. Translated from Zhurnal Tekhnicheskoĭ Fiziki, Vol. 70, No. 8, 2000, pp. 91–96.

Acousto-Optical Filtering Using Short Acoustic Trains

V. N. Parygin, A. V. Vershubskiĭ, and K. A. Kholostov

Moscow State University, Vorob'evy gory, Moscow, 119899 Russia

Received June 7, 1999

Abstract—The problem of controlling the characteristics of collinear acousto-optical filters is studied experimentally. It is shown that the use of an acoustic pulse in the form of a step-function signal makes it possible to considerably reduce the side lobes of the instrument function of a collinear acousto-optical filter. The changes in the shape of the transmission curve that occur as a result of the variations in the number of acoustic pulses simultaneously propagating in the crystal and in their duration are investigated. An experimental study of a spectrum consisting of two close lines is performed using a tunable collinear acousto-optical filter. © *2000 MAIK "Nauka/Interperiodica".*

INTRODUCTION

Tunable collinear acousto-optical filters are among the most promising optoelectronic devices. These filters have a narrow transmission band that can be electronically tuned within an octave [1–3]. In the literature, two types of acousto-optical filters are described: collinear and noncollinear ones [4, 5]. Collinear filters, which usually have a narrow transmission band, are characterized by higher selectivity, and this property is important for the spectral analysis of optical radiation and for the channel multiplexing purposes.

In our recent publications [6–9], it was shown theoretically that, in collinear acousto-optical filters, an electronic tuning of not only the central frequency but also the width of the transmission band and the shape of the transmission curve is possible when the filter is controlled by a pulsed acoustic signal rather than by a continuous one. In this case, the duration of the control pulse determines the transmission band, and the form of the pulsed signal governs the shape of the transmission curve of the collinear filter. Our previous experiments [10] demonstrated the possibility of controlling the characteristics of a collinear filter by using single acoustic trains.

If we use a sequence of short acoustic trains with a relatively small distance between them (less than the crystal length), several acoustic pulses may simultaneously propagate in the cell. In this case, the transfer characteristic of the cell has the form of a series of several narrow peaks. The spacing between the peaks depends on the number of peaks in the crystal, and the number of peaks depends on the duration of each individual pulse.

In this paper, we describe the experimental study of the dependence of the characteristics of a collinear acousto-optical filter on the form and duration of successive acoustic trains.

THEORY OF THE COLLINEAR ACOUSTO-OPTICAL INTERACTION

The propagation of acoustic trains in a crystal is accompanied by an elastic strain wave described by the strain tensor $S_{lm}a(x, y, z, t)$. The strain wave changes the refractive indices of the medium. This change is related to the elasto-optical effect described by the tensor p_{jklm}. The change in the components of the permittivity tensor of the medium under the effect of the acoustic field has the form $\Delta\varepsilon_{jk} = -N_j^2 N_k^2 \sum_{l,m=1}^{3} p_{jklm} S_{lm}$. Here, N_j and N_k are the main refractive indices of the medium, and j, k, l, and m are the coordinate indices.

The diffraction of light by sound is described by the wave equation

$$\mathrm{rot}\,\mathrm{rot}\,\mathbf{E} + \frac{1}{c^2}\frac{\partial^2}{\partial t^2}\hat{\varepsilon}_0\mathbf{E} = -\frac{1}{c^2}\frac{\partial^2}{\partial t^2}\Delta\hat{\varepsilon}(a\mathbf{E}), \qquad (1)$$

where $\mathbf{E}(x, y, z, t)$ is the electric vector of the light wave; $\hat{\varepsilon}_0$ is the permittivity of the medium in the absence of sound; $\Delta\hat{\varepsilon}$ is the variation of $\hat{\varepsilon}_0$ in the presence of sound, this variation being proportional to the acoustic strain; and $a(x, y, z, t)$ is the distribution of the acoustic strain in the medium. The latter quantity can be represented in the form

$$a(x, y, z, t) = a_0 W(x, y, z) V(x, t) \times \exp[j(Kx - \Omega t)] + \text{c.c.}, \qquad (2)$$

where a_0 is the amplitude of the wave at the cell input (at $x = 0$), and K and Ω are the wave number and the frequency of the acoustic train, respectively. In the general case, the functions $W(x, y, z)$ and $V(x, t)$ describe the spatial distribution of the amplitude and the time envelope of the trains, respectively.

It should be noted that, for light beams of finite dimensions, we have $\mathrm{rot}\,\mathrm{rot}\,\mathbf{E} \neq \nabla^2\mathbf{E}$, because $\mathrm{grad}\,\mathrm{div}\,\mathbf{E}$

1063-7842/00/4508-1045$20.00

cannot be considered as zero even in an isotropic medium.

It is known that, in the case of a collinear diffraction, the polarization of the diffracted light beam is orthogonal to the polarization of light incident on the acousto-optical cell. Therefore, in the region of the interaction of light and sound, it is quite natural to represent the light beam as a sum of the transmitted and diffracted beams with orthogonal polarizations:

$$\begin{aligned}\mathbf{E} &= \mathbf{e}_t E_t(x, y, z, t)\exp[j(\mathbf{k}_t x - \omega_t t)] \\ &+ \mathbf{e}_d E_d(x, y, z, t)\exp[j(\mathbf{k}_d x - \omega_d t)],\end{aligned} \tag{3}$$

where $\mathbf{e}_t$ and $\mathbf{e}_d$ are the polarization directions of the transmitted and diffracted beams, respectively; ω_t and ω_d are the frequencies of the transmitted and diffracted light beams; and $E_t(x, y, z, t)$ and $E_d(x, y, z, t)$ are their amplitudes slowly varying along the x-axis.

We substitute the vector $\mathbf{E}$ determined by expression (3) into equation (1). We use the diffraction condition $\omega_d = \omega_t + \Omega$ and equate the amplitudes of $\exp\{j\omega_t t\}$ and $\exp\{j\omega_d t\}$. Neglecting the quantities $\partial^2 E_t/\partial x^2$ and $\partial^2 E_d/\partial x^2$, as well as $\partial E_t/\partial t$ and $\partial E_d/\partial e$, we apply a two-dimensional Fourier transform to both sides of equation (2) in the yz plane. Then, omitting the mathematical transformations analogous to those described in [6–9] and taking into account the orthogonality of the polarizations $\mathbf{e}_t$ and $\mathbf{e}_d$, we arrive at a system of scalar equations for the spectra of the transmitted and diffracted light U_t and U_d:

$$\begin{aligned}j\frac{\partial U_d}{\partial x} + \frac{k_y^2}{2k_d}U_d &= q_1\exp(-j\eta x)V(x, t) \\ \times \iint A(K_y, K_z, x)U_t(k_y + K_y, k_z + K_z, x, t)dK_y dK_z,\end{aligned} \tag{4}$$

$$\begin{aligned}j\frac{\partial U_t}{\partial x} + \frac{k_z^2}{2k_t}U_t &= q_2\exp(j\eta x)V(x, t)\iint A^*(K_y, K_z, x) \\ &\times U_d(k_y - K_y, k_z - K_z, x, t)dK_y dK_z.\end{aligned} \tag{5}$$

Here, $q_1 = k_d(\mathbf{e}_d\Delta\hat{\varepsilon}\,\mathbf{e}_t)/n_d^2$; $q_2 = k_t(\mathbf{e}_t\Delta\hat{\varepsilon}\,\mathbf{e}_d)/n_t^2$; $\eta = k_t + K - k_d$ is the parameter of detuning; k_y, k_z and K_y, K_z are the transverse components of the wave vectors of light and sound, respectively; and $A(K_y, K_z, x) = \pi R^2\exp\{-(K_y^2 + K_z^2)R^2(1 - jDx)/4\}$ is the Fourier spectrum of the function $W(x, y, z)$ for the case of a Gaussian distribution of the acoustic pulse amplitude in the yz plane. In the latter expression, R denotes the transverse dimensions of the train at $x = 0$ and $t = 0$, $D = 2\zeta/KR$ is the train divergence in the transverse directions, and ζ characterizes the transverse anisotropic spread. We represent the functions U_t and U_d in the form

$$\begin{aligned}U_t(k_y, k_z, x, t) &= f_t(x, t)\exp\{jxk_z^2/2k_t\} \\ &\times \exp\{-(k_y^2 + k_z^2)r_t^2(x)/4\},\end{aligned} \tag{6}$$

$$\begin{aligned}U_d(k_y, k_z, x, t) &= f_d(x, t)\exp\{jxk_y^2/2k_d\} \\ &\times \exp\{-(k_y^2 + k_z^2)r_d^2(x)/4\}.\end{aligned} \tag{7}$$

Here, $f_t(x, t)$ and $f_d(x, t)$ are the light beam amplitudes depending on x and t and taken along the axis at $k_y = k_z = 0$; $r_i(x)$ (where $i = t, d$) are the slowly varying radii of the Gaussian beams. According to our previous calculations [7], the variations of the radii with the coordinate are negligibly small. In addition, the radii of the incident r_t and diffracted r_d light beams are related as $r_d = r_t/\sqrt{1 + r_t^2/R^2}$.

Let us substitute expressions (6) and (7) into equations (4) and (5). The integrals over dK_y and dK_z in the right-hand members of equations (4) and (5) can be calculated analytically. Neglecting the variations of the light beam radii, we obtain a system of two first-order differential equations describing the collinear diffraction of light by Gaussian acoustic trains in the case of a strong acousto-optical interaction:

$$\frac{\partial f_d}{\partial x} = -jq_1 f_t(x, t)V(x, t)\frac{\exp\{-jx\eta\}}{(1 - jDx) + \rho_t^2}, \tag{8}$$

$$\frac{\partial f_t}{\partial x} = -jq_2 f_d(x, t)V(x, t)\frac{\exp\{jx\eta\}}{(1 + jDx) + \rho_d^2}, \tag{9}$$

where $\rho_i = r_i/R$.

The use of finite beams in describing the diffraction of light by sound makes it possible to determine the efficiency of the diffraction not through the ratio of the power densities of incident and diffracted light but through the ratio of the luminous fluxes in the diffracted and incident light beams, as it is always done in the experiment. The luminous flux in a light beam can be calculated by using either the integral of the squared magnitude of the light field distribution over the beam cross-section or the integral of the squared magnitude of the Fourier spectrum of the field over the angular coordinates k_y and k_z (the Parseval theorem).

The luminous flux at the input of the acousto-optical cell is determined by the formula $P_0 = 0.5\iint\exp\{-(k_y^2 + k_z^2)r_t^2/2\}dk_y dk_z$, because $f_t(0) = 1$; at the cell output, it is calculated by the formula $P = 0.5\iint f_d(L)f_d^*(L)\exp\{-(k_y^2 + k_z^2)r_d^2/2\}dk_y dk_z$, where expression (8) should be used for $f_d(L)$. The ratio P/P_0 characterizes the efficiency of the acousto-optical diffraction, and this quantity can be directly determined from the experimental data.

EXPERIMENT

In our experimental studies, we used a collinear acousto-optical filter made on the basis of a $CaMoO_4$

crystal of length $L = 4$ cm. The time of the acoustic pulse propagation through the crystal was $L/v = 11.6$ μs. The acoustic wave was excited in the crystal by a piezoelectric transducer, which converted the electric energy of the generator to the energy of the acoustic wave.

For our experiments, we used a specially designed generator that was capable of producing signals with an arbitrary envelope, i.e., arbitrarily shaped pulses. The envelope of the signal is formed by setting the value of the signal amplitude every 0.1 μs; i.e., the envelope has the form of a set of rectangles of duration 0.1 μs each. In this way, one can specify any form and duration of the acoustic train, as well as the entire sequence of trains. The maximum duration of a pulse produced by the generator is 200 μs, and the minimum duration is about 0.5 μs. The rate of the pulse series repetitions may vary from 0.5 to 1 kHz. After the amplification, the output power reaches a level of 3 W.

The block diagram of the generator is shown in Fig. 1. The high-frequency unit generates the fundamental frequency 35–48 MHz, and this is precisely the sound frequency at which the diffraction of light takes place. The envelope is formed by the following units: the read-only memory (ROM), the processor, the random-access memory (RAM), and the digital-to-analog (D/A) converter. The initial pulse or pulse series was modeled on a PC and saved in the text format. Then, the envelope was sent through the corresponding port to the generator processor and to the ROM. After this, the communication between the computer and the generator was cut off. When the generator was turned off, the information on the pulse form was stored in the ROM. Within several seconds after the termination of the data transfer from the PC to the generator, or after turning on the generator, the processor supplies the data on the pulse form to the RAM from which the digital data are sent to the D/A converter. As a result of the described process, the desired envelope of the signal is formed. Then, by means of a multiplier, the high-frequency oscillation of frequency 35–48 MHz is modulated by the envelope. The resulting pulse (or series of pulses) is supplied to an amplifier and amplified to the necessary amplitude.

In common practice, to obtain acoustic trains of finite length, rectangular pulses are used; for such trains, the transfer characteristic has the form of the function $\sin c^2(x)$. For rectangular pulses, the level of the side lobes does not depend on the pulse duration and is as high as 5% of the central maximum (in the weak-interaction approximation). It should be noted that, in contrast to rectangular pulses for which the level of the side lobes is constant, for Gaussian pulses, this quantity varies from zero (for short pulses, $\tau \ll L/v$) to the level corresponding to rectangular pulses (for long pulses, $\tau > L/v$).

The possibility of considerably reducing the side lobes allows one to improve the characteristics of the

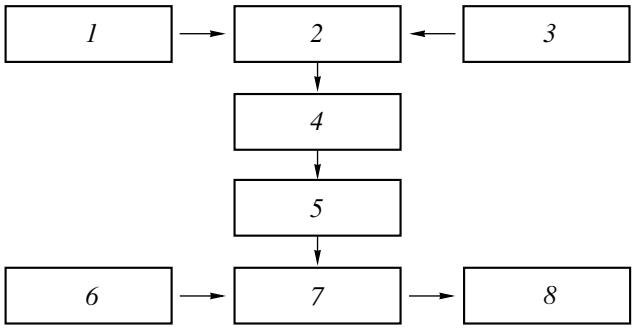

Fig. 1. Block diagram of the generator of arbitrarily shaped acoustic pulses: (*1*) a com-nopra interface, (*2*) a processor, (*3*) memory (ROM), (*4*) memory (RAM), (*5*) a D/A converter, (*6*) a high-frequency oscillator, (*7*) a multiplier, and (*8*) an amplifier.

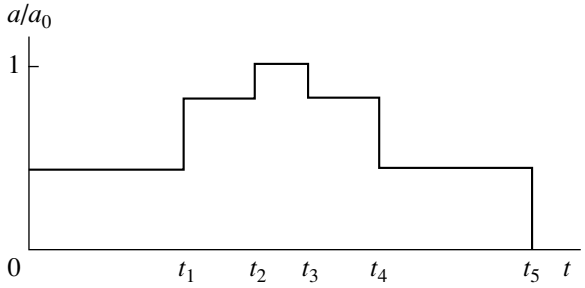

Fig. 2. Time envelope of an acoustic pulse in the form of a step-function signal.

filter. This improvement is most pronounced for the pulse lengths somewhat less than the crystal length, because in this case the transmission band is practically not broadened, while the side lobes are already noticeably suppressed. On the other hand, with a further decrease in the acoustic train duration, the filter bandwidth increases. This fact can be used in practice for controlling the characteristic of the collinear filter, but a strong suppression of the side lobes can be achieved only with smooth control pulses.

We experimentally studied the level of the side lobes of the instrument function of a collinear filter controlled by an acoustic pulse in the form of a step-function signal. It was found that, in the case of an optimal choice of the form of the step-function signal, the level of the side lobes is considerably reduced. For example, if an acoustic train with the time envelope shown in Fig. 2 is used, its form can be described by the expression

$$V(x,t) = A\,\mathrm{rect}\left(\frac{t - x/v}{t_5} - \frac{1}{2}\right)$$

$$+ B\,\mathrm{rect}\left(\frac{t - x/v - t_1}{t_4 - t_1} - \frac{1}{2}\right) + C\,\mathrm{rect}\left(\frac{t - x/v - t_2}{t_3 - t_2} - \frac{1}{2}\right),$$

where the constants A, B, and C determine the width and the height of the steps.

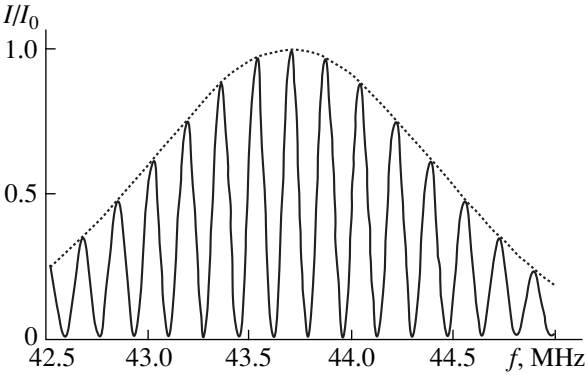

Fig. 3. Instrument function of a filter controlled by two acoustic pulses of duration 3 μs. The solid line corresponds to the distance between the pulses 6 μs; the dotted line shows the instrument function of a filter with a single pulse of duration 1 μs.

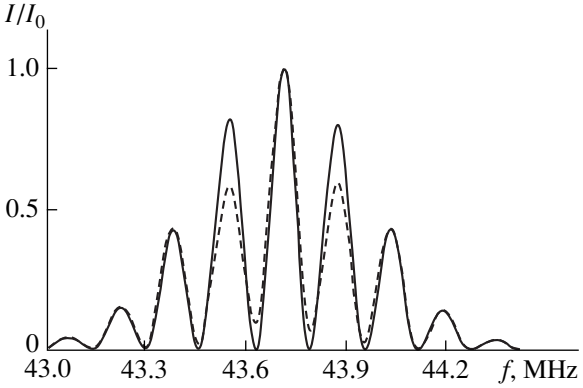

Fig. 4. Instrument function of a filter controlled by two acoustic pulses of duration 3 μs with the distance between them 6 μs. The solid line corresponds to the theory, and the dashed line shows the experimental data.

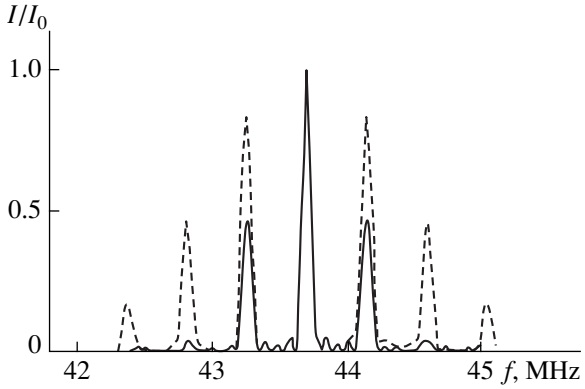

Fig. 5. Theoretical dependence of the transmission factor on the sound frequency for an acousto-optical filter in the case of five acoustic trains being present inside the crystal. The distance between the trains is 2 μs; the train duration is (solid line) 2 and (dashed line) 1 μs.

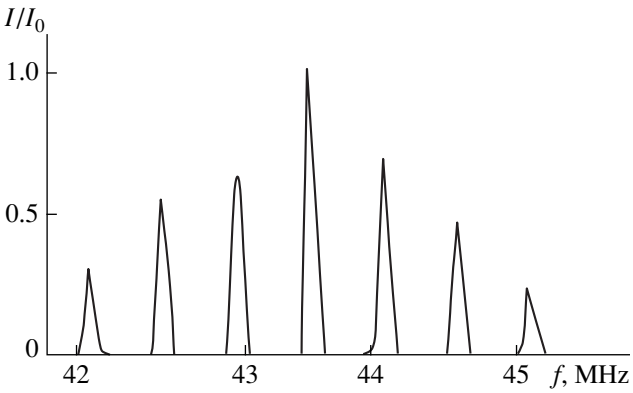

Fig. 6. Experimental instrument function of a filter controlled by five acoustic pulses of duration 1 μs with the distance 2 μs between them.

When uniform rectangular pulses are used and the condition of weak interaction is fulfilled, the levels of the first, second, and third side lobes are 4.7, 2.7, and 1.0%, respectively. With the use of a step-function signal shown in Fig. 2, it was possible to suppress the side lobes down to a level of 0.7%.

In the case of the generation of short acoustic trains (with the duration less than 3–4 μs), several pulses may simultaneously occur within the crystal. In such a situation, it is of interest to study the dependence of the shape of the transmission curve on the pulse duration and the number of pulses that simultaneously propagate in the crystal (the number of pulses depends on the distance between them). Below, we will consider a sequence of acoustic trains with a Gaussian time envelope.

For a single short acoustic train, we obtain a broad transmission band with a Gaussian characteristic without any side lobes (the dotted line in Fig. 3). When two trains of the same duration are present in the crystal, beats are observed (the solid line in Fig. 3). The calculation is performed for the pulses of duration 1 μs with the distance between them 6 μs. The envelope width and, correspondingly, the number of maxima are determined by the duration of the short pulse. The use of acoustic trains of longer duration leads to a narrowing of the envelope of the filter characteristic and to a decrease in the number of maxima. This was observed in the experiment (Fig. 4) with the trains of duration 3 μs with a distance of 6 μs between them.

With a further increase in the number of trains in the crystal, the envelope of the transmission characteristic is retained, because it is determined exclusively by the duration of the pulses forming the sequence (the shorter the acoustic train, the broader the envelope). As the number of pulses increases, the beats take the form shown in Fig. 5. The transmission function tends to a set of isolated narrow peaks whose width is determined

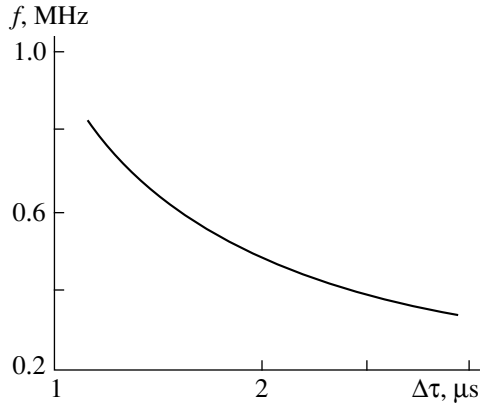

Fig. 7. Dependence of the frequency interval between the peaks of the comb, Δf, on the pulse-repetition interval $\Delta\tau$.

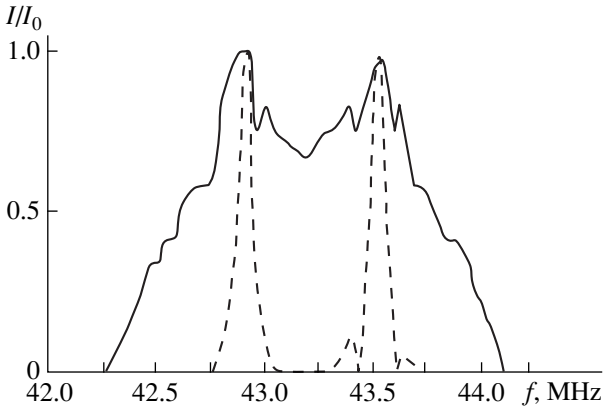

Fig. 8. Study of the optical spectrum consisting of two lines by an acousto-optical filter controlled by the pulses of different duration: τ = (solid line) 2 and (dashed line) 12 μs.

by the size of the crystal, i.e., by the length of interaction in the case of a continuous-wave operation.

Figure 6 presents the experimental shape of the transmission curve for a series of five pulses of duration 1 μs spaced at 2 μs intervals. One can see that the experimental data agree well with the theoretical ones. Thus, using a series of short trains whose individual frequency bands are very wide, it is possible to create a filter with a comb-shaped transmission curve whose peaks are characterized by bandwidths about those of long pulses or even a continuous-wave signal.

As one can see from Figs. 5 and 6, in the case of a simultaneous propagation of several acoustic trains in the crystal, the transmission band of the filter has the form of a set of equidistant peaks. Figure 7 shows the theoretical dependence of the frequency interval between the peaks of the comb on the time interval between the acoustic pulses. This dependence is a hyperbolic one. It is evident that the interval between the acoustic pulses determines the number of pulses simultaneously propagating in the crystal. It should be noted that the frequency interval between the peaks depends on the time interval between the acoustic trains rather than on the number of pulses inside the crystal. Therefore, we obtain a continuous and smooth dependence rather than a step function. Correlating the experimental dependence shown in Fig. 6 with the calibration dependence given in Fig. 7, we obtain the interval between the acoustic pulses 2 μs, which is in complete agreement with the experiment.

An important application of tunable acousto-optical filters is in the measurements of optical spectra. In our experiments, we studied a spectrum consisting of two close lines that differed by 91 Å. The spectrum was obtained by simultaneously supplying the optical signals from a He–Ne laser ($\lambda_1 = 0.6328$ μm) and a semiconductor laser ($\lambda_2 = 0.6419$ μm) to the filter input. The measurements were performed by using long acoustic pulses ($\tau \approx L/v$).

The results of the experiment are shown by the dashed line in Fig. 8. One can see that the acousto-optical filter well resolves the spectral lines. The solid line shows the same spectrum studied by using short acoustic pulses with $\tau \ll L/v$. In this case, the filter bandwidth exceeds the distance between the spectral lines, and the resolution of the system is insufficient for observing the two separate lines of the spectrum. This experiment confirms the fact that the filter bandwidth increases with a decrease in the control pulse length.

For a spectrum consisting of two lines, there still is an interesting possibility to determine the exact distance between the lines even with the use of short pulses. When we use a single short pulse, we cannot resolve two close lines of the spectrum because of the broad transmission band. However, using a series of short pulses, we can tune the system in such a way that the peaks of the filter characteristic will coincide with the lines of the spectrum. In this case, the spectral characteristic of the filter remains a periodic one for the optical spectrum consisting of two lines.

CONCLUSION

The experimental studies described above showed that the use of acoustic trains of finite length for controlling the characteristics of a collinear acousto-optical filter is of great interest, because it provides a possibility to vary the characteristics of the filter over wide limits. The filter bandwidth can be increased by using short pulses. At the same time, the level of the side lobes of the transmission function depends on the form of the acoustic train and its duration. In the case of a Gaussian (or close to it) acoustic train, the side maxima are absent when the pulse duration is less than the time of the pulse propagation through the crystal $\tau = L/v$. As the pulse duration increases, the level of the side lobes tends to the value characteristic of a rectangular pulse. By using pulses in the form of a step-function signal (with adequately chosen parameters), it is possible to

suppress the side lobes down to a level of 0.7%. The use of a series of Gaussian pulses allows one to obtain a filter characteristic that has the form of a set of equidistant peaks with a broad envelope.

An acousto-optical cell can also be used as a spectrometer with a varying resolution, the latter being varied by changing the pulse duration. Interesting possibilities for spectrum identification are offered by the use of a series of acoustic trains simultaneously propagating in the crystal.

REFERENCES

1. L. G. Magdich, Izv. Akad. Nauk SSSR, Ser. Fiz. **44**, 1683 (1980).
2. A. Harris, S. Mieh, and R. Fiegelson, Appl. Phys. Lett. **17**, 223 (1970).
3. Jieping Xu and R. Stroud, *Acousto-Optic Devices* (Wiley, New York, 1992).
4. A. Korpel, *Acousto-Optics* (Marcel Dekker, New York, 1988; Mir, Moscow, 1993).
5. A. P. Goutzoulis and D. R. Pape, *Design and Fabrication of Acousto-Optic Devices* (Marcel Dekker, New York, 1989).
6. V. N. Parygin and A. V. Vershubskiĭ, Vestn. Mosk. Univ., Ser. 3: Fiz., Astron. **39** (1), 28 (1998).
7. V. N. Parygin, A. V. Vershubskiĭ, and Yu. G. Rezvov, Opt. Spektrosk. **84**, 1005 (1998) [Opt. Spectrosc. **84**, 911 (1998)].
8. V. N. Parygin and A. V. Vershubskiĭ, Akust. Zh. **44**, 615 (1998) [Acoust. Phys. **44**, 529 (1998)].
9. V. N. Parygin and A. V. Vershubskiĭ, Radiotekh. Élektron. (Moscow) **43**, 1369 (1998).
10. V. N. Parygin, A. V. Vershubskiĭ, and K. A. Kholostov, Zh. Tekh. Fiz. **69** (12), 76 (1999) [Tech. Phys. **44**, 1467 (1999)].

Translated by E. Golyamina

Technical Physics, Vol. 45, No. 8, 2000, pp. 1051–1053. Translated from Zhurnal Tekhnicheskoĭ Fiziki, Vol. 70, No. 8, 2000, pp. 97–99.

RADIOPHYSICS

Calculation of the Relaxation Time from the Frequency Spectra of Ferrites

K. Yu. Bazhukov, Yu. V. Gol'chevskiĭ, and L. N. Kotov

Syktyvkar State University, Syktyvkar, 167001 Komi Republic, Russia

E-mail: kotov@ssu.edu.komi.ru

Received July 27, 1999

Abstract—A method for determining the relaxation times of the magnetic moments of ferrites from inverse Fourier transforms is suggested. The effect of the alternating external magnetic field strength on the relaxation times was studied. It was found that the dispersion and absorption ranges in the magnetic spectra are associated with changes in the relaxation times of magnetic moments of ferromagnets. *© 2000 MAIK "Nauka/Interperiodica".*

DETERMINATION OF RELAXATION TIME

Relaxation time is a key parameter of ferromagnets that specifies their frequency properties, such as the frequency curve of the permeability (its slope), the width of the absorption range, etc. The relaxation time τ is traditionally found from the width of the peak of the imaginary part μ'' of the permeability: $\tau = 2\pi/\Delta\omega$, where $\Delta\omega$ is the half-peak width of μ''. This method is applied to saturation-magnetized magnets (single-domain crystals and polycrystals). The most pressing problem is however to find relaxation times at small and vanishing magnetizing fields, since ferromagnets are most frequently applied just in this range of magnetization. For most of ferromagnets, experimental data for μ'' can be obtained only at lower-than-resonance frequencies presumably because of large losses (defined as μ''/μ' ratio, where μ' is the real part of the permeability) at higher values. Therefore, the need for a method that can overcome these difficulties is obvious.

In this work, the relaxation time τ of the magnetic moments of ferrites is derived from inverse Fourier transformation applied to the frequency dependence of the permeability

$$\mu(t) = \frac{1}{\sqrt{2\pi}}\int_{-\infty}^{+\infty}(\mu'(\omega) - i\mu''(\omega))\exp(i\omega t)d\omega. \quad (1)$$

For inverse Fourier transformation, the integrand must be defined in $(-\infty, +\infty)$ and the functions $\mu'(\omega)$ and $\mu''(\omega)$, in $[0, +\infty)$. We assume μ' and μ'' to be even in order to define them in the $(-\infty, +\infty)$ range. The inverse Fourier transform is then a real time function $\mu(t)$ [1]. The relaxation time τ of magnetic moments is defined as a time during which $\mu(t)$ becomes e times smaller than $\mu(t = 0)$. To apply this method, μ' and $\mu''(\omega)$ must be taken as continuous functions approximating experimental data. Inverse Fourier transformation imposes constraints on the approximating functions. Two of the constraints make integration easier [$\mu''(\omega = 0) = 0$ and $\mu''(\omega \longrightarrow \infty) = 0$], and the third one has a physical meaning [$\mu'(\omega \longrightarrow \infty) = 0$]. They also help to solve the problem associated with the broadening of the natural ferromagnetic resonance (FMR) peak. This effect is related to domain wall motion at zero static fields and makes the evaluation of τ difficult. At such fields, τ can be determined only in ferrites for which the contribution from wall motion is small in the FMR frequency range. With the above restrictions, the approximating curves eliminate this contribution.

Real $\mu'(\omega)$ and imaginary $\mu''(\omega)$ curves found in experiments were approximated as $\mu'(\omega) = A_1\exp(-B_1/\omega) + A_2\exp(-B_2/\omega)$ and $\mu''(\omega) = A\omega\exp(-B\omega^n)$, where n is a positive rational number. These expressions are fairly simple and provide a good fit to experimental data. Approximating and experimental curves for several samples are shown in Figs. 1–4.

OBJECTS OF INVESTIGATION

Using the inverse transform method, we calculated the relaxation time for the magnetic subsystem of man-

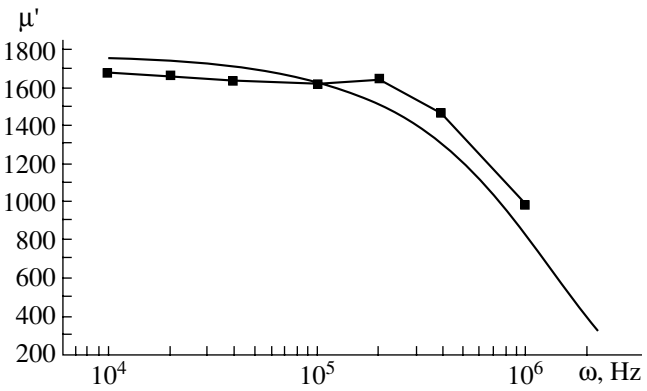

Fig. 1. μ' vs. frequency for the (211) single-crystal MnZ spinel. $h_0 = 1$ mOe. Symbols denote data points.

1063-7842/00/4508-1051$20.00 © 2000 MAIK "Nauka/Interperiodica"

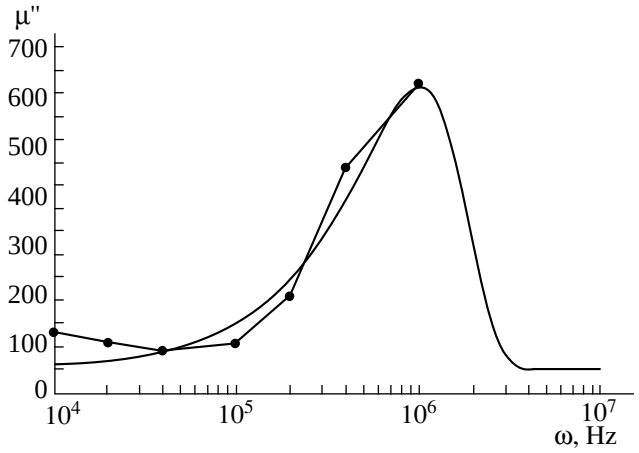

Fig. 2. μ" vs. frequency for the (211) single-crystal MnZ spinel. h_0 = 1 mOe.

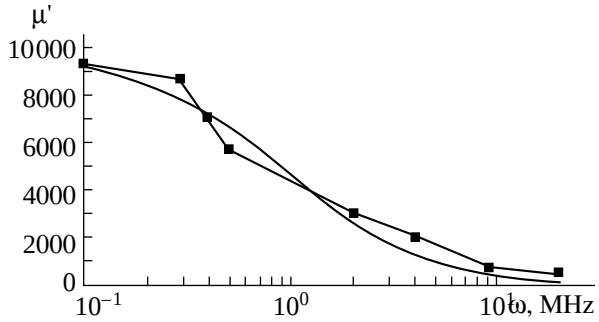

Fig. 3. μ' vs. frequency for the polycrystals. h_0 = 20 mOe.

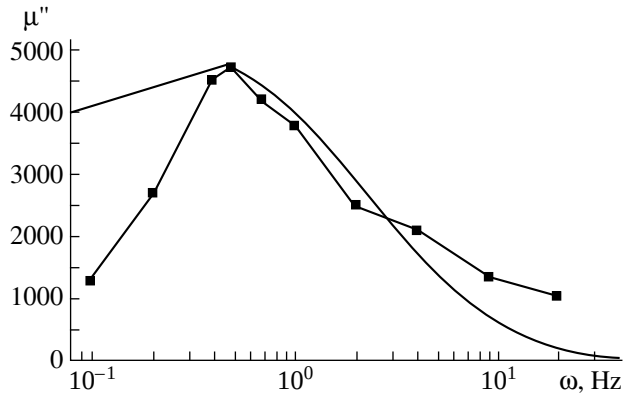

Fig. 4. μ" vs. frequency for the polycrystals. h_0 = 20 mOe.

ganese–zinc spinel (MnZ spinel) from experimental frequency spectra μ(ω). A specific feature of MnZ spinel is that the range of dispersion and the absorption peak in the μ" curve are due largely to magnetization rotation [2–4], i.e., to FMR. Since MnZ spinel has low fields of anisotropy H_A (below 1 Oe), FMR and domain wall resonance in them are observed in the 0.1–10 MHz and 1–10 kHz ranges, respectively [4]. Hence, they add little to the total permeability at high frequencies [5]. A small contribution from wall displacement must improve the accuracy of determination of the true magnetic moment relaxation times, not the effective times, which are severely affected by wall motion. Moreover, along with the suggested method, the conventional approach to determining the relaxation time is also applicable in this case.

Calculations were carried out on (1) $Mn_{0.54}Zn_{0.36}Fe_{2.09}O_4$ (111), (110), (211), and (100) spinel single crystals (the ring (torus) plane was parallel to the plane of orientation) subjected to different alternating magnetic fields h_0 (1, 7, and 20 mOe) and (2) $Mn_{0.63}Zn_{0.29}Fe_{2.08}O_4$ spinel polycrystals with a porosity of 0.003, mean grain size 20.2 μm, and field of anisotropy H_A = 0.04 Oe. In the latter case, h_0 equaled 1 and 2 mOe. Experimental dependences μ(ω) were taken from [6, 7].

COMPARISON OF THE METHODS FOR τ DETERMINATION

The relaxation times obtained by inverse Fourier transformation lie near 10^{-7} s, while those derived from the half-peak width are in the 10^{-6}–10^{-7} s range. In [3], the magnetic moment relaxation times in MnZ spinel were estimated at 10^{-7}–10^{-8} s; hence, the inverse Fourier transform gives the more accurate value. This is explained as follows. In calculations using the inverse Fourier transform, both the real, μ', and the imaginary, μ", parts of the permeability are used. Therefore, due to a greater number of data points, the accuracy of calculation is improved. A frequency dependence of μ' at high frequencies is easier to predict, since its slope, as a rule, is represented more comprehensively. Hence, μ' can be approximated with a much better accuracy than μ" (Figs. 1, 2).

When the relaxation time was calculated with the conventional method, data points only for μ" were used. Note that the component μ' was approximated at frequencies from 10^4 to 10^7 Hz. Conversely, in the case of μ", data at h_0 = 1 mOe were obtained only for the ascending branch (in the 10^4–10^6 Hz range, Fig. 2). The further behavior of μ" was predicted very roughly from the conditions μ"(0) = 0 and μ"(∞) = 0.

From experimental data for μ", the position of its peak remains unclear; hence, the height of the peak may be in great error. For the peak value of μ", we took the highest-frequency data point. As follows from calculations, such an assumption is usually valid and the relaxation times estimated by both methods are close to each other.

Thus, for the experimental data considered, inverse Fourier transformation is the method of choice, since it provides more accurate values of the relaxation times of ferrites.

For polycrystals, the relaxation times obtained by both methods coincide. Here, we used experimental data for a wide frequency range and the peak of μ'' is distinct. In this case, the conventional method gives fairly accurate values of τ (related approximations are shown in Figs. 3, 4).

DISCUSSION

For the single crystals, the relaxation times calculated from the experimental permeability data were found to be independent of the crystallographic orientation and alternating external field amplitude h_0 within 1–20 mOe. The times remain constant at a level of 3×10^{-7} s. For polycrystals, the relaxation time at small h_0's is 4×10^{-7} s, i.e., roughly equal to that of the single crystals. As h_0 rises, the situation changes drastically. At $h_0 = 20$ mOe, the magnetic moment relaxation time increases about twofold. Unlike the single crystals, the structure of the polycrystals undergoes substantial modification (damage). In this case, the vector of magnetization may slowly return to the equilibrium position, causing the relaxation time to increase. Similar results were obtained in [8–10]. It was found in these works that the relaxation time increases as the energy delivered to the magnetic subsystem grows. In [9], nickel ferrite was studied; and in [10], nickel–chromium alloys. It is likely that such an energy dependence of the relaxation time is typical of all spinel-like ferrites within a certain range of field amplitudes.

CONCLUSIONS

If the relaxation time is difficult to estimate with the traditional method, inverse Fourier transformation can be used. When the frequency range is such that the vicinity of the imaginary component peak is fully covered, both methods give similar results. In this case, the traditional method is even preferred, since inverse Fourier transformation requires data preprocessing.

We can conclude that the relaxation time is independent of the mutual arrangement of the crystallographic axes and alternating field in the single-domain ferrites. The field amplitude affects the relaxation time only in the polycrystals. It can be suggested that frequency characteristics of many radio engineering devices based on polycrystalline ferrites can easily be controlled by varying the amplitude of an external alternating field.

REFERENCES

1. E. C. Titchmarsh, *Introduction to the Theory of Fourier Integrals* (Clarendon Press, Oxford, 1948, 2nd ed.; Gostekhizdat, Moscow, 1948).
2. S. Chikasumi, *The Physics of Ferromagnetism. Magnetic Characteristics and Engineering Applications* (Syokabo, Tokyo, 1984; Mir, Moscow, 1987).
3. S. Krupicka, *Physik der Ferrite und der verwandten magnetischen Oxide* (Academia, Praha, 1973; Mir, Moscow, 1976).
4. J. Smit and H. P. J. Wijn, *Ferrites* (Wiley, New York, 1959; Inostrannaya Literatura, Moscow, 1969).
5. A. G. Gurevich, *Magnetic Resonance in Ferrites and Antiferromagnets* (Nauka, Moscow, 1973).
6. S. G. Abarenkova, S. A. Kochnov, I. V. Saenko, *et al.*, Élektron. Tekh., Ser. 6: Mater. **8** (264), 28 (1991).
7. M. A. Kharinskaya and S. G. Abarenkova, Élektron. Tekh., Ser. 6: Mater. **3** (248), 23 (1990).
8. D. Park, Phys. Rev. **97**, 60 (1955).
9. L. Torres, M. Zazo, and J. Iniguez, IEEE Trans. Magn. **29**, 3434 (1993).
10. F. I. Stetsenko, Fiz. Tverd. Tela (St. Petersburg) **37**, 598 (1995) [Phys. Solid State **37**, 326 (1995)].

Translated by V. Isaakyan

Technical Physics, Vol. 45, No. 8, 2000, pp. 1054–1057. Translated from Zhurnal Tekhnicheskoĭ Fiziki, Vol. 70, No. 8, 2000, pp. 100–103.

Electron Acceleration by Gaussian Electromagnetic Beam in a Stationary Magnetic Field

V. P. Milantiev and Ya. N. Shaar

Peoples' Friendship University of Russia, ul. Miklukho-Maklaya 6, Moscow, 117198 Russia

E-mail: vmilantiev@mx.pfu.edu.ru

Received June 22, 1999

Abstract—Relativistic electron motion in the electromagnetic Gaussian beam that propagates along a stationary magnetic field is studied. It is shown that, if the cyclotron resonance conditions are initially satisfied, electrons can be efficiently accelerated over a relatively small interval at a slightly lower rate than in a plane accelerating wave. *© 2000 MAIK "Nauka/Interperiodica".*

INTRODUCTION

Among various charged particle acceleration mechanisms, the cyclotron autoresonance mechanism discovered by Kolomenskiĭ and Lebedev [1] and, independently, by Davydovskiĭ [2] is of great interest. This mechanism provides a high acceleration rate and sufficiently low radiation losses [3]. A variety of designs of microwave [4–6] and laser [7, 8] electron accelerators based on the cyclotron autoresonance have been proposed. At the same time, strictly speaking, the cyclotron autoresonance, being a relativistic effect, exists only in the plane transverse electromagnetic wave traveling at the speed of light in vacuum along a stationary magnetic field if electrons are in the cyclotron resonance with the wave at the initial moment of time. If these conditions are violated, various techniques can be used to support the forced synchronism [3]. It was shown [7] that electrons can be accelerated to extremely high energies in the field of high-power laser radiation at a very high rate with very small radiative losses. However, these results were obtained under the assumption that the laser radiation has the form of a plane wave. Actually, this assumption is usually invalid. In many cases, laser and microwave radiation can be considered in the quasi-optical approximation as a Gaussian beam. Clearly, in this case, the cyclotron autoresonance conditions are *a fortiori* violated. Therefore, the electron energy does not necessarily grow monotonically. In this paper, we show that, despite this circumstance, particles in the Gaussian beam can also acquire a significant energy over a short acceleration interval. A high acceleration rate can be achieved by shaping the guiding magnetic field to fit an appropriate profile or by optimizing the parameters of the electron injection and of the Gaussian beam.

ASSUMPTIONS AND BASIC EQUATIONS

In the paraxial approximation, laser radiation can be represented as a Gaussian beam (GB) [9] that propagates along a stationary magnetic field aligned with the z-axis:

$$\mathbf{E} = (E\cos\Theta, -E\sin\Theta, 0). \tag{1}$$

Here,

$$\begin{aligned} \Theta &= -\omega t + kz + k\psi, \\ k\psi &= r^2 D/a^2(1 + D^2) - \arctan D, \\ E &= E_1(1 + D^2)^{-1/2}\exp\{-r^2/a^2(1 + D^2)\} \\ &\equiv E_1 f(x, y, z), \end{aligned} \tag{1a}$$

where $D = 2z/ka^2 \equiv z/z_q$; $z_q = ka^2/2$ is the Rayleigh length; ω is the wave frequency; $k = \omega/c$ is the wave number in vacuum; a is the radius of the beam's waist, i.e., its minimal radius at $z = 0$; and $r = \sqrt{x^2 + y^2}$ is the transverse coordinate.

The magnetic components of the GB field can be found from Maxwell's induction equation:

$$\mathbf{B} = (B_x, B_y, B_z), \tag{2}$$

where

$$B_x = E_1(G\cos\Theta + fQ\sin\Theta), \tag{2a}$$

$$B_y = -E_1(G\sin\Theta - fQ\cos\Theta), \tag{2b}$$

$$\begin{aligned} B_z &= -\frac{2fE_1}{ka^2(1 + D^2)} \\ &\times ((xD - y)\sin\Theta + (yD + x)\cos\Theta). \end{aligned} \tag{2c}$$

1063-7842/00/4508-1054$20.00

Here,

$$Q = 1 + \frac{\partial k\psi}{\partial kz}, \quad G = -\frac{\partial f}{\partial kz}.$$

The phase velocity of the GB is

$$v_{ph} = \frac{\omega}{k(1+\psi')},$$

where

$$k\psi'(z) \equiv \frac{dk\psi}{dz} = \frac{1}{a^2 z_q}\frac{r^2(1-D^2) - a^2(1+D^2)}{(1+D^2)^2}.$$

At a distance of about the Rayleigh length, $D \approx 1$, so that $\psi'/k \approx (1/kz_q) \ll 1$ when $r < a$. Therefore,

$$v_{ph} \approx c\left(1 - \frac{\psi'}{k}\right) > c.$$

That is, the phase velocity is higher than the velocity of light. This means that the cyclotron autoresonance cannot exist in the GB.

In order to extract the cyclotron rotation of a particle, we represent its momentum vector as

$$\mathbf{p} = p_x\mathbf{e}_z + p_\perp(\mathbf{e}_x\cos\Theta_0 + \mathbf{e}_y\sin\Theta_0). \quad (3)$$

Here, $\mathbf{e}_x$, $\mathbf{e}_y$, and $\mathbf{e}_z$ are the unit vectors of the Cartesian coordinate system; p_z and $p_\perp$ are the momentum components, respectively, along and perpendicular to the guiding magnetic field; and Θ_0 is the phase of the particle cyclotron rotary motion in this field. The phase of field (1), as it acts on the electron, is governed by the equation

$$\frac{d\Theta}{dt} = -\omega + \frac{d\mathbf{r}}{dt}\nabla\Theta. \quad (4)$$

Equations of electron motion in the GB field combined with equation (4) constitute a two-period (or two-frequency) system, which contains oscillating factors with phases Θ, Θ_0, and their combinations $\Theta \pm \Theta_0$. In the region of the electron cyclotron resonance, $\Theta + \Theta_0 \equiv \Theta_+$ is a slowly varying quantity. When the oscillation frequency is high and the magnetic field is strong, phases Θ, Θ_0, and $\Theta - \Theta_0$ must be regarded as rapidly varying quantities. Smoothing over rapidly varying phases [10] in the electron cyclotron resonance region yields

$$\frac{dP_\perp}{d\tau} = -\frac{\varepsilon}{\gamma}f\{\gamma - P_z Q\}\cos\Theta_+ + \varepsilon\frac{P_z}{\gamma}G\sin\Theta_+, \quad (5)$$

$$\frac{d\Theta_+}{d\tau} = \frac{\Omega_0 - \gamma + P_z Q}{\gamma} + \varepsilon\frac{f}{P_\perp\gamma}\{\gamma - P_z Q\}\sin\Theta_+ + \varepsilon\frac{P_z}{P_\perp\gamma}G\cos\Theta_+, \quad (6)$$

$$\frac{dP_z}{d\tau} = -\varepsilon\frac{P_\perp}{\gamma}\{fQ\cos\Theta_+ + G\sin\Theta_+\}, \quad (7)$$

$$\frac{d\gamma}{d\tau} = -\frac{\varepsilon}{\gamma}P_\perp f\cos\Theta_+, \quad (8)$$

$$\frac{dZ}{d\tau} = \frac{P_z}{\gamma}, \quad \frac{dX}{d\tau} \approx 0, \quad \frac{dY}{d\tau} \approx 0. \quad (9)$$

Here, $\tau = \omega t$; $\mathbf{R} = k\mathbf{r}$; $\mathbf{P} = \mathbf{p}/m_0 c$, and $\varepsilon = eE_1/m_0 c\omega$ are the dimensionless parameters and variables; m_0 is the electron rest mass; $\omega_0 = eB_0/m_0 c$ is the classical frequency of the electron cyclotron rotation in the guiding magnetic field; $\Omega_0 = \omega_0/\omega$; the electron charge is $-e$, where $e > 0$; and $\gamma = \sqrt{1 + P_z^2 + P_\perp^2}$ is the relativistic factor (dimensionless electron energy). In the case of a plane electromagnetic wave, $Q = 1$ and function $f = 1$ such that $G = 0$. Then, system (5)–(9) yields the integral of motion $\gamma - P_z = Y = \text{const}$, which coincides with the cyclotron resonance condition at $Y = \Omega_0$. This is the autoresonance [3]. If the electromagnetic field has the form of GB (1) and (2), according to (5)–(9), the cyclotron resonance occurs when

$$\gamma - P_z Q \approx \Omega_0. \quad (10)$$

Since the phase velocity of the GB is higher than the velocity of light, the electron cyclotron resonance condition, imposed at the initial time moment, is not preserved during the electron motion. This effect occurs because (10) is not an integral of motion.

NUMERICAL RESULTS

It is difficult to derive an analytical solution to system (5)–(9). Therefore, we solved it numerically by the Runge–Kutta method. The motion of electrons injected at $Z \le 0$ was studied in the region $x^2 + y^2 < a^2$. The cyclotron resonance condition (10) was assumed to be fulfilled exactly at the initial moment of time. This requirement imposes rather stringent constraints on the domain of parameters Ω_0 and Q_0. In fact, initially, the transverse momentum component must comply with the relationship

$$P_{\perp 0}^2 = \gamma_0^2 - 1 - \frac{(\gamma_0 - \Omega_0)^2}{Q_0^2} \ge 0, \quad (11)$$

which yields the constraint on parameters Ω_0 and Q_0 mentioned above

$$\Omega_0^2 + Q_0^2 \ge 1. \quad (12)$$

We will study the motion of electrons that satisfy initial condition (10) and have an initial energy of 25 MeV or higher. The electron motion will be studied within a rather small 100-cm-long interval. This interval is chosen because it is necessary to find the optimal parameters that provide a high electron acceleration

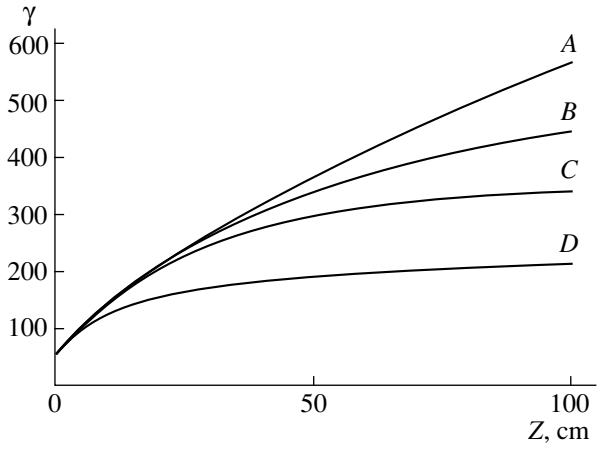

Fig. 1. Electron energy γ on the acceleration interval versus GB width (parameter $q = a^2k^2$) for microwave radiation ($\lambda = 1$ mm and $\Omega_0 = 1$) at $\gamma_0 = 50$ and $\varepsilon = 1$: (*A*) plane wave and the GB at $q = 10^5$ and the GB at $q =$ (*B*) 10^4, (*C*) 5×10^3, and (*D*) 10^3.

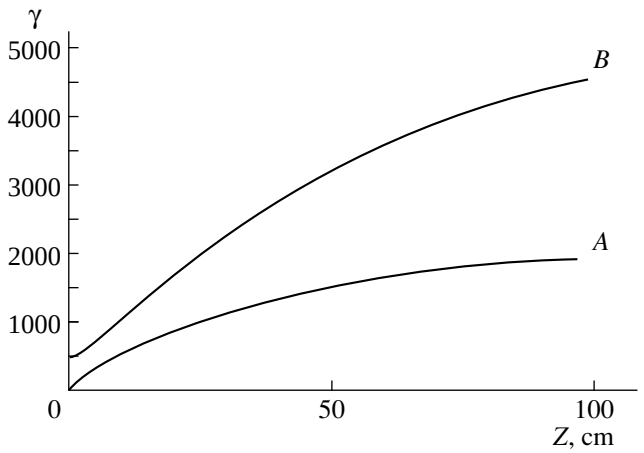

Fig. 2. Electron energy in the laser GB and stationary magnetic field $B_z = 100$ kG at $\varepsilon = 1$ for (*A*) $\gamma_0 = 50$ and $\lambda = 10$ μm (CO_2 laser) and for (*B*) $\gamma_0 = 500$ and $\lambda = 1$ μm (neodymium glass laser).

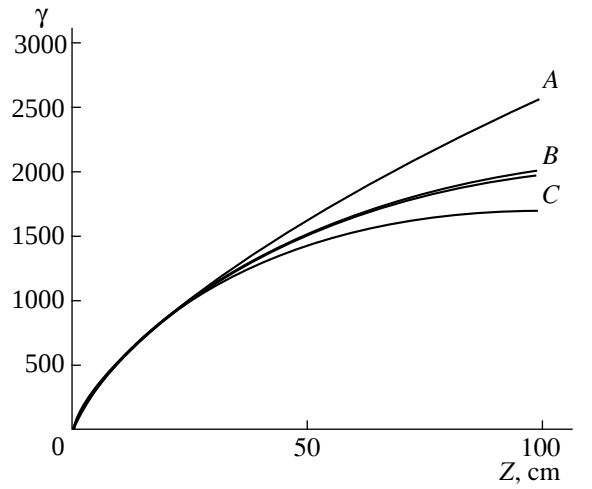

Fig. 3. Energy of electrons accelerated in the GB under the approximate initial cyclotron resonance conditions at $\lambda = 10$ μm (CO_2 laser), $\Omega_0 = 0.01$, $\gamma_0 = 50$, and $\varepsilon = 1$: (*A*) plane wave with the exact cyclotron resonance; (*B*) the GB with $C = 0.01$, 0.00985, and 0.0101; and (*C*) the GB with $C = 0.011$.

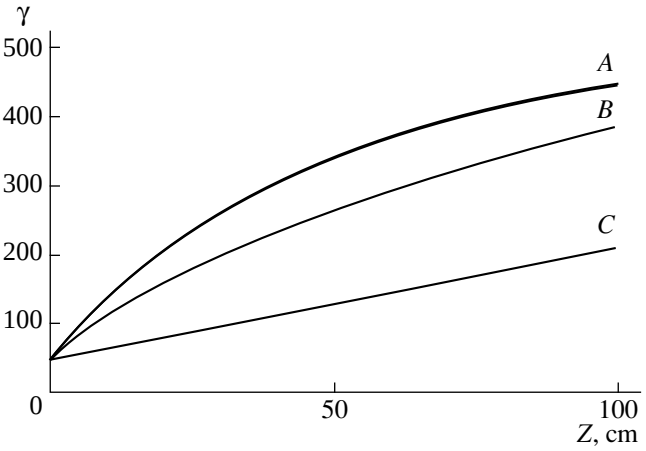

Fig. 4. Energy of electrons injected at different points of plane $z_0 = 0$ (beam's waist) versus z at $\lambda = 1$ mm, $\Omega_0 = 1$, $\gamma_0 = 50$, and $\varepsilon = 1$: (*A*) $\sqrt{x^2 + y^2} \equiv r \le 0.1a$; (*B*) $r = 0.5a$; and (*C*) $r = a$.

rate with the Rayleigh length being noticeably longer than the acceleration interval.

Figure 1 shows the electron energy on this interval as a function of the GB width (parameter $q = a^2k^2$) for microwave radiation ($\lambda = 1$ mm and $\Omega_0 = 1$). It can be seen that the particle acceleration rate increases with the beam width at a constant wavelength. At $q = 10^5$, the energy grows as fast as in the plane wave. Under these conditions, the electron energy can rise by more than an order of magnitude. The acceleration process involves all electrons regardless of the spread in the initial phases, which govern the electron motion at the initial stage; the electron energy increases by a factor of 7–8. The acceleration rate significantly increases with the radiation power.

At shorter wavelengths (less than 20 μm, laser radiation) and the same guiding magnetic field, Ω_0 is very small; hence, by virtue of constraint (12), the initial cyclotron resonance conditions (10) cannot be satisfied. Therefore, when the particles are accelerated in the laser field, we impose the initial condition $\gamma_0 - P_{z0} = \Omega_0$, which corresponds to the electron cyclotron resonance in the plane wave. The results are presented in Fig. 2. It can be seen that, similarly to the plane wave [7], the GB can also efficiently accelerate electrons on the considered interval, though at a slower rate. The initial GB width was specified such that the beam intensity

decreased by a factor of no more than e at a distance z = 150 cm from the beam's waist. Figure 2 plots the electron energy as a function of z in a stationary magnetic field B_z = 100 kG at $\varepsilon = 1$ for (*A*) $\gamma_0 = 50$ and $\lambda = 10$ μm (CO_2 laser) and for (*B*) $\gamma_0 = 500$ and $\lambda = 1$ μm (neodymium glass laser).

Figure 3 shows the electron energy as a function of z when, at the initial moment of time, the cyclotron resonance condition is satisfied approximately ($\gamma_0 - p_{z0} = \text{const} \equiv C \neq \Omega_0$) rather than exactly. The energy of electrons accelerated by the plane wave with the initial cyclotron resonance condition that is satisfied exactly is plotted for reference. It can be seen that such particles can be accelerated on the 100-cm-long interval of our interest if the difference between C and Ω_0 is small. If C is significantly higher than Ω_0, the energy oscillates rather than grows monotonically.

Figure 4 shows the energy of electrons injected at different points of plane $z_0 = 0$ (beam's waist): (*A*) $\sqrt{x^2 + Y^2} \equiv r \leq 0.1a$; (*B*) $r = 0.5a$; and (*C*) $r = a$. All remaining parameters of the GB and electron are the same as above. As shown in the figure, the acceleration rate decreases as the injection point moves away from the GB center because the GB energy decreases. Thus, all particles of a given cross section of the electron beam are accelerated, though at different rates.

In order to validate our calculations, we compared our solution to system (5)–(9) for the plane wave with results given in [7, 11]; the agreement was perfect. Let us focus on the results presented in [7], which predict that relativistic electrons can be accelerated in a high-power laser plane wave to extremely high energies at a high rate if the electron cyclotron autoresonance is maintained. At first sight, this statement contradicts the conclusion [1, 3] that the acceleration rate decreases with increasing energy as $1/\sqrt{\gamma}$. However, it can easily be seen that the energy is also proportional to the wave frequency and the dimensionless parameter ε. Therefore, increasing the energy and acceleration rate with the power and frequency of the laser radiation at a given ε is justified.

CONCLUSION

Our calculations show that an electron beam can be accelerated at a sufficiently high rate in the electromagnetic Gaussian beam that propagates along an external stationary magnetic field despite the fact that the initial cyclotron resonance between the wave and particle is violated during the particle motion. All particles are involved in the acceleration process regardless of their initial phases.

We studied the motion of a separate electron, thereby ignoring the effect of the intrinsic field of the beam and the back effect of the beam on the accelerating electromagnetic wave. This approximation is valid when the beam concentration (and current) is sufficiently low. The single-particle model of interaction between the electron beam and the electromagnetic wave was shown to be valid if the beam current is lower than a certain tolerable value $J(kA) \ll 8\varepsilon\omega R_b/c$, where R_b is the beam radius [8]. As for the radiation losses, their effect is of very small significance even at very high electron energies [7].

ACKNOWLEDGMENTS

This work was supported by the project "Fundamental Studies in Russian Universities."

REFERENCES

1. A. A. Kolomenskiĭ and A. N. Lebedev, Dokl. Akad. Nauk SSSR **145**, 1259 (1962) [Sov. Phys. Dokl. **7**, 745 (1963)]; Zh. Éksp. Teor. Fiz. **44**, 259 (1963) [Sov. Phys. JETP **17**, 177 (1963)].
2. V. Ya. Davydovskiĭ, Zh. Éksp. Teor. Fiz. **43**, 886 (1962) [Sov. Phys. JETP **16**, 629 (1963)].
3. V. P. Milant'ev, Usp. Fiz. Nauk **167**, 3 (1997) [Phys. Usp. **40**, 1 (1997)].
4. A. A. Vorobev, A. N. Didenko, A. P. Ishkov, *et al.*, At. Énerg. **22** (1), 3 (1967).
5. H. R. Jory and A. W. Trivelpiece, J. Appl. Phys. **39**, 3053 (1968).
6. E. T. Protasevich, Zh. Tekh. Fiz. **65** (6), 133 (1995) [Tech. Phys. **40**, 1 (1995)].
7. A. Loeb and L. Friedland, Phys. Rev. A **33**, 1828 (1986).
8. A. Loeb and L. Friedland, Phys. Lett. A **129** (5/6), 329 (1988).
9. M. B. Vinogradova, O. V. Rudenko, and A. P. Sukhorukov, *The Theory of Waves* (Nauka, Moscow, 1990).
10. V. P. Milant'ev, Zh. Tekh. Fiz. **64** (6), 166 (1994) [Tech. Phys. **39**, 608 (1994)].
11. C. S. Roberts and S. J. Buchsbaum, Phys. Rev. A **135**, 381.

Translated by A.D. Khzmalyan

Technical Physics, Vol. 45, No. 8, 2000, pp. 1058–1062. Translated from Zhurnal Tekhnicheskoĭ Fiziki, Vol. 70, No. 8, 2000, pp. 104–107.

ELECTRON AND ION BEAMS, ACCELERATORS

Six-Electrode Deflectron

L. P. Ovsyannikova and T. Ya. Fishkova

Ioffe Physicotechnical Institute, Russian Academy of Sciences, Politekhnicheskaya ul. 26, St. Petersburg, 194021 Russia

E-mail: L.Ovsyannikova@pop.ioffe.rssi.ru

Received July 20, 1999

Abstract—In the two-dimensional approximation, the potential of a six-electrode deflectron (which was previously proposed by the authors) is obtained in a closed form. The field nonuniformity is calculated for this deflectron. The field distributions are computed on the axes of finite-length deflectrons using certain analytical formulas. In deflectrons, the axial trajectory of the beam can be horizontally and vertically deflected by a maximum angle which depends on the structure geometry. The nonlinearity of this deflection is calculated. The results are compared to those obtained for four- and eight-electrode deflectrons. © *2000 MAIK "Nauka/Interperiodica".*

In order to create a scan on a sample, electrostatic omnidirectional deflection systems with spatially superposed deflection centers (so-called deflectrons) are used in scan electron microscopes, electron-beam tubes, high- and low-energy electron diffractometers; in the techniques of secondary-ion and atom mass spectroscopy; etc. Deflectrons do not focus beams of charged particles (in the first-order approximation). The main requirement imposed on these structures is that the field in the operation region should be as uniform as possible.

Electrostatic deflectrons are most often designed as cylinders or cones which are cut along generatrices into an even number of fragments [1, 2], having the forms of planar electrodes placed on the sides of rectangular (square) boxes [3, 4] and cut planar capacitors [5, 6].

In [7], we proposed a six-electrode deflectron with identical angular dimensions of electrodes equal to $\pi/3$ (assuming that the gaps between the electrodes are infinitely small). The electrodes are located on a cylinder (cone) surface. The cross section of the deflectron is shown in Fig. 1. Inside an infinitely long cylinder that is cut along the generatrices, the potential distribution can be represented in Cartesian coordinates as a series. When feeding voltages are applied as we propose (Fig. 1), the series coefficients of the potential for the six-electrode deflectron are expressed as follows:

$$K_{(2n-1)x} = 4/\pi/(2n-1)\sin[(2n-1)\pi/3],$$
$$K_{(2n-1)y} = 4/\pi/(2n-1)\{b + (1-b)\cos[(2n-1)\pi/3]\}. \quad (1)$$

These expressions imply that $K_{3x} = 0$ always and $K_{3y} = 0$ only at $b = 0.5$. The six-electrode deflectron provides a more uniform field than a standard four-electrode deflectron. According to (1), the higher coefficients, which govern the sensitivities of the horizontal and vertical deflections, are, respectively, $K_{1x} = 2\sqrt{3}/\pi$ and $K_{1y} = 3/\pi$. Therefore, equal deflections in both directions are provided by the feeding voltages that are coupled by the relationship $V_x/V_y = \sqrt{3}/2$.

In a closed form, the potential distribution of the six-electrode deflectron that involves the corrected third harmonics has the form

$$\Phi(6) = 1/\pi\{(V_x + 1/2V_y)\arctan[(\sqrt{3} + y)/(1 - x^2 - y^2)] + (V_x - 1/2V_y)\arctan[(\sqrt{3}x - y)/(1 - x^2 - y^2)] + V_y\arctan[2y/(1 - x^2 - y^2)]\}. \quad (2)$$

Here and below, the x and y coordinates are expressed in terms of cylinder radius R. The field intensity components of this deflectron are

$$E_x(6) = -1/(\pi R)\{(V_x + 1/2V_y)[\sqrt{3}(1 + x^2 - y^2) + 2xy]/[(1 - x^2 - y^2)^2 + (\sqrt{3}x + y)^2] + (V_x - 1/2V_y) \times [\sqrt{3}(1 + x^2 - y^2) - 2xy]/[(1 - x^2 - y^2)^2 + (\sqrt{3}x - y)^2] + 4V_y xy/[(1 - x^2 - y^2)^2 + 4y^2]\},$$

$$E_y(6) = -1/(\pi R)\{(V_x + 1/2V_y) \times [1 - x^2 + y^2 + 2\sqrt{3}xy]/[(1 - x^2 - y^2)^2 + (\sqrt{3}x + y)^2] - (V_x - 1/2V_y)[1 - x^2 + y^2 - 2\sqrt{3}xy]/[(1 - x^2 - y^2)^2 + (\sqrt{3}x - y^2)] + 2V_y[(1 - x^2 + y^2)/[(1 - x^2 - y^2]^2 + 4y^2]\}. \quad (3)$$

1063-7842/00/4508-1058$20.00

Expressions (3) imply that, when $V_x/V_y = \sqrt{3}/2$, the field intensity components on the axis are $E_x(x = y = 0) = E_y(x = y = 0) = E_h$, where E_h is the intensity of the corresponding uniform field.

Figure 2 demonstrates field nonuniformity ΔE normalized to the intensity of the uniform field versus the distance to the axis. These results are calculated for the six-electrode deflectron using (3) (curves *2*) and compared to the field nonuniformities of the elementary four- and the more complicated eight-electrode [2] deflectrons with the electrode angular dimensions of $\pi/2$ (curves *1*) and $\pi/4$ (curves *3*). Specifying the value of the field nonuniformity necessary for solving a problem under consideration, one can find the maximum possible distance between the trajectory and the structure axis and, finally, determine the deflection angle. Thus, when $\Delta E/E_h = 0.1\%$, the distance from the axis must not exceed $0.02R$, $0.17R$, and $0.025R$ for the four-, six-, and eight-electrode deflectrons, respectively. We should note that the difference in the distances is small for the two latter deflectrons and, in most cases, the six-electrode deflectron is not inferior to the eight-electrode one. Below, this circumstance is demonstrated by analyzing the trajectories and determining the nonlinearities of deflection through equal angles.

For arbitrary deflectrons, the field distribution along the axis (in the proximity of the axis) coincides with the field of a planar capacitor when the deflectrons have equal lengths and interelectrode distances. In the case when the deflectron is located in the free space, the field distribution is calculated using the TEO program [8]. The field intensities are calculated on the longitudinal axes of deflectrons of different lengths and normalized to the field intensity AE_h observed at the center (see Fig. 3a). Coefficient A as a function of deflectron length is shown in Fig. 3b. Taking into account the data given in Fig. 3, we have chosen an analytical formula for the field distribution. For short deflectrons ($1 \le l/R \le 2$), it has the form

$$E(z) = AE_h \cos^3(Bz/R), \qquad (4)$$

where $B = 0.9 - 0.2l/R$.

The origin $z = 0$ coincides with the deflectron center. In Fig. 3a, the field distribution calculated by (4) is marked with crosses. For long deflectrons ($l/R > 3$), $A = 1$. In this case, one can notice a section with E_h = const, whose length depends on the structure length. For this section, we have found the empirical formula

$$z_0/R = l/R - 2.8. \qquad (5)$$

In addition, long deflectrons are characterized by an edge field that is virtually independent of the deflectron length. This field can be represented in a simple form as

$$E_k = E_h \cos^2[z/(2R)]. \qquad (6)$$

In Fig. 3a, the edge field calculated by (6) is marked with dots surrounded by circles. The effective lengths

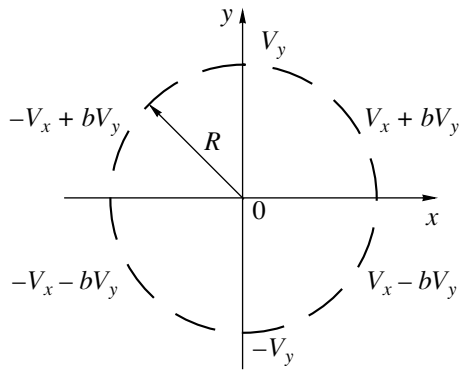

Fig. 1. The cross section of the six-electrode deflectron.

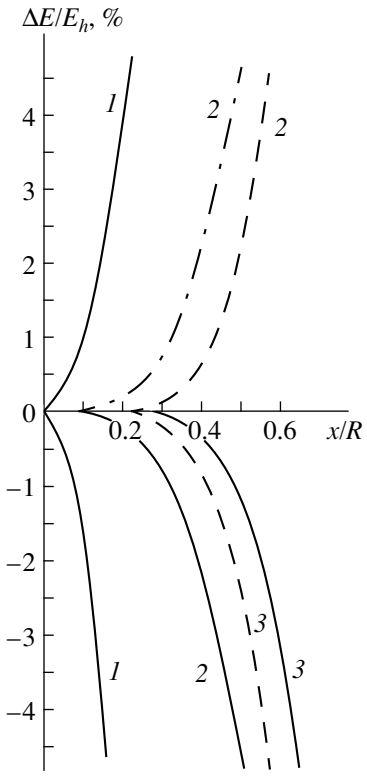

Fig. 2. The field nonuniformity of electrostatic deflectrons: (solid curves) deflection in the *x*-axis direction, (dash-and-dot curves) deflection in the *y*-axis direction, and (dashed curves) the diagonal deflection.

of deflectrons are determined using (4)–(6). For the short and long structures, the effective lengths are, respectively,

$$L = 2\int_0^{\pi/(2B)} \cos^3(Bz/R)dz = 4R/(3B) \qquad (7)$$

and

$$L = z_0 + 2\int_0^{\pi} \cos^2(z/2R)dz = l + 0.3R. \qquad (8)$$

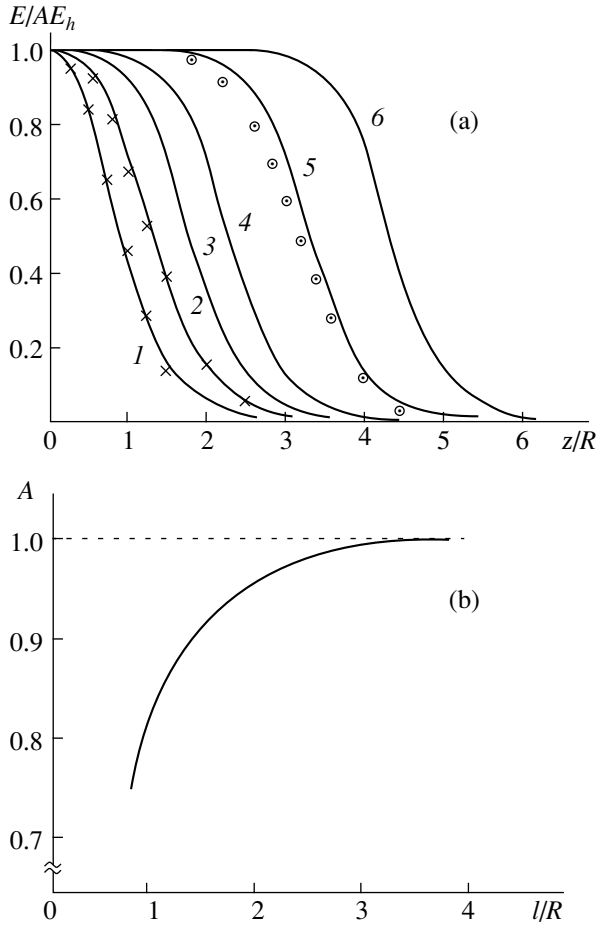

Fig. 3. (a) The field intensity of deflectrons of different length [l/R: (*1*) 1, (*2*) 2, (*3*) 3, (*4*) 4, (*5*) 6, and (*6*) 8] and (b) the coefficient governing the field intensity at the center of the structure.

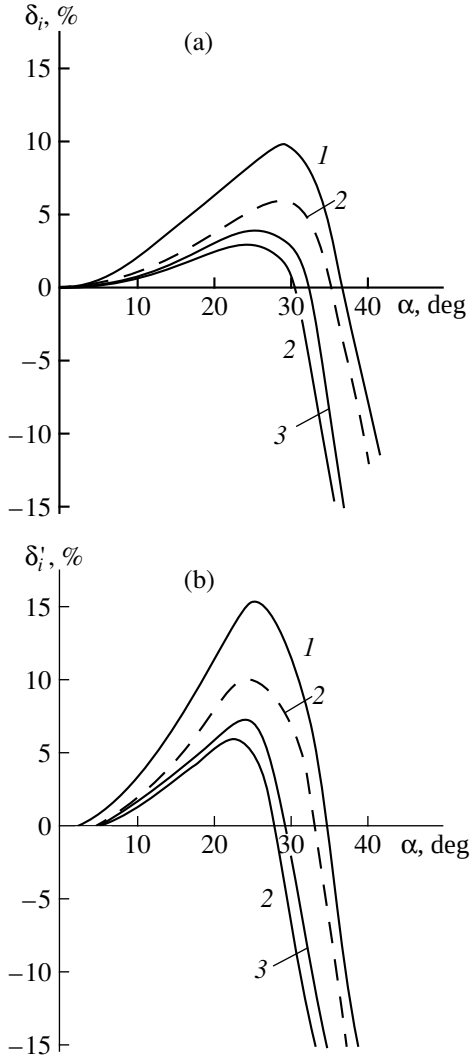

Fig. 4. (a) The coordinate and (b) angle deflection nonlinearity of the axial beam trajectory at the exit of deflectrons of the length $l = 2R$: (*1*) the four-, (*2*) the six-, and (*3*) the eight-electrode deflectrons. (Solid curves) deflections in the x- and (dashed curves) y-axis directions.

The trajectories of the charged-particle beam in the deflection structures are computed using the DEF program, which utilizes the MathCAD system of computer-aided mathematical calculations. In this program, each second-order equation is reduced to a system of two first-order differential equations. The error in the solution is 10^{-6}.

The axial trajectories of the beams in the short and long six-electrode deflectrons are calculated by the DEF program. The fields of these deflectrons are specified by (3)–(6). The coordinates and slope angles obtained at the exit of the field region are compared with the calculations performed using a rectangular model with the effective lengths found from (7) and (8). The comparison shows that the difference observed for short deflectrons reaches 100% and, for long deflectrons, this difference does not exceed 10%. This fact means that the longer the deflectrons, the less the beam parameters are affected by the form of the edge field and, starting with a certain length, the variation of the radial field becomes a determining factor.

Using calculations of the parameters of the axial trajectory, we find the nonlinearity of the coordinate (δ_i) and slope angle (δ_i') deflections observed at the exit of the field region by using the following formulas:

$$\delta_i = r_i/r_{ih} - 1; \quad \delta_i' = r_i'/r_{ih}' - 1, \tag{9}$$

where r_i and r_i' are the distance from the axis and the slope angle of the axial beam trajectory at the exit of the field region, respectively, and r_{ih} and r_{ih}' are the same parameters for a uniform field.

Then, the deflection nonlinearity on the object is

$$\Delta = \delta_i' + \delta_i'\lambda, \quad \Delta' = \delta_i', \tag{10}$$

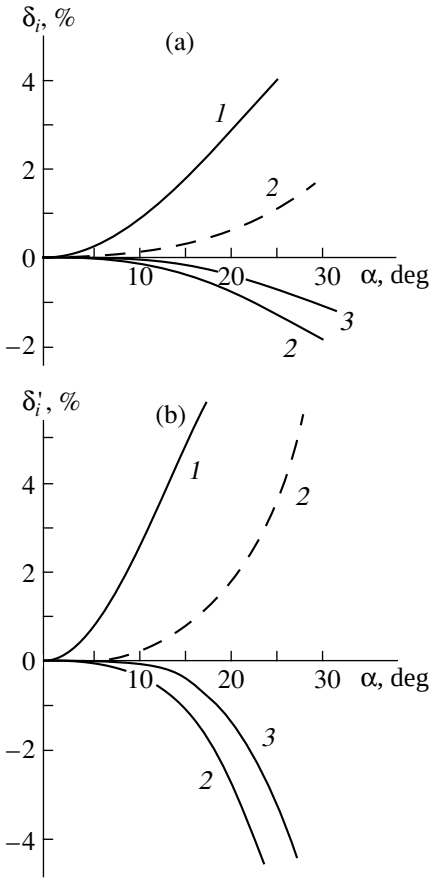

Fig. 5. (a) The coordinate and (b) angle deflection nonlinearity of the axial beam trajectory at the exit of deflectrons of the length $l = 4R$: (*1*) the four-, (*2*) six-, and (*3*) eight-electrode deflectrons. (Solid curves) deflections in the *x*- and (dashed curves) *y*-axis directions.

where λ is the distance from the exit of the field region to the object.

Figure 4 demonstrates the nonlinearities of the coordinate (a) and angle (b) deflections for the short six-electrode deflectron whose length is equal to the diameter of its aperture (curves *2*). Figure 5 shows the same parameters calculated using the rectangular field model for the deflectron with the length equal to the doubled aperture diameter. The data characterizing the coupling of the efficiency of the deflection structure with the deflection angle, as well as with the coordinate of the axial trajectory at the exit of the field region, are summarized in the table. The efficiency of the deflection structure is governed by the ratio between the main feeding electrode voltages ($\pm V$) and the acceleration potential (Φ_0). Note that $V_y = V$ and $V_x = \sqrt{3}/2V$.

From Figs. 4 and 5, one can see that the long and short deflectrons exhibit a substantially different behavior of the deflection nonlinearity. For the long deflectron, the deflection-angle dependence corresponds to the field nonuniformity of the infinitely long deflectron observed when the distance from its longitudinal axis increases. This nonuniformity mainly governs the deflection nonlinearity, which is virtually independent of the edge field. For the short deflectron, the edge-field effect is essential. At deflection angles which do not exceed 25°, the deflection nonlinearity of the long deflectron is less than that of the short one by a factor of 2–4.

We should note that, when the deflection angle exceeds 25–30° in the short deflectron, the deflection nonlinearity abruptly varies and, hence, the shape of the spot is distorted due to a considerable difference between the axial and edge beam trajectories. Therefore, it is inexpedient to use these modes in precision instruments such as scanning electron microscopes.

The parameters of four- (curves *1*) and eight-electrode (curves *3*) deflectrons are compared in Figs. 4 and 5. These parameters are calculated using the DEF program in the case when the field distribution along the longitudinal axis is identical to the corresponding field distribution of the six-electrode deflectron. As expected, the four-electrode structure exhibits the max-

Table

	$l/R = 2$				$l/R = 4$			
V/Φ_0	α_x^0	x_i/R	α_y^0	y_i/R	α_x^0	x_i/R	α_y^0	y_i/R
0.05	3.5	0.192	3.5	0.192	5.9	0.225	5.9	0.225
0.1	7.0	0.386	7.0	0.386	11.6	0.449	11.8	0.450
0.2	14.1	0.779	14.3	0.782	21.7	0.891	23.1	0.907
0.25					26.2	1.100	28.8	1.140
0.3	21.2	1.183	21.8	1.202				
0.4	26.8	1.577	28.0	1.627				
0.5	30.5	1.918	32.4	2.004				
0.6	32.8	2.196	35.0	2.320				
0.8	35.5	2.630	38.4	2.840				
1.0	37.1	2.972	41.1	3.330				

imum nonlinearity. For example, if we assume that $\delta = 1\%$, the deflection angle must not exceed 5°. In this situation, the beam can be deflected by an angle of up to 8° in the short six-electrode and in the eight-electrode deflectrons and up to 18° and 15°, respectively, in the long eight-electrode and the six-electrode deflectrons.

Thus, in certain cases, the proposed six-electrode deflectron with the corrected third harmonics in the expansion of the potential is superior because its parameters are close to those of the eight-electrode deflectron and the design is simpler.

REFERENCES

1. B. É. Bonshtedt, USSR Inventor's Certificate No. 143479, Byull. Izobret., No. 24 (1961).
2. J. Kelly, Adv. Electron. Electron Phys. **43**, 116 (1977).
3. L. P. Ovsyannikova and T. Ya. Fishkova, Zh. Tekh. Fiz. **56**, 1348 (1986) [Sov. Phys. Tech. Phys. **31**, 791 (1986)].
4. L. P. Ovsyannikova and T. Ya. Fishkova, USSR Inventor's Certificate No. 1365179, Byull. Izobret., No. 1 (1988).
5. L. P. Ovsyannikova, T. Ya. Fishkova, and V. V. Moseev, USSR Inventor's Certificate No. 1557603, Byull. Izobret., No. 14 (1990).
6. L. P. Ovsyannikova and T. Ya. Fishkova, Zh. Tekh. Fiz. **58**, 1176 (1988) [Sov. Phys. Tech. Phys. **33**, 692 (1988)].
7. T. Ya. Fishkova, A. A. Shaporenko, L. P. Ovsyannikova, *et al.*, RF Inventor's Certificate No. 1729247, Byull. Izobret., No. 23 (1993).
8. L. P. Ovsyannikova, S. V. Pasovets, and T. Ya. Fishkova, Zh. Tekh. Fiz. **62** (12), 171 (1992) [Sov. Phys. Tech. Phys. **37**, 1215 (1992)].

Translated by Efimova

Technical Physics, Vol. 45, No. 8, 2000, pp. 1063–1069. Translated from Zhurnal Tekhnicheskoĭ Fiziki, Vol. 70, No. 8, 2000, pp. 108–113.

Emission of Charged Clusters during Metal Sputtering by Ions

V. I. Matveev

Department of Thermal Physics, Academy of Sciences of Uzbekistan, ul. Karatal 28, Tashkent, 700135 Uzbekistan

E-mail: matveev@vict.silk.org

Received May 24, 1999

Abstract—A method for simulating processes of metal sputtering by ion bombardment in the form of large neutral and charged clusters with a number of atoms $N \geq 5$ based on simple physical assumptions and in fair agreement with experiment is suggested. As an example, the ionization degrees and ionization coefficients, as well as the relative cluster yields, are calculated as a function of the number of atoms in clusters of different metals (Ag, Nb, and Ta) bombarded by singly charged Ar^{+1} and Au^{-1} ions. A fluctuation mechanism of charge state formation for large clusters, which describes the dependence of the charge state distributions on cluster size and target temperature, is developed. *© 2000 MAIK "Nauka/Interperiodica".*

INTRODUCTION

Sputtering of solids by ion bombardment plays an important role in many fields of science and technology. This is primarily associated with technological applications in micro- and nanoelectronics and space and fission technologies. The number of papers devoted to both the application and fundamental studies of sputtering has increased considerably in recent years (see, for example, recent reviews [1–5] and the literature cited therein). A theoretical description and calculations of sputtering processes are extremely difficult, first of all because of the many-particle nature of the problem both at the stage of ion penetration into a solid and at the stage of formation of sputtering products, which consist not only of single target atoms but also of polyatomic particles, i.e., clusters. Sputtering processes involving single target atoms are usually described [1] using the so-called collision cascade sputtering mechanism [6]. Sputtering mechanisms in the form of two or more bonded target atoms are still the subject of discussion [1, 2, 5], since they describe the formation of large clusters inadequately and differ considerably from the cluster formation mechanisms in gas and plasma. At the present time, hopes of performing calculations based on "first principles" are connected with computer simulations using molecular dynamics methods [1, 2, 5] (see also the calculations in [7, 8]). However, these calculations are technically complicated, especially as the number of atoms in the cluster increases, and are hard to reproduce in other investigations. The formation of the charge state of the sputtered surface material is also a complicated problem. The ionization degree $\eta = J^Q/J$ is usually used as a quantitative characteristic of the charge state, where J^Q is the flow of particles of charge Q escaping the surface and $J = \Sigma_Q J_Q$ is the total flow of escaping particles. However, to characterize the charge state of the sputtering products in the form of clusters, it is convenient to use the following more specific characteristics: the ionization coefficient

$$\kappa_N^Q = \frac{J_N^Q}{J_N^{Q=0}} \quad (1)$$

and the ionization degree of clusters with number of atoms N

$$\eta_N^Q = \frac{J_N^Q}{J_N}, \quad (2)$$

where J_N^Q is the flow of clusters escaping a surface consisting of N atoms and having a charge $Q = 0, \pm1, \pm2, \ldots$ and $J_N = \Sigma_Q J_N^Q$ is the total flow of neutral and charged clusters of N atoms.

A large number of both experimental and theoretical works (see, for example, [9]) are devoted to studies of charge state formation for monatomic particles sputtered or scattered at a metal surface. The mechanism of charge state formation for polyatomic particles has been studied much less extensively, both theoretically and experimentally. Notably, in [10], the ionization coefficient κ_N^{+1} was found to depend on the number of atoms in a cluster: κ_N^{+1} increases drastically with increasing N, saturating at $N \geq 5$, so that variations of κ_N^{+1} with a further increase in N are negligible. From this observation, a conclusion was made about the universal character of the power law established empirically for the relative yield of large clusters, both neutral and charged. In [11], an attempt based on semiempirical estimates of the degree of cluster excitation was

1063-7842/00/4508-1063$20.00

undertaken to account for the formation of singly charged positive clusters as they leave the metal by suggesting that the thermionic emission of an electron from the cluster occurs as it leaves the metal. However, agreement with experimental results could only be reached by assuming the existence of clusters with extremely high temperatures of ~1 eV. Moreover, the formation mechanisms for clusters with charges other than +1, including negative clusters, are not clear. In this paper, we have suggested a mechanism for ion bombardment sputtering of a metal in the form of neutral and charged clusters with number of atoms $N \geq 5$. The mechanism is based on simple physical assumptions and is in good agreement with experimental results.

FORMULATION OF THE PROBLEM

The process of charge state formation is an integral part of the sputtering mechanism. Our consideration largely relies on the suggestion made earlier in many works [1] that large clusters leave a solid as an integral block of atoms. This assumption was further developed in a sputtering model proposed in [12, 13]. According to [12, 13], the probability of events corresponding to the correlated motion of a block of N atoms with total momentum $\mathbf{k}$ can be expressed as

$$W_n = \left[\frac{\exp\left\{-\frac{\beta}{n_0\hbar^2}\left(q-\frac{k}{N}\right)^2\right\} - \exp\left\{-\frac{\beta}{n_0\hbar^2}\left(q+\frac{k}{N}\right)^2\right\}}{4q\frac{k}{N}\frac{\beta}{n_0\hbar^2}}\right]^N, \quad (3)$$

where $\beta = 1/(2m\omega/\hbar)$; ω is the characteristic oscillation frequency of the target atoms, m is the mass of the target atoms, and q has the meaning of the average momentum received by a metal atom at the early development stage of a collision cascade.

The probability (3) is the result of summing over all vibrational excited states of the cluster up to some principal quantum number n_0 when the energy accumulated in excited oscillations is sufficient to destroy the cluster. This can be realized at $n_0 \approx \Delta/(\hbar\omega)$ when the oscillation energy of all the oscillators (atoms in the cluster) becomes sufficient to remove one atom from the potential well of depth Δ describing the bonds between target atoms.

Model of Charge State Formation

Let us define the charge state of a block of N atoms. As in the statistical derivation of the Saha–Langmuir equation [14], we will assume that as the cluster moves a certain distance ξ (called critical) away from the metal surface, an exchange of electrons between the conduction band of the metal and the atoms of the cluster is possible. When the distance between the cluster and the metal exceeds ξ, the electron exchange process is stopped nonadiabatically. Below, when speaking of electrons in the cluster, we mean only valance electrons and we call the set of corresponding states the cluster conduction band. We assume that an exchange process between the conduction bands of the cluster and the metal is possible. Then, the average number of electrons $\overline{n_\tau}$ occupying the energy level ε_τ according to the Fermi distribution is equal to $\overline{n_\tau} = \{\exp[(\varepsilon_\tau - \mu)/\Theta] + 1\}^{-1}$, where Θ is the temperature and μ is the chemical potential. Let us denote by $\overline{\Delta n_\tau^2}$ the rms deviation of the occupation numbers n_τ from their equilibrium values $\overline{n_\tau}$; then, $\overline{\Delta n_\tau^2} = \overline{(n_\tau - \overline{n_\tau})^2} = \overline{n_\tau}(1 - \overline{n_\tau})$ [15]. Obviously, the average number of electrons is $\overline{N_e} = \Sigma_\tau \overline{n_\tau}$. The number of electrons in the cluster conduction band is N_e; therefore, by definition, $\overline{\Delta N_e^2} = \overline{(N_e - \overline{N_e})^2} = \Sigma_\tau \overline{\Delta n_\tau^2}$. A cluster with N_e electrons in the conduction band will be neutral if $N_e = \overline{N_e}$, where $\overline{N_e}$ is the average number of electrons in the cluster conduction band, equal to the number of atoms N in the cluster multiplied by the valence γ (more precisely, by the number of electrons a neutral metal atom gives to the conduction band). Thus, the cluster charge is $Q_e = (N_e - N\gamma)e$, where e is the electron charge.

Further calculations by these equations require information about the cluster's electron structure and cannot be performed in the general case. However, assuming that the cluster size is large enough and the electron states are quasi-continuous, summation over the electron states can be replaced, in the standard way, by integration over the band by the rule given in [15]

$$\sum_\tau f(\varepsilon_\tau) = \int_0^\infty f(\varepsilon) 2^{1/2} \frac{V m_e^{3/2} \sqrt{\varepsilon}}{\pi^2 \hbar^3} d\varepsilon,$$

where m_e is the mass of the conduction band electron and V is the cluster volume.

Thus,

$$\overline{\Delta N_e^2} = 2^{1/2} \frac{V m_e^{3/2}}{\pi^2 \hbar^3} \int_0^\infty d\varepsilon \sqrt{\varepsilon} \frac{\exp[(\varepsilon_\tau - \mu)/\Theta]}{\{\exp[(\varepsilon_\tau - \mu)/\Theta] + 1\}^2} = 2^{1/2} \frac{V m_e^{3/2}}{\pi^2 \hbar^3} \int_{-\mu/\Theta}^\infty dz \Theta \sqrt{\Theta z + \mu} \frac{\exp z}{\{\exp z + 1\}^2}. \quad (4)$$

At temperatures less than the degeneracy tempera-

ture, i.e., at $\mu/\Theta \gg 1$,

$$\overline{\Delta N_e^2} \approx 2^{1/2}\frac{Vm_e^{3/2}}{\pi^2\hbar^3}\sqrt{\mu}\Theta,$$

where the chemical potential of a degenerate Fermi gas with the number of particles $\overline{N_e}$ in a volume V is [15]

$$\mu = (3\pi^2)^{\frac{2}{3}}\frac{\hbar^2}{2m_e}\left(\frac{\overline{N}_e}{V}\right)^{\frac{2}{3}}.$$

Thus, the rms deviation of the cluster charge from the equilibrium value $\overline{Qe} = \overline{(N_e - N\gamma)}\,e = 0$ is equal to:[1]

$$\overline{(\Delta Q_N)^2} = e^2\overline{\Delta N_e^2} = e^2\frac{3^{\frac{1}{2}}}{\pi^{\frac{4}{3}}}\frac{m_e\Theta}{\hbar^2}\left(\frac{\overline{N}_e}{V}\right)^{\frac{1}{3}},$$
$$V = \frac{3^{\frac{1}{2}}}{\pi^{\frac{4}{3}}}\frac{m_e\Theta}{\hbar^2}\left(\frac{V}{N}\right)^{\frac{2}{3}}\gamma^{\frac{1}{3}}N. \quad (5)$$

Probabilities $P_N(Q)$ for values of Q can be determined from the standard equation for the probability of fluctuations

$$P_N(Q) = \frac{1}{D_N}\exp\left\{-\frac{1}{2}\frac{Q^2}{\overline{(\Delta Q_N)^2}}\right\}, \quad (6)$$

where the normalization factor D_N is determined by summing over all possible values of $Q = 0, \pm1, \pm2, \ldots$ and is equal to

$$D_N = \sum_Q \exp\left\{-\frac{1}{2}\frac{Q^2}{\overline{(\Delta Q_N)^2}}\right\}. \quad (7)$$

Thus, to obtain the probability W_N^Q for a cluster with N atoms and charge Q_e to leave the metal, it is necessary to multiply the probability W_N (see formula (3)) by $P_N(Q)$:

$$W_N^Q = W_N P_N(Q). \quad (8)$$

Equation (8) describes the probability for a cluster of N atoms to escape the metal if the cluster's kinetic energy is sufficient to break the bonds between the cluster of N atoms and other atoms of the metal. If the cluster is neutral, this energy is proportional to the square of the contacting surface S_N between the block of N atoms and the metal. Let us assume that the contacting surface is a hemisphere with its center on the initial metal surface before sputtering. Its radius is obviously connected with the number of atoms in the cluster

$$R_N = \left[N\frac{3}{2\pi d}\right]^{\frac{1}{3}}, \quad (9)$$

where d is the number of atoms in a unit volume.

Then, the binding energy of a neutral cluster, which is proportional to S_N, is

$$U_N^0 = \sigma S_N = \sigma 2\pi R_N^2 = \sigma\left(\frac{3}{2\pi d}\right)^{\frac{2}{3}}N^{\frac{2}{3}} = \delta N^{\frac{2}{3}}, \quad (10)$$

where δ obviously means the surface binding energy of a neutral cluster per atom in the cluster.

If a cluster carries away a charge Q_e, an energy U_c of interaction with the image charge should be added to U_N^0 to obtain its binding energy with the metal U_N^Q. The energy of interaction can be expressed as

$$U_c = \frac{|Qe|}{4\chi}, \quad (11)$$

where χ is some effective distance at which the overlapping of the wave functions of electrons of the cluster and the metal conduction bands vanishes as the cluster moves away. Therefore, we shall assume that χ is connected with the work function φ of the target metal as[2]

$$\chi = \frac{\hbar}{\sqrt{2m_e\phi}}. \quad (12)$$

Thus, the energy binding the cluster of charge Q_e and the metal can be expressed as

$$U_N^Q = \delta N^{\frac{2}{3}} + U_c. \quad (13)$$

A cluster that before escaping (before overcoming the binding energy U_N^Q) was imparted the momentum $\mathbf{k}$ will then move with the kinetic energy T_N equal to

$$T_N = \frac{k^2}{2mN} - \sigma S_N - U_c. \quad (14)$$

Taking $T_N = 0$, we find from (14) the minimum momentum k_{QN} the cluster needs to overcome the binding energy U_N^Q:

$$k_{QN} = \sqrt{k_{0N}^2 + 2mNU_c}, \quad (15)$$

[1] In principle, the fact that the equilibrium cluster charge is equal to zero follows from the assumption that the Fermi levels in the cluster and the metal coincide; if this is not the case, asymmetry between positively and negatively charged clusters will be observed. The corresponding changes to the resulting formulas can easily be made.

[2] In the strict sense, χ is defined only to within an order of magnitude, but we put the sign of equality in the definition of χ so as not to introduce extra fitting parameters.

$$k_{0N} = [2mN\sigma S_N]^{\frac{1}{2}} = [2m\delta]^{\frac{1}{2}} N^{\frac{5}{6}} = k_{01} N^{\frac{5}{6}}, \quad (16)$$

where $k_{01} = (2m\delta)^{\frac{1}{2}}$ is the minimum momentum per atom in a cluster necessary to eject a neutral cluster.

Now, to obtain the escape probability of a whole cluster of N atoms, it is necessary to integrate the probability formula (8) over all possible values of $\mathbf{k}$, under the condition that $|\mathbf{k}| > k_{QN}$ and $\mathbf{k}$ is directed outside, i.e., is found within the solid angle of 2π:

$$\overline{W}_N^Q = \int_{|\mathbf{k}| > k_{0N}} W_N^Q d^3k = \int_{k > k_{0N}}^{\infty} 2\pi k^2 dk W_N P_N(Q). \quad (17)$$

To integrate (17), we can write the probability in the form in which the integrand represents the distribution of the kinetic energy T_N of the clusters; thus, we write (14) in the form

$$T_N = \frac{1}{2mN}(k^2 - k_{0N}^2 - U_c). \quad (18)$$

By substituting the variables in (17), we obtain the final expression for the escape probability of a cluster of N atoms with charge Q

$$\overline{W}_N^Q = 2\pi \int_0^{\infty} kmN dT_N P_N(Q) \left[4\frac{q}{k_{01}}\frac{k}{Nk_{01}}\frac{\delta}{\Delta}\right]^{-N} \times \left[\exp\left\{-\frac{\delta}{\Delta}\left(\frac{q}{k_{01}} - \frac{k}{Nk_{01}}\right)^2\right\} - \exp\left\{-\frac{\delta}{\Delta}\left(\frac{q}{k_{01}} + \frac{k}{Nk_{01}}\right)^2\right\}\right]^N, \quad (19)$$

Values of energy δ (eV) [16] and variable parameter q (at.u.) for various ion–target combinations

Incident ion	Target	Binding energy δ, eV [16]	q, au
Ar^+ (5 keV)	Ta	8.1	550
Au^- (6 keV)	Ta	8.1	550
Ar^+ (5 keV)	Nb	7.47	380
Au^- (6 keV)	Nb	7.47	310
Ar^+ (5 keV)	Ag	2.96	170

Note: Some differences in the values of the fitting parameter q from those we used earlier [12, 13] for tantalum and niobium can be explained by the fact that in [12, 13], charge state formation was not considered and that for tantalum, the value of the sublimation energy was taken from a different source.

where $k = \sqrt{2mNT_N + (k_{0N})^2 + U_c}$, $k_{0N} = k_{01}N^\nu$, $\nu = 5/6$, and the fact that $\beta k_{01}^2 / n_0 = \delta/\Delta$ is taken into account.

We define the ionization degree (2) as

$$\eta_N^Q = \frac{\overline{W}_N^Q}{W_N}, \quad (20)$$

where

$$W_N = \sum_Q \overline{W}_N^Q$$

is $\overline{W}_N^Q$ summed over all possible values of $Q = 0, \pm1, \pm2, \ldots$. The ionization coefficient, which according to (1) is the ratio of the number of clusters with charge Q to the number of neutral clusters (for a given cluster size N), can be defined as

$$\kappa_N^Q = \frac{\overline{W}_N^Q}{\overline{W}_N^{Q=0}}. \quad (21)$$

RESULTS

Our consideration apparently cannot be used to describe the sputtering of single atoms or small clusters, while comparison with experimental results has led to the conclusion [12, 13] that the model is valid for clusters containing a certain minimum number of atoms ($N \geq 5$). In experiments, the relative probability of the yield of clusters with different numbers of atoms is usually measured. Thus, to compare it with experimental data, the probability given by (19) should first be divided by the probability of escape of a cluster with $N = 5$ (to be exact, any value in the range $N \geq 5$ can be chosen, but $N = 5$ is more convenient in this case); experimental results are normalized in a similar way. Also, any arbitrary units can be defined to meet particular needs.

Values of the binding energy δ (eV) and the variable parameter q (atomic units $\hbar = m_e = e = 1$) for different ion–target combinations are given in the table. In all cases listed in the table, good agreement with experiment is observed. In the calculations, we kept the number of fitting parameters to a minimum and assumed $\Delta = \delta$. In general, analysis of the direct consequences from Eq. (19) is difficult; thus, we shall consider the results of numerical simulations and experiments presented in Figs. 1–8, which appropriately illustrate the general situation.

The simplest characteristics of the charge state distribution of clusters with a given number of atoms N is the ionization coefficient κ_N^Q equal to the ratio of the number of clusters with charge $Q \neq 0$ to the number of neutral clusters of the same size N. The dependence of

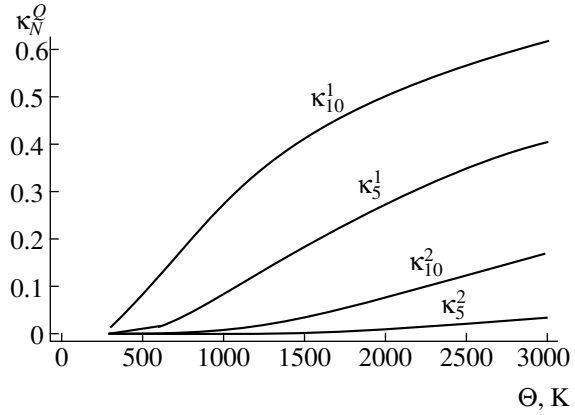

Fig. 1. The dependence of the coefficients of single and double ionization of clusters on target temperature Θ.

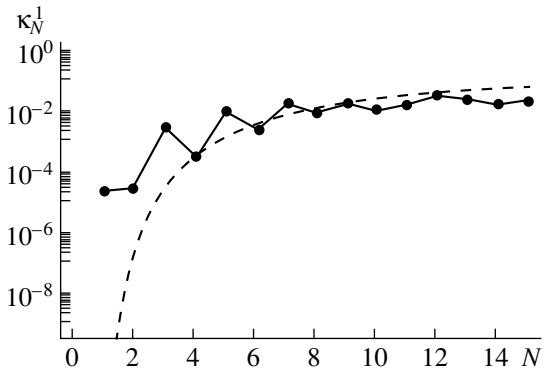

Fig. 2. The dependence of the single ionization coefficient on the number of atoms in Ag clusters: dots, experiment [10]; dashed line, calculation.

the ionization coefficients of Ta clusters with $N = 5$ and 10 atoms as a function of target temperature Θ is given in Fig. 1, illustrating the following general conclusions: (1) The charge state varies with target temperature, and the ionization coefficient increases with increasing temperature. (2) The larger the cluster charge, the more rarely that cluster occurs; for example, the number of clusters with charge 2 is, as a rule, much less than those with charge 1. (3) Larger clusters are more strongly ionized; for example, $\kappa_{10}^1 > \kappa_5^1$ and $\kappa_{10}^2 > \kappa_5^2$.

The dependence of the ionization coefficient for Ag clusters on cluster size N at a target temperature Θ = 700 K is shown by the dashed line in Fig. 2. An important feature is the tendency to saturation of the ionization coefficients with increasing cluster size. Qualitatively similar behavior was observed in experiments [10],[3] whose results are also presented in Fig. 2. Since an ionization coefficient describing only charged clusters cannot account for the behavior of neutral clusters, it is necessary to introduce the ionization degree η_N^Q as the ratio of the number of clusters (of size N) with charge $Q = 0, \pm1, \pm2, \ldots$ to the total number of clusters of the same size N. The ionization degree shows charge redistribution between clusters of a given size; for example, a rise in the number of charged clusters is accompanied by a corresponding fall in the number of neutral clusters. This behavior of the ionization degree is shown in Fig. 3 (for $N = 5$) and Fig. 4 (for $N = 10$). The relative yields $Y_N^Q = \overline{W}_N^Q / \overline{W}_5^Q$ for singly charged (Y_N^1) and neutral (Y_N^0) clusters of Ta_N and Nb_N as a function of the number of their atoms are shown in Figs. 5–8. Tantalum and niobium targets were sputtered by singly charged Au^{-1} ions at an energy of 6 keV and Ar^{+1} ions at an energy of 5 keV at target temperatures

[3] To be precise, in these experiments, the target temperature was not registered, despite its possible dependence on laser irradiation.

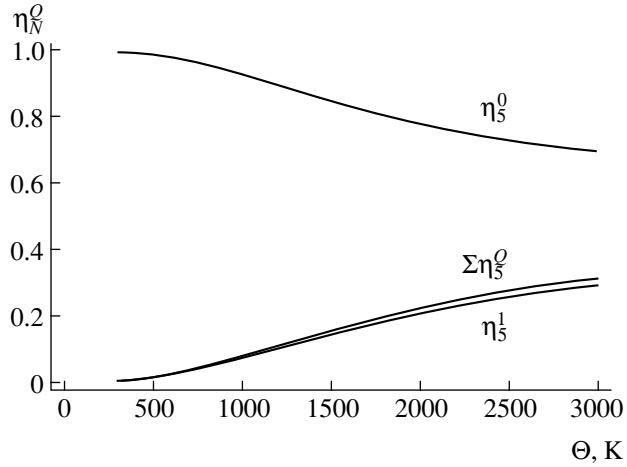

Fig. 3. The ionization degree of Ta clusters as a function of target temperature. $N = 5$; $\sum\eta_5^Q$, the ionization degree summed over all cluster charges corresponding to the total relative number of clusters with arbitrary, but nonzero, charge, i.e., $\sum\eta_5^Q = 1 - \eta_5^0$.

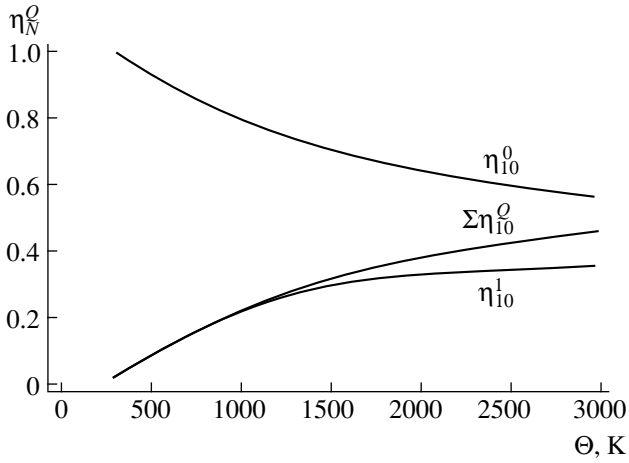

Fig. 4. Same as in Fig. 3 for $N = 10$.

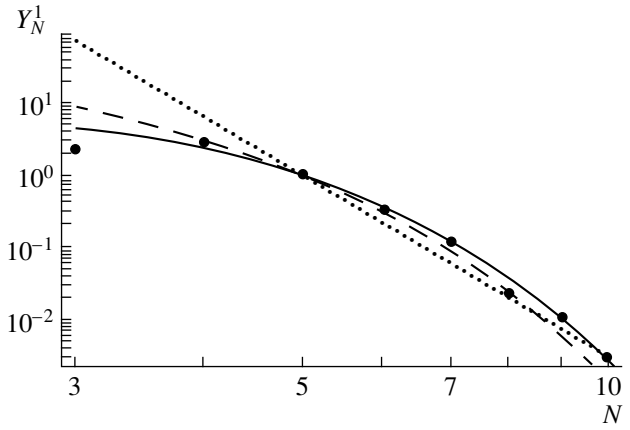

Fig. 5. The relative yield Y_N^1 of Ta_N^{+1} singly charged clusters as a function of N. Bombardment by Au^{-1} ions, Θ = 2273 K. Solid line, calculated Y_N^1 values; heavy dots, experiment [17, 18]; dashed line, calculated mass spectrum of neutral Y_N^0 clusters; dotted line, power law curve [19] normalized to $N = 5$, i.e., values of the function $N^{-8.5}/5^{-8.5}$.

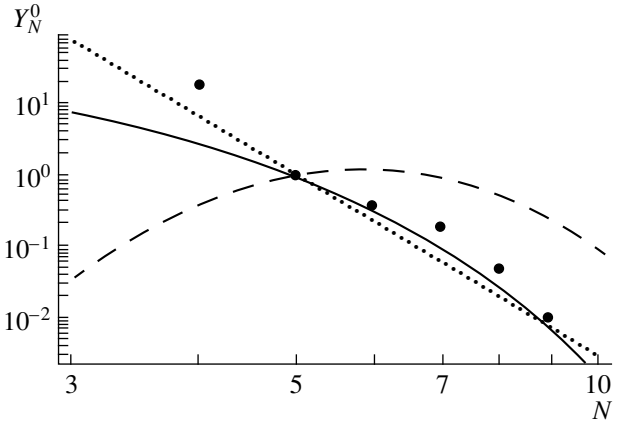

Fig. 6. The relative yield Y_N^0 of Ta_N^0 neutral clusters as a function of N. Bombardment by Ar^{+1} ions, Θ = 300 K. Solid line, calculated values of Y_N^0; dots, experiment [19]; dashed line, calculated mass spectrum of singly charged Y_N^1 clusters; dotted line, see Fig. 5.

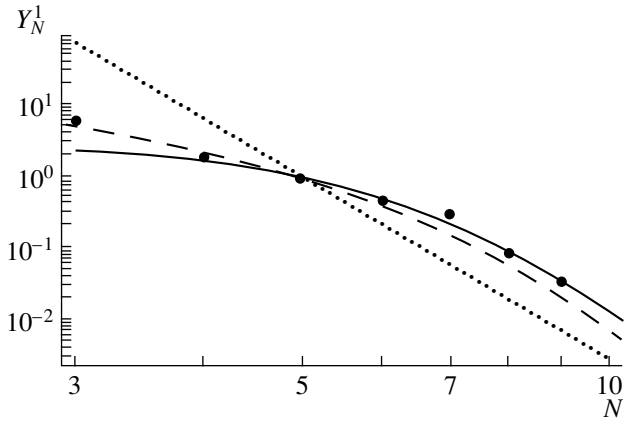

Fig. 7. The relative yield Y_N^1 of Nb_N^{+1} singly charged clusters as a function of N. Bombardment by Au^{-1} ions, Θ = 2273 K. Solid line, calculated values of Y_N^1; dots, experiment [20]; dashed line, calculated mass spectrum of neutral Y_N^0 clusters; dotted line, power law curve [19] normalized to $N = 5$, i.e., values of the function $N^{-8.1}/5^{-8.1}$.

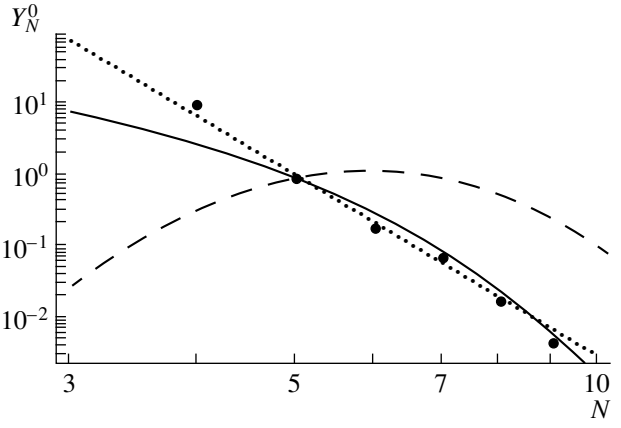

Fig. 8. The relative yield Y_N^0 of Nb_N^0 neutral clusters as a function of N. Bombardment by Ar^{+1} ions, Θ = 300 K. Solid line, calculated values of Y_N^0; dots, experiment [19]; dashed line, calculated mass spectrum of singly charged clusters Y_N^1; dotted line, see Fig. 7.

Θ = 2273 K and Θ = 300 K, respectively. The power law curve [19] normalized to a cluster with 5 atoms, i.e., values of the functions $N^{-8.5}/5^{-8.5}$ for tantalum and $N^{-8.1}/5^{-8.1}$ for niobium, is also plotted in the figures for comparison. It is worth noting that mass spectra of the neutral clusters are weakly dependent on temperature, whereas mass spectra of singly charged clusters are appreciably affected by target temperature but approach the mass spectra of the neutral clusters as the temperature increases.

Thus, only on the assumption that a cluster escapes as a whole can the fluctuation mechanism of cluster charge state formation be developed and the dependence of the charge state distribution on cluster size and target temperature be described. It is known that it is technically much simpler to register charged particles than neutral ones. Charge state formation processes, i.e., emission processes of charged and neutral particles, are often interrelated. Therefore, experimental results for charged particles provide an indirect way to

recover data for neutral particles and thus allow one to simplify the experimental setup.

REFERENCES

1. *Sputtering of Solids: Fundamentals and Applications*, Collection of Articles, Ed. by E. S. Mashkova (Mir, Moscow, 1989).
2. H. H. Andersen, K. Dan. Vidensk. Selsk. Mat.-Fys. Medd. **43**, 127 (1993).
3. H. M. Urbassek and W. O. Hofer, K. Dan. Vidensk. Selsk. Mat.-Fys. Medd. **43**, 97 (1993).
4. I. A. Baranov, Yu. V. Martynenko, S. O. Tsepelevich, and Yu. N. Yavlinskiĭ, Usp. Fiz. Nauk **156**, 478 (1988) [Sov. Phys. Usp. **31**, 1015 (1988)].
5. G. Betz and K. Wien, Int. J. Mass Spectrom. Ion Processes **140**, 1 (1994).
6. P. Sigmund, Phys. Rev. **184**, 383 (1969).
7. A. Wucher and B. Y. Garrison, J. Chem. Phys. **105**, 5999 (1996).
8. Th. J. Colla, H. M. Urbassek, A. Wucher, *et al.*, Nucl. Instrum. Methods Phys. Res. **143**, 284 (1998).
9. M. L. Yu, in *Topics of Applied Physics Sputtering by Particle Bombardment III*, Ed. by R. Behrisch and K. Wittmaack (Springer-Verlag, New York, 1991), pp. 91–160.
10. W. Wahl and A. Wucher, Nucl. Instrum. Methods Phys. Res. **94**, 36 (1994).
11. V. Kh. Ferleger, M. B. Medvedeva, and I. A. Wojciechowski, Nucl. Instrum. Methods Phys. Res. B **125**, 214 (1997).
12. V. I. Matveev and P. K. Khabibullaev, Dokl. Akad. Nauk **362**, 191 (1998).
13. V. I. Matveev, S. F. Belykh, and I. V. Verevkin, Zh. Tekh. Fiz. **69** (3), 64 (1999) [Tech. Phys. **44**, 323 (1999)].
14. L. N. Dobretsov and M. V. Gomoyunova, *Emission Electronics* (Nauka, Moscow, 1966).
15. L. D. Landau and E. M. Lifshitz, *Statistical Physics* (Nauka, Moscow, 1976; Pergamon, Oxford, 1980), Part 1.
16. C. Kittel, *Introduction to Solid State Physics* (Wiley, New York, 1976; Nauka, Moscow, 1978).
17. S. P. Belykh, U. Kh. Rasulov, A. V. Samartsev, and I. V. Veryovkin, Nucl. Instrum. Methods Phys. Res. B **136**, 773 (1998).
18. S. F. Belykh, U. Kh. Rasulov, A. V. Samartsev, *et al.*, Mikrochim. Acta., Suppl. **15**, 379 (1998).
19. A. Wucher and W. Wahl, Nucl. Instrum. Methods Phys. Res. B **115**, 581 (1996).
20. S. F. Belykh, B. Habets, U. Kh. Rasulov, *et al.*, in *Abstract Book of SIMS Europe, Muenster, 1998*, p. 5.

Translated by M. Astrov

Technical Physics, Vol. 45, No. 8, 2000, pp. 1070–1074. Translated from Zhurnal Tekhnicheskoĭ Fiziki, Vol. 70, No. 8, 2000, pp. 114–117.

EXPERIMENTAL INSTRUMENTS AND TECHNIQUES

Coordinate Correction for Parallax for Gamma-Ray Beams Detected by Counters Based on Thin-Film Drift Tubes

S. P. Lobastov, V. M. Lysan, V. D. Peshekhonov, and V. I. Smirichinskiĭ

Joint Institute for Nuclear Research, Dubna, Moscow oblast, 141980 Russia

E-mail: lyssan@sunse.jinr.ru

Received June 1, 1999

Abstract—A model was put forward for finding the angle of incidence of a narrow gamma-ray beam and refining its coordinate when the beam is detected by cathode-readout counters based on thin-film drift tubes. The model can be used in solving small-angle scattering problems, which are widely met in X-ray diffraction analysis. *© 2000 MAIK "Nauka/Interperiodica".*

INTRODUCTION

The determination of neutral particle coordinates with the use of gas-filled detectors based on thin-film drift tubes is always complicated by parallax. If the particle path is deflected from the plane normal to the anode wire, the performance of these detectors degrades in comparison with the usual case. The spatial resolution of the detector can be improved by introducing a correction for parallax [1] on condition that the beam coordinate distribution in the detector is given by the Gaussian function.

This paper deals with an experimental check of the parallax-correction method and extends it to the case when a linear position cathode-readout detector on the base of thin-film drift tubes is used [2, 3].

EXPERIMENTAL

A special collimator (Fig. 1) with orthogonal slit *3* of width 40 μm and inclined slit *4* of width 80 μm was designed for investigations. The detector [2] was purged by a $Ar : CH_4$ (80 : 20) or $Xe : CH_4$ (80 : 20) gas mixture under normal pressure. It was irradiated by a ^{55}Fe source through slits *3* and *4* simultaneously. The collimator can move up and down over a distance of 1 mm with a precision of better than 20 μm. Beam orthogonality was thought to be provided if collimator movement did not change the coordinate of the peak leaving slit *3* (within the accuracy defined by the spatial resolution of the detector).

Typical coordinate distributions after passing both slits for the argon and xenon mixtures are presented in Fig. 2. It is evident that a gas mixture with a great absorption factor is preferable. In this case, two or more nearby peaks from narrow gamma-ray beams that are not orthogonal to the anode wire may be resolved. A similar problem appears, for instance, in structure analysis related to small-angle scattering; in this case, the xenon mixture under excessive pressure is more appropriate.

RESULTS AND DISCUSSION

Model

It follows from experimental data (Figs. 2a, 2b) that, if a narrow beam is strongly deflected from the normal, the coordinate distribution of gamma quanta cannot be represented by a broadened and shifted Gaussian function. To treat the data, we assumed, in contrast to [1], that, for each gamma quantum absorbed in the detector, the coordinate distribution obeys a Gaussian curve, and the parameter σ of this distribution is the spatial resolu-

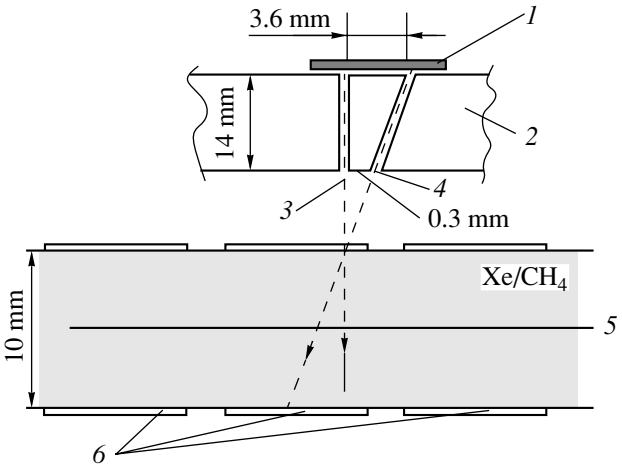

Fig. 1. Schematic of experiment: *1*, ^{55}Fe source; *2*, collimator; *3* and *4*, slits; *5*, anode; and *6*, strips.

1063-7842/00/4508-1070$20.00

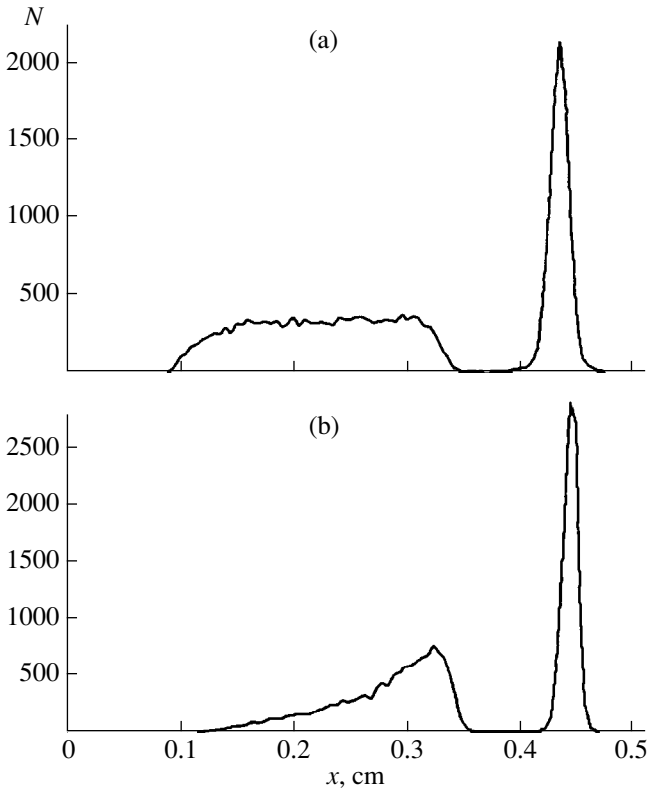

Fig. 2. Typical coordinate distributions of the number of gamma quanta for (a) argon and (b) xenon gas mixtures (one bin along the *x*-axis equals 50 μm).

tion of the detector. We assume also that σ is constant for each single event, being independent of the drift path of the primary electron cloud toward the anode wire. Physically, this means that we neglect the diffusion of the drifting primary electron cloud.

The geometry of the experiment is shown in Fig. 3. The situation when the gamma flux vector, the normal to the plane of the flux, and the anode-wire axis are noncomplanar was not considered. According to our assumption, the differential probability that the event will occur at a point x is given by the normal distribution

$$dP_g \sim \exp(-(x - x_m)^2/2\sigma^2), \quad (1)$$

where x_m is the projection of the point where a gamma quantum is absorbed (Fig. 4).

The probability that the gamma quantum will be absorbed in the gas mixture is given by

$$dP_a \sim \exp(-\mu s), \quad (2)$$

where μ is the absorption factor of the gas mixture in the detector and s is the gamma quantum range in the mixture.

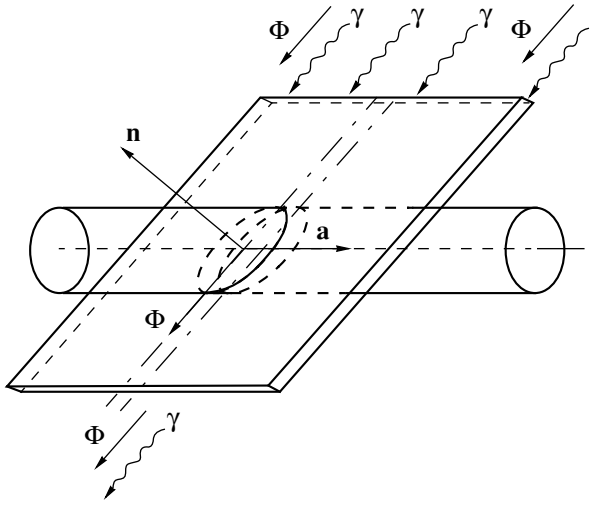

Fig. 3. Geometry of the experiment.

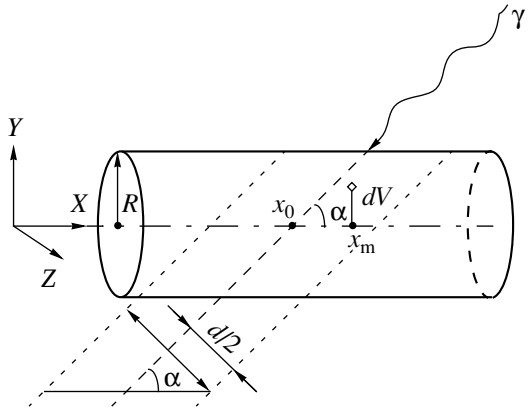

Fig. 4. Schematic of the process.

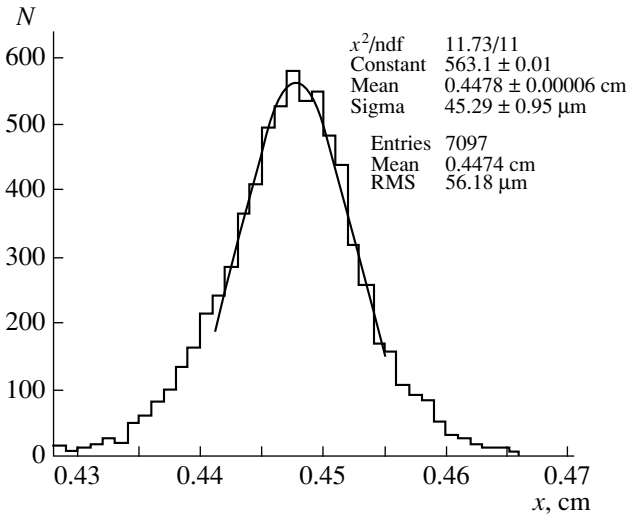

Fig. 5. Fitting by the Gaussian function (one bin along the *x*-axis equals 10 μm).

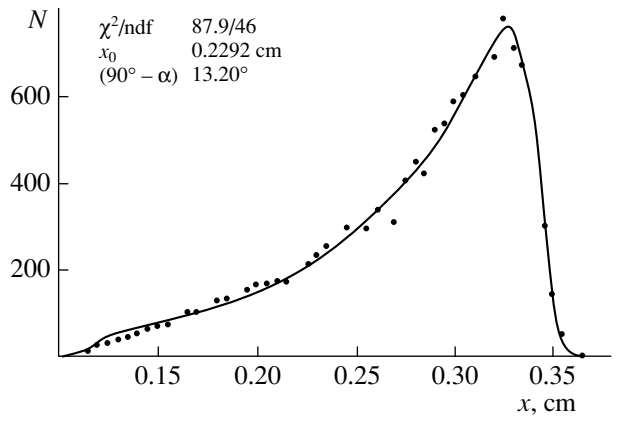

Fig. 6. Fitting by model (4) (one bin along the *x*-axis equals 50 μm).

These processes are mutually independent; then, the total differential probability that the event will be detected at the anode, including the probability that the gamma quantum is absorbed in a volume *dV*, takes the form

$$dP(x) \sim \exp(-\mu s)\exp(-(x-x_m)^2/2\sigma^2)dV. \qquad (3)$$

Integrating (3) over the region where gamma quanta meet the gas mixture, we obtain the total probability that the event will be detected at a point *x*:

$$P(x) \sim \int_{x_0-d/(2\sin\alpha)}^{x_0+d/(2\sin\alpha)} dx_0' \int_{-R}^{R} dz \int_{-\sqrt{R^2-z^2}}^{\sqrt{R^2-z^2}} dy \times \{\exp(-\mu s)\exp(-(x-x_m)^2/2\sigma^2)\}, \qquad (4)$$

where

$$s = [(R^2-z^2)^{1/2} - y]/\sin\alpha, \quad x_m = x_0' + y\cot\alpha,$$

x_0 is the intersection point of the anode wire and midplane of a gamma flux (by definition, the midplane is parallel to the collimator slit), and *d* is the gamma flux width (we neglect the beam divergence).

Thus, the model is specified by the function $P(x, x_0, \sigma, \alpha)$.

Fitting

The parameter σ is determined as follows: in the absence of parallax (α = 90°), the peak leaving slit *3* (Fig. 2b) is approximated with expression (4). This gives σ ≈ 50 μm. For this experimental distribution, the root-mean-square deviation is *RMS* ≈ 56 μm (Fig. 5). If this peak is approximated by a normal Gaussian function within the range where a good correlation with the experiment is observed, we obtain $\sigma_G \approx 45$ μm.

Now, putting σ = 50 μm, we apply this model to approximate the data for inclined slit *4* (Fig. 2b) and find $x_0 = 0.2292 \pm 0.0011$ cm and $(90° - \alpha) = 13.20° \pm 0.12°$. The latter value agrees well with the measured angle (13.25° ± 0.15°) of the used collimator. The fitting results are presented in Fig. 6.

CONCLUSIONS

Mathematical model (4) for coordinate distribution in a cathode-readout detector based on thin-film drift tubes is presented. The model takes into account the detector and incident beam geometries. It gives a good fit to the experimental data and can be employed in experiments with space-separated gamma-ray beams, for instance, in X-ray diffraction analysis.

A method [see (5)] is suggested that not only significantly refines the coordinate x_0 but also finds the parallax-related angular coordinate α for a narrow gamma beam from the shape of the peak in its coordinate distribution.

Experimental coordinate distributions were obtained for the designed detector (Fig. 2). The angular coordinate of a narrow beam of gamma quanta, which are absorbed for the most part through photoeffect, was first obtained from these data.

The method can be employed for creating planar detectors for synchrotron beam imaging [4].

The use of numerical integration (see Appendix) will inevitably increase the computational time when the model becomes more complicated to improve the accuracy of obtaining the coordinates x_0 and α (for instance, if diffusion or a more intricated incident beam geometry is considered). Clearly, the greater the computational resource, the less the computational time.[1]

APPENDIX

The main difficulties in taking the integral in (4),

$$P(x) \sim \int_{x_0-d/(2\sin\alpha)}^{x_0+d/(2\sin\alpha)} dx_0' \int_{-R}^{R} dz \int_{-\sqrt{R^2-z^2}}^{\sqrt{R^2-z^2}} dy \times \{\exp(-\mu s)\exp(-(x-x_m)^2/2\sigma^2)\},$$

are as follows: (1) This triple integral cannot be taken analytically and (2) Immediate numerical integration requires much computational time because of the three-dimensional domain of integration.

However, (4) can be analytically integrated successively for the variables *y* and x_0'. On simplification, we

[1] In this work, an AMD-K-6-II (333 MHz/32-Mb RAM) computer was used. The time to compute the data presented in Fig. 6 was 25 min.

obtain

$$I(x, x_0, \sigma, \alpha) \equiv \int_{-R/2}^{R/2} dz \Bigg(\Bigg(-2 + \exp(2\sqrt{R^2 - z^2}\mu\,\mathrm{cosec}(\alpha)) \mathrm{Erf}\left(\frac{2x - 2x_0 - 2\sqrt{R^2 - z^2}\cot(\alpha) + d\,\mathrm{cosec}(a)}{2\sqrt{2}\sigma} \right)$$
$$+ \exp(2\sqrt{R^2 - z^2}\mu\,\mathrm{cosec}(\alpha)) \mathrm{Erf}\left(\frac{-2x + 2x_0 + 2\sqrt{R^2 - z^2}\cot(\alpha) + d\,\mathrm{cosec}(a)}{2\sqrt{2}\sigma} \right)$$
$$+ \exp(2\sqrt{R^2 - z^2}\mu\,\mathrm{cosec}(\alpha)) \Bigg(\Bigg(\exp\left(\frac{\mu\sec(\alpha)(2x - 2x_0 - d\,\mathrm{cosec}(\alpha) + \mu\sigma^2\sec(\alpha))}{2} \right) \Bigg)$$
$$\times \Bigg(\mathrm{Erf}\left(\frac{-2x + 2x_0 - 2\sqrt{R^2 - z^2}\cot(\alpha) + d\,\mathrm{cosec}(\alpha) - 2\mu\sigma^2\sec(\alpha)}{2\sqrt{2}\sigma} \right)$$
$$- \mathrm{Erf}\left(\frac{-2x + 2x_0 + 2\sqrt{R^2 - z^2}\cot(\alpha) + d\,\mathrm{cosec}(\alpha) - 2\mu\sigma^2\sec(\alpha)}{2\sqrt{2}\sigma} \right) \Bigg)$$
$$+ \exp\left(\frac{\mu\sec(\alpha)(2x - 2x_0 + d\,\mathrm{cosec}(\alpha) + \mu\sigma^2\sec(\alpha))}{2} \right)$$
$$\times \Bigg(-\mathrm{Erf}\left(\frac{2x - 2x_0 - 2\sqrt{R^2 - z^2}\cot(\alpha) + d\,\mathrm{cosec}(\alpha) + 2\mu\sigma^2\sec(\alpha)}{2\sqrt{2}\sigma} \right)$$
$$+ \mathrm{Erf}\left(\frac{2x - 2x_0 + 2\sqrt{R^2 - z^2}\cot(\alpha) + d\,\mathrm{cosec}(\alpha) + 2\mu\sigma^2\sec(\alpha)}{2\sqrt{2}\sigma} \right) \Bigg) \Bigg)$$
$$+ \mathrm{Erfc}\left(\frac{-2x + 2x_0 - 2\sqrt{R^2 - z^2}\cot(\alpha) + d\,\mathrm{cosec}(\alpha)}{2\sqrt{2}\sigma} \right)$$
$$+ \mathrm{Erfc}\left(\frac{2x - 2x_0 + 2\sqrt{R^2 - z^2}\cot(\alpha) + d\,\mathrm{cosec}(\alpha)}{2\sqrt{2}\sigma} \right) \Bigg) \sin(\alpha) \Bigg) \frac{1}{\exp(2\sqrt{R^2 - z^2}\mu\,\mathrm{cosec}(\alpha))\mu}. \quad (5)$$

It only remains for us to integrate over z numerically.[2] The normalization factor is defined by

$$K = \frac{1}{\int_{-\infty}^{\infty} dx I(x, x_0, \sigma, \alpha)}. \quad (6)$$

In the final form, the model is given by

$$p(x, x_0, \sigma, \alpha) = \frac{I(x, x_0, \sigma, \alpha)}{\int_{-\infty}^{\infty} dx I(x, x_0, \sigma, \alpha)} \equiv KI, \quad (7)$$

where the integration of the numerator and denominator is performed numerically with an accuracy of five significant digits.

Because of the complexity of mathematical model (7), the Newton method was initially used to minimize the χ^2 functional, which provides a rapid convergence with the minimum number of iterations. However, this numerical method does not give an explicit functional dependence of the parameters $\{x_{0\min}, \alpha_{\min}, \sigma_{\min}\}$, minimizing the functional, on experimental values $\{N_i, x_i\}$. This makes the accurate estimation of errors (standard deviations) introduced into the obtained parameters more difficult. Therefore, model (7) was first interpolated in x and the parameters in the vicinity of $\{x_{0\min}, \alpha_{\min}, \alpha_{\min}\}$ by a third-degree polynomial. Then the min-

[2] Here, the domain of integration over z differs from that in general expression (4), because actually the collimator (window) is R = 0.5 mm wide throughout the tubes.

imum of the χ^2 functional is searched using polynomial regression [5]. This method provides an explicit dependence of $\{x_{0\min}, \alpha_{\min}, \sigma_{\min}\}$ on $\{N_i, x_i\}$, resulting in a more accurate estimation of errors in the sought parameters.

ACKNOWLEDGMENT

We thank Yu.K. Potrebennikov for helpful consultations.

REFERENCES

1. S. Yu. Grachev and V. D. Peshekhonov, Communication JINR, No. E13-96-83 (1996).
2. V. N. Bychkov *et al.*, Nucl. Exp. Tech. **41**, 315 (1998).
3. R. A. Astabatyan *et al.*, Communication JINR, No. P13-98-271 (1998).
4. V. N. Bychkov *et al.*, Nucl. Instrum. Methods Phys. Res. A **367**, 276 (1995).
5. J. R. Taylor, *An Introduction to Error Analysis* (Univ. Science Books, California, 1982; Mir, Moscow, 1985).

Translated by B.A. Malyukov

Technical Physics, Vol. 45, No. 8, 2000, pp. 1075–1080. Translated from Zhurnal Tekhnicheskoĭ Fiziki, Vol. 70, No. 8, 2000, pp. 118–124.

EXPERIMENTAL INSTRUMENTS AND TECHNIQUES

Advantages of Anhysteretic Magnetooptic Films in Nondestructive Testing

V. V. Randoshkin[1], M. Yu. Gusev[2], Yu. F. Kozlov[2], and N. S. Neustroev[2]

[1] *Magnitooptoelektronika Laboratory, Institute of General Physics, Ogarev Mordovian State University, Russian Academy of Sciences, Bol'shevistskaya ul. 68, Saransk, 430000 Russia*

[2] *Malinin Materials Science Research Institute, Moscow, 103460 Russia*

Received August 3, 1999

Abstract—The potentialities provided by bismuth-containing garnet ferrite films with uniaxial anisotropy and easy-plane anisotropy for the visualization of spatially nonuniform magnetic fields in magnetooptic nondestructive testing are compared. © *2000 MAIK "Nauka/Interperiodica".*

Nondestructive testing and several physically similar techniques designed for other purposes [1–26] can exploit the magnetooptic visualization of spatially nonuniform magnetic fields [1, 8, 27, 28]. Two types of bismuth-containing single-crystal garnet ferrite films (BcSCGFFs) with giant Faraday rotation [1, 29] are used: with uniaxial magnetic anisotropy (type I) and with easy-plane magnetic anisotropy (type II). For BcSCGFFs of type I, an inhomogeneous magnetic field can be judged from the domain configuration, while for the films of type II, the surface distribution of the angle between the magnetization and film plane bears necessary information.

In the absence of an external magnetic field, the films of type I split up into oppositely polarized domains and the areas covered by the domains of either polarity are roughly equal. The difference between the areas increases with coercive force H_c, which is usually 0.1–1 Oe for these films. Owing to coercive force, the films of type I exhibit hysteresis at magnetization reversal under a bias field H_b applied normally to the film.

In the films of type I, the plane of polarization in the neighboring domains rotates in the opposite direction by the same angle Θ_F, which does not depend on the bias magnetic field. As H_b increases, the area occupied by domains with the magnetization aligned with the field grows at the expense of unfavorably magnetized domains up to the complete magnetization of the film. The motion of domain walls (DWs) accounts for this process. By changing the angle between the analyzer and polarizer in a polarizing microscope, one can completely suppress monochromatic light passing through the domains of a specific polarity. If white light is used, domains become differently colored, the color depending on the angle φ between the optical axes of the polarizer and analyzer. When the polarizer and analyzer are crossed ($\varphi = 0$), domains have the same color and DWs appear dark.

In the films of type II not subjected to an external magnetic field, the magnetization vectors lie in the film plane even if the film splits up into domains of opposite polarities. Therefore, the plane of polarization of light propagating normally to the film does not rotate. The plane of polarization may rotate only in the case of Bloch walls. Bloch lines separating DW parts where the plane of polarization rotates in the opposite directions can be visualized.

The influence of a time-invariable but space-independent magnetic field on the films of type I depends on the field intensity and gradient. A sufficiently intense alternating magnetic field with the spatial period considerably exceeding the equilibrium size of domains splits up the film into large oppositely polarized domains with smooth walls. These films visualize the lines of equal intensity $H = 0$. In particular, a gradient magnetic field $H_b = \beta x$ that can be produced by two permanent magnets with the *C*-shaped section forms planar straight DWs. If then a constant bias field H_b is applied perpendicular to the film surface, the DWs will move to another equilibrium position, again going through the points where the total magnetic field equals zero. In other words, lines of equal intensity $H = -H_b$ are visualized. By varying the bias field, one can visualize lines of equal intensity for any H.

Lines of equal intensity can be visualized even if an intense magnetic field varies very smoothly (the gradient is small). In this case, the border between two oppositely magnetized domains is no longer a planar DW, but a transient region of strip domains. The smaller the gradient, the wider this transient region. In particular, a gradient magnetic field $H_b = \beta x$ induces a "comb" of strip domains. It is significant that the curves enveloping the transient region go through points where the external magnetic field H is equal to the saturation field of the film $\pm H_s$. If then a bias field is applied to the film, these two curves will shift. The monodomain areas of one polarity will expand; and those of the other, shrink.

1063-7842/00/4508-1075$20.00

The new lines of equal intensity will relate to $H = H_b + H_s$ and $H = H_b - H_s$, respectively. Note that, in both cases, high-resolution magnetic field mapping requires a fine measurement step.

In the case of a low magnetic field (less than H_s), monodomain areas in the films of type I are absent and field nonuniformity can be judged by the local ratio of the areas occupied by domains with different polarity. It is evident that, in this case, the spatial resolution sharply drops. To remedy the situation, the bias field should be chosen such that the total magnetic field exceeds the saturation field. As for mapping of a nonuniform magnetic field that consists of weak variable and intense constant components, it is advisable to cancel out the constant component using an external bias field.

The most problematic is the visualization of an alternating close-to-saturation magnetic field whose period coincides on the order of magnitude with the equilibrium period of domains in the films of type I. In this case, the spatial period of the magnetic field may be misestimated several times [30].

Magnetization reversal in the films of type II subjected to a bias field does not cause hysteresis (Fig. 1), since this phenomenon is not inherent in the rotation of magnetization. If even a relatively weak magnetic field is applied, the magnetization vectors come out of the film plane, their direction being the same for domains of different polarity. Consequently, the plane of polarization rotates. As the bias field grows, Θ_F increases almost linearly until the film is magnetized to saturation and the magnetization vectors come out at right angles to the film surface (Fig. 1). With a further increase in H_s, the Faraday rotation angle remains constant.

When a nonuniform magnetic field is applied to the films of type II and white light is used for illuminating, the films change their color throughout the surface (for monochromatic light, the transmitted intensity changes). Being proportional to the normal component of the magnetization, the local angle of Faraday rotation depends on the corresponding component of the external magnetic field. It is significant that, with the films of type II (in contrast to those of type I), mapping of a nonuniform magnetic field does not require the application and variation of an additional external magnetic field. The films of type II provide information about the field nonuniformity via the distribution of the Faraday rotation angle over the film surface.

The films of type I are magnetized to saturation when the total magnetic field reaches H_s, which is less than but comparable to the saturation magnetization $4\pi M_s$. In the films of type II, saturation occurs when the total magnetic field equals the field of magnetic anisotropy H_K, which can be both much less and much more than $4\pi M_s$. Since the films of type II respond to a weak external magnetic field by a slight rotation of the magnetization vector, their sensitivity is considerably higher than that of the films of type I. For this reason, a range of magnetic fields to be visualized may be broad and accommodated to applications. Experiments show that the films of type II are suitable for magnetooptic nondestructive testing at magnetic fields within the 10^{-8}–10^5 Oe range.

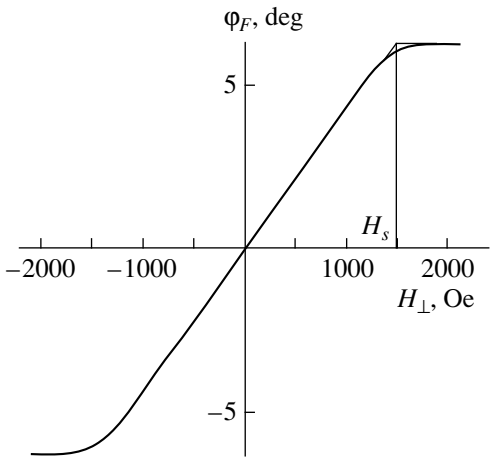

Fig. 1. Hysteresis loop typical of films of type II magnetized perpendicularly to the film surface.

When a magnetooptic signal from the films of type II is photometrically recorded with a linear measuring channel, the output is defined by the Malus law

$$U = U_0 \sin^2(\varphi - \Theta_F),$$

where U_0 is the input signal.

The linearity of the transfer characteristic can considerably be increased by applying the two-channel differential measurement mode, which means the automatic subtraction of two images of the same visual field that are obtained at two different angles between the polarizer and analyzer axes ($+\varphi$ and $-\varphi$). In this case, the output signal looks like

$$U = U_0 \sin 2\varphi \sin 2\Theta_F.$$

This form ensures the high linearity of conversion and simplifies the calibration of results in absolute magnetic units.

The experimental setup, built around a polarizing microscope, was connected to a personal computer through a CCD video camera. The surface of a visualizing film was covered first by a mirror coating and then by a protective layer. The thus-prepared film and a biasing coil were placed on the microscope stage. The source of a magnetic field to be studied was placed near the surface of the visualizing film.

The most obvious application of magnetooptic visualization of nonuniform magnetic fields is the nondestructive control of magnetically hard products, for example, magnetic-recording media or permanent magnets.

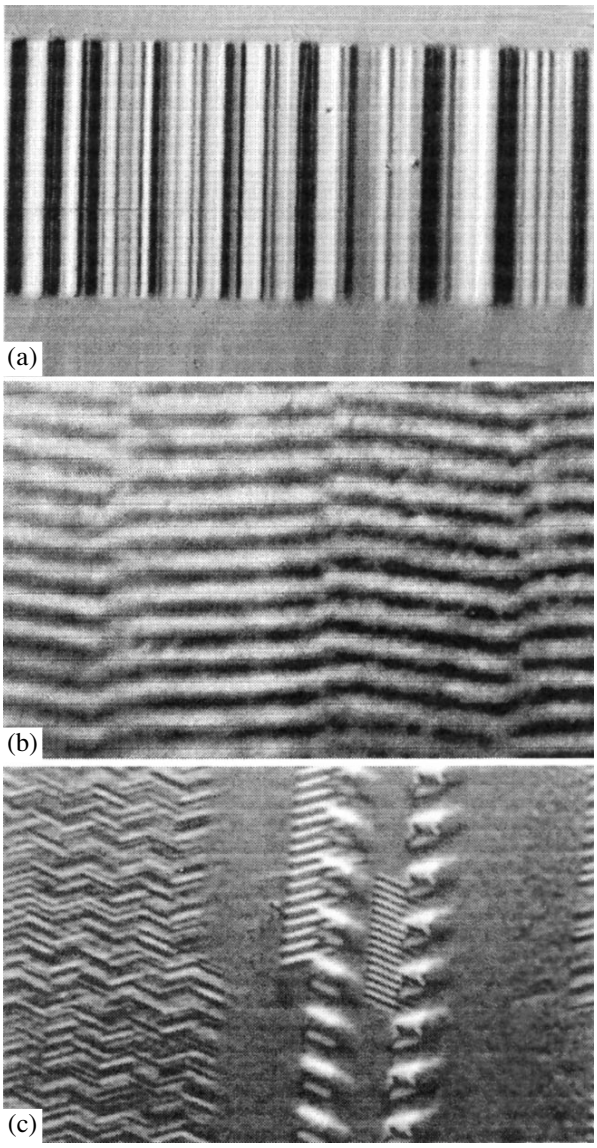

Fig. 2. Magnetooptic images of a (a) sound record on a magnetic tape, (b) VHS-tape record, and (c) R-DAT digital record visualized with the use of the film of type II.

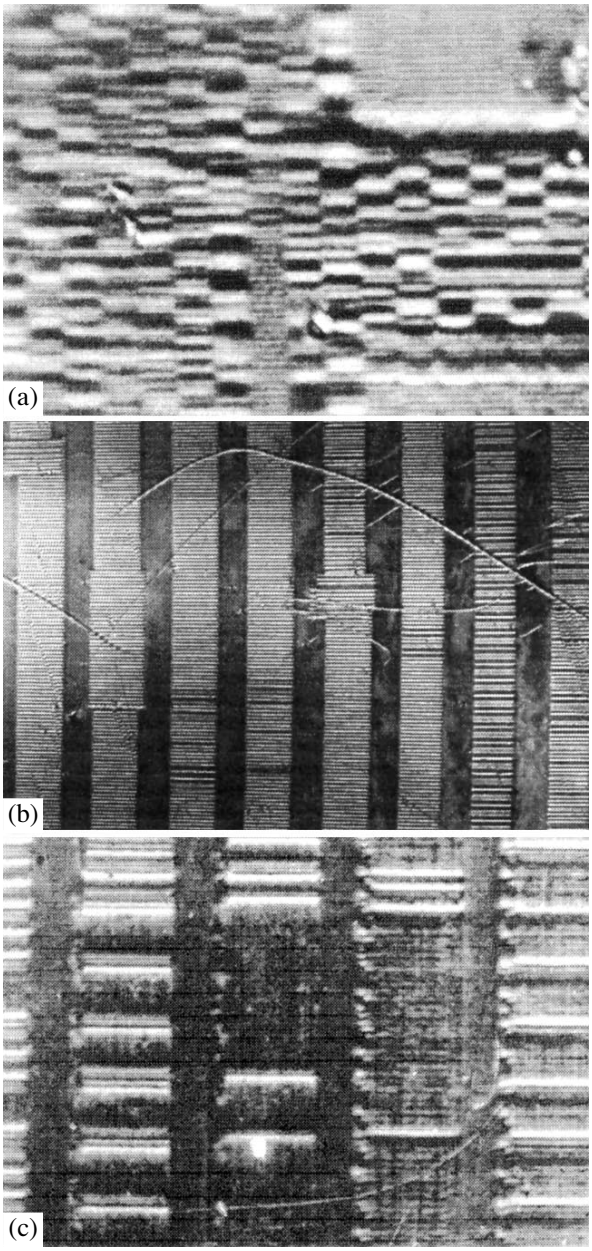

Fig. 3. Magnetooptic images of records on a (a) hard magnetic disk, (b) flexible magnetic disk, and (c) metallic tape of a "black box" that are visualized with the use of the film of type II.

Fig. 2a shows the black-and-white magnetooptic image of a recorded tape. A colored image obtained with the experimental setup consists of a number of colored fringes (brown, yellow, and various tints of green) of different width with diffused borders against a yellow-green background (unfortunately, on a black-and-white picture, a significant part of information on a sample under study is lost). This means that an analog record is visualized. In experiments, the dynamic range was found to be no less than 56 dB (this value depends only on the capability of metrological equipment). Note that each of two tape tracks is about 450 μm wide.

Fig. 2b shows the magnetooptic image of a recorded VHS tape (the color picture is a set of narrow fringes of various brown tints). A video tape track is about 30 μm wide; and the recording period, about 5 μm.

Fig. 2c shows the magnetooptic image of a tape with a digital sound record made in the R-DAT standard. The record shows up as narrow alternate yellow-brown fringes of different tints and widths. Also shown are timing tracks (wide and narrow yellow and green fringes of equal width). The periods of timing pulses were 170, 40, and 30 μm.

Fig. 3a shows the magnetooptic image of a record and labels on a hard magnetic disk. The width of the

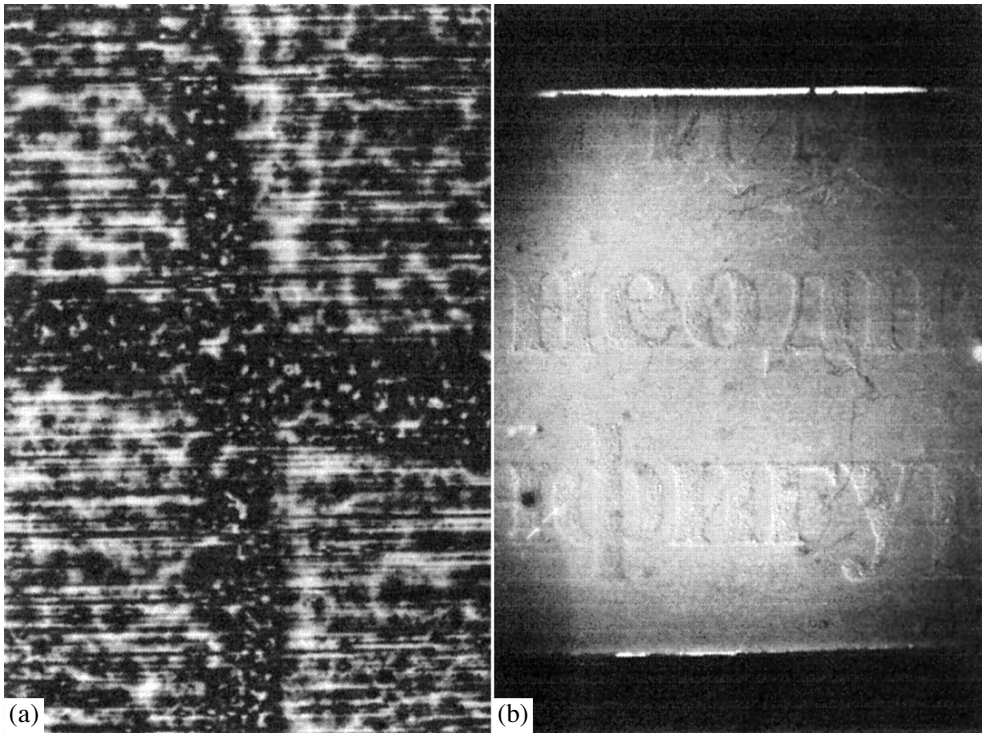

Fig. 4. Magnetooptic images of (a) the permanent magnet surface and (b) a part of laser-printed text that are visualized with the use of the film of type II.

visualized lines is less than 0.7 μm, which is unattainable when the films of type I are used.

Fig. 3b shows the magnetooptic image of a record on a faulty flexible disk. Long curved lines are disk surface defects, while horizontal lines, which form vertical tracks, depict records. Sharp local variations of the track width and location, which are caused by start-stop faults of the recording head, are noteworthy. In particular, the track width varies stepwise by about 50 μm. This means that the visualization of magnetic records discovers the faults of a recording head.

The films of type II are indispensable in restoring corrupted or lost information written on the metallic tape of a "black box." As seen from Fig. 3c, distinct black and white fringes alternate with low-contrast lines, which result from incomplete deletion of the previous record (color contrast gives additional information). Moreover, the noncoincidence between the tracks of the previous and subsequent records results in the presence of the previous one as bright dots at the track edges.

Fig. 4 shows the black-and-white magnetooptic image from the surface of a barium permanent magnet, which is used for producing a bias magnetic field in bubble technology [31, 32]. The image is brown to green in the color image. In particular, narrow vertical dark fringes on the light background correspond to dark-brown ones on the orange background. These fringes seem to be associated with polishing defects on the magnet surface. Dark intersecting fringes with light spots represent aggregates of particles with another structure or saturation magnetization. In the color original, these spots are yellow with a green border (in black-and-white images, the contrast between green and dark brown parts is lost). Figure 4a indicates that the magnetooptic visualization of spatially nonuniform magnetic fields may be helpful in the phase analysis of various materials.

Figure 4b shows the magnetooptic image of a laser-printed text (the text is not seen because of the mirror coating). The need for reading such a text appears in the case of a latent marking [33], specifically, when a text is written with a "magnetic paint" on a nonmagnetic background of the same color. A text and an image may contain fragments that are drawn with both magnetic and ordinary paints of the same color and grade into one another (a $100 banknote is an example). In this case, the use of magnetooptic visualization of spatially nonuniform magnetic fields is appropriate both for developing and controlling printing processes and for revealing counterfeit banknotes.

The main difference between magnetically soft and magnetically hard materials is that, in the normal state, the former do not produce stray fields, since the magnetic flux closes inside a magnet. Stray fields, however, arise if a magnetically soft sample is duly magnetized (magnetically "illuminated"). If the field required for this purpose is significantly lower than the field of

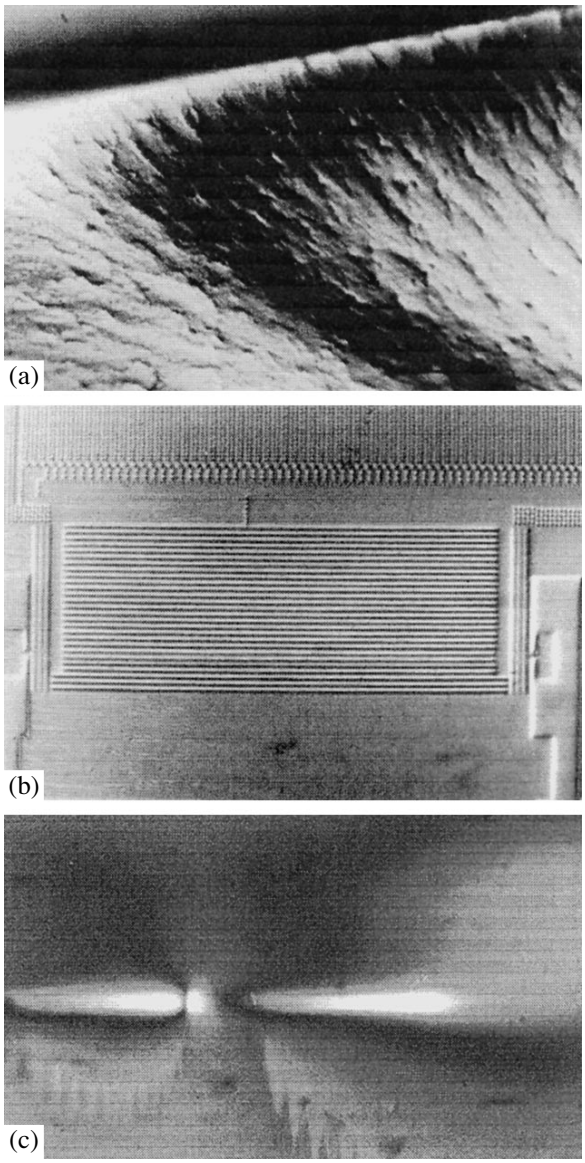

Fig. 5. Magnetooptic images of the (a) edge of a magnetically soft material, (b) magnetic path and gap of a record head for hard disk recording, and (c) bubble chip expander. Visualization with the use of the magnetically illuminated film of type II.

uniaxial anisotropy for the films of type I, then the domain structure of a defect-free magnetically soft material remains unchanged. Conversely, the rearrangement of domains indicates the presence of defects. With the films of type II, defects show themselves through the local variation in the Faraday rotation angle.

Figure 5a shows the magnetooptic image of the edge of a piece of a magnetically soft material. Stray fields were observed under the constant field 150 Oe. They arise at the edges and in the vicinity of defects and are visualized with a BcSCGF film. The areas of different contrast in Fig. 5a correspond to yellow, green, and dark brown colors in the color magnetooptic image. This variation of contrast suggests that the magnetic properties of the sample are nonuniform.

"Magnetic illumination," as applied to BcSCGF films, seems to be promising for the control of magnetic head manufacturing and positioning. By way of example, Fig. 5b shows the magnetooptic image of the magnetic path and head gap for hard disk recording. The irregularity and asymmetry of the image, specifically beard-like domains near the magnetic path, point to head faults and misarrangement.

Fig. 5c shows the magnetooptic image of a 256-kbit bubble chip expander. Control elements of the bubble chip are made of magnetically soft permalloy. The stray fields, which are produced at the edges of the permalloy elements by "magnetic illumination," are visualized by using the film of type II. As a consequence, these elements become visible.

The high sensitivity of the BcSCGFFs is demonstrated by the fact that 3-μm-wide domains are seen in the color image of the bubble film (saturation magnetization is $4\pi M_s$ = 320 Gs). Recall that this film and BcSCGFF are separated by the several protective layers and the mirror layer (in the black-and-white image, this faint contrast is lost). In other words, the films of type II enable the magnetization control of various magnetic substances that do not possess magnetooptic properties.

The magnetooptic images presented in Figs. 2–5 by no means exhaust the capabilities of the films of type II in the magnetooptic visualization of nonuniform magnetic fields. Yet, they give an idea of the range of the intensities and characteristic spatial dimensions of nonuniform magnetic fields that can be visualized with the films of type II. It is obvious that the use of the same BcSCGFF to solve many problems, even if possible, is unjustified. For every specific problem, it is advantageous to select the film with an optimal set of properties. This can be done because of the unique possibility of modifying the BcSCGFF composition. In particular, the presence of three cation interstices of different size allows more than half of the known chemical elements to be incorporated into the film, thus providing a variety of its properties [34–37].

REFERENCES

1. V. V. Randoshkin and A. Ya. Chervonenkis, *Applied Magnetooptics* (Énergoatomizdat, Moscow, 1990).
2. N. F. Kubrakov, A. Ya. Chervonenkis, G. Ya. Merkulova, *et al.*, Zh. Tekh. Fiz. **54**, 1163 (1984) [Sov. Phys.—Tech. Phys. **29**, 662 (1984)].
3. A. Ya. Chervonenkis, N. F. Kubrakov, N. G. Svenskiĭ, and T. P. Kisileva, USSR Inventor's Certificate No. 1072095, Byull. Izobret., No. 5 (1984).
4. N. F. Kubrakov, A. Ya. Chervonenkis, and M. V. Kashcheev, Zh. Tekh. Fiz. **56**, 1215 (1986) [Sov. Phys.—Tech. Phys. **31**, 714 (1986)].
5. N. F. Kubrakov, Proc. SPIE **1126**, 85 (1989).

6. A. V. Antonov, M. V. Gusev, E. I. Il'yashenko, and L. S. Vomov, in *Program and Abstract of the International Symposium on Magnetooptics, Kharkov, 1991*, p. 70.
7. V. L. Gribkov, N. N. Kirukhin, V. A. Liskov, *et al.*, in *Advances in Magnetooptics II, Proceedings of the 2nd International Symposium on Magnetooptics*; Fiz. Nizk. Temp., Suppl. S1 **18**, 429 (1992).
8. N. F. Kubrakov, *Single-Crystal Garnet Ferrite Films and Their Application* (Nauka, Moscow, 1992), pp. 136–164.
9. V. V. Randoshkin and M. V. Logunov, Pis'ma Zh. Tekh. Fiz. **19** (6), 62 (1993) [Tech. Phys. Lett. **19**, 182 (1993)].
10. V. V. Randoshkin and V. N. Dudorov, Pis'ma Zh. Tekh. Fiz. **19** (22), 79 (1993) [Tech. Phys. Lett. **19**, 731 (1993)].
11. V. V. Randoshkin and M. V. Logunov, Pis'ma Zh. Tekh. Fiz. **20** (5), 17 (1994) [Tech. Phys. Lett. **20**, 182 (1994)].
12. A. A. Aĭrapetov, V. L. Gribkov, A. P. Gubarev, *et al.*, International Patent Appl. PCT/RU92/00210 (1999), Bull. PCT, No. WO 93/11427.
13. M. V. Logunov and V. V. Randoshkin, USSR Patent No. 1813217, Byull. Izobret., No. 16 (1993).
14. M. V. Logunov and V. V. Randoshkin, USSR Inventor's Certificate No. 1824619, Byull. Izobret., No. 24 (1993).
15. M. V. Logunov and V. V. Randoshkin, RF Patent No. 2017182, Byull. Izobret., No. 14 (1994).
16. A. A. Aĭrapetov, V. L. Gribkov, V. A. Lyskov, *et al.*, RF Patent No. 2002247, Byull. Izobret., Nos. 39–40 (1993).
17. A. A. Aĭrapetov, V. L. Gribkov, V. A. Lyskov, *et al.*, RF Patent No. 2011187, Byull. Izobret., No. 7 (1994).
18. V. L. Gribkov, V. V. Randoshkin, and A. Ya. Chervonenkis, RF Patent No. 2022365, Byull. Izobret., No. 20 (1994).
19. V. V. Randoshkin, Defektoskopiya, No. 11, 34 (1994).
20. M. V. Logunov and V. V. Randoshkin, RF Patent No. 2047170, Byull. Izobret., No. 30 (1995).
21. R. M. Grechishkin, V. Yu. Goosev, S. E. Il'yashenko, and N. S. Neustroev, J. Magn. Magn. Mater. **157/158**, 305 (1996).
22. A. Ya. Chervonenkis, A. P. Gubarev, N. N. Kiryukhin, *et al.*, in *Proceedings of the XV All-Russia Seminar "New Magnetic Materials for Microelectronics," Moscow, 1996*, pp. 182–183.
23. A. A. Aĭrapetov, V. L. Gribkov, A. P. Gubarev, *et al.*, RF Patent No. 2060491, Byull. Izobret., No. 14 (1997).
24. V. V. Randoshkin, RF Patent No. 2047170, Byull. Izobret., No. 23 (1997).
25. V. V. Randoshkin, RF Patent No. 2092832, Byull. Izobret., No. 28 (1997).
26. R. M. Grechishkin, M. Yu. Gusev, N. S. Neustroev, *et al.*, in *Proceedings of the XVI International Seminar "New Magnetic Materials for Microelectronics", Moscow, 1998*, pp. 445–446.
27. B. S. Vvedenskiĭ, F. V. Lisovskiĭ, and A. Ya. Chervonenkis, Tekh. Kino Telev., No. 6, 11 (1978).
28. A. Ya. Chervonenkis and N. F. Kubrakov, Pis'ma Zh. Tekh. Fiz. **8**, 696 (1982) [Sov. Tech. Phys. Lett. **8**, 303 (1982)].
29. A. K. Zvezdin and V. A. Kotov, *Magnetooptics of Thin Films* (Nauka, Moscow, 1988).
30. S. V. Gerus, S. V. Lisovskiĭ, and E. G. Mansvetova, Mikroélektronika **10**, 506 (1981).
31. A. H. Eschenfelder, *Magnetic Bubble Technology* (Springer-Verlag, Berlin, 1980; Mir, Moscow, 1983).
32. *Bubble-Based Elements and Devices: Reference Book*, Ed. by N. N. Evtikhiev and B. N. Naumov (Radio i Svyaz', Moscow, 1987).
33. A. Ya. Chervonenkis, A. P. Gubarev, N. N. Kiryukhin, *et al.*, in *Proceedings of the XV All-Russia Seminar "New Magnetic Materials for Microelectronics," Moscow, 1996*, pp. 182–183.
34. V. V. Randoshkin, *Single-Crystal Garnet Ferrite Films and Their Application* (Nauka, Moscow, 1992), pp. 49–107.
35. A. M. Balbashov and A. Ya. Chervonenkis, *Magnetic Materials for Microelectronics* (Énergiya, Moscow, 1979).
36. V. V. Randoshkin and A. Ya. Chervonenkis, in *Radioelectronics: The Current Status and Prospects* (NIIÉIR, Moscow, 1985), Vol. 2, pp. 71–78.
37. V. V. Randoshkin, Defektoskopiya, No. 6, 58 (1997).

Translated by A. Sidorova

Technical Physics, Vol. 45, No. 8, 2000, pp. 1081–1084. Translated from Zhurnal Tekhnicheskoĭ Fiziki, Vol. 70, No. 8, 2000, pp. 125–128.

BRIEF COMMUNICATIONS

Local Plasma Parameters and Integral Characteristics of a Magnetogasdynamic Channel under Conditions of Ionization Instability

R. V. Vasil'eva, E. A. D'yakonova, A. V. Erofeev, and T. A. Lapushkina

Ioffe Physicotechnical Institute, Russian Academy of Sciences, Politekhnicheskaya ul. 26, St. Petersburg, 194021 Russia

Received July 16, 1999

Abstract—Results are presented from an experimental investigation of the onset of ionization instability in a disk-shaped Faraday magnetogasdynamic channel attached to a shock tube. The experiments were carried out in a pure inert gas (xenon) without alkaline additives. A relation is found between the integral plasma characteristics of a nonequilibrium magnetogasdynamic channel and the local parameters of a plasma that is unstable against the ionization instability. Mechanisms for amplifying perturbations and increasing the effective conductivity are revealed. It is concluded that these effects stem mainly from the features of three-body recombination in rare gases. © *2000 MAIK "Nauka/Interperiodica".*

The goal of this paper is to develop a self-consistent physical model that accounts for the effect of an increase in the effective conductivity during the onset of the ionization instability in pure inert gases. The model is based on the measurements of the local plasma parameters and exploration of the structure of plasma irregularities.

The experimental facility (see [1, 2]) consists of a shock tube with a disk-shaped 32-cm-diameter and 1-cm-high magnetogasdynamic (MGD) channel. The magnetic induction is up to 1.4 T. Experiments were carried out in xenon at an incident shock wave Mach number of 6.9 and initial pressure of 26 torr. At the entrance to the disk channel, plasma parameters were as follows: r = 0.04 m, $u_0 = 1.27 \times 10^3$ m/s, ρ_0 = 0.45 kg/m^3, T_{a0} = 2600 K, T_{e0} = 3100 K, $\alpha_0 = 2.6 \times 10^{-4}$, and M = 2.45. A circular Faraday current and radial Hall field were induced in the disk channel. The channel operated either in a short-circuit Faraday channel mode or with a narrow insert shaped as a sector with three pairs of electrodes for connecting load resistors. The load coefficient was varied within the $0 < k < 0.2$ range.

The methods for determining the parameters of the gas-dynamic stream; measuring the effective plasma conductivity, the Hall parameter, the electron density and temperature, and the value of the magnetic induction B_{cr} that is critical for the onset of the ionization instability; and recording glow irregularities are described in [1–5].

The main results of the previous studies [1–3] used in this paper are the following. At $B > B_{cr}$, the effective plasma conductivity, the average electron density, and the level of the electron density fluctuations grow as the plasma moves along the channel. An increase in the magnetic induction results in an increase in these parameters.

The experimental results show that the ratio between the electron temperature T_e and the temperature of the heavy plasma component T_g attains $T_e/T_g = 4$. At $B = 0$, the plasma is in the recombination state ($\alpha > \alpha_{eq}$), whereas with selective heating of electrons in an induced electric field, the degree of ionization α is below the equilibrium value (both in the initial state and in the presence of fluctuations); i.e., in the MGD mode, the plasma is being ionized ($\alpha < \alpha_{eq}$). The degree of ionization is high enough ($\alpha > 10^{-4}$) for the electron velocity distribution to be considered Maxwellian. A characteristic feature of the plasma is that an increase in the magnetic field leads to an increase in the degree of ionization; as a result, the ratio between the electron–neutral and electron–ion collision frequencies,

$$\nu_{ea} = n_a c_e Q_{ea}, \quad \nu_{ei} = n_e c_e Q_{ei}$$

changes. Here, n_a and n_e are the densities of atoms and ions, respectively; c_e is the average electron velocity; and Q_{ea} and Q_{ei} are the cross sections (averaged over the Maxwellian distribution) for the electron momentum transfer in collisions with atoms and in Coulomb collisions, respectively. Under our experimental conditions, we have $0.2 < \nu_{ei}/\nu_{ea} < 1$. In this case, the collision frequency depends not only on the electron temperature and atom density, but also on the electron density. The main distinguishing feature of a rare-gas plasma is a fairly low recombination coefficient K_r. This feature stems from a specific structure of energy

1063-7842/00/4508-1081$20.00 © 2000 MAIK "Nauka/Interperiodica"

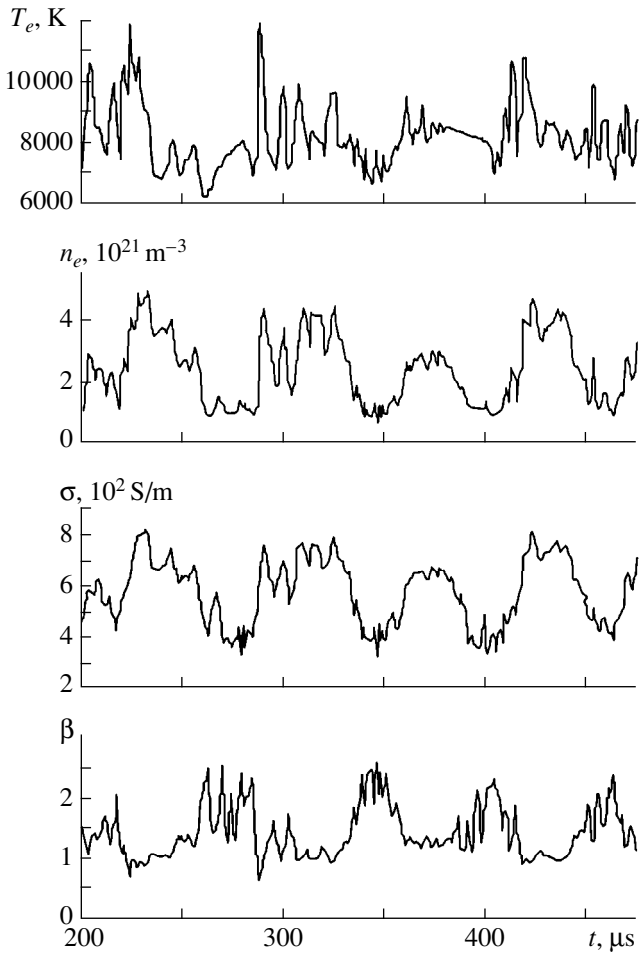

Fig. 1. Time evolutions of the measured electron temperature and density and the calculated conductivity and Hall parameter at $B = 1$ T and $r = 0.09$ m.

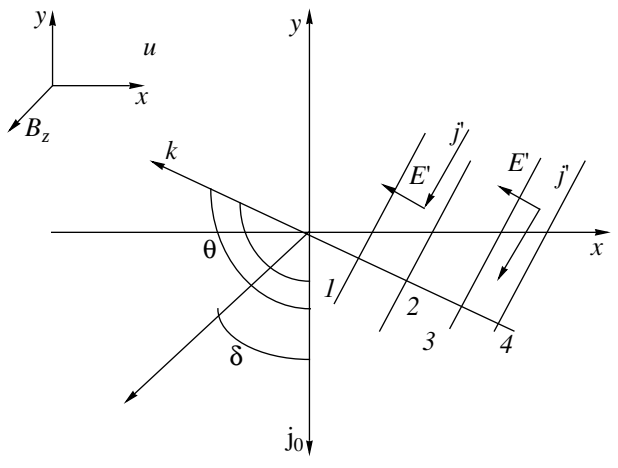

Fig. 2. Schematic diagram of current and field fluctuations under conditions of the ionization instability.

levels. Thus, at $T_e = 8000$ K, the value of K_r for alkali metals equals 5×10^{-39} m^6/s, whereas for rare gases, $K_r = 5 \times 10^{-41}$ m^6/s.

Figure 1 presents the typical time behavior of the local plasma parameters at a fixed point of the channel ($r = 0.09$ m) during the onset of the ionization instability. In the experiment, we measured the electron temperature and density. Both the conductivity and the Hall parameter were deduced from the measured values of T_e and n_e and the known density of atoms (at $B = 0$, $n_a = 10^{24}$ m^{-3}). Low-frequency fluctuations with a duration of 20–50 μs are seen in the dependences $T_e(t)$ and $n_e(t)$. There, fluctuations are caused by plasma processes. Higher frequency oscillations with a period of less than 5 μs are likely attributed to a photomultiplier noise. For this reason, below, we only consider low-frequency oscillations. Note that the intervals with higher (lower) values of T_e correspond to the intervals with higher (lower) values of the electron density and conductivity. The Hall parameter varies in the opposite phase with the conductivity, because Coulomb collisions play an important role under given conditions and the momentum transfer rate increases with an increase in the electron density. Based on the above dependences, we can find the average values $\langle T_e \rangle$, $\langle n_e \rangle$, $\langle \sigma \rangle$, and $\langle \beta \rangle$. However, they do not clarify how the fluctuations with respect to the average values are related to those with respect to the initial, unperturbed plasma parameters. Therefore, the role of positive and negative perturbations in the build-up of oscillations should be revealed.

The irregularities are oriented in space in a definite manner. This was found by a frame-by-frame imaging of the plasma glow [2]. The glowing irregularities turned out to be shaped as spokes inclined at an angle of 20° with respect to the azimuthal direction. The propagation velocity of the spokes was on the order of the flow velocity as if the they were "frozen" in the flow. As a spoke moves, the brightness of its glow increases. On average, there are two spokes in the channel simultaneously. They arise with definite time intervals. At radii much greater than the initial radius, the glowing spokes can be approximately represented as strips in rectangular coordinates (Fig. 2). In the disk geometry, the φ and r directions correspond to the y and x directions, respectively. Figure 2 displays the coordinate system and the vectors of the initial current j_0 and the initial electric field E_0^* in the plasma. Here, $\tan\delta = \beta$, and θ is the angle between the current and the normal to the sheet plane ($\pi/2 < \theta < \pi$). We denote the changes in the main plasma parameters as $j' = j - j_0$, $\sigma' = \sigma - \sigma_0$, $\beta' = \beta - \beta_0$, $T_e' = T_e - T_{e0}$, and $n_e' = n_e - n_{e0}$ (subscript 0 stands for the parameter values in the unperturbed surrounding medium). In [6, 7], it was shown that, in an unbounded plasma, the fluctuations of the current and electric field are related to the fluctuations of conductivity and the Hall parameter as follows:

$$j' = J_0(\sin\theta - \beta\cos\theta)\frac{\sigma'}{\sigma_0} + J_0\beta'\cos\theta, \qquad (1)$$

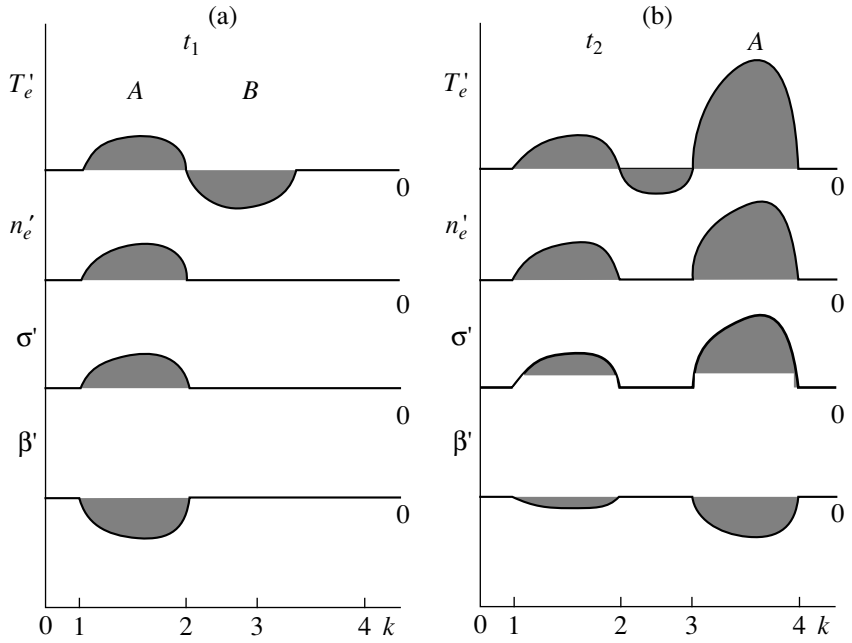

Fig. 3. Illustration of the mechanism for amplifying positive electron density perturbations.

$$\pm E' = -\frac{1+\beta_0^2}{\sigma_0^2} J_0 \cos\theta \frac{\sigma'}{\sigma_0} + \frac{J_0}{\sigma_0}(\sin\theta + \beta_0 \cos\theta)\beta'. \quad (2)$$

Here, the plus sign is used if the vectors E and k are of the same direction and the minus sign is used in the opposite case.

Therefore, positive fluctuations of σ and negative fluctuations of β lead to an increase in the electric field and a fluctuation current in the direction of j_0. The perturbations of the main plasma parameters along the normal to the observed irregularities are shown schematically in Fig. 3. The numerals stand for certain dimensionless distances along the normal corresponding to those in Fig. 2. Let us trace the evolution of positive and negative fluctuations of the electron density and temperature. Let the fluctuation of T_e shown in Fig. 3a occur at the instant t_1. According to the ionization kinetics [8], the higher the electron temperature, the higher the electron density in region *A* (under our experimental conditions, the characteristic ionization time is about (1–5) × 10^{-5} s). In region *B*, where the electron temperature is decreased, the electron density decreases only slightly with respect to the initial value because of the low rate of three-body recombination in rare gases (under our experimental conditions, the characteristic recombination time is about 10^{-1} s). Accordingly, in region *A*, the conductivity increases, whereas in region *B*, it remains almost the same. The change in the Hall parameter may be opposite in phase to the change in the conductivity σ', as shown in Fig. 3a. A positive change in σ and a negative change in β in region *A* result in an increase in the fluctuation current, which adds to the initial current, thus providing an additional Joule heating and increasing the electron temperature and density. Therefore, positive perturbations of T_e and n_e are increasing, whereas negative ones have no chance to rise. Indeed, let us assume that a negative fluctuation of n_e has occurred. This would lead to a decrease in the conductivity and, according to formula (1), a decrease in the current, which, in turn, would result in a decrease in the Joule heating and T_e, but not in a further drop in n_e.

During the time interval between t_1 and t_2, the plasma volume *A* moves along the channel from region 1–2 to region 3–4 (Fig. 3b). During this time, positive perturbations of T_e, n_e, and σ and negative perturbations of β further develop and a new fluctuation arises in region 1–2.

In a bounded plasma, the structure of fluctuation currents will be different compared to that in Fig. 2. The current distributions in a Faraday channel with perfectly sectionalized electrodes were calculated in [6, 7]. It was shown in those papers that the Faraday current flowing along the isolines of the electron density closes mainly via the electrodes and partly inside the plasma. All of this influences the effective values of the conductivity and the Hall parameter. Here, we define the effective conductivity σ_{eff} and the effective Hall parameter β_{eff} as follows:

$$\sigma_{\text{eff}} = \langle j_\varphi \rangle / (uB), \quad (3)$$

$$\beta_{\text{eff}} = \langle E_r \rangle / (uB), \quad (4)$$

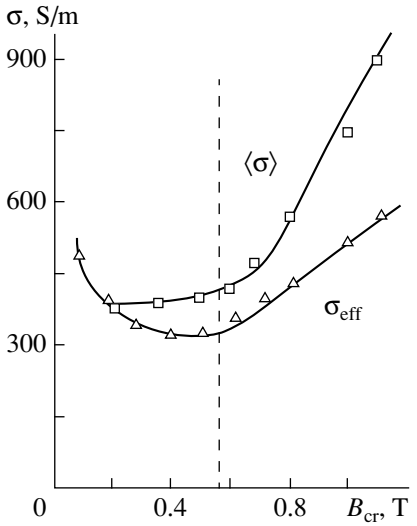

Fig. 4. Dependences of the average conductivity $\langle\sigma\rangle$ (□) and effective conductivity σ_{eff} (△) on the magnetic induction.

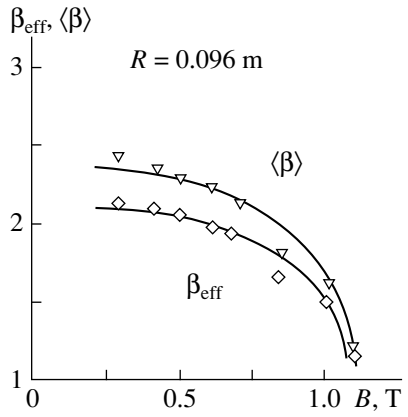

Fig. 5. Dependences of the average (▽) and effective (◇) values of the Hall parameter on the magnetic induction.

where $\langle j_\varphi\rangle$ is the azimuth current density at the load coefficient $k \longrightarrow 0$.

In essence, the values of σ_{eff} and β_{eff} are the integral characteristics of the MGD channel.

The dependences of the average and effective conductivities on the magnetic induction are shown in Fig. 4. Being close to each other at $B < B_{cr}$, both $\langle\sigma\rangle$ and σ_{eff} increase with an increase in the magnetic induction. This is caused by the increase in both σ_0 (due to selective electron heating) and positive perturbations of σ (due to the onset of the ionization instability). At the highest value of the magnetic induction, the effective conductivity is somewhat less than the average conductivity ($\sigma_{eff}/\langle\sigma\rangle = 0.7$), which is due to a partial closing of fluctuation currents inside the plasma.

Figure 5 presents the average and effective values of the Hall parameter. Their decrease with an increase in the magnetic induction is caused by an increase in the electron density and a subsequent increase in the Coulomb collision frequency and the average momentum transfer rate. As a result, the Hall parameter decreases in both the irregularities and the surrounding medium. As is seen from Fig. 5, the values of β and β_{eff} are nearly the same. According to theoretical predictions, this can occur if the irregularity direction is close to that of the initial current [7]. Under our experimental conditions, which correspond to $\langle\beta\rangle = \beta_{eff}$, irregularities in the shape of the spokes are only slightly inclined to the azimuthal direction, the instability develops at moderate values of $\beta \approx 1$–2, the fluctuations in the Hall parameter attain 40%, and the momentum transfer rate depends on the plasma parameters in a complicated way.

The results obtained can be summarized as follows: (i) a relation between the local plasma parameters and the integral characteristics of an MGD channel is established, (ii) mechanisms for amplifying perturbations and increasing the effective conductivity under conditions of the ionization instability are revealed, and (iii) it is shown that these effects stem mainly from the features of three-body recombination in rare gases.

REFERENCES

1. R. V. Vasil'eva, A. L. Genkin, V. L. Goryachev, *et al.*, *Low-Temperature Nonequilibrium-Ionization Plasma of Inert Gases and MHD Generators* (Ioffe Physicotechnical Inst., St. Petersburg, 1991), p. 206.
2. T. A. Lapushkina, R. V. Vasil'eva, A. V. Erofeev, and A. D. Zuev, Zh. Tekh. Fiz. **67** (12), 12 (1997) [Tech. Phys. **42**, 1381 (1997)].
3. R. V. Vasil'eva, A. V. Erofeev, D. N. Mirshanov, and T. A. Alekseeva, Zh. Tekh. Fiz. **59** (7), 27 (1989) [Sov. Phys. Tech. Phys. **34**, 728 (1989)].
4. T. A. Lapushkina, E. A. D'yakonova, and R. V. Vasil'eva, Pis'ma Zh. Tekh. Fiz. **24** (2), 58 (1998) [Tech. Phys. Lett. **24**, 66 (1998)].
5. A. V. Erofeev, R. V. Vasil'eva, A. D. Zuev, *et al.*, in *Proceedings of the 12th International Conference on MHD Electrical Power Generation, Japan, 1996*, vol. 1, p. 74.
6. A. V. Nedospasov and V. D. Khait, *Principles of Physical Processes in Low-Temperature Plasma Devices* (Énergoatomizdat, Moscow, 1991).
7. L. A. Vulis, A. L. Genkin, and B. A. Fomenko, *The Theory and Analysis of Magnetogasdynamic Flows in Channels* (Atomizdat, Moscow, 1971).
8. L. M. Biberman, V. S. Vorob'ev, and I. T. Yakubov, *Kinetics of Nonequilibrium Low-Temperature Plasmas* (Nauka, Moscow, 1982; Consultants Bureau, New York, 1987).

Translated by N. N. Ustinovskiĭ

Technical Physics, Vol. 45, No. 8, 2000, pp. 1085–1087. Translated from Zhurnal Tekhnicheskoĭ Fiziki, Vol. 70, No. 8, 2000, pp. 129–132.

BRIEF COMMUNICATIONS

Free-Running Emerald Laser

V. V. Antsiferov

Institute of Nuclear Physics, Siberian Division, Russian Academy of Sciences, pr. Akademika Lavrent'eva 11, Novosibirsk, 630090 Russia

E-mail: vita@stu.ru

Received July 20, 1999

Abstract—The spectral and energy characteristics of an emerald laser are studied experimentally. Its performance is compared with that of an alexandrite laser. For free-running oscillation under normal conditions, undamped pulsating behavior of output intensity is observed, as is the case with other lasing media containing Cr ions. © *2000 MAIK "Nauka/Interperiodica".*

INTRODUCTION

Lasing due to the ${}^4T_2 \longrightarrow {}^4A_2$ electronic vibrational transitions in Cr^{3+} ions of emerald was first reported in [1]. Next were studies of tunable emerald lasers, which used the ${}^4T_2 \longrightarrow {}^4A_4$ transition and laser pumping [2–4] or the *R*-lines of Cr^{3+} [4, 5]. Energy characteristics of a flashlamp-pumped laser with a flux-grown crystal were presented in [6].

Emerald, or chromium-doped beryl Cr^{3+} : $Be_3Al_2(SiO_3)_6$, is a negative uniaxial crystal with refractive indexes $n_0 = 1.58$ and $n_e = 1.575$. The crystal is green when the concentration of Cr^{3+} is 0.01–1%. The melting point is 1470°C, which is 400°C lower than that of alexandrite. The thermal conductivity of emerald is 0.04 W cm^{-1} deg^{-1}, being nearly six times less than that of alexandrite. Emerald crystals are grown by the hydrothermal or flux method. The latter yields crystals with a higher optical quality and lower impurity content. The nonselective loss of hydrothermally grown crystals is of the order of 0.1 cm^{-1}.

In an emerald laser, lasing due to the ${}^4T_2 \longrightarrow {}^4A_2$ electronic vibrational transitions occurs in the 700–850 nm range. The energy gap between the ${}^4T_2$ and ${}^2E$ levels of Cr^{3+} is 400 cm^{-1}, being half as high as that of alexandrite. At room temperature, the lifetime of the excited state of Cr^{3+} is 65 μs and the transition cross section σ is 3.3×10^{-20} cm^2.

Optical absorption spectra of emerald (Fig. 1) are typical of Cr^{3+} ions enclosed by the octahedral configuration of oxygen ions. The wide bands in the blue and red (*Y, U*) regions represent the allowed transitions ${}^4A_2 \longrightarrow {}^4T_1$ and ${}^4A_2 \longrightarrow {}^4T_2$, respectively. The triplet levels are split by the trigonal component of the crystal field, hence the differences in the π and σ components. The narrow absorption lines at 681 and 684 nm stem from the spin-forbidden transitions ${}^4A_2 \longrightarrow {}^2E$ (the R_1 and R_2 lines). The fine structure of the *U* band is due to electron–phonon interaction. Compared with alexandrite, emerald has a more complex crystal structure and a weaker crystal field, the latter being indicated by the position of the *U* band. The crystal field of emerald is $D_q = 1600$ cm^{-1} (for alexandrite, $D_q = 1740$ cm^{-1}).

In emerald, strong ultraviolet (UV) absorption arises at shorter wavelengths, than in alexandrite, namely in the 300-nm band for flux-grown crystals and in the 360-nm band for hydrothermally grown ones; in the latter case, there are additional bands in the 380–450 nm region. Short-wave absorption of emerald proceeds mainly from impurities, especially from iron. The iron content is 0.001 wt % in flux-grown crystals and 0.1 wt % in hydrothermally grown ones.

In luminescence spectra of Cr^{3+} ions of emerald (Fig. 2), the most noticeable component is the wide

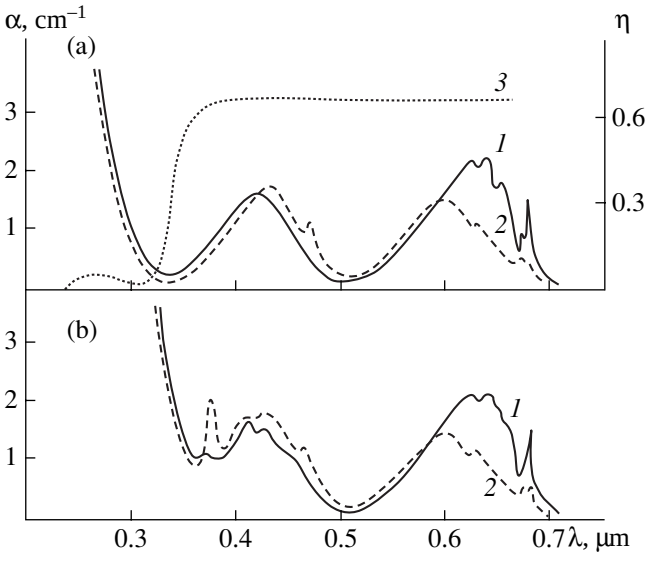

Fig. 1. Optical properties of (a) flux-grown and (b) hydrothermally grown emerald crystals at $T = 300$ K: the absorptance α for (*1*) $E \parallel C$ and (*2*) $E \perp C$ and (*3*) the luminescence quantum yield η vs. wavelength.

1063-7842/00/4508-1085$20.00 © 2000 MAIK "Nauka/Interperiodica"

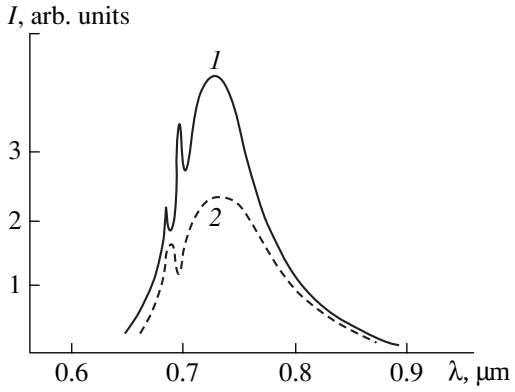

Fig. 2. Emerald luminescence intensity vs. wavelength at $T = 300$ K for (*1*) $E \parallel C$ or (*2*) $E \perp C$.

peak at 770 nm, corresponding to the ${}^4T_2 \longrightarrow {}^4A_2$ transition. The R_1 and R_2 lines are not so strong as in alexandrite because of the smaller energy gap, ΔE, between the levels ${}^2E$ and ${}^4T_2$. In emerald, the levels are near thermal equilibrium even at room temperature ($kT = 208$ cm^{-1}) and the metastable level ${}^2E$ is intensely depleted via the short-lived level ${}^4T_2$. In alexandrite, this occurs at higher temperatures, since its ΔE is as large as 800 cm^{-1}.

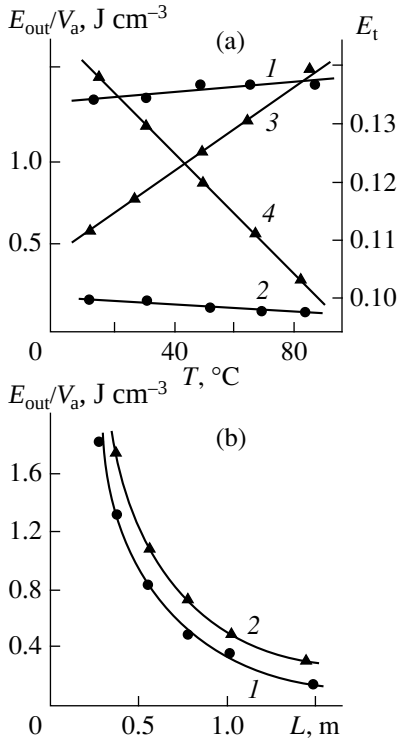

Fig. 3. (a) (*1*, *3*) Output energy density E_{out}/V_a and (*2*, *4*) threshold pump energy E_t vs. crystal temperature T for $E_p = 0.4$ kJ and $L = 0.4$ m and (b) output energy density vs. cavity length L for $E_p = 0.4$ kJ and $T = 70$°C. The emerald laser is represented by curves *1* and *2* in panel (a) and curve *1* in panel (b). The alexandrite laser is represented by curves *3* and *4* in panel (a) and curve *2* in panel (b).

The absolute quantum yield of Cr^{3+} luminescence is 0.7 for flux-grown emerald crystals and of the order of 0.01 for hydrothermally grown ones. The yield is flat in the absorption region of chromium ions, decreasing at wavelengths shorter than 380 nm. This testifies that Cr^{3+} ions are responsible for the short-wave absorption.

Emerald lasers have received only marginal application. It is difficult to produce emerald crystals of adequate size, since their growth rate is an order of magnitude less than that of alexandrite crystals. Another demerit is the toxicity of beryllium.

EXPERIMENTAL SETUP

In this study, we tested a 3 × 35-mm flux-grown emerald crystal [7] with an active volume V_a of 0.21 cm^3 and a Cr^{3+} concentration of 0.7 wt %. The end faces of the crystal were beveled (the bevel was one degree) and supplied with antireflection coatings. The laser was pumped by an ISP-250 flashlamp in a monoblock quartz clarifier. The UV pump radiation was cut off by a liquid filter. The energy characteristics were

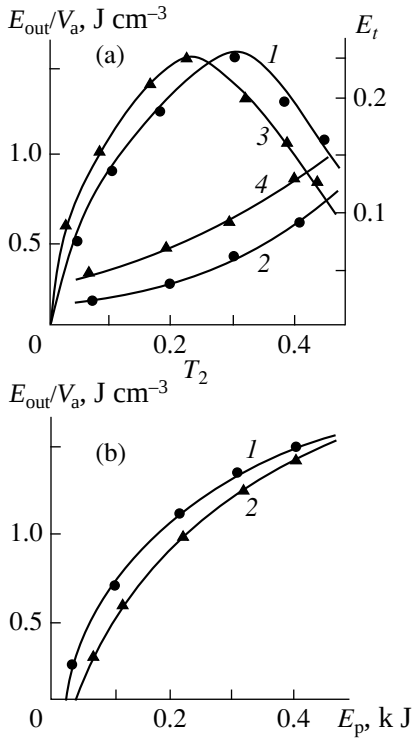

Fig. 4. (a) (*1*, *3*) Output energy density E_{out}/V_a and (*2*, *4*) threshold pump energy E_t vs. output-mirror transmittance T_2 for $E_p = 0.4$ kJ, $L = 0.4$ m, and $T = 70$°C. (b) Output energy density vs. pump energy E_p for $L = 0.4$ m and $T = 70$°C. The emerald laser is represented by curves *1* and *2* in panel (a) and curve *1* in panel (b). The alexandrite laser is represented by curves *3* and *4* in panel (a) and curve *2* in panel (b).

compared with those of an alexandrite laser [8–10] operated under similar conditions.

Lasing was examined with a photodiode and an oscilloscope. The output spectrum was recorded with an STÉ-1 spectrograph, and the output energy was measured with an IMO-2 meter.

OUTPUT-ENERGY AND SPECTRUM CHARACTERISTICS

Figure 3 shows the output-energy density E_{out}/V_a against (a) the crystal temperature T or (b) cavity length L. The emerald laser is represented by curves *1* and *2* in Fig. 3a and curve *1* in Fig. 3b. The alexandrite laser is represented by curves *3* and *4* in Fig. 3a and curve *2* in Fig. 3b. It is seen that the output of the emerald laser is much less sensitive to temperature variation (Fig. 3a). The reason is that, in emerald, the energy gap between the metastable ^2E and upper $^4T_2$ levels is much narrower and the latter becomes populated even at room temperature. The dependence on cavity length is stronger for the emerald laser (Fig. 3b) due to the much lower thermal conductivity of the medium. As is known, a positive spherical thermal lens arises in lasing solids under flashlamp pumping, which is equivalent to replacing a flat cavity with a spherical one. The focal length of the thermal lens is much smaller in emerald. That is why the cavity of an emerald laser becomes unstable at a smaller length, hence a more prominent and sharper fall in the output energy.

We also compared the dependences of the output energy on the transmittance T_2 of the output mirror at the pump energy $E_p = 0.4$ kJ (Fig. 4a). The emerald laser was found to attain its maximum output energy at the higher T_2. The threshold pump energy E_t of the emerald laser was much lower throughout the range of T_2.

The output energy was also studied as a function of E_p at optimal T_2's (Fig. 4b). A nonlinear rise was observed for both lasers, except for small values of E_p. The output energy of the emerald laser increased more steeply at modest E_p's and saturated more rapidly at high E_p's, so that the output energy densities of the lasers at $E_p = 0.5$ kJ were nearly equal. This stems from more severe strains in the emerald crystal.

For the emerald laser, the spectra of the TEM_{mnq} modes (Fig. 5) were virtually the same as those for the alexandrite laser [9]. The lasers exhibited a fine discrete spectral structure. This stems from spurious longitudinal-mode selection, no matter how weak it is, imparted by the beveled and coated end faces. At room temperature and moderate values of E_p, the emerald laser emitted in a wide wavelength band with the maximum at 770 nm. As E_p grew, the output spectrum broadened predominantly toward shorter wavelengths. An eightfold increase in E_p above the threshold resulted in an output bandwidth of about 20 nm. The bandwidth was an almost linear function of E_p.

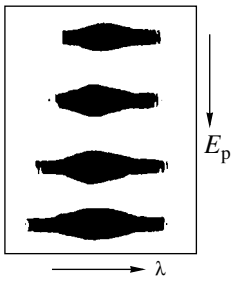

Fig. 5. TEM_{mnq} mode spectra of the emerald laser at T = 20°C for pump energies E_p = 3, 4, 6, and 8 E_t (from the top down).

The laser was tuned by means of a dispersive cavity with three prisms made of TF-5 glass. The total angular dispersion was about 3′/nm. The tuning range was 710–830 nm, the output wavelength being stable within ~1 nm.

For the TEM_{ooq} and TEM_{mnq} modes of the emerald laser, its output always has the form of undamped oscillation, as is the case with other lasing media containing Cr ions. The evolution of the output spectrum depended on the physical state of the emerald crystal and was affected by the spurious longitudinal-mode selection in the cavity, as in the case of the alexandrite laser. With partial cutoff of UV pump radiation, the spectral evolution changed materially.

REFERENCES

1. M. L. Shand and J. C. Walling, IEEE J. Quantum Electron. **18**, 1829 (1982).
2. J. Buchert and R. R. Alfano, Laser Focus, No. 9, 117 (1983).
3. M. L. Shand and S. T. Lai, IEEE J. Quantum Electron. **20**, 105 (1984).
4. J. Buchert, A. Katz, and R. R. Alfano, IEEE J. Quantum Electron. **19**, 1477 (1983).
5. Z. Hasan, S. T. Keany, and N. B. Manson, J. Phys. C **19**, 6381 (1986).
6. V. S. Gulev, A. P. Eliseev, V. P. Solntsev, *et al.*, Kvantovaya Élektron. (Moscow) **14**, 1990 (1987).
7. V. V. Antsiferov and G. I. Smirnov, Preprint No. 98-97, IYaF Sib. Otd. RAN (Budker Institute of Nuclear Physics, Siberian Division, Russian Academy of Sciences, Novosibirsk, 1998).
8. V. V. Antsiferov, V. A. Kalyagin, G. V. Khaburzaniya, and A. V. Sharpov, Preprint No. 89-1, SFTI (Ioffe Physicotechnical Institute, Russian Academy of Sciences, St. Petersburg, 1989).
9. V. V. Antsiferov, A. I. Alimpiev, E. V. Ivanov, and G. V. Khaburzaniya, Zh. Tekh. Fiz. **62** (3), 9 (1992) [Sov. Phys. Tech. Phys. **37**, 239 (1992)].
10. V. V. Antsiferov, E. V. Ivanov, and G. I. Smirnov, Preprint No. 93-107, IYaF Sib. Otd. RAN (Budker Institute of Nuclear Physics, Siberian Division, Russian Academy of Sciences, Novosibirsk, 1993).

Translated by A. A. Sharshakov

Technical Physics, Vol. 45, No. 8, 2000, pp. 1088–1090. Translated from Zhurnal Tekhnicheskoĭ Fiziki, Vol. 70, No. 8, 2000, pp. 133–135.

BRIEF COMMUNICATIONS

Adiabatic Compression of Matter by a Shell

V. V. Prut

Russian Research Center Kurchatov Institute, pl. Kurchatova 1, Moscow, 123182 Russia

E-mail: prut@wowa.net.kiae.ru

Received August 4, 1999

Abstract—The problem of the spherical compression of condensed matter by a shell was solved in an incompressible medium approximation. Parameter values at the inner boundary of the shell are defined by the solution of a self-modeling problem. At collapse, the velocity and kinetic energy of the shell behave asymptotically. © *2000 MAIK "Nauka/Interperiodica".*

Matter compression by a spherical shell is considered under the assumption that the shell compressibility is much less than that of the matter. Such problems are of interest in the production and metrology of high energy densities, in particular, in treating target compression during inertial nuclear fusion. Let us simplify the problem by assuming the shell to be incompressible: $d\rho/dt = 0$. Then, shell motion is described by the ordinary differential equation

$$\rho_h\left(2r_1u_1^2 + r_1^2\frac{\partial u_1}{\partial t}\right)\left(\frac{1}{r_1} - \frac{1}{r_2}\right) + \frac{1}{2}(u_2^2 - u_1^2) = -p_2 + p_1;$$

$$r_1^2u_1 = r_2^2u_2; \quad \frac{4\pi}{3}(r_2^3 - r_1^3) = V_h,$$

where ρ_h is the shell density; V_h, its initial volume; r, radii; u, velocities; and p, the pressure at the shell boundaries. Subscripts 1 and 2 refer to the inner and outer boundaries, respectively. All parameters are taken as dimensionless with respect to the matter being compressed.

Parameter values at the inner boundary of the shell are defined by the solution of a self-modeling problem. The associated equations are derived from the mass and momentum conservation equations at constant entropy. A self-modeling variable is represented as $\xi = t/r$, and self-modeling functions will be denoted as $U = u\xi$ and $C = c\xi$, where u is the mass velocity and c is the sound adiabatic velocity. Time is counted backward from $t = 1$ (initial state) to $t = 0$ (collapse). Then, in terms of the independent variable C, the self-modeling mass and momentum conservation equations have the form

$$\partial\ln U/\partial\ln C = ((1-U)^2 - \nu C^2)/H,$$

$$\partial\ln\xi/\partial\ln C = ((1-U) - C^2)/H,$$

where $H = (1-U)(1-\eta U) - C^2$ and $\eta = (\nu - 1)(\gamma - 1)/2 + 1$. Here, $\nu = 1$, 2, and 3 for planar, cylindrical, and spherical space geometry, respectively, and $\gamma = \gamma(V)$ is defined by the equation of state. Acceleration is expressed as $\partial u_1/\partial t = (dU/dC - U\partial\ln\xi/\partial C)/(\xi dt/dC)$.

For γ = const, the self-modeling equations are split: we solve the first equation and then find ξ using quadrature. In the general case $\gamma \neq$ const, the equations must be solved jointly. The self-modeling problem specifies the piston path in such a way that the entire mass is isoentropically compressed to a point, i.e., to collapse. The self-modeling compression of the finite plasma mass by a piston (on condition that the equation of the perfect gas (plasma) state is $p = p_0\rho^\gamma$) was considered, e.g., in [1–12]. In this work, we suggest an equation of state of real gas. Namely, if the specific volume $V \longrightarrow 0$, the thermodynamic functions depend on the properties of perfect degenerate nonrelativistic electron gas. For the normal density, they depend on two experimental parameters: bulk modulus $B = -V(\partial p/\partial V)_s$ and exponent $\gamma = -(\partial\ln B/\partial\ln V)_s$. Cold pressure is introduced in the form

$$p = p_0(e^{-aV^\alpha}/V^{5/3} - e^{-a}),$$

where $p_0 = (2/5)c_F(Z/V_0)^{5/3}$ and Z is the atomic number. The constant $c_F = (3\pi^2)^{2/3}\hbar^2/2m_e$ enters into the Fermi energy according to the expression $\varepsilon_F = c_F n_e^{2/3}$.

We will use conventional designations: specific volume V, which is dimensionless relative to V_0; dimensionless density $\rho = 1/V$; and parameters p and B, dimensionless relative to B_0. Hence, at $V = 1$, the dimensionless sound velocity c equals 1.

The values of a and α were calculated from B_0 and γ_0 obtained from shock-wave and static measurements. In the former, B_0 and γ_0 are determined from the dependence of the shock wave velocity on mass $D \approx c_0 + D_1u$; at $V = 1$, $\gamma = 4D_1 - 1$. The value of B_0 varies between ~1 kbar (for hydrogen, its isotopes, and helium) and several megabars, and $3 \le \gamma \le 7$. Calculations of a and α indicated that the interpolation formula for $p(V)$ is well realizable throughout the range of B_0. Figure 1 shows the dimensionless dependences of B and γ on V for hydrogen. The transition from the initial value of γ

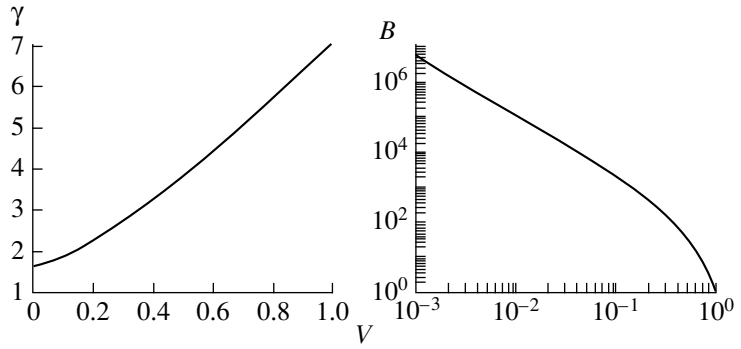

Fig. 1. γ and bulk modulus B vs. V.

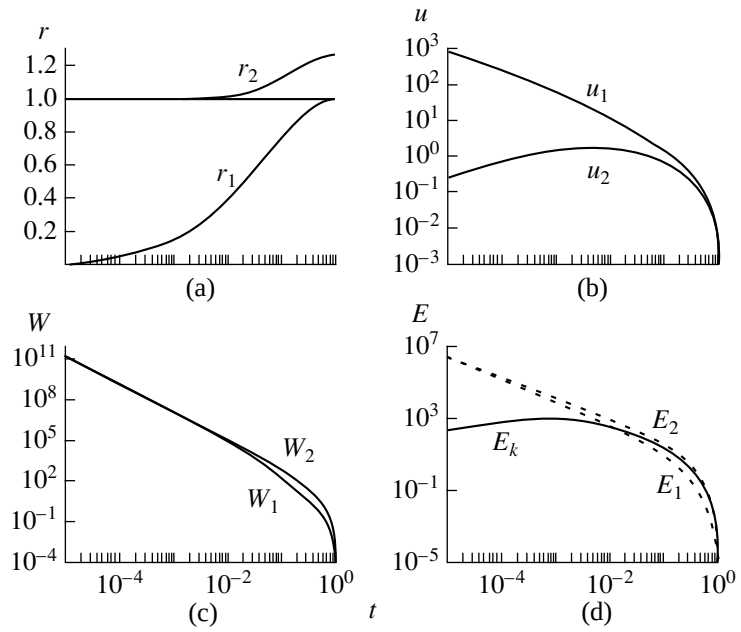

Fig. 2. Time dependences of (a) r, (b) u, (c) W, and (d) E for the inner and outer boundaries. Panel (d) also shows the variation of the shell kinetic energy E_k.

to its final value is observed at $\rho \cong 10$. The energy (per unit mass) is determined from the relationship $p = -(\partial e/\partial V)_z$ with a normalization $e(1) = 0$. At $V \ll 1$, the dimensionless sound velocity is $c^2 = c_\infty^2 \rho^{\gamma-1}$.

The desired integral curve must start and end on the (C, U) plane at singular points $N = (1, 0)$ (node) and $S = (C_s, U_s)$ (saddle). At S, $\xi = 0$, and at N, $\xi = 1$. At $\xi = 0$ or 1, $V = 0$ or 1, respectively. The parameters of singular points defined by $\gamma(V)$ are calculated for both V's. The desired integral curve $U(C)$ comes out of the saddle S and enters the node N along the separatrix. The parameters of S (having the subscript s) are $U_s = 2/(\nu(\gamma-1)+2)$ and $C_s = \sqrt{\nu}\,(\gamma-1)/(\nu(\gamma-1)+2)$. At small $\Delta = C - C_s$, the curve leaves the saddle, following the analytical formula $\xi = \Omega\Delta^\omega$, where $\omega = (\nu-1)k/(\eta(2U_s-1)-1-k)$, k is the slope of the separatrix, and Ω is a variable parameter that is determined from the condition $\xi = 1$ at N. The piston path is found from the equation $\partial \ln t/\partial \ln \xi = 1 - U$.

The power is defined as $W = 4\pi r_2^2 u_2 p_2$, the kinetic energy of the shell is

$$E_k = 4\pi\rho_h \int_{r_1}^{r_2} \frac{u^2}{2} r^2 dr = 2\pi\rho_h r_1^4 u_1^2 \left(\frac{1}{r_1} - \frac{1}{r_2}\right),$$

and its internal energy $E_i = 0$ because of incompressibility.

The problem involves two dimensionless parameters: ρ_h and V_h. In the above calculations, we put $\rho_h = 10$ and $V_h = 4\pi/3$, which is the initial volume of the matter. Hence, $r_2 = 1$ at collapse. Qualitatively, these quantities do not have an effect on the results. Figure 2

shows the obtained relationships. A number of compression features deserve attention. Near collapse, $r_1 = (\zeta t)^{U_s}$ and $u_1 = \zeta^{U_s} U_s t^{U_s - 1}$, where $\zeta = c_\infty/\nu^{1/4} C_s^{(\gamma+1)/2}$. Then, $u_2 \approx \zeta^{3U_s} U_s t^{3U_s - 1}/r_2^2$ ($r_2 \approx$ const). The exponent $3U_s - 1 = (4 - \nu(\gamma - 1))/(\nu(\gamma - 1) + 2)$ and changes sign when $\gamma_u = 1 + 4/\nu$. This means that, near collapse, the velocity of the outer boundary of the shell may increase (for $\gamma > \gamma_u$), decrease, or remain unchanged. From Fig. 2, it follows that u_2 first grows and then, starting with $t \approx 5 \times 10^{-3}$, drops. Also, near collapse ($r_1 \ll r_2$), $E_k = 2\pi\rho_h r_1^3 u_1^2 = 2\pi\rho_h \zeta^5 U_s^2 t^{5U_s - 2}/r_2^2$. The exponent $5U_s - 2 = (6 - 2\nu(\gamma - 1))/(\nu(\gamma - 1) + 2)$ at $\gamma_k = 1 + 3/\nu$ also changes sign. Finally, the kinetic energy near collapse may increase (at $\gamma > \gamma_k$), decrease, or remain constant. Since $\gamma_h < \gamma_n$, there exists a range $\gamma_k < \gamma < \gamma_u$ where the velocity of the outer boundary decreases and the kinetic energy grows. This is explained by velocity and accelerated-mass redistributions in the shell. However, for physically ultimate values, $\gamma = 5/3 < \gamma_k = 2$; therefore, at collapse, both the outer boundary velocity u_2 and the kinetic energy of the shell E_k tend to zero. Figure 2 implies that the difference $E_2 - E_1$ due to the pressure drop $p_2 - p_1$ and power difference $W_2 - W_1$ contributes to the kinetic energy $E_k = E_2 - E_1$. At $t < 10^{-3}$, E_k slowly drops: $E_k \propto t^{1/2}$. It is clear, however, that $E_2 \longrightarrow \infty$ and $W_2 \longrightarrow \infty$, since the total energy of the collapsing matter $E \longrightarrow \infty$.

REFERENCES

1. K. P. Stanyukovich, *Unsteady Motions of Continuous Medium* (Nauka, Moscow, 1971).
2. N. V. Zmitrenko and S. P. Kurdyumov, Prikl. Mekh. Tekh. Fiz., No. 1, 3 (1977).
3. M. A. Anufrieva and A. P. Mikhaĭlov, Differ. Urav. **19**, 483 (1983).
4. A. F. Sidorov, Prikl. Mat. Mekh. **55**, 779 (1991).
5. R. E. Kidder, Nucl. Fusion **14**, 53 (1974).
6. M. M. Basko, Nucl. Fusion **35**, 87 (1995).
7. S. K. Zhdanov and B. A. Trubnikov, Pis'ma Zh. Éksp. Teor. Fiz. **21**, 371 (1975) [JETP Lett. **21**, 169 (1975)].
8. Ya. M. Kazhdan, Prikl. Mekh. Tekh. Fiz., No. 1, 23 (1977).
9. I. E. Zababakhin and V. A. Simonenko, Prikl. Mat. Mekh. **42**, 573 (1978).
10. S. I. Anisimov and N. A. Inogamov, Prikl. Mekh. Tekh. Fiz., No. 4, 20 (1980).
11. A. M. Svalov, Izv. Akad. Nauk SSSR, Mekh. Zhidk. Gaza, No. 3, 171 (1982).
12. A. N. Kraĭko and N. I. Tillyaeva, Teplofiz. Vys. Temp. **36**, 120 (1998).

Translated by V. Isaakyan

Technical Physics, Vol. 45, No. 8, 2000, pp. 1091–1093. Translated from Zhurnal Tekhnicheskoĭ Fiziki, Vol. 70, No. 8, 2000, pp. 136–138.

BRIEF COMMUNICATIONS

Electroviscous Effect in an Alternating Electric Field

A. A. Ostapenko

Radiophysics Research Institute, St. Petersburg State University, St. Petersburg, 198904 Russia

Received October 28, 1998; in final form, October 20, 1999

Abstract—Experimental dependence of the relative dynamic viscosities of liquid dielectrics on the applied alternating voltage amplitude and frequency is presented. The voltage frequency was varied from 20 Hz to 2 kHz. The variation of viscosity can be attributed to a change in the liquid structure, with ion–molecule complexes centered at the ions produced as a result of charge injection from an electrode. A change in the injection regime leads to a change in viscosity. *© 2000 MAIK "Nauka/Interperiodica".*

In previous publications, it was pointed out that an electroviscous effect is observed in electric fields that are transverse to the dielectric flow [1, 2]. The change in viscosity was attributed to momentum transfer due to ion electrophoresis, the development of electrohydrodynamic flows, and the formation of ion–dipole clusters near electrodes [3]. In some studies, it was noted that the electroviscous effect is not observed in nonpolar liquids, but it was observed in the presence of small amounts of polar additives [1]. The addition of a polar additive to a nonpolar liquid can substantially affect the conductivity of the medium. Indeed, it was noted in a number of studies (e.g., see [1, 2]) that conductivity affects the intensity of the electroviscous effect. Apart from polar additives, an important factor that affects the intensity of the electroviscous effect is the presence of an injecting electrode. The process referred to as charge injection into a medium was not studied specifically, and only the consequences of charge injection from an electrode were discussed. It was shown in [2] that charge injection plays a very important role in the electroviscous effect as manifested in constant electric fields. The production of ions and ion–molecule complexes can change the structure of a liquid dielectric medium and considerably affect the viscosity observed in an electric field. The regime of charge injection from an electrode can be changed by applying an alternating electric field to the electrode gap.

In this paper, the behavior of the observed viscosity of polar liquid dielectrics as a function of the frequency of the external alternating electric field is discussed. It should be noted that the effect of the frequency of the applied field on the viscosity of a liquid dielectric has previously been studied only at 50 and 1000 Hz [1], and the frequency-dependent behavior has remained unclear. In other papers, the existence of this effect was ruled out completely. To this day, no acceptable explanation has been given for these controversial results.

For processes that take place near the electrodes (electrochemical reactions) responsible for charge injection to take place, it is necessary that charge build up in the vicinity of the electrodes. The change in the regime of charge production due to a change in the frequency of the external electric field can affect the rate of charge buildup or completely suppress it. Within the framework of the conventional model of the electrode double layer, injection can take place if a charge at least equal to the total double-layer charge has accumulated:

$$q = C_{dl}\Phi, \tag{1}$$

where C_{dl} is the capacity of the double layer and Φ is the voltage drop across the double layer. A rough estimate shows that the double-layer capacity is ~10 μF/cm^2, and the voltage drop is ~1 V for media of the kind considered here [4]. In an alternating field, such a double layer is discharged and charged during a half-period of every voltage cycle. Therefore, for injection to take place, a charge equal to q must build up in the layer during at least a quarter-period of the applied voltage; i.e.,

$$q \le \int_{T/4}^{T/2} i(t)dt, \tag{2}$$

where $i(t) = \sigma E_0 \sin 2\pi f t$, σ is the conductivity of the liquid, E_0 is the amplitude of the external field intensity, and f is its frequency. This yields an expression for the critical frequency above which the required charge cannot build up in the double layer:

$$f_{cr} = \frac{\sigma U_{max}}{2\pi d}, \tag{3}$$

where U_{max} is the amplitude of the applied voltage and d is the electrode-gap width.

When $f > f_{cr}$, charge injection does not take place, and vice versa. The setup used in the experiment was described in a previous paper [2]: a channel of rectangular cross section, 20 mm long and 3.5 mm wide, had top and bottom walls made of metal plates that served as electrodes. The electrode gap (channel height) was 200 μm. The passage time of the liquid flow between

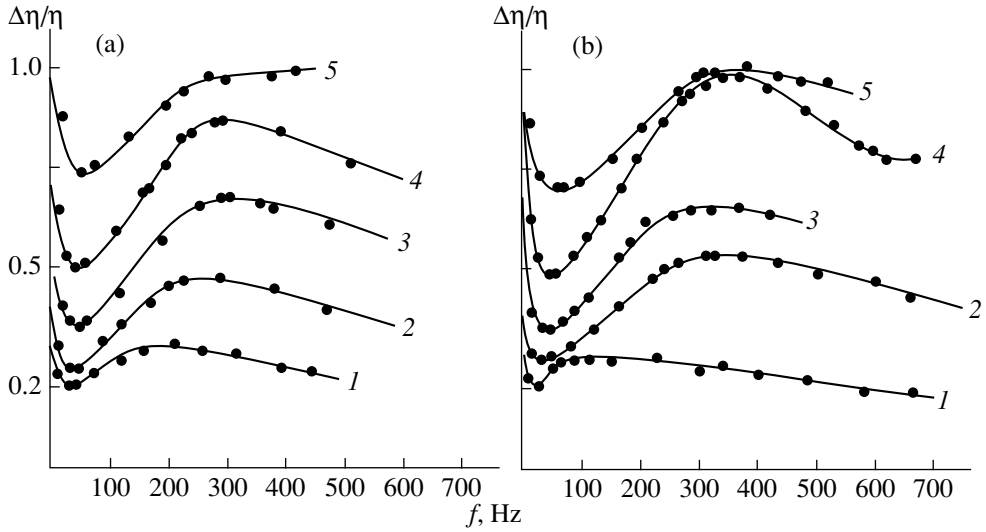

Fig. 1. Relative change in viscosity versus the frequency of applied alternating voltage for (a) acetone and (b) nitrobenzene at (*1*) 10, (*2*) 20, (*3*) 30, (*4*) 40, and (*5*) 50 kV/cm.

marks on the capillary walls was measured by a photodetector within 0.1 s. The alternating voltage generated by a special power supply was applied to the electrodes of the experimental cell. The error of frequency measurement did not exceed 3%. The length of the segment upstream of the capillary cell was adjusted so that the flow was steady along the entire cell. Since dynamic viscosity can be represented as $\eta = A\Delta P/\Delta Q$, where A is a calibration constant and ΔP is the pressure drop required to keep the flow rate at $\Delta Q = V_0/t$ (V_0 is the volume of flowing liquid), the change in the observed viscosity is $\Delta\eta/\eta = (\eta_{el} - \eta)/\eta = (t_{el} - t)/t$, where η_{el} is the viscosity observed when voltage is applied to the cell, t_{el} is the time required for the liquid volume to flow through the passage in the presence of the field, and t is the time required for the liquid volume to flow through the passage in the absence of the field.

The polar liquids under study had high permittivities ($\varepsilon \sim 36$–20), and decane (with $\varepsilon \approx 1.2$–1.4) was used as a reference nonpolar liquid. These liquids are typical liquid dielectrics. The change in viscosity (i.e., the time required for a liquid to pass through the cell) was measured as a function of the frequency of the applied voltage at different amplitudes of the voltage for various liquids. All of the curves obtained for the polar liquids involved portions characterized by similar behavior (see Figs. 1 and 2). At low frequencies, as the frequency is increased, the relative viscosity drops, reaches a minimum, and then rapidly increases. With a further increase in frequency, viscosity exhibits a slow decline. For example, the relative viscosity of acetone the relative viscosity at 400 Hz was equal to that observed at ~60 Hz when the voltage amplitude was held at 10 kV, whereas the minimum relative viscosity $(\Delta\eta/\eta)_{min}$ increased with the applied voltage. In particular, the value of $(\Delta\eta/\eta)_{min}$ at $E = 40$ kV/cm is three times higher than that observed at $E = 10$ kV/cm for all curves (see Figs. 1 and 2).

The minima of the curves discussed here may be associated with the critical frequencies for the charge buildup in the electrode double layer. Indeed, comparing the frequencies corresponding to $(\Delta\eta/\eta)_{min}$ with the critical frequency given by (3), one finds that they close (see table). It should be noted that the critical frequen-

Table

E, kV/cm	Nitrobenzene		Nitromethane		Acetone		Decane	
	f_{cr}, Hz	f_{min}, Hz (experiment)	f_{cr}, Hz	f_{min}, Hz (experiment)	f_{cr}, Hz	f_{min}, Hz (experiment)	f_{cr}, Hz	f_{min}, Hz (experiment)
10	16	12	80	60	10	10	1.6×10^{-6}	–
20	32	25	160	120	20	15	3.2×10^{-6}	–
30	48	42	240	180	32	26	4.8×10^{-6}	–
40	64	60	320	260	40	35	6.4×10^{-6}	–
50	80	75	400	350	53	48	8.0×10^{-6}	–

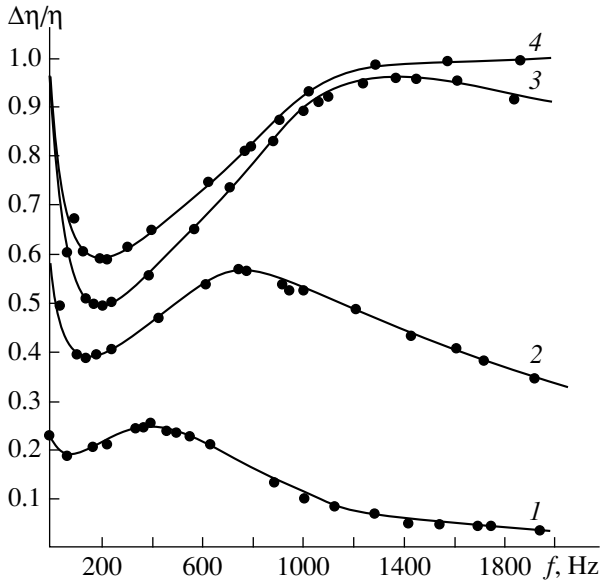

Fig. 2. Relative change in viscosity versus the frequency of applied voltage for nitromethane at (*1*) 10, (*2*) 20, (*3*) 30, and (*4*) 40 kV/cm.

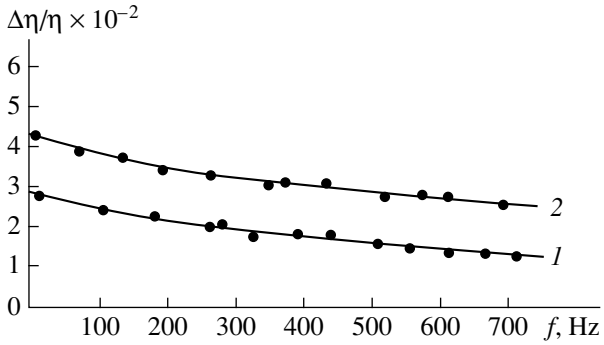

Fig. 3. Relative change in viscosity versus frequency for decane at (*1*) 20 and (*2*) 40 kV/cm.

cies measured for all liquids used in this study lie within 10–500 Hz (see table), i.e., in a domain of relatively low frequencies. For a nonpolar liquid such as decane, no minimum of this type was observed in the frequency range explored here (see Fig. 3). The relative viscosity of decane decreases with increasing frequency. In particular, as the frequency of the applied voltage is reduced by a factor of one hundred, the relative viscosity decreases by ~30%. As the applied voltage amplitude is increased, the value of $\Delta\eta/\eta$ increases by a factor of less than 1.5. It should be noted that when a constant voltage was applied to a flow cell containing a nonpolar liquid, the value of $\Delta\eta/\eta$ also exhibited a relatively slow increase as the voltage was increased [2].

The table compares the values of the critical frequency f_{cr} calculated by (3) with $f_{\min\,exp}$ measured in the experiment. The table demonstrates that the frequencies corresponding to the minima of curves in Figs. 1 and 2 are in good agreement with that predicted by (3), whereas experiments with decane did not reveal any critical frequency. According to (3), the critical frequency for decane at the field intensity 10 kV/cm would lie at ~10^{-2} Hz, i.e., in the far low-frequency domain, which is also consistent with experimental results.

After the injection was "switched off," the observed viscosity slightly increased with frequency and then slowly declined. These trends can be explained by effects of the bulk conductance of the liquid due to the molecular dissociation of the additive.

Thus, the studies described here have shown that the presence of injected space charge in a liquid medium plays an important role in the mechanism of the electroviscous effect. When the injection is prevented either by isolating the electrode from the liquid [2] or by changing the frequency of the applied voltage results in a decrease in relative viscosity. This may occur because the concentration of ion–molecule complexes decreases with injection intensity, i.e., because the formation of an ion–molecule complex is centered at an injected charge. An increase in the size of a structural element of a liquid would then lead to an increase in viscosity and, under certain conditions, to manifestations of other electrohydrodynamic effects.

REFERENCES

1. P. E. Sokolov and S. L. Sosinskiĭ, Dokl. Akad. Nauk SSSR **4**, 1037 (1939).
2. A. A. Ostapenko, Zh. Tekh. Fiz. **68** (1), 40 (1998) [Tech. Phys. **43**, 35 (1998)].
3. Yu. M. Rychkov, V. A. Liopa, *et al.*, Élektron. Obrab. Mater., No. 5, 34 (1994).
4. B. Gosse, J. Electroanal. Chem. Interfacial Electrochem. **61**, 265 (1975).

Translated by A.S. Betev

Technical Physics, Vol. 45, No. 8, 2000, pp. 1094–1095. Translated from Zhurnal Tekhnicheskoĭ Fiziki, Vol. 70, No. 8, 2000, pp. 139–140.

BRIEF COMMUNICATIONS

The Behavior of Higher Manganese Silicide Single Crystals under Electrochemical Treatment

F. Yu. Solomkin

Ioffe Physicotechnical Institute, Russian Academy of Sciences, Politekhnicheskaya ul. 26, St. Petersburg, 194021 Russia

Received October 21, 1999

Abstract—For higher manganese silicide single crystals of certain geometry and superstructure orientation, an unusual metallization process is observed. This anomaly can be associated either with bulk processes similar to thermogalvanic effects or with the carrier redistribution in the near-surface regions that is due to the high thermoelectric power anisotropy and complex crystal structure. © *2000 MAIK "Nauka/Interperiodica".*

The use of electrochemical techniques in the technology of high-temperature thermoelectric devices makes it possible to integrate electrochemical cleaning (chemical activation) of the surface and subsequent deposition of metal contacts into a continuous fabrication process [1]. Also, it allows researchers to study the distributions of heat fluxes and electric currents.

Higher manganese silicide (HMS) is viewed as the best candidate for high-temperature generators and sensors that operate in a wide spectral range. This material has the tetragonal crystal structure, which consists of loosely bonded manganese and silicon sublattices. The spacings of the sublattices along the tetragonal *C*-axis are generally incommensurable. Their incommensurability and the existence of many crystal structures in the narrow range of compositions ($MnSe_{1.71–1.75}$) cause the precipitation of manganese monosilicide on planes normal to the *C*-axis [2].

When HMS polycrystals are subjected to electrochemical metallization (nickel plating), no anomalies (from the electrochemistry viewpoint) are observed. Ohmic contacts with a resistivity of 10^{-5}–10^{-6} Ω cm^2 are produced [3].

The electrochemical deposition of nickel on HMS single crystals in the form of a parallelepiped whose end face is dipped into an electrolyte proceeds in several stages. Within the initial five seconds, the blanket metallization of the electrolyte-covered surface takes place. Then, the metal begins to dissolve at the specimen corners and edges, forming metal islands on the side faces. The islands extend toward the end face (see figure). On the end face, the dissolving metal film first takes the oval shape, then its central part narrows to form a dumb-bell, and eventually two metal spots remain. If the process continues further, the central part of the spots also dissolves and two metal rings are left on the surface. The same is reproduced on another specimen in the same electrolyte.

This observation seems to be an anomaly from the standpoint of conventional electrochemistry. During the electrochemical application of metal films (cathode polarization), preferential deposition on edges, corners, and surface ridges, not etching, is common.

This effect is most prominent when the *C*-axis makes an angle of 45° with the largest side of the parallelepiped (see figure). When the *C*-axis deviates from this direction, the island length on the side faces may change and the process on the end side may be completed with the formation of the oval or dumb-bell. The shape of the end face metallization strongly depends on the parallelepiped dimensions. The two metal rings appeared on the end face when $a : b = 1 : 3$ and specimens were sufficiently long in the current passing direction. The effect was absent for short specimens.

It can be inferred that the residual metallization patterns on the end side (rings) and side surfaces are due to bulk processes similar to thermogalvanic effects [4]. It appears that, when the carriers move along streamlines, their paths twist and eventually two parallel flows are produced where the carries spiral. This becomes possible because of the specific superstructure orientation, specimen geometry, and temperature distribution. The situation looks as if the carriers were drawn in two parallel-mounted "solenoids" instead of being spent on metal reduction at cathode polarization. Eventually, metal reduction on the surface changes to its dissolution, causing an oval, dumb-bell, spots, and rings to appear successively on the end face. On the side surfaces, the tendency to complete metal etching off is observed.

An alternative explanation is the redistribution of the carriers in the near-surface region because of the high thermopower anisotropy and complex crystal structure. Cathodic and anodic areas forming on the surface begin to act in parallel. As the specimen temperature changes during the electrochemical reaction,

1063-7842/00/4508-1094$20.00

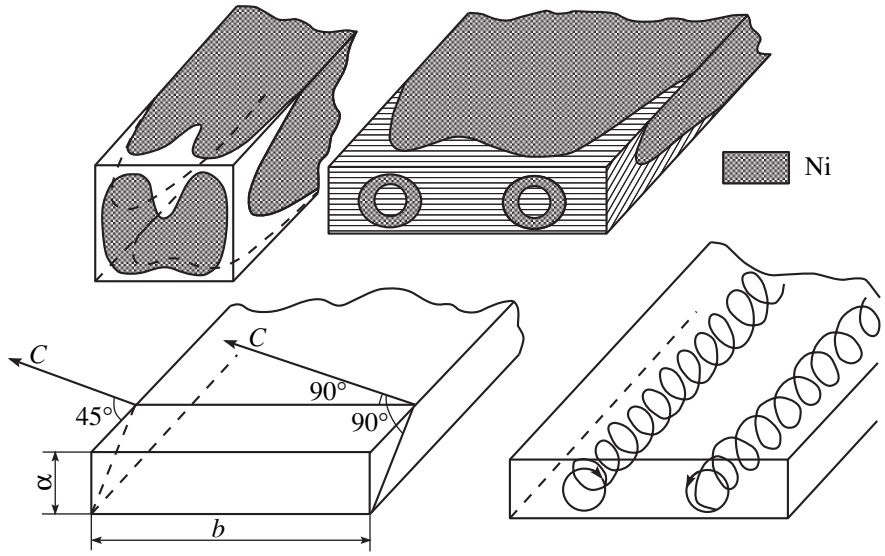

Anomalous electrochemical metallization of HMS single crystals with the certain superstructure orientation and different geometry.

so do the mutual arrangement and shapes of the areas with different polarization. In this way, the residual metal film is patterned.

Thus, an anomalous metallization process is observed in HMS single crystals of the specific geometry and superstructure orientation. This anomaly can be associated either with bulk processes similar to thermogalvanic effects or with the carrier redistribution in the near-surface regions that is due to the high thermoelectric power anisotropy and complex crystal structure.

REFERENCES

1. M. I. Fedorov, V. K. Zaĭtsev, F. Yu. Solomkin, and M. V. Vedernikov, Pis'ma Zh. Tekh. Fiz. **27** (15), 64 (1997) [Tech. Phys. Lett. **27**, 602 (1997)].
2. V. K. Zaitsev, in *Handbook of Thermoelectrics*, Ed. by D. M. Rowe (CRC Press, New York, 1995), pp. 299–309.
3. F. Yu. Solomkin, RF Patent No. 2009571, Byull. Izobret., No. 5 (1994).
4. L. S. Stil'bans, *The Physics of Semiconductors* (Sov. Radio, Moscow, 1967).

Translated by V. Isaakyan

Technical Physics, Vol. 45, No. 8, 2000, pp. 1096–1097. Translated from Zhurnal Tekhnicheskoĭ Fiziki, Vol. 70, No. 8, 2000, pp. 141–142.

BRIEF COMMUNICATIONS

Generation and Amplification of Electromagnetic Waves by an Annular Electron Beam in a Radial Electric Field in Free Space

Yu. V. Kirichenko

National Science Center, Kharkov Institute of Physics and Technology, Akademicheskaya ul. 1, Kharkov, 310108 Ukraine

Received November 22, 1999

Abstract—Mechanisms for the generation and amplification of electromagnetic waves by a thin-walled annular beam of electrons rotating in a radial electric field in free space are studied theoretically. It is shown that electromagnetic waves can be generated and amplified under the Cherenkov resonance conditions. The frequencies and growth rates of the generated waves are determined, and the propagation characteristics and amplification coefficients of the amplified waves are found. *© 2000 MAIK "Nauka/Interperiodica".*

The theory of the generation and amplification of electromagnetic waves by annular electron beams in waveguides (in particular, plasma-filled waveguides) is widely covered in the literature (see, e.g., [1, 2]). Under certain conditions (such as a small beam diameter in comparison with the waveguide diameter, the field falls off exponentially in the radial direction with distance from the beam, and the wavelengths are short), the waveguide walls have essentially no effect on the dispersion properties of electromagnetic waves. On the other hand, the problem of the generation and amplification of waves by a thin-walled annular beam of electrons moving simultaneously in the azimuthal and axial directions in free space is of interest in its own right.

We introduce the cylindrical coordinates (r, φ, z) and consider an unbounded (along the z-axis) cylindrical electron layer in which the electrons rotate in the azimuthal direction. Let us assume that a positively charged metal rod with radius a, linear charge density Q, and a high but finite conductivity σ is located at the coordinate axis. The electrons are held on circular equilibrium orbits by the radial electrostatic field of the rod, $F_0(r) = 2Q/r$. We neglect the constant magnetic and electric self-fields of the electron layer and assume that the perturbations of the electromagnetic field, electron density, and electron velocity all depend on the coordinates z and φ and time t as $\exp[i(m\varphi + k_z z - \omega t)]$, where $m \neq 0$ is an integer, k_z is the projection of the wave vector onto the z-axis, and ω is the frequency. We treat the problem in the hydrodynamic approximation. The unperturbed electron density $n(r)$ is assumed to be nonzero in the layer between the surfaces $r = r_-$ and $r = r_+$. We also assume that the following conditions are satisfied:

$$|k_z| \gg \left|\frac{\omega}{c}\right|, \quad |k_\varphi| \gg \left|\frac{\omega}{c}\right|, \quad |k_z r_-| \ll 2(\bar{m})^{1/2}, \qquad (1)$$

where $k_\varphi = m/r_-$ is the azimuthal component of the wave vector, c is the speed of light, and $\bar{m} = |m|$.

Inequalities (1) allow us to apply the potential approximation [3, 4]. Using the method described by Dolgopolov *et al.* [5], we can show that, in the case of a thin layer such that

$$r_+ - r_- = \delta r \ll r_-, \qquad (2)$$

the electrostatic potential Φ treated in a linear approximation under the Cherenkov resonance conditions satisfies the boundary conditions

$$\Phi|_{r_+} = \Phi|_{r_-}, \quad \left.\frac{d\Phi}{dr}\right|_{r_+} - \left.\frac{d\Phi}{dr}\right|_{r_-} = \kappa\Phi|_{r_-}, \qquad (3)$$

where

$$\kappa = \frac{m^2}{r_-^2\omega_m^2}\int_{r_-}^{r_+} dr\Omega^2(r)\frac{2V_\varphi^2 - \Omega^2(r)r^2}{2V_\varphi^2 + \Omega^2(r)r^2}, \qquad (4)$$

$\Omega^2(r) = 4\pi e^2 n(r)/m_e$, $\omega_m = \omega - mV_\varphi/r_- - k_z V_z$, V_φ and V_z are the azimuthal and axial components of the unperturbed electron velocity, and $-e < 0$ and m_e are the charge and the mass of an electron.

Formulas (3) and (4) were derived under the Cherenkov resonance condition

$$\omega_m \simeq 0 \qquad (5)$$

and with allowance for the fact that, by virtue of conditions (1), the quantity k_z/k_φ is small. Taking (2) into account, we match $\Phi(r)$ and $d\Phi(r)/dr$ at the boundaries between the rod and the layer to obtain the dispersion

1063-7842/00/4508-1096$20.00

relation

$$\omega_m^2 = -\frac{\bar{m}\eta_m}{\eta^{2\bar{m}}}(1 - i\omega\delta_\sigma)\frac{1}{r_-}\int_{r_-}^{r_+} dr\Omega^2(r)\frac{2V_\varphi^2 - \Omega^2(r)r^2}{2V_\varphi^2 + \Omega^2(r)r^2}, \quad (6)$$

where $\eta = r_-/a$, $\eta_m = (\eta^{2\bar{m}} - 1)/2$, $\delta_\sigma = 1/(4\pi\sigma\eta_m)$, and $|\omega\delta_\sigma| \ll 1$.

The parameter δ_σ accounts for energy losses in the rod. We introduce the averaged quantity $\bar{\Omega}$:

$$\bar{\Omega}^2\frac{2V_\varphi^2 - \Omega^{-2}r_-^2}{2V_\varphi^2 + \Omega^{-2}r_-^2} = \frac{1}{\delta r}\int_{r_-}^{r_+} dr\Omega^2(r)\frac{2V_\varphi^2 - \Omega^2(r)r^2}{2V_\varphi^2 + \Omega^2(r)r^2}. \quad (7)$$

We start by solving the problem of the excitation of electromagnetic waves. To do this, we must set $\mathrm{Im}(k_z) = 0$ in (6), which then implies that $\mathrm{Im}(\omega) \neq 0$ and $|\mathrm{Im}(\omega)| \ll \mathrm{Re}(\omega)$. Under the condition

$$2V_\varphi^2 > r_-^2\bar{\Omega}^2 \quad (8)$$

equation (6) yields

$$\mathrm{Re}(\omega) = \frac{mV_\varphi}{r_-} + k_zV_z + 0\left(\left(\frac{\delta r}{r_-}\right)^{1/2}\delta_\sigma\right), \quad (9)$$

$$\mathrm{Im}(\omega) = \bar{\Omega}\left(\frac{\bar{m}\eta_m}{\eta^{2\bar{m}}}\right)^{1/2}\left(\frac{2V_\varphi^2 - \bar{\Omega}^2r_-^2}{2V_\varphi^2 + \bar{\Omega}^2r_-^2}\right)^{1/2}\left(\frac{\partial r}{r_-}\right)^{1/2}; \quad (10)$$

under the condition

$$2V_\varphi^2 < r_-^2\bar{\Omega}^2, \quad (11)$$

equation (6) yields

$$\mathrm{Re}(\omega) = \frac{mV_\varphi}{r_-} + k_zV_z - 0\left(\left(\frac{\partial r}{r_-}\right)^{1,2}\right), \quad (12)$$

$$\mathrm{Im}(\omega) = \frac{1}{2}\delta_\sigma\bar{\Omega}\left(\frac{mV_\varphi}{r_-} + k_zV_z\right)\left(\frac{\bar{m}\eta_m}{\eta^{2\bar{m}}}\right)^{1/2} \times\left(\frac{r_-^2\bar{\Omega}^2 - 2V_\varphi^2}{r_-^2\bar{\Omega}^2 + 2V_\varphi^2}\right)^{1/2}\left(\frac{\delta r}{r_-}\right)^{1/2}. \quad (13)$$

We can see that, under condition (8), which indicates that the angular electron velocity is high and the electron density is low, the growth rate is considerably higher than that under the opposite condition (11), according to which the instability is triggered by the dissipation of the wave energy in the rod. Note that the growth rate (10) increases with $\bar{m}$ as $\bar{m}^{1/2}$, while the growth rate (13) is exponentially decreasing. However, we must keep in mind that, by virtue of inequalities (1), the positive integer $\bar{m}$ is limited by the condition

$$\bar{m} \ll \frac{k_zrc}{V_\varphi}. \quad (14)$$

In addition, dispersion relation (6) enables us to solve the problem of the amplification of an electromagnetic wave travelling along the z-axis by an annular electron beam under the Cherenkov resonance condition (5). To do this, we must set $\mathrm{Im}(\omega) = 0$ in equation (6), in which case we have $\mathrm{Im}(k_z) \neq 0$ and $|\mathrm{Im}(k_z)| \ll \mathrm{Re}(k_z)$. Under condition (8), equation (6) gives the following expression for the amplification coefficient $|\mathrm{Im}(k_z)|$:

$$|\mathrm{Im}(k_z)| = \frac{\bar{\Omega}}{V_z}\left(\frac{\bar{m}\eta_m}{\eta^{2\bar{m}}}\right)^{1/2}\left(\frac{2V_\varphi^2 - \bar{\Omega}^2r_-^2}{2V_\varphi^2 + \bar{\Omega}^2r_-^2}\right)^{1/2}\left(\frac{\delta r}{r_-}\right)^{1/2}; \quad (15)$$

under condition (11), we obtain

$$|\mathrm{Im}(k_z)| = \frac{\omega\bar{\Omega}\delta_\sigma}{2V_z}\left(\frac{\bar{m}\eta_m}{\eta^{2\bar{m}}}\right)^{1/2} \times\left(\frac{r_-^2\bar{\Omega}^2 - 2V_\varphi^2}{r_-^2\bar{\Omega}^2 + 2V_\varphi^2}\right)^{1/2}\left(\frac{\delta r}{r_-}\right)^{1/2}. \quad (16)$$

The amplification coefficient (15) is much larger than (16). Under condition (11), the coefficient $|\mathrm{Im}(k_z)|$ is governed by the energy losses in the rod and is proportional to the frequency of the amplified wave.

Note that, according to the first inequality in (1), the magnetic and electric fields are both exponentially decreasing in the radial direction. Consequently, during the generation or amplification of a wave, an infinite annular beam in free space emits no electromagnetic waves, thereby keeping its energy unchanged. In contrast, a generated or amplified wave will be emitted by a semi-infinite annular beam (bounded, e.g., by the coordinate z_0) through its end into a half-space $z > z_0$.

ACKNOWLEDGMENT

I am grateful to V.V. Dolgopolov for fruitful discussions and valuable remarks.

REFERENCES

1. Ya. B. Faĭnberg, Fiz. Plazmy **11**, 1398 (1985) [Sov. J. Plasma Phys. **11**, 803 (1985)].
2. A. N. Kondratenko, *Plasma Waveguides* (Atomizdat, Moscow, 1976).
3. R. C. Davidson, *Theory of Nonneutral Plasmas* (Benjamin, New York, 1974; Mir, Moscow, 1978).
4. V. V. Dolgopolov, Yu. V. Kirichenko, Yu. F. Lonin, and I. F. Kharchenko, Zh. Tekh. Fiz. **68** (8), 91 (1998) [Tech. Phys. **43**, 959 (1998)].
5. V. V. Dolgopolov, M. V. Dolgopolov, and Yu. V. Kirichenko, Izv. Vyssh. Uchebn. Zaved. Radioelektron. **40** (12), 16 (1997).

Translated by O. E. Khadin

Technical Physics, Vol. 45, No. 8, 2000, pp. 955–962. Translated from Zhurnal Tekhnicheskoĭ Fiziki, Vol. 70, No. 8, 2000, pp. 1–7.

Analytical Solution to the Skin-Effect Problem for an Arbitrary Accommodation Coefficient of Electron Tangential Momentum

A. V. Latyshev and A. A. Yushkanov

Moscow Pedagogical University, ul. Radio 10a, Moscow, 107005 Russia

E-mail: gslobod@arc.ru

Received February 23, 1999

Abstract—An analytical solution to the boundary-value problem of an electric field and electrons in a metal-filled half-space is obtained for arbitrary values of the tangential-momentum accommodation coefficient. The frequency of an external electromagnetic field directed tangentially to the surface is allowed to take on complex values. Both the normal and anomalous skin effects are considered. In the latter case, the low- and high-frequency limits are examined. *© 2000 MAIK "Nauka/Interperiodica".*

INTRODUCTION

The skin-effect problem has been solved analytically for the specular and diffuse reflections of electrons from a metal surface. The former case corresponds to zero accommodation of electron tangential momentum; and the latter, to total accommodation (the tangential-momentum accommodation coefficient q is 0 or 1, respectively). For intermediate q's, analytical solutions have not yet been found. The aim of this study is to fill the gap.

For conventional boundary conditions, the behavior of gases or electrons near the surface defies analytical description if the specular reflection coefficient α takes on arbitrary values. However, modified boundary conditions were developed in the kinetic theory of gases [1] so as to allow for an arbitrary q ($q = 1 - \alpha$ for the specular or diffuse case). They make the boundary-value problems solvable in an analytical form (e.g., for the isothermal or thermal slip of gas, etc.). We are going to extend this approach to electrons in metals.

The tangential momentum accommodation coefficient q is the ratio of the tangential momentum flux of electrons reflected from the surface to that of electrons impinging on the surface:

$$q = \int\limits_{(+)} v_n v_\tau f d^3 v \left[\int\limits_{(-)} v_n v_\tau d^3 v \right]^{-1}.$$

Here, v_n and v_τ are, respectively, the normal and tangential components of the electron velocity. The plus and minus signs correspond to $v_n > 0$ and $v_n < 0$, respectively. The surface is assumed to be planar.

An analytical solution to the problem of the anomalous skin effect in a half-space was first obtained by the Wiener–Hopf method [2–4]. Generalizations of the problem were addressed in [5, 6]. Studies [7, 8] of high-frequency processes in metals highlighted the efficiency of the Case method [9], which expands a solution in the singular generalized eigenfunctions of the associated characteristic equation. In [10, 11], diffuse boundary conditions were applied to an electron plasma subjected to an electromagnetic field perpendicular to the surface. In contrast to the Wiener–Hopf method [3–6], Case's method yields explicit expressions for discrete modes of the solution. As emphasized by some authors (see, e.g., [12]), under certain conditions, such modes define to the largest extent the properties of both the electromagnetic field and conduction electrons. Furthermore, the Case method provides the deepest understanding of different types of skin effect. That is why it is followed here.

In this study, we apply the expansion in singular eigenfunctions to finding the impedance at $0 \le q \le 1$. In particular, formulas for diffuse ($q = 1$) and specular ($q = 0$) boundary conditions are derived. The normal and anomalous skin effects are considered. In the latter case, the high- and low-frequency limits are explored. For the anomalous skin effect, a relation is revealed between the macroscopic response (impedance) of a metal to an external field and the discrete spectrum. The beauty of the Case method is that it dispenses with intuitive ideas, such as the concept of inefficiency [1, 13].

FORMULATION OF THE PROBLEM

We restrict ourselves to the case of a spherical Fermi surface and small oscillation frequencies, neglecting displacement current. The external field is assumed to be weak, which allows us to view the problem in a linear context. Consider a metallic medium occupying a half-space. Let us introduce Cartesian coordinates so that the origin lies on the surface, the x-axis is perpen-

1063-7842/00/4508-0955$20.00

dicular to the surface and is directed into the metal, the y-axis is aligned with the electric field $E(x)\exp(\alpha t)$, and the z-axis is perpendicular to the magnetic field $H(x)\exp(\alpha t)$.

After the time variable is separated, the equations for electric field and electrons in the metal have the form [2]

$$v_x\frac{\partial f_1}{\partial x} + (\nu + \alpha) f_1(x, v) = e v_y E(x)\frac{\partial f_0}{\partial \varepsilon},$$

$$E''(x) = Aj(x).$$

Here, f_0 is the Fermi distribution of electrons; f_1 is the correction to f_0; $f = f_0 + f_1\exp(\alpha t)$; ε, e, m, v, and ν are the electron energy, charge, mass, velocity, and collision rate, respectively; j is the current density; and $A = 4\pi\alpha c^{-2}$. The current density is given by

$$j(x) = -2e\left(\frac{m}{2\pi\hbar}\right)^3\int v_y f_1(x, v)d^3v.$$

Let us introduce the notation

$$e(x) = E(x)/E_0, \quad w_0 = 1 + \alpha/\nu,$$

$$x' = x/(\tau v_F), \quad \mu = v_x/v_F,$$

$$f_1 = v_y\delta(v - v_F)\psi, \quad k = -\frac{eE_0}{2m\nu v_F},$$

$$\beta = \frac{e v_F^6\alpha}{\nu^2\pi\hbar^3c^2E_0}.$$

Here, v_F is the electron velocity on the Fermi surface, E_0 is the electric field amplitude on the surface of the metal, and $\delta(x)$ is the delta function. In what follows, instead of x', we will write x. Then, the equations become

$$\mu\frac{\partial\psi}{\partial x} + w_0\psi(x, \mu) = ke(x),$$

$$e''(x) = \beta\int_{-1}^{1}(1 - \mu'^2)\psi(x, \mu')d\mu'. \tag{1}$$

The conditions on the surface and away from it are assumed to have the form

$$\psi(0, \mu) = d, \quad 0 < \mu < 1;$$

$$\psi(\infty, \mu) = 0, \quad -1 < \mu < 0; \tag{2}$$

$$e(0) = 1, \quad e(\infty) = 0,$$

where d relates to the mean velocity of the electrons reflected from the surface.

Suppose that the momentum flux of reflected electrons equals $1 - q$ times the momentum flux of impinging electrons:

$$(1 - q)\int_{-1}^{0}(1 - \mu'^2)\psi(0, \mu')\mu'd\mu'$$

$$= -\int_{0}^{1}(1 - \mu'^2)\psi(0, \mu')\mu'd\mu'.$$

Here, q is the tangential-momentum accommodation coefficient, i.e., the probability of electron reflection. The last two conditions imply

$$d = -4\frac{1 - q}{q}\int_{-1}^{1}(1 - \mu'^2)\psi(0, \mu')\mu'd\mu'. \tag{3}$$

EIGENFUNCTIONS

Let us separate the variables according to

$$\psi_\eta(x, \mu) = \exp(-x/\eta), \quad e_\eta(x) = \exp(-x/\eta)E(\eta),$$

where η is the spectral parameter. We thus arrive at the characteristic system

$$(\eta - \mu)\Phi(\eta, \mu) = kw_0^{-1}\eta E(\eta),$$

$$E(\eta) = \beta w_0^{-2}\eta n(\eta), \quad b = \beta w_0^{-2},$$

where

$$n(\eta) = \int_{-1}^{1}(1 - \mu^2)\Phi(\eta, \mu)d\mu.$$

Eliminating $E(\eta)$ from the last two equations results in the characteristic equation

$$(\eta - \mu)\Phi(\eta, \mu) = \frac{1}{2}a\eta^3 n(\eta),$$

where

$$a = -a_0\frac{\alpha}{(\nu + \alpha)^3}, \quad a_0 = \frac{e^2 v_F^5}{\pi m\hbar^3c^2}, \quad \nu = \frac{1}{\tau}.$$

If $\eta \in (-1, 1)$ and $n(\eta) \equiv 1$, the characteristic equation immediately yields its continuum eigenfunctions [14]:

$$\Phi(\eta, \mu) = \frac{1}{2}a\eta^3 P\frac{1}{\eta - \mu} + \frac{\lambda(\eta)}{1 - \eta^2}\delta(\eta - \mu).$$

Here, Px^{-1} denotes a distribution, i.e., the principal value of the integral of x^{-1}; $\delta(x)$ is the Dirac function; and $\lambda(z)$ is the dispersion function of the problem,

$$\lambda(z) = 1 - az^2 + az^2(1 - z^2)\lambda_c(z),$$

where

$$\lambda_c(z) = 1 + \frac{1}{2}\int_{-1}^{1}\frac{d\tau}{\tau - z}$$

is the Case dispersion function [9].

By definition, the discrete spectrum of the characteristic equation comprises the zeros of the dispersion function that lie outside the cut [–1, 1]. The structure of the spectrum can be found by the technique developed in [15]. First, we will consider the homogeneous Riemann boundary-value problem

$$X^+(\mu) = G(\mu)X^-(\mu), \quad 0 < \mu < 1, \tag{4}$$

where

$$G(\mu) = \lambda^+(\mu)/\lambda^-(\mu) = \omega^+(\mu)/\omega^-(\mu).$$

Here,

$$\omega^\pm(\mu) = \lambda^\pm/a = \delta_1 - p(\mu) + i(\delta_2 \pm q(\mu)),$$
$$\delta = 1/a = \delta_1 + \delta_2,$$

and

$$p(\mu) = \mu^2[1 - (1 - \mu^2)\lambda_c(\mu)],$$
$$q(\mu) = \frac{\pi}{2}\mu^3(1 - \mu^2).$$

Let $\Theta(\mu)$ denote the regular branch of $\arg G(\mu)$ such that $\Theta(0) = 0$. Let us find the index [16] of problem (4). We have

$$\kappa = \frac{1}{2\pi}[\Theta(\mu)]_{(0.1)} = \frac{1}{4\pi}[\Theta(\mu)]_{(-1.1)} = \frac{1}{4\pi}[\arg\omega(z)]_\gamma,$$

where γ is a contour that runs clockwise around the cut [–1, 1] and does not enclose the zeros of the dispersion function.

Let N and P respectively denote the total numbers of the zeros and poles of $\omega(z)$ outside the cut [–1, 1]. As follows from the last equality and the principle of argument [16], the index of problem (4) is $\kappa = (N - P)/2$. In the δ plane, consider the region

$$\Delta^+ = \{\delta = \delta_1 + i\delta_2;\ 0 < \delta_1 < 1, |\delta_2| < q(\delta_1)\}.$$

Let Δ^- and γ_0 respectively denote the exterior and boundary of $\delta \in \Delta^+$. As in [15], it can be shown that, if $\delta \in \Delta^+$, $\kappa = 1$ and hence $N = 4$, since $P = 2$ for all $\delta \in \Delta^\pm$. Also, if $\delta \in \Delta^-$, $\kappa = 0$ and hence $N = 2$. That $P = 2$ follows from the expansion

$$\omega(z) = -\frac{2}{3}z^2 + \delta - \frac{2}{15} + o(1), \quad |z| \longrightarrow \infty. \tag{5}$$

For problem (4), let us select a solution that is nonvanishing and bounded at the extremes of the interval of integration. In view of the behavior of $\kappa = \kappa(\delta)$ for $\delta \in \Delta^+(\Delta^-)$, we take the function

$$X(z) = z^{-\kappa}\exp V(z),$$
$$V(z) = \frac{1}{2\pi i}\int_0^1[\ln G(\tau) - 2\pi i\kappa]\frac{d\tau}{\tau - z}.$$

Explicit expressions for the zeros of the dispersion function can be obtained from its factorization formulas (presented without derivation):

$$\omega(z) = \frac{2}{3}(\eta_0^2 - z^2)(\eta_1^2 - z^2)X(z)X(-z), \quad z \in \Delta^+,$$

$$\omega(z) = \frac{2}{3}(\eta_0^2 - z^2)X(z)X(-z), \quad z \in \Delta^-.$$

The eigenfunctions associated with the discrete spectrum at hand are as follows:

$$\Phi(\pm\eta_k, \mu) = \pm\frac{1}{2}a\eta_k^3\frac{1}{\pm\eta_k - \mu},$$

$$E(\pm\eta_k) = b\eta_k^2 \quad (k = 0, 1).$$

We skip over the boundary regime, since this topic has been carefully treated in the context of the Rayleigh problem [17]. In [17], the continuity of the distribution function and its integral characteristics in the plane of complex frequency were also demonstrated for the case when the index of the Rayleigh problem varies in steps.

Let us find explicit expressions for the zeros of the dispersion function in two limiting cases: $|\delta| \ll 1$ and $|\delta| \gg 1$.

If $|\delta| \ll 1$, we are dealing with the anomalous skin effect. Then, $\omega^\pm = \delta \pm i\pi\mu^3/2$. If δ is in the second quadrant, the discrete spectrum consists of two zeros: $\eta_1 = r\exp(i\arg\delta/3) + i\pi/6$ and $\eta_2 = -\eta_1$, where $r = \sqrt[3]{2|\delta|/\pi}$. The zero η_1 is in the first quadrant ($\Re\eta_1 > 0$), since $\pi < \arg\delta < \pi/2$. The zero η_2 is in the third quadrant. If δ is in the third quadrant, the spectrum also consists of two zeros: $\eta_1 = r\exp(i\arg\delta/3 + i\pi/6 + i2\pi/3)$ and $\eta_2 = -\eta_1$. The zero η_1 is in the second quadrant now, since $-\pi < \arg\delta < -\pi/2$. Note that, if δ is real and negative ($\arg\delta = \pi$), the dispersion function has two purely imaginary zeros: $\eta_0 = ri$ and $\eta_1 = -\eta_0$. On the other hand, if δ is a purely imaginary number, then $\eta_0 = r\exp(i\pi/3)$ and $\eta_1 = -\eta_0$ for $\arg\delta = \pi/2$ and $\eta_0 = r\exp(-i\pi/3)$ and $\eta_1 = -\eta_0$ for $\arg\delta = -\pi/2$.

Let δ be in the right half-plane. In this case, the dispersion function has four zeros, two of which,

$$\eta_k = r\exp[i(\arg\delta/3 + \pi/6 + 2\pi k/3)] \quad (k = 0, 1),$$

lie in the upper half-plane (with $\Re\eta_0 > 0$ and $\Re\eta_1 < 0$) and the other zeros are $\eta_2 = -\eta_1$ and $\eta_3 = -\eta_0$.

In the context of the anomalous skin effect, we single out two important cases: the high- and low-fre-

quency conditions. Under the low-frequency conditions, the field frequency is much lower than the electron collision rate: $|\alpha| \ll \nu$ and also $\nu|\alpha| \ll a_0$. Furthermore, $w_0 = 1 + \alpha/\nu = 1$ and $\delta = -(\nu + \alpha)^3/\alpha a_0 = -\nu^3/\alpha a_0 = -\nu^3 i/\omega a_0$. We then have two zeros: $\pm\eta_0$, where $\eta_0 = r\exp(-i\pi/3)$. Under the high-frequency conditions (which are close to an oscillatory regime), the field frequency is much higher than the electron collision rate: $|\alpha| \gg \nu$. This situation occurs at low temperatures and low impurity concentrations. Here, $w_0 = \alpha\tau = -i\omega\tau$ and $\delta = -\alpha^2/a_0$. The dispersion function has four zeros, since $\alpha = -i\omega$, so that $\delta = \omega^2/a_0 > 0$. The expressions for the zeros are as in the above.

The case $|\delta| \gg 1$ corresponds to the normal skin effect. Now the dispersion function has two zeros. As follows from (5), the expression for them is

$$\eta_k = r\exp[i(\arg\delta/2 + \pi k)], \quad r = \sqrt{3|\delta|/2} \quad (k = 0, 1).$$

If δ lies in the negative portion of the real axis, then $\Re\eta_0 > 0$ always. If $\delta < 0$, then $\eta_0 = ri$. If $\delta > 0$, then the zeros are real: $\pm\eta_0$.

EXPANDING THE GENERAL SOLUTION IN EIGENFUNCTIONS

Let us represent the general solution of system (1) in terms of the discrete and continuum eigenfunctions in such a way as to satisfy boundary conditions (2) (away from the surface). The expansions read as follows:

$$\psi(x, \mu) = \sum_{k=0}^{1} \frac{1}{2} a\eta_k^3 \frac{1}{\eta_k - \mu} \exp\left(-w_0 \frac{x}{\eta_k}\right) + \int_0^1 \exp\left(-w_0 \frac{x}{\eta}\right) \Phi(\eta, \mu) A(\eta) d\eta, \tag{6}$$

$$e(x) = \sum_{k=0}^{1} A_k b\eta_k^2 \exp\left(-w_0 \frac{x}{\eta_k}\right) + b\int_0^1 \exp\left(-w_0 \frac{x}{\eta}\right) \eta^2 A(\eta) d\eta. \tag{7}$$

Here, A_k ($k = 0, 1$) are unknown coefficients associated with the discrete spectrum, with $A_1 = 0$ for $\delta \in \Delta^-$; $A(\eta)$ is an unknown function associated with the continuous spectrum (continuous expansion coefficient); and $\Re w_0/\eta_k > 0$ ($k = 0, 1$), with $\Re w_0 > 0$.

Based on the boundary conditions, let us determine the expansion coefficients in (6) and (7). Let $\delta \in \Delta^+$. At $x = 0$, we obtain

$$\sum_{k=0}^{1} A_k \frac{1}{2} \frac{\eta_k^3}{\eta_k - \mu} + a\frac{1}{2}\int_0^1 \frac{\eta^3 A(\eta)}{\eta - \mu} d\eta + \frac{\lambda(\mu)}{1 - \mu^2} A(\mu) = d, \quad 0 < \mu < 1, \tag{8}$$

$$A_0\eta^2 + A_1\eta^2 + \int_0^1 \eta^2 A(\eta) d\eta = 1/b. \tag{9}$$

It is seen that (8) is a *complete* singular integral equation with the Cauchy kernel. To prove this, substitute expansion (6) into boundary condition (3) for d. We solve equation (8) by the Carleman–Vekua regularization [15]. The approach is built around an explicit solution of the characteristic equation.

Let us introduce the auxiliary function

$$N(z) = \frac{1}{2}\int_0^1 \frac{\eta^3 A(\eta)}{\eta - z} d\eta.$$

Using the boundary values of $N(z)$ and $\lambda(z)$ reduces equation (8) to the nonhomogeneous Riemann boundary-value problem

$$\lambda^+(\mu)\left[N^+(\mu) - d - \frac{1}{2}\sum_{k=0}^{1} \frac{A_k\eta_k^3}{\mu - \eta_k}\right] = \lambda^-(\mu)\left[N^-(\mu) - d - \frac{1}{2}\sum_{k=0}^{1} \frac{A_k\eta_k^3}{\mu - \eta_k}\right], \quad 0 < \mu < 1.$$

Now recall the results for problem (4) and reduce the last equation to the problem of finding an analytic function from its zero jump over a cut:

$$X^+(\mu)\left[N^+(\mu) - d - \frac{1}{2}\sum_{k=0}^{1} \frac{A_k\eta_k^3}{\mu - \eta_k}\right] = X^-(\mu)\left[N^-(\mu) - d - \frac{1}{2}\sum_{k=0}^{1} \frac{A_k\eta_k^3}{\mu - \eta_k}\right], \quad 0 < \mu < 1.$$

Its general solution is

$$N(z) = d + \frac{1}{2}\sum_{k=0}^{1} \frac{\eta^3 A(\eta)}{z - \eta_k} + X(z)^{-1}\sum_{k=0}^{1} \frac{c_k}{z - \eta_k}, \tag{10}$$

where c_0 and c_1 are arbitrary constants.

Eliminating poles from (10) gives

$$c_k = -\frac{1}{2} A_k\eta_k^3 X(\eta_k) \quad (k = 0, 1).$$

The condition $N(\infty) = 0$ implies

$$d + c_0 + c_1 = 0. \quad (11)$$

To the auxiliary function $N(z)$, we apply the Sokhotskiĭ formula. Then we substitute (10) into the resultant expression and determine the continuum expansion coefficient:

$$\pi i \mu^3 A(\mu) = \left(\frac{1}{X^+(\mu)} - \frac{1}{X^-(\mu)}\right)\sum_{k=0}^{1}\frac{c_k}{\mu - \eta_k}. \quad (12)$$

Using (12), we will calculate the integral in (9). First, notice that

$$\int_0^1 \eta^2 A(\eta)d\eta = \sum_{k=0}^{1}\frac{2c_k}{\eta_k}[J(\eta_k) - J(0)],$$

where

$$J(\eta_k) = \frac{1}{2\pi i}\int_0^1\left[\frac{1}{X^+(\mu)} - \frac{1}{X^-(\mu)}\right]\frac{d\mu}{\mu - \eta_k} \quad (k = 0, 1).$$

The integral appearing in the formula for $J(\eta_k)$ is calculated via the following integral expression (presented without derivation):

$$\frac{1}{X(z)} = z - V_1 + \frac{1}{2\pi i}\int_0^1\left[\frac{1}{X^+(\mu)} - \frac{1}{X^-(\mu)}\right]\frac{d\mu}{\mu - z},$$

where

$$V_1 = -\frac{1}{2\pi i}\int_0^1[\ln G(\tau) - 2\pi i]d\tau.$$

It is now clear that $J(\eta_k) = X(\eta_k)^{-1} = \eta_k + V_1$. Hence,

$$J(\eta_k) - J(0) = \frac{1}{X(\eta_k)} - \eta_k - \frac{1}{X(0)}.$$

Furthermore, $J'(0) = -X'(0)/X^2(0) - 1$. Thus, the integral in (9) is

$$\int_0^1 \eta^2 A(\eta)d\eta = \sum_{k=0}^{1}\frac{2c_k}{\eta_k}\left[\frac{1}{X(\eta_k)} - \eta_k - \frac{1}{X(0)}\right],$$

which implies

$$R_2 = -\sum_{k=0}^{1}\frac{2c_k}{\eta_k}\left(\eta_k + \frac{1}{X(0)}\right), \quad (13)$$

where

$$R_l = \int_0^1 \eta^l A(\eta)d\eta + \sum_{k=0}^{1} A_k \eta_k^l \quad (l = 1, 2, 3).$$

In view of (11), substituting (13) into (9) gives

$$-\frac{2c_0 b}{X(0)}\left(\frac{1}{\eta_0} - \frac{1}{\eta_1}\right) + 2bd\left(1 + \frac{1}{\eta_1 X(0)}\right) = 1.$$

Now substitute expansion (6) into boundary condition (3). In doing so, we will take into account that the first moments of the continuum and discrete eigenfunctions are respectively expressed as

$$\int_{-1}^{1}(1 - \mu^2)F(\eta, \mu)\mu d\mu = \eta - \frac{2}{3}a\eta^3,$$

$$\int_{-1}^{1}(1 - \mu^2)F(\eta_k, \mu)\mu d\mu = \eta_k - \frac{2}{3}a\eta_k^3 \quad (k = 0, 1).$$

We thus obtain the equation

$$d\frac{q}{4(1-q)} + R_1 - \frac{2}{3}aR_3 = 0.$$

Due to (13) and (11), we finally arrive at

$$R_1 = \frac{2c_0}{X(0)}\left(\frac{1}{\eta_0} - \frac{1}{\eta_1}\right)\left(\frac{X'(0)}{X(0)} - \frac{1}{\eta_0} - \frac{1}{\eta_1}\right) - \frac{2d}{\eta_1 X(0)}\left(\frac{X'(0)}{X(0)} - \frac{1}{\eta_1}\right),$$

$$R_3 = 2c_0(\eta_1 - \eta_0) + 2d(\eta_1 - V_1).$$

The resultant system of equations uniquely determines the parameters d and c_0 of general solution (10). This completes the proof of expansions (6) and (7) for $\delta \in \Delta^+$.

EXACT IMPEDANCE FORMULAS

First, consider the case $\delta \in \Delta^+$. Differentiating (7) for electric field gives

$$e'(0) = -bw_0\left[\sum_{k=0}^{1} A_k\eta_k + \int_0^1 \eta A(\eta)d\eta\right].$$

According to the above notation, $e'(0) = -bw_0R_1$, where R_1 is determined from (13). To calculate the impedance, we start from the formula $Z = Ae(0)/e'(0)$. Since $e(0) = 1$ [see (2)], we have $Z = A/e'(0)$. With the notation

$$g(\eta_0, \eta_1) = \frac{X'(0)}{X(0)} - \frac{1}{\eta_0} - \frac{1}{\eta_1}.$$

the desired exact expression is

$$Z = \frac{A}{w_0}\frac{g - 1/\eta_0\eta_1 X(0) + q/8(1-q) - 2a(\eta_0\eta_1 X(0) + \eta_0 + \eta_1 - V_1)/3}{g[q/8(1-q) - 2a(\eta_0 + \eta_1 - V_1)/3] - 2a/3}. \quad (14)$$

With $q = 0$, formula (14) becomes

$$Z = -\frac{3A}{2aw_0}\frac{g - 1/\eta_0\eta_1 X(0) - 2a(\eta_0\eta_1 X(0) + \eta_0 + \eta_1 - V_1)/3}{g(\eta_0 + \eta_1 - V_1) + 1}. \quad (15)$$

As $q \longrightarrow 1$ (diffuse boundary conditions), the impedance tends to

$$Z = \frac{A}{w_0} g(\eta_0, \eta_1)^{-1}.$$

Now look at the case $\delta \in \Delta^-$. The same reasoning as above leads to the exact formula

$$Z = \frac{A}{w_0}\frac{g(\eta_0) + 1/\eta_0 X(0) + q/8(1-q) + 2a(\eta_0 X(0) - \eta_0 + V_1)/3}{g(\eta_0)[q/8(1-q) - 2a(\eta_0 - V_1)/3] - 2a/3}, \quad (16)$$

where $g(\eta_0) = X'(0)/X(0) - 1/\eta_0$.

For (16), consider the limits $q = 0$ and $q \longrightarrow 1$, which refer to the zero accommodation of electron tangential momentum and to diffuse boundary conditions, respectively. With $q = 0$, the impedance is

$$Z = -\frac{3A}{2aw_0} \times \frac{g(\eta_0) + 1/\eta_0 X(0) + 2a(\eta_0 X(0) + \eta_0 - V_1)/3}{g(\eta_0)(\eta_0 - V_1) + 1}. \quad (17)$$

With $q \longrightarrow 1$,

$$Z = \frac{A}{w_0} g(\eta_0)^{-1}. \quad (18)$$

LIMITING CASES

We begin with the normal skin effect. If $\delta \in \Delta^-$ ($\delta < 0$), then

$$\frac{X'(0)}{X(0)} = V'(0) = \frac{1}{\pi}\int_0^1 \arctan\frac{\pi\mu^3(1-\mu^2)}{2(\delta - p(\mu))}\frac{d\mu}{\mu^2}.$$

For large $|\delta|$'s, this yields

$$V'(0) = \frac{1}{2\delta}\int_0^1 \mu(1-\mu^2)d\mu = \frac{1}{8\delta}.$$

Since the normal skin effect is characterized by $\delta < 0$, $\eta_0 = -ri$, and $r = \sqrt{3|\delta|/2}$, we have $V'(0) - 1/\eta_0 \approx -1/\eta_0$. Consequently, if $q \longrightarrow 1$, then $Z = -A\eta_0/w_0$ [see (18)].

Furthermore,

$$V(0) = \frac{1}{\pi}\int_0^1 \arctan\frac{\pi\mu^3(1-\mu^2)}{2(\delta - p(\mu))}\frac{d\mu}{\mu},$$

$$V_1 = -\frac{1}{\pi}\int_0^1 \arctan\frac{\pi\mu^3(1-\mu^2)}{2(\delta - p(\mu))}d\mu.$$

For large $|\delta|$'s, these yield

$$V(0) = \frac{1}{2\delta}\int_0^1 \mu^2(1-\mu^2)d\mu = \frac{1}{15\delta},$$

$$V_1 = -\frac{1}{2\delta}\int_0^1 \mu^3(1-\mu^2)d\mu = -\frac{1}{24\delta}.$$

Then consider the case $q = 0$. Based on (17), we obtain the same formula: $Z = -A\eta_0/w_0$. With an arbitrary q, formula (16) gives

$$Z = -\frac{A\eta_0}{w_0}\left[1 - \frac{2(1-q)}{9\delta(q\delta + 1 - q)}\right].$$

Now, we proceed to the anomalous skin effect. First, consider the low-frequency limit. It is characterized by $w_0 = 1 + \alpha/\nu \approx 1$, $\delta = -i\delta_0$ ($\delta_0 > 0$), $\eta_0 = r\exp(-i\pi/3)$, and $r = \sqrt[3]{2|\delta|/\pi}$. Let us employ the following asymptotics for $\omega(z)$: $\omega^{\pm}(\mu) = \delta \pm i\pi\mu^3/2$. Hence,

$$V'(0) = \frac{1}{2\pi i}\int_0^1 \ln\frac{\delta + i\pi\tau^3/2}{\delta - i\pi\tau^3/2}\frac{d\tau}{\tau^2}.$$

After the change of the variable, we have $V'(0) = V'/(3r)$, where

$$V' = \frac{1}{2\pi i}\int_0^\infty x^{-4/3}\ln\frac{1-x}{1+x}dx = i\frac{\sqrt{3}}{2}(1+i\sqrt{3}).$$

Consequently, $V'(0) = V'\exp(-i\pi/3)/(3\eta_0) = i/(\sqrt{3}\eta_0) = V_0'/\eta_0$, where $V_0' = i/\sqrt{3}$. Finding the asymptotics of the expressions for $V(0)$ and V_1 as $\delta \longrightarrow 0$ and using (16), we arrive at

$$Z = \frac{A}{w_0}\frac{\eta_0}{V_0'-1},$$

or $Z = -Ar/(2w_0)$.

Turn to the high-frequency limit. It is characterized by $w_0 = -i\omega/\nu$ and $\delta > 0$. Furthermore, there are four discrete modes, for which $\eta_0 = r\exp(-i\pi/6)$ and $\eta_1 = r\exp(-i5\pi/6)$, where $r = \sqrt[3]{2\delta/\pi}$.

Let us expand $X(z)$ as $X(z) = (z-1)^{-1}\exp V_0(z)$, where

$$V_0(0) = \frac{1}{\pi}\int_0^1 \arctan\frac{\pi\tau^3(1-\tau^2)}{2(\delta - p(\tau))}\frac{d\tau}{\tau - z}.$$

Notice that V_1 is bounded if $\delta \longrightarrow 0$. Furthermore,

$$\eta_0\eta_1 X(0) = \sqrt{3\delta/2},$$

$$X'(0)/X(0) = V_0'(0) + 1, \quad \eta_0\eta_1 = -r^2.$$

The asymptotics for $\omega(z)$ enable us to find

$$V_0'(0) = \frac{1}{\pi}\int_0^1 \arctan\frac{\pi\tau^3}{2\delta}\frac{d\tau}{\tau^3}.$$

Hence, $V_0'(0) = V_0'/r$, where

$$V_0' = \frac{1}{\pi}\int_0^1 x^{-4/3}\arctan x\,dx = \frac{3}{2}\left[\frac{1}{\pi}\ln 2 - \frac{1}{2} + \frac{\sqrt{3}}{3}\right].$$

Due to (14) [or (15)], the impedance is

$$Z = \frac{A}{w_0}\frac{r}{V_0'-1}.$$

The same formula applies to diffuse boundary conditions as well. Let us find $V(0)$, $V'(0)$, and V_1. The above factorization of the dispersion function yields

$$\delta = \frac{2}{3}\eta_0^2\eta_1^2\exp(2V(0)),$$

so that $X(0) = i(\pi/4)^{2/3}\sqrt{3}\,\delta^{-1/6}$. We will demonstrate that V_1 is bounded if $\delta \longrightarrow 0$. Since $p(\mu) \approx \mu^3$, the equality

$$V_1 = -\frac{1}{\pi}\int_0^1 \arctan\frac{\pi\mu^3(1-\mu^2)}{2(\delta - p(\mu))}d\mu$$

implies

$$V_1 \approx \frac{1}{2}\int_0^1 (1-x^2)dx = \frac{1}{3}.$$

To calculate $V'(0)$, we use the following asymptotic representation of the function ω: $\omega^{\pm}(\mu) = \delta \pm i\pi\mu^3/2$. Then, we have

$$V_0'(0) = \frac{1}{\pi}\int_0^1 \arctan\frac{\pi\mu^3}{2\delta}\frac{d\mu}{\mu^2}.$$

Let x denote $\pi\mu^2/(2\delta) = x$, so that $\mu = \sqrt[3]{2\delta/\pi}$. Then

$$V_0'(0) = \frac{1}{r}\frac{1}{\pi}\int_0^\infty \arctan x\frac{dx}{x^{4/3}} = \frac{3}{\pi r}\left[\ln\sqrt{2} + \frac{\pi}{2}\left(-\frac{1}{2} + \frac{\sqrt{3}}{3}\right)\right].$$

In short, $V_0'(0) = V_0'/r$, where $V_0' = 3[\ln\sqrt{2} + \pi(-1/2 + \sqrt{3}/3)/2]/\pi$. Thus, the impedance for diffuse boundary conditions is

$$Z = \frac{A}{w_0}\frac{\sqrt{2\delta/\pi}}{V_0' - i}.$$

It can easily be proven that this formula applies in the general case as well [see (15)].

CONCLUSIONS

We developed a novel technique to obtain an analytical solution to the classical skin-effect problem in a generalized form. According to our approach, the frequency of the external electric field may take on complex values and the accommodation coefficient of electron tangential momentum q may lie anywhere between 0 and 1. The technique consists in expanding the solution to the boundary-value problem in the singular generalized eigenfunctions of the associated characteristic equation. This enabled us to investigate the problem comprehensively. In particular, we derived explicit expressions for the discrete modes of the solution and constructed the frequency region D^+ such that the problem has four discrete solutions if the frequency lies in D^+ and two discrete solutions if the frequency is outside D^+. The D^+ region boundary represents the line of critical frequencies: crossing the boundary of D^+ from the inside changes the structure of the solution.

Remarkably, the singular-eigenfunction method enabled us to reduce the problem to a complete singular integral equation with the Cauchy kernel rather than to the characteristic equation. This seems to be the first

result of its kind in transport theory. The skin-effect problem is thus opened up to the Carleman–Vekua regularization based on an explicit solution of the characteristic equation.

REFERENCES

1. C. Cercignani, *Theory and Application of the Boltzmann Equation* (American Elsevier, New York, 1975; Mir, Moscow, 1978).
2. A. A. Abrikosov, *Introduction to the Theory of Normal Metals* (Nauka, Moscow, 1972).
3. G. E. H. Reuter and E. H. Sondheimer, Proc. R. Soc. London, Ser. A **195**, 336 (1948).
4. R. B. Dingle, Physica (Amsterdam) **19**, 311 (1953).
5. P. M. Platzman and P. A. Wolff, in *Solid State Physics*, Suppl. 13 (Academic, New York, 1973; Mir, Moscow, 1975).
6. I. F. Voloshin, V. G. Skobov, L. M. Fisher, and A. S. Chernov, Zh. Éksp. Teor. Fiz. **80**, 183 (1981) [Sov. Phys. JETP **53**, 92 (1981)].
7. A. V. Latyshev, A. G. Lesskis, and A. A. Yushkanov, Teor. Mat. Fiz. **90**, 179 (1992).
8. A. V. Latyshev and A. A. Yushkanov, Zh. Vychisl. Mat. Mat. Fiz. **33**, 259 (1993).
9. K. M. Case and P. F. Zweifel, *Linear Transport Theory* (Addison-Wesley, Reading, Mass., 1967; Mir, Moscow, 1972).
10. A. V. Latyshev and A. A. Yushkanov, Zh. Vychisl. Mat. Mat. Fiz. **33**, 600 (1993).
11. A. V. Latyshev and A. A. Yushkanov, Poverkhnost, No. 2, 25 (1993).
12. V. M. Gokhfel'd, M. A. Gulyanskiĭ, M. I. Kaganov, and A. G. Plyavenek, Zh. Éksp. Teor. Fiz. **89**, 985 (1985) [Sov. Phys. JETP **62**, 566 (1985)].
13. J. M. Ziman, *Electrons and Phonons* (Clarendon, Oxford, 1960; Inostrannaya Literatura, Moscow, 1962).
14. V. S. Vladimirov, *Generalized Functions in Mathematical Physics* (Nauka, Moscow, 1976).
15. A. V. Latyshev and A. A. Yushkanov, Teor. Mat. Fiz. **92**, 127 (1992).
16. F. D. Gakhov, *Boundary-Value Problems* (Nauka, Moscow, 1977, 3rd ed.; Addison-Wesley, Reading, Mass., 1966).
17. A. V. Latyshev and A. A. Yushkanov, Teor. Mat. Fiz. **116**, 305 (1998).

Translated by A. A. Sharshakov

Technical Physics, Vol. 45, No. 8, 2000, pp. 963–970. Translated from Zhurnal Tekhnicheskoĭ Fiziki, Vol. 70, No. 8, 2000, pp. 8–15.

Resonance Vibrations of Elastic Waveguides with Inertial Inclusions

D. A. Indeĭtsev, A. D. Sergeev, and S. S. Litvin

Institute of Problems in Machine Science, Russian Academy of Sciences, Vasil'evskiĭ Ostrov, Bol'shoĭ pr. 61, St. Petersburg, 199178 Russia

Received March 2, 1999

Abstract—The problem of resonance oscillations of inertial inclusions in contact with elastic waveguides has triggered a number of theoretical investigations. It was shown [1–3] that related phenomena may be treated by solving the spectral problem posed for a differential equation that is defined in an infinitely long interval. For specific waveguide and inclusion parameters, a composite system that includes interacting objects with lumped and distributed parameters may have a mixed (continuous and line) eigenfrequency spectrum. The line spectrum may be observed both before and after the boundary frequency. It was noted [3, 4] that the presence of an isolated lumped inertial element causes the line eigenfrequency spectrum, which extends to the boundary frequency. So-called trap oscillations are responsible for this spectrum. However, little is yet known about these effects, which hinders their effective use in practice. First, conditions for trap oscillations should be generalized for the case of multielement inclusions in various infinite waveguides. Second, the effect of edge conditions on the line spectrum in a semi-infinite waveguide calls for in-depth investigation. The solution to these problems would formulate proper ways of tackling engineering challenges associated with the interaction of a railway track with high-speed rolling stock [5]. Issues discussed in this paper are also concerned with object characterization from analysis of its eigenfrequency spectrum. In recent years, this technique has gained wide acceptance in crystallography and other fields of science and technology as a promising tool for the acquisition and processing of data on the internal structure of an object. © *2000 MAIK "Nauka/Interperiodica".*

INTRODUCTION

Any extended constructions represent objects with a complex internal structure. Such objects integrate, naturally or artificially, members of highly different density, modulus of rigidity, viscosity, etc. that deform simultaneously. One basic member of such objects is a so-called elastic inertial load-carrying continuum. Other members are mounted on, or placed into, it. A rail–cross tie array is an example of an artificial structure; crystals are natural objects of this kind.

The analysis efficiency in solving applied or experimental problems is closely related to the justified selection of a real object (physical) model. Then, the physical model is supplemented by an adequate mathematical model of the object. A model for the load-carrying continuum is of greatest importance. This model should be based on previous service experience or experiments with the given object. It may happen that, in experiment, various models of the inertial continuum predict similar qualitative and quantitative (accurate to an experimental error) results. In this case, designers first consider the traditional inertial continuum model (which is the simplest in terms of mathematical description). Then, this model is replenished by inertial, elastic, and other lumped-parameter members necessary for the rigorous description of subsequent experiments.

This may explain the wide use of the Bernoulli–Euler equation of a beam on a Winkler foundation in studying the interaction of a railway track with rolling stock [5] or the wave equation in the physics of crystal lattices [6].

However, the selection of a load-carrying continuum model imposes stringent restrictions on model-refining lumped members. Specifically, if the continuum is *a priori* assumed to have string properties, moment-type interactions of the continuum with any surrounding inertial and inertialess members must be immediately excluded from consideration. This strongly restricts the elaboration of the mathematical model. It may so happen that this model will be impossible to improve by adding any finite number of lumped members.

It is known that eigenfrequency spectra bear much information on a real object's properties, particularly, its internal structure. The agreement between the real object spectrum and its mathematical model is a necessary condition for the validity of any physical theory. We, however, consider the dynamics of an object with an unknown, but *a priori*, complex internal structure for which only its eigenfrequency spectra are known from experiments. In this case, the construction of a mathematical model with a spectrally similar operator leaves many "dark spots." It remains unclear how to integrate its elementary inertial links into macrostructures.

1063-7842/00/4508-0963$20.00

In this work, the behavior of the eigenfrequency spectra of complex objects was derived by rigorously solving formally stated problems of mathematical physics. The discovered effects provide a greater possibility to experimentally test the adequacy of available mathematical models of real objects. The discussed features are expected to show up in experiments with any systems whose dynamics is simulated by the above equations.

Consider the problem of free vibrations of an infinite elastic inertial line on a Winkler foundation. It is known that this problem involves a continuous eigenfrequency spectrum. This spectrum corresponds to eigenmodes in the form of propagating undamped waves. Such a spectrum is called continuous and lies above the boundary frequency. A Winkler classical foundation implies that a system has a single boundary frequency when interacting with infinite (or semi-infinite) one-dimensional elastic inertial continua, such that their behavior is described by the string equation, Bernoulli–Euler beam equation, or Timoshenko beam equation. The boundary frequency ω_b depends on the linear mass density of an elastic line ρ and modulus of rigidity of the Winkler foundation k; that is, $\omega_b = \sqrt{k/\rho}$. It was shown [1, 2] that, if lumped elastic inertial inclusions are embedded in these infinite or semi-infinite systems, the latter, along with the continuous spectrum, may exhibit line eigenfrequency spectra. These spectra correspond to localized, or trap, vibrations. It was found, in particular, that, for strings, the line spectra of studied inclusions always lie below the boundary frequency. In the case of beams (for certain combinations of their elastic and inertial properties and those of the inclusions), these spectra may appear above the boundary frequency. Some of the previous conclusions, being valid as applied to specific situations, however need, correction upon generalizing obtained results. This refers to the sufficient condition for the existence of line spectra and the effect of edge conditions on their behavior when inclusion parameters vary according to the intrinsic properties of the elastic inertial line.

In this work, we find trap vibration spectra in elastic systems of infinite length like a string or Bernoulli–Euler beam lying on a Winkler foundation. The systems have purely inertial inclusions that lack intrinsic vibratory dynamics. In this case, the line spectrum frequencies lie below the boundary frequency ω_b. As inclusions, the following objects were considered: (1) two material points of masses m_1 and m_2 spaced at an interval L, (2) a perfectly rigid body of mass m and moment of inertia J (with respect to the center-of-mass position) that is momentlessly fixed on an elastic line at two points spaced at an interval L, and (3) two perfectly rigid bodies of masses m_1 and m_2 and moments of inertia J_1 and J_2 (with respect to the center-of-mass positions) that are fixed on an elastic line in such a way that the center-of-mass displacement coincides with that of the point of fixing and the center-of-mass rotation coincides with that of the cross section at the point of fixing. Cases 1 and 2 refer to a so-called momentless contact between the elastic line and inclusions. Case 3 means a moment-type contact interaction. Note that a moment-type line–inclusion contact is possible for a beam but impossible for a string. Various limiting processes dealt with in the above problems allow the determination of trap frequencies for a wide variety of edge conditions. This gives a chance to trace a correlation between the appearance (or disappearance) of some trap spectrum and many physical factors, such as the elastic properties of the loaded line; type of degrees of freedom of an individual, purely inertial inclusion; type of line–inclusion contact; and inclusion size.

For steady-state vibrations of two-element point inclusions of masses m_1 and m_2, the amplitudes of their transverse (relative to the equilibrium position) displacements will be denoted as W_1 and W_2. For two rigid bodies, rotations Ψ_1 and Ψ_2 are added. The position of a single-element inclusion (rigid body) is specified by the transverse displacement of its center of mass W and a rotation Ψ. The rest of the parameters are designated as follows: s, longitudinal Lagrange coordinate of an elastic-line cross section; $()' = \partial/\partial s$; $w = w(s)$, transverse displacement amplitude of a cross section with a coordinate s; $c^2 = T/\rho$, velocity of a transverse disturbance in a string (T is the string tension); $\beta^4 = C/\rho$, elastic parameter of a Bernoulli–Euler beam (C is its flexural rigidity); and N_1 and N_2 are force amplitudes acting on the elastic line at points of contact with inclusions.

INTERACTION OF STRING AND BEAM WAVEGUIDES WITH TWO POINT MASSES

Consider how trap spectra depend on inclusion parameters when a purely inertial inclusion is in momentless contact with an elastic inertial line. For frequencies below the boundary frequency ω_b, the steady-state vibration amplitude of an elastic line (string) or Bernoulli–Euler beam that lies on a Winkler foundation and has a two-point moment-type contact with an inclusion is given by

$$\begin{aligned} w'' - \lambda^2 w &= -\frac{N_1}{\rho c^2}\delta(s) - \frac{N_2}{\rho c^2}\delta(s-L), \\ \lambda^2 &= \frac{\omega_b^2 - \omega^2}{c^2} > 0, \quad \text{string}, \\ w^{IV} + 4\lambda^4 w &= \frac{N_1}{\rho\beta^4}\delta(s) + \frac{N_2}{\rho\beta^4}\delta(s-L), \\ \lambda^4 &= \frac{\omega_b^2 - \omega^2}{4\beta^4} > 0, \quad \text{beam}. \end{aligned} \tag{1}$$

The vibration amplitudes of an inclusion with two

masses m_1 and m_2 satisfy conditions

$$m_1\omega^2 W_1 = N_1, \quad m_2\omega^2 W_2 = N_2, \qquad w(0) = W_1, \quad w(L) = W_2. \tag{2}$$

For the string, the solution of (1) bounded at infinity has the form

$$w(s) = \begin{cases} \dfrac{N_1 e^{\lambda s}}{2\lambda\rho c^2} + \dfrac{N_2 e^{-\lambda(L-s)}}{2\lambda\rho c^2}, & -\infty < s \le 0; \\ \dfrac{N_1 e^{-\lambda s}}{2\lambda\rho c^2} + \dfrac{N_2 e^{-\lambda(L-s)}}{2\lambda\rho c^2}, & 0 \le s \le L; \\ \dfrac{N_1 e^{-\lambda s}}{2\lambda\rho c^2} + \dfrac{N_2 e^{\lambda(L-s)}}{2\lambda\rho c^2}, & L \le s < \infty. \end{cases} \tag{3}$$

A similar solution for the Bernoulli–Euler beam is

$$w(s) = \begin{cases} \dfrac{N_1 e^{\lambda s}}{8\lambda^3\rho\beta^4}(\cos\lambda s - \sin\lambda s) \\ + \dfrac{N_2 e^{\lambda(s-L)}}{8\lambda^3\rho\beta^4}(\cos\lambda(s-L) - \sin\lambda(s-L)), \\ -\infty < s \le 0; \\ \dfrac{N_1 e^{-\lambda s}}{8\lambda^3\rho\beta^4}(\sin\lambda s + \cos\lambda s) \\ + \dfrac{N_2 e^{\lambda(s-L)}}{8\lambda^3\rho\beta^4}(\cos\lambda(s-L) - \sin\lambda(s-L)), \\ 0 \le s \le L; \\ \dfrac{N_1 e^{-\lambda s}}{8\lambda^3\rho\beta^4}(\sin\lambda s + \cos\lambda s) \\ + \dfrac{N_2 e^{-\lambda(s-L)}}{8\lambda^3\rho\beta^4}(\sin\lambda(s-L) + \cos\lambda(s-L)), \\ L \le s < \infty. \end{cases} \tag{4}$$

In both cases, the vibration amplitude exponentially drops with distance from the line–inclusion contact region; hence, waveguide vibrations are localized near the inclusions.

Matching the string or beam equation [equations (1)] with the inclusion equation [expression (2)] yields two expressions for the spectral parameter ω^2:

$$\frac{m_1 m_2 \omega^2_{\mathrm{I,II}}}{\lambda_{\mathrm{I,II}}\rho c^2 (m_1 + m_2)}(1 - e^{-2\lambda_{\mathrm{I,II}}L}) = 1 \mp \sqrt{1 - \frac{4m_1 m_2 (1 - e^{-2\lambda_{\mathrm{I,II}}L})}{(m_1 + m_2)^2}}. \tag{5}$$

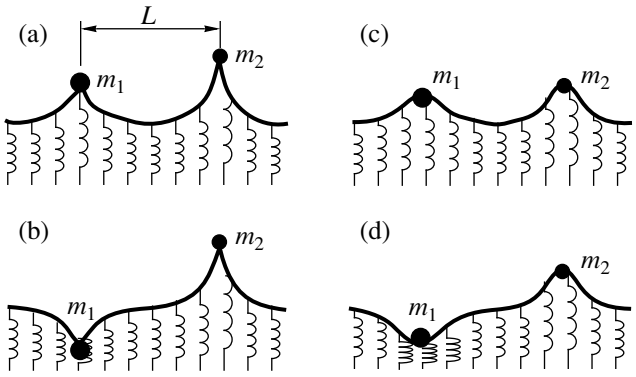

Fig. 1. Symmetric and asymmetric localized vibrations in (a, b) string and (c, d) beam waveguides with two-point inclusions. Shape "b" disappears when the interinclusion distance is less than L_*.

for the string and

$$\frac{m_1 m_2 \omega^2_{\mathrm{I,II}}(1 - e^{-2\lambda_{\mathrm{I,II}}L}(1 + \sin 2\lambda_{\mathrm{I,II}}L))}{4\lambda^3_{\mathrm{I,II}}\rho\beta^4(m_1 + m_2)} = 1 \mp \sqrt{1 - \frac{4m_1 m_2 (1 - e^{-2\lambda_{\mathrm{I,II}}L}(1 + \sin 2\lambda_{\mathrm{I,II}}L))}{(m_1 + m_2)^2}} \tag{6}$$

for the beam.

With the minus sign in (5) and (6), we find the eigenfrequency ω_{I}^2 of conventionally symmetric waveguide vibrations (Figs. 1a, 1c); the plus sign gives the eigenfrequency ω_{II}^2 of conventionally asymmetric waveguide vibrations (Figs. 1b, 1d) (if $m_1 = m_2$, vibrations become symmetric or asymmetric in the strict sense).

Consider limiting cases for (5) and (6). If $L \longrightarrow 0$, we have

$$\frac{(m_1 + m_2)\omega_{\mathrm{I}}^2}{2\rho c\sqrt{\omega_b^2 - \omega_{\mathrm{I}}^2}} = 1, \quad \frac{m_1 m_2 L \omega_{\mathrm{II}}^2}{\rho c^2 (m_1 + m_2)} = 1$$

for the string and

$$\frac{(m_1 + m_2)\omega_{\mathrm{I}}^2}{2\sqrt{2}\rho\beta(\omega_b^2 - \omega_{\mathrm{I}}^2)^{3/4}} = 1, \qquad \frac{m_1 m_2 L \omega_{\mathrm{II}}^2}{2\rho\beta^4(m_1 + m_2)(\omega_b^2 - \omega_{\mathrm{II}}^2)^{1/2}} = 1 \tag{7}$$

for the beam.

If one of the masses (e.g., m_1) in (5) is taken infinitely large, one comes to the frequency equation of vibration for an infinite string that has a point inertial inclusion of mass m_2 placed at a distance L from a hinged waveguide point with the coordinate $s = 0$. It is

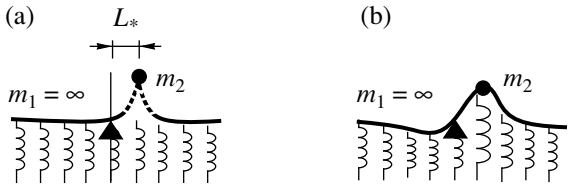

Fig. 2. Localized vibrations of a point inertial inclusion in a (a) semi-infinite string waveguide and (b) beam waveguide with hinged support. Shape "a" disappears when the distance between the inclusion and waveguide boundary is less than L_*.

easy to check that results thus obtained completely coincide with those for a semi-infinite string with a point inertial inclusion of mass m_2 placed at a distance L from the rigidly fixed beginning of the waveguide $s = 0$. If m_1 tends to infinity in the beam waveguide problem [that is, in (6)], we arrive at the frequency equation of vibration for an infinite beam with a point inertial inclusion of mass m_2 placed at a distance L from a hinged waveguide point with the coordinate $s = 0$ (but not for a semi-infinite beam!). Thus, we have

$$\omega_{\mathrm{I}}^2 = 0, \quad \frac{m_2\omega_{\mathrm{II}}^2}{\lambda_{\mathrm{II}}\rho c^2}(1 - e^{-2\lambda_{\mathrm{II}}L}) = 1$$

for the string and

$$\omega_{\mathrm{I}}^2 = 0, \quad \frac{m_2\omega_{\mathrm{II}}^2}{8\lambda_{\mathrm{II}}^3\rho\beta^4}(1 - e^{-2\lambda_{\mathrm{II}}L}(1 + \sin 2\lambda_{\mathrm{II}}L)) = 1 \quad (8)$$

for the beam.

At $L \longrightarrow 0$ in (8), we obtain the limiting equations

$$\omega_{\mathrm{I}}^2 = 0, \quad \frac{m_2\omega_{\mathrm{II}}^2 L}{\rho c^2} = 1$$

for the string and

$$\omega_{\mathrm{I}}^2 = 0, \quad \frac{m_2\omega_{\mathrm{II}}^2 L}{2\beta^2(\omega_b^2 - \omega_{\mathrm{II}}^2)^{1/2}} = 1 \quad (9)$$

for the beam.

The condition $\omega_{\mathrm{I}} = 0$ means that the system moves as a rigid unit. Since the hinged point with the coordinate $s = 0$ makes the infinitely large mass m_1 immobile, the zero frequency correlates with the system at rest in this case.

If the distance L between the masses is less than

$$L_* \approx \frac{\rho c^2(m_1 + m_2)}{m_1 m_2 \omega_b^2}, \quad L_* = L|_{m_1 = \infty} \approx \frac{\rho c^2}{m_2\omega_b^2}, \quad (10)$$

equations (7) and (9) for the string give real values of the trap frequency ω_{II} that no longer satisfy the condition $\omega_{\mathrm{II}} < \omega_b$. The former equation in (10) gives L_* for a string with a two-mass inclusion; and the latter, for a string with a single hinged point and one-mass inclusion.

As follows from (7) and (9) for a string waveguide, there should exist a distance between inertial inclusions such that the realness and positiveness conditions for the square of the eigenfrequencies are violated. In this case, the associated eigenfrequency spectrum becomes complex, the existence criteria for localized undamped vibrations responsible for the given eigenfrequency are violated, and this localized vibration mode disappears (Figs. 1b, 2a).

However, more thorough analysis is needed to generalize the conditions necessary for such a phenomenon to occur. The drift of ω_{II} beyond the boundary frequency with decreasing distance between the masses or to the fixed support (Fig. 2b) is not predicted from the above results for a Bernoulli–Euler beam with similar inclusions.

INTERACTIONS OF STRING AND BEAM WAVEGUIDES WITH A RIGID BODY UNDER MOMENTLESS TWO-POINT CONTACT

Consider elastic lines momentlessly interacting with a single rigid body. Recall that its location is specified by the center-of-mass position and a rotation about a certain axis. For a rigid inclusion in momentless symmetric contact with an elastic line, conditions (2) are replaced by

$$m\omega^2 W_0 = N_1 + N_2, \quad J\omega^2\Psi_0 = -\frac{L}{2}N_1 + \frac{L}{2}N_2,$$
$$w(0) = W_0 - \frac{L\Psi_0}{2}, \quad w(L) = W_0 + \frac{L\Psi_0}{2}. \quad (11)$$

From the latter, we come to the equations for frequencies of symmetric (subscript I) and asymmetric (subscript II) elastic-line vibrations:

$$\frac{m\omega_{\mathrm{I}}^2(1 + e^{-\lambda_{\mathrm{I}}L})}{4\lambda_{\mathrm{I}}\rho c^2} = 1, \quad \frac{J\omega_{\mathrm{II}}^2(1 - e^{-\lambda_{\mathrm{II}}L})}{\lambda_{\mathrm{II}}\rho c^2 L^2} = 1$$

for the string and

$$\frac{m\omega_{\mathrm{I}}^2(1 + e^{-\lambda_{\mathrm{I}}L}(\cos\lambda_{\mathrm{I}}L + \sin\lambda_{\mathrm{I}}L))}{16\lambda_{\mathrm{I}}^3\rho\beta^4} = 1,$$
$$\frac{J\omega_{\mathrm{II}}^2(1 - e^{-\lambda_{\mathrm{II}}L}(\sin\lambda_{\mathrm{II}}L + \cos\lambda_{\mathrm{II}}L))}{4\lambda_{\mathrm{II}}^3\rho\beta^4 L^2} = 1 \quad (12)$$

for the beam.

Localized vibrations of a string with a fixed rigid body are represented in Fig. 3a. Similar vibrations of a beam are shown in Figs. 3c and 3d.

If $m \longrightarrow \infty$, (12) can be recast as

$$\omega_{\mathrm{I}}^2 = 0, \quad \frac{J\omega_{\mathrm{II}}^2(1-e^{-\lambda_{\mathrm{II}}L})}{\lambda_{\mathrm{II}}\rho c^2 L^2} = 1$$

for the string and

$$\omega_{\mathrm{I}}^2 = 0,$$
$$\frac{J\omega_{\mathrm{II}}^2(1-e^{-\lambda_{\mathrm{II}}L}(\sin\lambda_{\mathrm{II}}L+\cos\lambda_{\mathrm{II}}L))}{4\lambda_{\mathrm{II}}^3\rho\beta^4 L^2} = 1 \qquad (13)$$

for the beam. Relationships (13) yield the frequency equations for a rigid solid that has a fixed center of mass and is in two-point contact with an elastic line. For $J \longrightarrow \infty$, we obtain

$$\frac{m\omega_{\mathrm{I}}^2(1+e^{-\lambda_{\mathrm{I}}L})}{4\lambda_{\mathrm{I}}\rho c^2} = 1, \quad \omega_{\mathrm{II}}^2 = 0$$

for the string and

$$\frac{m\omega_{\mathrm{I}}^2(1+e^{-\lambda_{\mathrm{I}}L}(\cos\lambda_{\mathrm{I}}L+\sin\lambda_{\mathrm{I}}L))}{16\lambda_{\mathrm{I}}^3\rho\beta^4} = 1,$$
$$\omega_{\mathrm{II}}^2 = 0 \qquad (14)$$

for the beam. These relationships are frequency equations for vibration of a rigid body that momentlessly interacts with an elastic line at two points without rotation.

If m and J in (12) jointly tend to infinity, we obtain $\omega_{\mathrm{I}}^2 = 0$ and $\omega_{\mathrm{II}}^2 = 0$ for both beam and string. This is a well-known result, indicating that string and beam systems with two fixed hinged supports do not have transverse vibration frequencies lying below the boundary frequency of line spectra.

If $L \longrightarrow 0$ in (12), we obtain

$$\frac{m\omega_{\mathrm{I}}^2}{2\rho c\sqrt{\omega_b^2-\omega_{\mathrm{I}}^2}} = 1, \quad \frac{J\omega_{\mathrm{II}}^2}{\rho c^2 L} = 1$$

for the string and

$$\frac{m\omega_{\mathrm{I}}^2}{2\sqrt{2}\rho\beta(\omega_b^2-\omega_{\mathrm{I}}^2)^{3/4}} = 1,$$
$$\frac{J\omega_{\mathrm{II}}^2}{2\rho\beta^2 L\sqrt{\omega_b^2-\omega_{\mathrm{II}}^2}} = 1 \qquad (15)$$

for the beam.

Thus, in this case, the beam does not have, but the string has, the limiting (maximum) distance between contact points. As this distance grows, the higher frequency of localized vibrations of a string with two purely mass inclusions disappears:

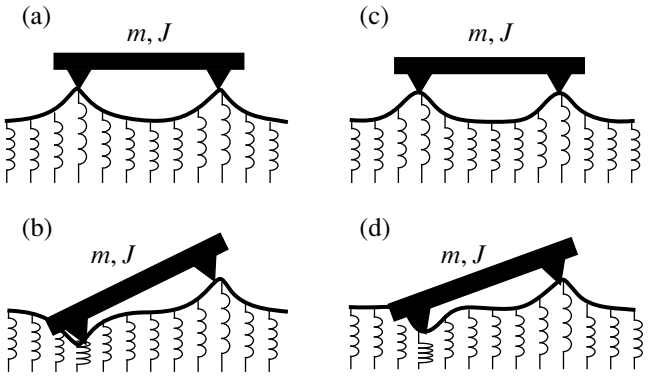

Fig. 3. Symmetric and asymmetric localized vibrations in (a, b) string and (c, d) beam waveguides in momentless contact with a rigid body. Shape "b" is disappearing.

$$\omega_b^2 > \omega_{\mathrm{II}}^2 \approx \frac{\rho c^2 L}{J}, \Rightarrow L_{**} \approx \frac{J\omega_b^2}{\rho c^2}. \qquad (16)$$

As was demonstrated, the effect of the disappearance or conservation of the higher trap spectrum immediately depends on the type of elastic inertial continuum. Also, this effect is not a mere consequence of a rising number of degrees of freedom of a single inclusion. Nor is it directly associated with types of elastic line–inclusion contact.

To confirm the last statement, we will present expressions for trap spectra of free vibrations in the case of a purely inertial inclusion that has two intrinsic degrees of freedom and is in moment-type contact with a Bernoulli–Euler beam. These are line spectra of free vibrations of a system consisting of a rigid body (bodies) fixed at its center of mass and lying on a Bernoulli–Euler beam supported by a Winkler foundation:

$$\frac{\beta^3 m\omega_{\mathrm{I}}^2}{\sqrt{2}\rho(\omega_b^2-\omega_{\mathrm{I}}^2)^{3/4}} = 1, \quad \frac{\beta J\omega_{\mathrm{II}}^2}{2\sqrt{2}\rho(\omega_b^2-\omega_{\mathrm{II}}^2)^{1/4}} = 1. \qquad (17)$$

Free vibrations at these frequencies are shown in Figs. 4a–4c.

Putting $m = \infty$ in (17), we arrive at the frequency equation for vibrations of an infinite beam hinged at a point with the coordinate $s = 0$. This point coincides with the center of mass of a perfectly rigid body interacting with a waveguide and having a moment of inertia J:

$$\omega_{\mathrm{I}}^2 = 0, \quad \omega_{\mathrm{II}}^2 = \frac{2\sqrt{2}\rho(\omega_b^2-\omega_{\mathrm{II}}^2)^{1/4}}{J\beta}. \qquad (18)$$

Putting $J = \infty$ in (17), we arrive at the frequency equation for vibrations of an infinite beam supported at a point with the coordinate $s = 0$. This support is a slid-

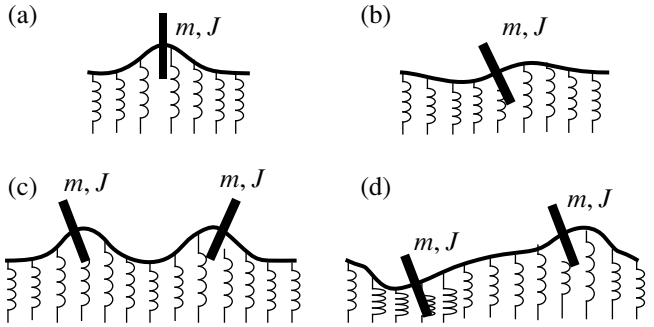

Fig. 4. Symmetric and asymmetric localized vibrations in a beam waveguide in point moment-type contact with (a, b) one- and (c, d) two-element rigid inclusions.

ing attachment of mass m:

$$\omega_{\mathrm{I}}^2 = \frac{2\sqrt{2}\rho(\omega_b^2 - \omega_{\mathrm{I}}^2)^{3/4}}{m\beta^3}, \quad \omega_{\mathrm{II}}^2 = 0. \tag{19}$$

It is easy to notice that the localized vibration mode disappears in none of the situations considered, as opposed to the previous cases for the string.

INTERACTION OF A BEAM WAVEGUIDE WITH TWO SOLIDS BEING IN MOMENT POINT CONTACT WITH AN ELASTIC INERTIAL CONTINUUM

To elucidate the effect of interest in an infinite beam system, we will determine steady-state vibration frequencies of a beam lying on a Winkler foundation and being in point moment contact with two rigid inclusions. We assume the frequencies to be below the boundary frequency ω_b. Divide the infinite region occupied by the elastic line into three sections: those on the left and on the right of both inclusions and the region between them. For each of the sections, we write the elastic line equations and edge conditions:

$$\begin{gathered} w^{\mathrm{IV}} + 4\lambda^4 w = 0, \quad \lambda^4 = \frac{\omega_b^2 - \omega^2}{4\beta^4} > 0, \\ w(0) = W_1, \quad w(L) = W_2, \\ w'(0) = \Psi_1, \quad w'(L) = \Psi_2, \end{gathered} \tag{20}$$

as well as the joining conditions for the partial (section) solutions:

$$\begin{aligned} m_1\omega^2 W_1 &= \rho\beta^4 w_+'''(0) - \rho\beta^4 w_-'''(0), \\ J_1\omega^2\Psi_1 &= -\rho\beta^4 w_+''(0) + \rho\beta^4 w_-''(0), \\ m_2\omega^2 W_2 &= \rho\beta^4 w_+'''(L) - \rho\beta^4 w_-'''(L), \\ J_2\omega^2\Psi_2 &= -\rho\beta^4 w_+''(L) + \rho\beta^4 w_-''(L). \end{aligned} \tag{21}$$

The solution of problem (20)–(21) bounded at infinity and localized near the contacts with the inclusions is given by

$$w(s) = \begin{cases} \dfrac{e^{\lambda s}}{4\lambda^3\beta^4}(A_1\cos\lambda s + D_1\sin\lambda s), \\ -\infty < s \le 0; \\ \dfrac{e^{-\lambda s}}{4\lambda^3\beta^4}(P\cos\lambda s + Q\sin\lambda s) \\ + \dfrac{e^{\lambda(s-L)}}{4\lambda^3\beta^4}(H\cos\lambda(s-L) + K\sin\lambda(s-L)), \\ 0 \le s \le L; \\ \dfrac{e^{-\lambda(s-L)}}{4\lambda^3\beta^4}(B_2\cos\lambda(s-L) + S_2\sin\lambda(s-L)), \\ L \le s < \infty, \end{cases} \tag{22}$$

where A_1, D_1, P, Q, H, K, B_2, and S_2 are constants.

The joining conditions give the set of equations

$$\begin{gathered} \frac{m_1\omega^2 W_1}{2\rho\beta^4} = P, \quad \frac{m_2\omega^2 W_2}{2\rho\beta^4} = H, \\ \frac{\lambda J_1\omega^2\Psi_1}{\rho\beta^4} = -P + Q, \quad \frac{\lambda J_2\omega^2\Psi_2}{\rho\beta^4} = H + K. \end{gathered} \tag{23}$$

Let both rigid bodies (two-element inclusion) be identical. Then, the frequencies of symmetric and asymmetric vibrations are found independently. Since the localized vibrations may disappear with decreasing interelement distance, the behavior of these spectra at $L \longrightarrow 0$ seems to be the most interesting.

We will find the symmetric vibration frequencies by putting $W_1 = W_2 = W_s$ and $\Psi_1 = -\Psi_2 = \Psi_s$. Then, at $L \longrightarrow 0$, one obtains from set (23)

$$\begin{gathered} \lambda L\left(\frac{m\omega^2}{4\lambda^3\rho\beta^4} - 1\right)\lambda W_s + \Psi_s = 0, \\ \lambda L\lambda W_s + \left(\frac{LJ\omega^2}{2\rho\beta^4} - 1\right)\Psi_s = 0. \end{gathered} \tag{24}$$

For the free symmetric vibrations of a beam waveguide with two rigid inclusions, the frequencies obtained from the existence condition for the nontrivial solution of (24) are

$$\omega_{s\mathrm{I}}^2 = 0, \quad \omega_{s\mathrm{II}}^2 = \frac{2\rho\beta^4}{JL} + \frac{4\lambda_{s\mathrm{II}}^3\rho\beta^4}{m}. \tag{25}$$

The symmetric vibrations are depicted in Fig. 4c.

The presence of zero frequency among the roots of the characteristic equation merits attention. As is known, the zero frequency implies that a system moves

as a rigid unit. However, in our infinite system, unlimited displacements of the inertial inclusions are impossible because of the Winkler foundation. This apparent conflict is due to the fact that the frequencies were calculated using the limiting equations obtained from (23) at $L \longrightarrow 0$. The frequency equation coincident with the first equation in (17) yields a more accurate value of $\omega_{s\mathrm{I}}^2$. For the refined frequency, system vibrations are shown in Fig. 4a.

For asymmetric vibrations, the frequencies are found by putting $W_1 = -W_2 = W_a$ and $\Psi_1 = \Psi_2 = \Psi_a$. At $L \longrightarrow 0$, we obtain from (23)

$$\begin{aligned} &\left(\frac{L^2 m\omega^2}{8\lambda\rho\beta^4} - 1\right)2\lambda W_a - \lambda L\Psi_a = 0, \\ &-2\lambda W_a + \left(\frac{LJ\omega^2}{2\rho\beta^4} - 1\right)\lambda L\Psi_a = 0. \end{aligned} \tag{26}$$

The frequencies of free asymmetric vibrations of the beam waveguide with two rigid inclusions are as follows:

$$\omega_{a\mathrm{I}}^2 = 0, \quad \omega_{a\mathrm{II}}^2 = \frac{2\rho\beta^4}{JL} + \frac{8\lambda_{a\mathrm{II}}\rho\beta^4}{mL^2}. \tag{27}$$

The corresponding asymmetric vibrations are given in Fig. 4d. Like the symmetric vibration spectrum, they possess the zero eigenfrequency. It is associated with the rotation of both inertial inclusions with equal constant velocities. The reason for its appearance is the same as in the previous case. The exact value of $\omega_{a\mathrm{I}}^2$ is derived from the frequency equation coincident with the second expression in (17). The shape of the vibrations for this case is shown in Fig. 4b.

The appearance of both zero frequencies is very important from the physical viewpoint. This means that, as the interinclusion distance diminishes, the approximate frequency equations become "insensitive" to the presence of the Winkler foundation. Under such conditions, these equations predict that the entire system will behave as a rigid unit.

For high-frequency components of the trap spectra, approximate frequency equations (25) and (27) give the same interinclusion distance, namely,

$$L_* \approx \frac{2\rho\beta^4}{J\omega_b^2}, \tag{28}$$

at which these spectra disappear when exceeding the boundary frequency.

Now we proceed with the limiting case when a rigid body interacts with a semi-infinite beam fixed at its beginning. We put the mass and moment of inertia of the body fixed at the point $s = 0$ tending to infinity. Then, $W_1 = 0$ and $\Psi_1 = 0$. Under such conditions, the frequency equation derived from (23) at $L \longrightarrow \infty$ results in the same effect: the upper frequency of the line spectrum disappears on exceeding the boundary frequency:

$$\omega_{\mathrm{I}}^2 = \frac{\rho\beta^2\sqrt{\omega_b^2 - \omega_{\mathrm{I}}^2}}{m_2 L_b}, \quad \omega_{\mathrm{II}}^2 = \frac{\rho\beta^4}{J_2 L_b}. \tag{29}$$

With (23), one can obtain frequency spectra of free localized vibrations for variously posed two-body problems: the centers of mass of both bodies are fixed, neither one can rotate, the center of mass of one body is fixed and the other cannot rotate, etc. In each of these problems, the localized vibration modes of the beam waveguide disappear. In fact, for this to take place, it is sufficient that at least one of the inertial elements of a two-element inertial inclusion interacting with a Bernoulli–Euler beam have the inertia of a rigid solid and that the beam–inclusion interaction be of moment-type character.

DISCUSSION

The string and beam waveguides considered in this work are partial mathematical models. They, however, to some degree of approximation account for the possible behavior of real objects under service or in experiments. The disappearance of one line spectrum when the parameters of an inertial inclusion are varied seems to be rather intriguing in this respect. Since the eigenfrequencies of a linear system become resonant in the presence of an external harmonic action on the system, this effect can be used for thoroughly examining the internal structure of a continuum with massive inertial inclusions. The very discovery of this effect is an indication that an object is of an essentially discrete–continuous nature. However, distributed members, lumped inclusions, and interactions between them need to be identified. If information on any of these components is available, the effect of the appearance or disappearance of the trap mode can help to clarify the properties of the others. As follows from the aforesaid, a new trap resonance frequency appears or disappears if variations of the geometric and inertial inclusion parameters are specially matched to the properties of all the components of complex systems (comprising elastic inertial continuum, noninertial elastic continuum, and purely inertial inclusions). The new mode is lost when the disturbance energy is transferred from the near-inclusion region to the elastic inertial continuum and disappears when the energy is confined in the vicinity of the inclusion [1–3].

With very simple mechanical models, it was demonstrated that the spectra of two closely related systems may qualitatively behave in a fundamentally different way when their parameters are varied similarly. It is noteworthy that the qualitative distinction due to radically differing internal properties of objects is observed only in a rather narrow frequency range. This is of special significance for systems where the variations occur in a natural manner; i.e., the parameters vary during

operation. Specifically, the case in point is transport problems. In fact, such a situation may arise when a train approaches some railway irregularity (bridge, viaduct, or switch). In these cases, the joint railway–track dynamics inevitably necessitates the solution to problems like those considered in this work. Obviously, some of them are still more complicated because of the need for taking into account the continuously varying interinclusion distance. For this reason, they cannot be treated rigorously. Here, the role of tests, which allow the qualitative prediction and correct interpretation of results, increases.

Analytical methods can be applied to one-dimensional elastic inertial (string and beam) and noninertial (Winkler foundation) continua with inclusions having no more than two elements. Only in these cases can we find analytical solutions to a number of like problems for each of the elastic lines and compare them. This is, however, a rarely encountered exception. In our opinion, the value of our results is that they provide a better insight into similar phenomena in two- and three-dimensional continua with a complex structure. Examples are the upper part of a railway track or crystals, where a model problem is hard to solve analytically.

REFERENCES

1. V. A. Babeshko, B. V. Glushkov, and N. F. Vinchenko, *Dynamics of Inhomogeneous Linearly Elastic Media* (Nauka, Moscow, 1989).
2. A. K. Abramyan, V. L. Andreev, and D. A. Indeĭtsev, Model. Mekh. **6**, 34 (1992).
3. A. K. Abramyan, V. V. Alekseev, and D. A. Indeĭtsev, Zh. Tekh. Fiz. **68** (3), 15 (1998) [Tech. Phys. **43**, 278 (1998)].
4. G. G. Denisov, E. K. Kugusheva, and V. V. Novikov, Prikl. Mat. Mekh. **49**, 691 (1985).
5. G. M. Shakhunyants, *Railway Track* (Transport, Moscow, 1987).
6. L. Brillouin and M. Parodi, *Wave Propagation in Periodic Structures* (Dover, New York, 1953; Inostrannaya Literatura, Moscow, 1959).

Translated by V. Isaakyan

Technical Physics, Vol. 45, No. 8, 2000, pp. 971–979. Translated from Zhurnal Tekhnicheskoĭ Fiziki, Vol. 70, No. 8, 2000, pp. 16–24.

A High-Gradient Accelerator Based on a Faster-than-Light Radiation Source

Yu. N. Lazarev and P. V. Petrov

All-Russia Research Institute of Technical Physics, Russian Federal Nuclear Center
Snezhinsk, Chelyabinsk oblast, 456770 Russia

Received March 23, 1999

Abstract—A wide-band microwave generator using a faster-than-light source is proposed to be used as a charged particle accelerator. According to theoretical estimates, an electric field amplitude as high as ~10^{11} V/m or more can be attained at the focus of a paraboloidal emitting surface with a focal parameter of ~1 m. These estimates are supported by numerical calculations. The schematic diagram of such an accelerator is suggested.

INTRODUCTION

Wide-band microwave generators based on a faster-than-light (FTL) emission source are very promising for applications [1]. In particular, emission directivity in these generators is provided by the shape of the emitting surface, and the direction of emission coincides with that of the specular reflection of emission-inducing radiation. Thus, the focusing of FTL emission presents no problems. This raises the question of whether the electric field intensity at the focus can be increased to the point where it can be used for accelerating charged particles.

Consider a plane laser beam propagating along the axis of a paraboloid. Let the paraboloid consist of radiating elements similar to those described in [1]. Let also the inner surface of the paraboloid be exposed to the laser beam (Fig. 1).

Electromagnetic radiation generated by such an FTL emission source must be focused at the paraboloid focus and must greatly increase the field intensity. The electromagnetic energy fluxes near the paraboloid surface and at the focus should coincide:

$$E_0^2 r_0^2 \sim E^2 \lambda\!\!\!^{-2}. \tag{1}$$

Hence, the electric field at the focus can be estimated as

$$E \sim E_0 \frac{r_0}{\lambda\!\!\!^{-}}, \tag{2}$$

where E is the electric field at the paraboloid focus, E_0 is the electric field near the paraboloid surface, r_0 is the paraboloid radius in the focal plane, and $2\pi\lambda\!\!\!^{-}$ is the electromagnetic radiation wavelength. The field amplitude near the paraboloid surface can readily be determined using the results obtained in [1]:

$$E_0 \sim \frac{\varepsilon_f}{e\lambda\!\!\!^{-}}, \tag{3}$$

where ε_f is the energy of electrons emitted from the anode of the microwave source placed on the paraboloid surface.

Thus,

$$E \sim \frac{\varepsilon_f}{e\lambda\!\!\!^{-}} \frac{r_0}{\lambda\!\!\!^{-}}. \tag{4}$$

If a particle of charge e and mass M is accelerated by this field, it gains a momentum p,

$$p \sim eE\frac{\lambda\!\!\!^{-}}{c} \sim \frac{\varepsilon_f}{c}\frac{r_0}{\lambda\!\!\!^{-}}, \tag{5}$$

and energy ε_a,

$$\varepsilon_a \sim \begin{cases} \varepsilon_f \dfrac{r_0}{\lambda\!\!\!^{-}}, & \dfrac{p}{Mc} > 1, \\ \dfrac{\varepsilon_f^2}{Mc^2}\left(\dfrac{r_0}{\lambda\!\!\!^{-}}\right)^2, & \dfrac{p}{Mc} < 1. \end{cases} \tag{6}$$

The values of $\varepsilon_f \sim 10^2$–10^3 keV, $\lambda\!\!\!^{-} \sim 0.1$–1 cm, and

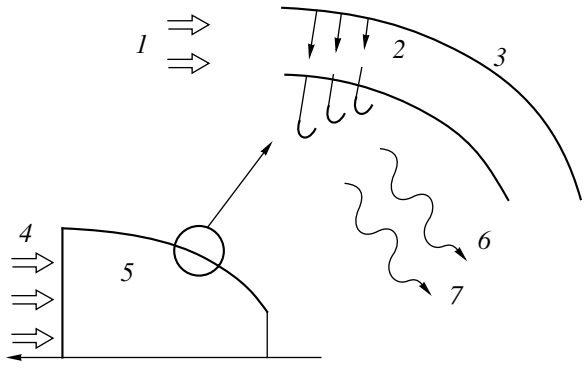

Fig. 1. Schematic diagram of an FTL paraboloid source: (*1*) photons, (*2*) emitted electrons, (*3*) photoemitter, (*4*) laser radiation front, (*5*) paraboloid surface, (*6*) accelerating charge; and (*7*) electromagnetic wave.

1063-7842/00/4508-0971$20.00 © 2000 MAIK "Nauka/Interperiodica"

$r_0/\lambda\!\!\!^{-} \sim 10^2$–$10^3$ seem to be attainable. Thus, it is hoped that the energy of the accelerated particle may run to about 1 GeV with a comparatively small-size accelerator (several meters). Since the acceleration length is about $\lambda\!\!\!^{-}$, the accelerating gradient can be as high as ~10 GeV/m or even more. Rigorous treatment of the problem using analytical and numerical methods supports this result.

ANALYTICAL CALCULATIONS

Electron acceleration. The analytical expression for the intensity of an electric field generated by an FTL pulse on the inner surface of the paraboloid,

$$z_p(\rho) = \frac{\rho^2}{2r_0} - \frac{r_0}{2},$$

can be obtained with the retarded potentials in the Lorentz gauge:

$$\varphi(\mathbf{r}) = \int dv' \frac{\rho\left(t - \frac{|\mathbf{r}-\mathbf{r}'|}{c}\right)}{|\mathbf{r}-\mathbf{r}'|}$$
$$\mathbf{A}(\mathbf{r}) = \int dv' \frac{\mathbf{j}\left(t - \frac{|\mathbf{r}-\mathbf{r}'|}{c}\right)}{|\mathbf{r}-\mathbf{r}'|}. \quad (7)$$

Considering that

$$\mathbf{E} = -\nabla\varphi - \frac{1}{c}\frac{\partial \mathbf{A}}{\partial t} \quad (8)$$

and assuming that the emission current is directed normally to the paraboloid surface, i.e.,

$$\mathbf{j}(t, z, \rho) = j_\perp\left(t + \frac{z}{c}, z, \rho\right)\mathbf{n},$$
$$\mathbf{n} = \frac{1}{\sqrt{1 + \left(\frac{\rho}{r_0}\right)^2}}\left\{-\frac{\rho}{r_0}; 1\right\}, \quad (9)$$

we obtain the expression for the field component along the paraboloid axis

$$E_z = -\frac{1}{c^2}\int \frac{dv'}{r}\sin(\alpha)\cos\left(\frac{\alpha}{2}\right)\frac{\partial j_\perp}{\partial t}, \quad (10)$$

where α is the angle between the axis OZ and vector $\mathbf{r}'$ (Fig. 2).

In our case, the dipole approximation can be applied:

$$E_z = E_0 \int_0^{2\pi}\frac{d\varphi}{2\pi}\int_{\omega_0}^{\omega_k} d\omega \frac{1+\omega}{1-\omega} f\left(\tau + \frac{z}{\lambda\!\!\!^{-}}\omega + \frac{\rho}{\lambda\!\!\!^{-}}\sqrt{1-\omega^2}\cos(\varphi)\right), \quad (11)$$
$$E_0 = \frac{2\pi r_0 P_0}{\lambda\!\!\!^{-2}}.$$

Here, $\omega = z'/z' + r_0$, z' is the coordinate of the vector $\mathbf{r}'$, (z_0, ρ_0) and (z_k, ρ_k) are the coordinates of the extreme points of the paraboloid, $\omega_0 = z_0/z_0 + r_0$, $\omega_k = z_k/z_k + r_0$, z and ρ are the cylindrical coordinates of the vector $\mathbf{r}$, $\mathbf{P}_0$ is the amplitude of the dipole moment surface density,

$$\tau = \frac{1}{T_p} - \frac{(z_k - z')}{cT_p},$$

T_p is the characteristic time of variation of the dipole moment, $\lambda\!\!\!^{-} = cT_p$, r_0 is the paraboloid radius in the focal plane,

$$f(x) = \eta(x)\frac{d}{dx}F(x), \quad F(x) = 2.17x^2\exp(-x) \quad (12)$$

is a dimensionless function specified for a pumping source that provides a linear growth of the radiation intensity, and $\eta(x)$ is the Heaviside function.

At the paraboloid axis,

$$E_z = E_0\int_{\omega_0}^{\omega_k} d\omega \frac{1+\omega}{1-\omega} f\left(\tau + \frac{z}{\lambda\!\!\!^{-}}\omega\right). \quad (13)$$

The parameter ω varies from –1 to +1 over the paraboloid surface. It follows from the expression for

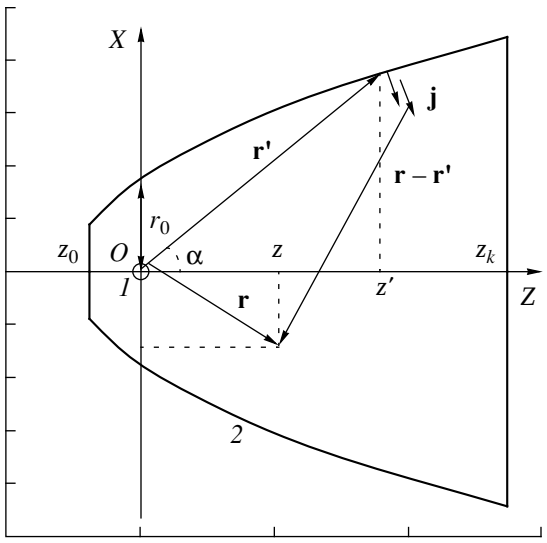

Fig. 2. Geometry used in computations: (*1*) focus and (*2*) paraboloid surface.

E_z that the phase velocity of the field is $c/\omega > c$, because

$$\frac{\omega}{\lambda}\frac{dz}{dt} + \frac{d\tau}{dt} = 0 \Rightarrow \frac{dz}{dt} = \frac{c}{\omega}. \quad (14)$$

Obviously, the closer the velocity of particles to the phase velocity of the field, the higher the acceleration efficiency. Therefore, truncated paraboloids with $|\omega| \approx 1$ are of particular interest. Paraboloids with $\omega \sim 1$ are preferable because of the factor $(1 + \omega)/(1 - \omega)$ in the integrand for E_z. The physical meaning of this factor is clear: the dipole radiation field is maximum in the plane perpendicular to the dipole axis, whereas the dipole does not emit along its axis. When $\omega \longrightarrow -1$, the angle between the dipole axis and direction toward the focus tends to zero; when $\omega \longrightarrow 1$, this angle tends to $\pi/2$. Only paraboloids with ω_k, $\omega_0 \approx 1$ are therefore considered in further discussions.

For the points with coordinates (z, $\rho = 0$) lying on the paraboloid axis in the vicinity of the focus,

$$\frac{z}{\lambda}(\omega_k - \omega_0) < 1, \quad (15)$$

the expression for E_z at the paraboloid axis can further be simplified to

$$E_z \cong E_0 f\left(\tau + \frac{z}{\lambda}\bar{\omega}\right)\overline{\left(\frac{1+\omega}{1-\omega}\right)}(\omega_k - \omega_0). \quad (16)$$

If ω_k is far from unity ($\omega_k < 0.95$), the following equation is valid:

$$\overline{\left(\frac{1+\omega}{1-\omega}\right)} \approx \frac{1+\bar{\omega}}{1-\bar{\omega}}, \quad \bar{\omega} = \frac{\omega_k + \omega_0}{2}. \quad (17)$$

Actually, the values of ω_k close to unity are of no practical significance, because the required power of the light source is inversely proportional to the sine of the glancing angle. When $\omega \longrightarrow 1$, the sine decreases, whereas the power increases as $1/\sqrt{1-\omega}$. In addition, a significant difference between ω_k and ω_0 (very long paraboloid) results in nonuniform illumination and makes the wavelength λ dependent on the coordinates of the emission point.

Consider the process of electron acceleration. For a relativistic electron (the electron velocity is close to the velocity of light, $v \approx c$), the equation of motion is written as

$$z_e = z_i + c(t - t_i) = z_i + \lambda(\tau - \tau_i). \quad (18)$$

Using this equation, we obtain the formula for the momentum of the accelerated electron:

$$\frac{dp_z}{dt} = eE_0\overline{\left(\frac{1+\omega}{1-\omega}\right)}(\omega_k - \omega_0) f((1-\bar{\omega})(\tau - \tau_i)), \quad (19)$$
$$\tau_i = -\frac{z_k}{\lambda}\bar{\omega}.$$

It follows that

$$p_z(\tau) = p_i + \frac{eE_0}{c}\lambda\frac{(1+\bar{\omega})}{(1-\bar{\omega})^2}(\omega_k - \omega_0) \times F((1-\bar{\omega})(\tau - \tau_i)), \quad p_i \equiv p_z(\tau_i). \quad (20)$$

Expression (16) for the field component E_z was obtained under the assumption that

$$\frac{z}{\lambda}(\omega_k - \omega_0) < 1. \quad (21)$$

Hence, within this approximation,

$$(\tau - \tau_i)(\omega_k - \omega_0) < 1. \quad (22)$$

This inequality defines the time interval where the above approximation is valid. The function $F(\tau)$ has a broad maximum at $\tau = 2$. Therefore, the energy of the accelerated electron increases until τ_{max}:

$$\tau_{max} - \tau_i \approx \frac{2}{1-\bar{\omega}}. \quad (23)$$

According to (22), the following inequality should be met:

$$\frac{2}{1-\bar{\omega}}(\omega_k - \omega_0) < 1. \quad (24)$$

Otherwise, τ_{max} should be determined from (22). Thus, it can be assumed that $F = F_{max} = 1$, and the momentum of the accelerated relativistic electron can attain the value p_{max} equal to

$$p_{max} = p_i + \frac{eE_0}{c}\lambda\frac{(1+\bar{\omega})}{(1-\bar{\omega})^2}(\omega_k - \omega_0). \quad (25)$$

The quantity

$$\frac{1+\bar{\omega}}{(1-\bar{\omega})^2}(\omega_k - \omega_0) = 2K\left(\frac{z_0}{r_0}, \frac{\Lambda}{r_0}\right)\frac{\Lambda}{r_0}, \quad \Lambda = z_k - z_0 \quad (26)$$

is the effective length of the paraboloid, which varies over a wide range. The value of K attains its maximum ($K \approx 1$) at $\Lambda \approx 0.5r_0$. For paraboloids of moderate length $\Lambda \sim (1–5)r_0$, which are of practical significance, we have

$$K\left(\frac{z_0}{r_0}, \frac{\Lambda}{r_0}\right) > 0.5. \quad (27)$$

Assuming $K = 0.5$, we obtain

$$p_{max} \approx p_i + \frac{2\pi e\Lambda P_0}{c\lambda}. \quad (28)$$

Since $P_0 = \frac{\varepsilon_f}{2\pi e}$,

$$\frac{p_{\max}}{m_e c} \approx \frac{p_i}{m_e c} + \frac{\lambda}{\lambda\!\!\!^{-}} \frac{\varepsilon_f}{m_e c^2}. \quad (29)$$

If $\frac{\varepsilon_f}{m_e c^2} = \gamma_f - 1 \sim 1$, $\frac{p_i}{m_e c} \sim 1$, and $\frac{\Lambda}{\lambda\!\!\!^{-}} \gg 1$, then

$$\frac{p_{\max}}{m_e c} \approx \frac{\Lambda}{\lambda\!\!\!^{-}} \frac{\varepsilon_f}{m_e c^2}; \quad (30)$$

that is,

$$(\gamma - 1)_{\max} \approx \frac{\Lambda}{\lambda\!\!\!^{-}} (\gamma_f - 1). \quad (31)$$

Hence, if $\Lambda/\lambda\!\!\!^{-} \sim 10^3$, the energy of the accelerated electron is approximately 1 GeV. So far, the acceleration of a relativistic electron has been considered. If an electron is nonrelativistic but the condition

$$\frac{\Lambda}{\lambda\!\!\!^{-}} (1 - \omega) \gg 1, \quad (32)$$

is met, all the estimates obtained above remain valid in the order of magnitude. If an accelerated particle is out of phase with the accelerating field (this is true for nonrelativistic velocities $v \ll c$), the time of acceleration decreases in proportion to $1 - \bar{\omega}$. However, if condition (32) is met, the electron soon becomes relativistic, whereupon acceleration proceeds as described above.

Proton acceleration. Protons and electrons have opposite electric charges. Therefore, when the accelerating field reverses at $\tau > 2$, the directions of the proton velocity, phase velocity of the accelerating field, and accelerating force will coincide. The proton mass is approximately 1840 times the mass of an electron. Therefore, it is reasonable to suggest that the proton remains nonrelativistic throughout the acceleration process. We cannot say in advance how the proton position in space will vary with time. However, this information is not necessary for making the required estimates. It is sufficient to obtain the formal solution of the equation of motion for the coordinate $z_n(t)$:

$$z_n = z_i + \int_{\tau_i}^{\tau} d\tau' \frac{v}{c} \lambda\!\!\!^{-} = z_i + (\tau - \tau_i) \frac{\overline{v(\tau)}}{c} \lambda\!\!\!^{-}, \quad \frac{\overline{v(\tau)}}{c} \ll 1, \quad (33)$$

where $\bar{v} = \overline{v(\tau)}$ is the mean velocity of the particle.

Substituting the current coordinate of the proton into the expression for the field phase, we obtain

$$\tau + \frac{z_n}{\lambda\!\!\!^{-}} \omega = \tau + \frac{z_i}{\lambda\!\!\!^{-}} \bar{\omega} + \bar{\omega} \frac{\bar{v}}{c} (\tau - \tau_i) = \left(1 - \frac{\bar{v}}{c} \bar{\omega}\right)(\tau - \tau_i) \approx \tau - \tau_i \quad \left(\frac{z_i}{\lambda\!\!\!^{-}} = -\tau_i\right). \quad (34)$$

Now, the solution of the equation for proton momentum can easily be obtained:

$$P \approx P_i + \frac{eE_0}{c} \lambda\!\!\!^{-} \frac{1 + \bar{\omega}}{1 - \bar{\omega}} (\omega_k - \omega_0) F(\tau - \tau_i). \quad (35)$$

It follows that

$$\frac{P_{\max}}{Mc} \sim \frac{r_0}{\lambda\!\!\!^{-}} \frac{m_e}{M} (\gamma_f - 1) \quad \left(\frac{P_i}{Mc} \ll 1\right) \quad (36)$$

If $r_0/\lambda\!\!\!^{-} \sim 2 \times 10^3$ and $\gamma_f - 1 \approx 1$,

$$\frac{P_{\max}}{Mc} \approx 0.5. \quad (37)$$

In this case, a proton can be accelerated to about 100 MeV.

ANTICIPATED DESIGN AND PERFORMANCE OF THE ACCELERATOR

From the obtained results, the possible design and performance of the accelerator can be envisioned.

Electron accelerator. The condition $\Lambda/\lambda\!\!\!^{-} = 10^3$ specifies the accelerator size. The value of $\lambda\!\!\!^{-} \approx 0.2$ cm seems to be attainable. In this case, the accelerating gap L should be approximately 0.2 cm at $\gamma_f \approx 2$. The paraboloid length should be $\Lambda = 2$ m. If $\omega_k = 0.8$ and $\omega_0 = 0.5$, the paraboloid radius in the focal plane should be $r_0 = 2/3$ m and the paraboloid surface area, $S \approx 22$ m^2. The amount of energy accumulated in the accelerating gap near the paraboloid surface is easily estimated at

$$U \sim 116 \frac{(\gamma_f - 1)^2}{L} S(\mathbf{J}) \approx 13(\mathbf{J}). \quad (38)$$

The output power of a laser with the light quantum energy $\varepsilon_k \cong 2$ eV that provides electron emission from the paraboloid surface (quantum efficiency $Y \approx 0.2$) can also be easily assessed:

$$J \sim 1.4 \times 10^7 \frac{\varepsilon_k}{Y} \frac{(\gamma_f - 1)^{\frac{3}{2}}}{L^2} S(W) \approx 7 \times 10^{10} \text{ (W)}. \quad (39)$$

If the pulse duration is approximately 10 ps, the laser energy is ≈0.4 J.

The schematic diagram of the accelerator is shown in Fig. 3. Obviously, a device accelerating particles to energies lower than 1 GeV would have smaller dimensions. Let us estimate the energy acquired by an elec-

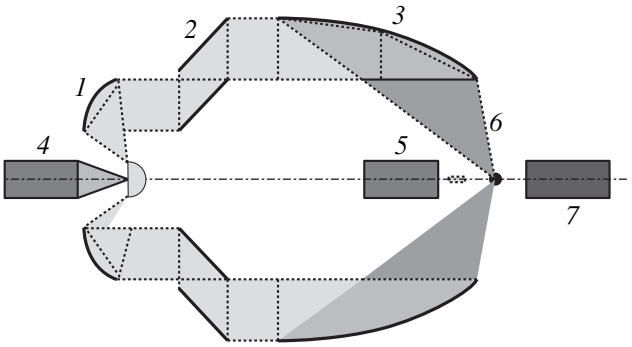

Fig. 3. Schematic diagram of the accelerator: (*1*) paraboloidal mirrors of optical system, (*2*) conical mirrors, (*3*) paraboloidal microwave source, (*4*) laser, (*5*) injector, (*6*) focus, and (*7*) beam outlet.

tron in such an accelerator with a characteristic size of 1 m.

If $r_0 \approx 6.7$ cm, $\omega_k = 0.8$, and $\omega_0 = 0.5$, the distance between the extreme point of the paraboloid and its focus is approximately 27 cm and $\Lambda = 20$ cm. Assuming, as above, that $\lambda\!\!\!^{-} = 0.2$ cm, we find that all the parameters of the accelerator should be decreased a hundred times in comparison with the case considered above: $S \approx 0.22$ m^2, $J \sim 7 \times 10^8$ W, and $U \sim 130$ J. The energy ε_a acquired by an electron upon acceleration decreases only tenfold: $\varepsilon_a \sim 100$ MeV. The total length of the accelerator, including a laser and an optical system, is approximately 1 m. The injection of particles into such a system can be performed in two ways: (1) synchronously with the generation of a laser pulse (in this case, particles are accelerated in the vicinity of the paraboloid focus) or (2) prior to focusing the electromagnetic pulse (a dipole layer of low-energy electrons is produced over the injecting surface, and the electromagnetic pulse captures as many electrons from this layer as it can accelerate).

Proton accelerator. The energy of a proton attains 1 GeV at $P_{max} \approx 1.8Mc$. Assuming that $\gamma_f \approx 3$, $\lambda\!\!\!^{-} = 0.3$ cm, $\omega_k = 0.67$, and $\omega_0 = 0$, we obtain, using starting

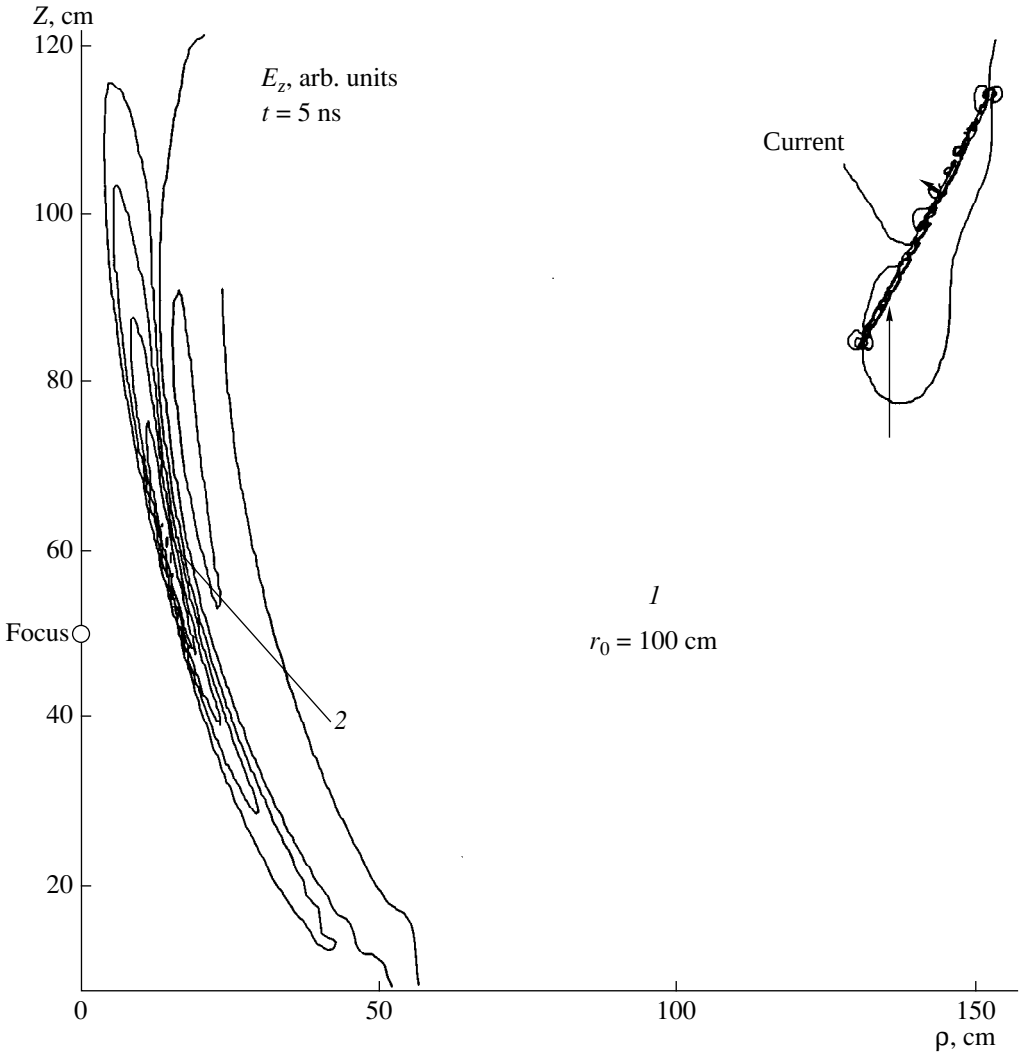

Fig. 4. Electric field level lines: (*1*) paraboloid surface and (*2*) electric current.

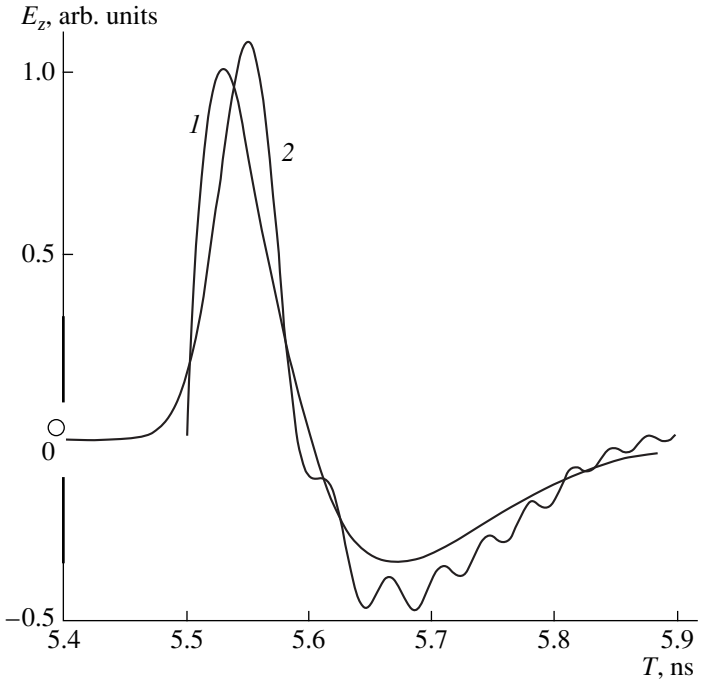

Fig. 5. Electric field at the paraboloid focus (ρ = 0, $z = z_f$, and $T_0 = 0.05$ ns): (*1*) analytical solution and (*2*) numerical solution.

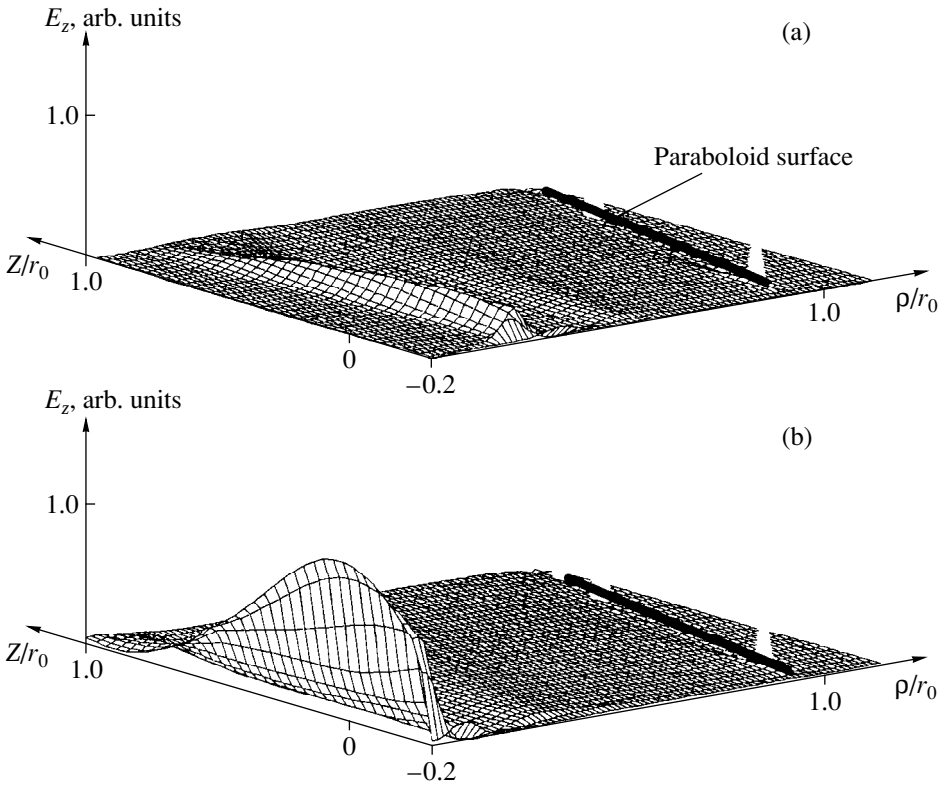

Fig. 6. Spatial distribution of the electric component E_z of the electromagnetic wave focused onto the paraboloid focus. t/T_0 = (a) 6 and (b) 0.8.

equation (9),

$$\frac{P_{\max}}{Mc} \approx 1.8 \times 10^{-3} \frac{r_0}{\lambda}; \qquad (40)$$

hence, $r_0 \approx 10^3 \lambda$. Therefore, the paraboloid radius $r_0 \approx$ 3 m; the paraboloid length, 6 m; and the maximum radius, 6.7 m. A 100-MeV accelerator should have the

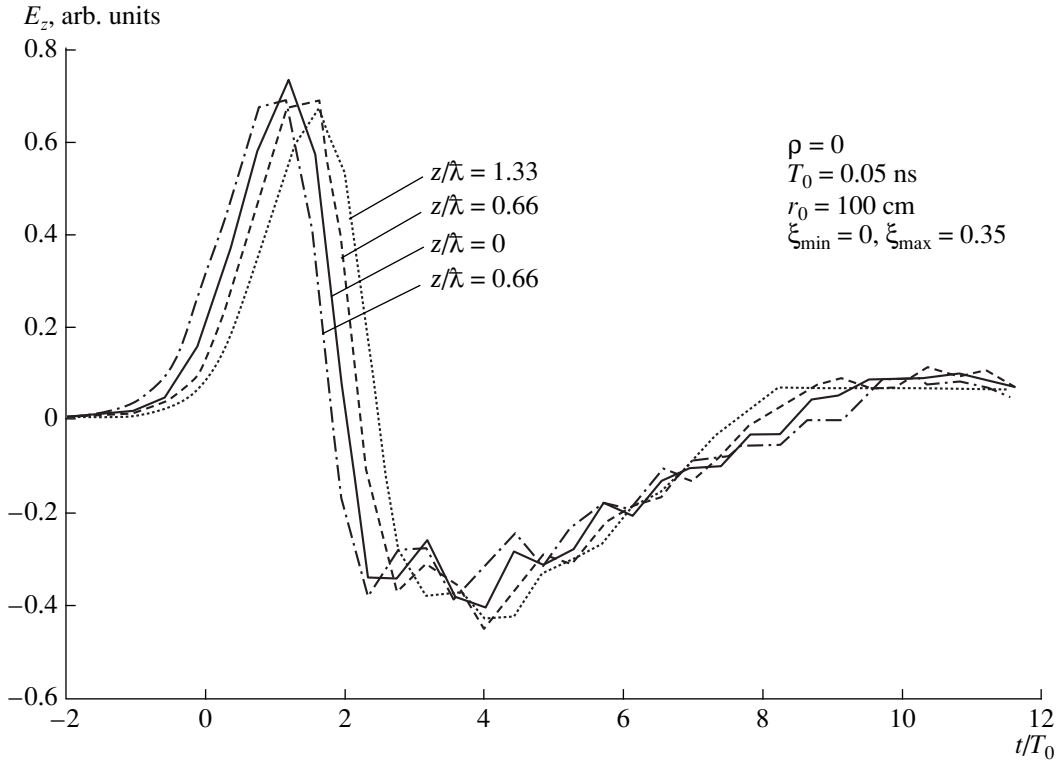

Fig. 7. Time dependence of E_z in the vicinity of the paraboloid focus.

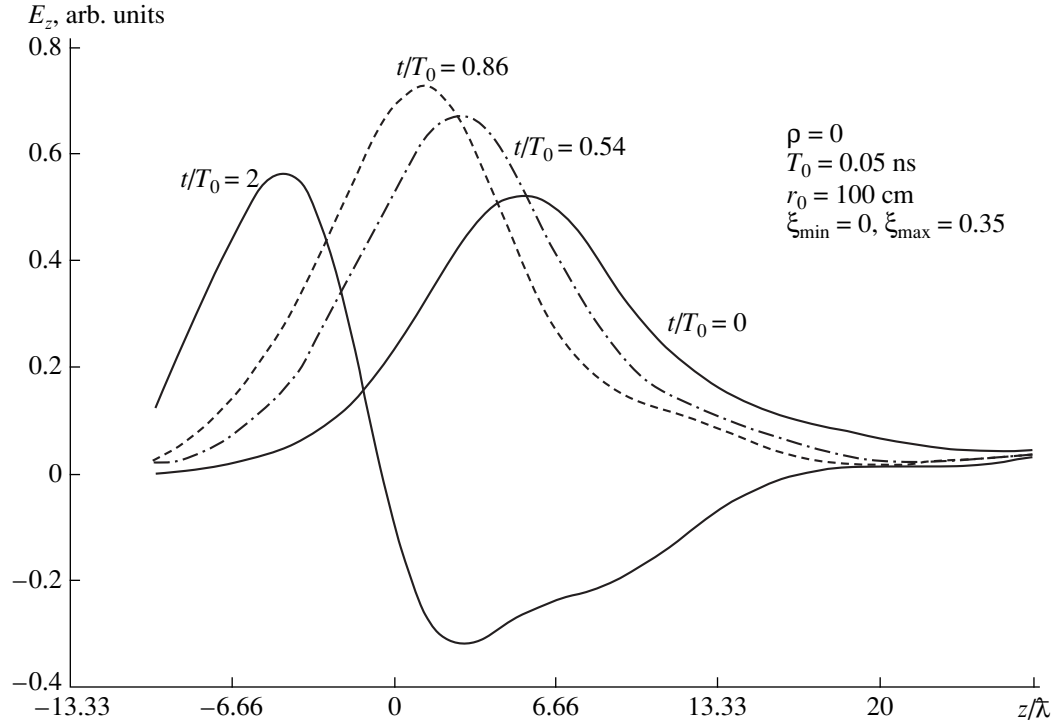

Fig. 8. Spatial distribution of E_z in the vicinity of the paraboloid focus at various time instants.

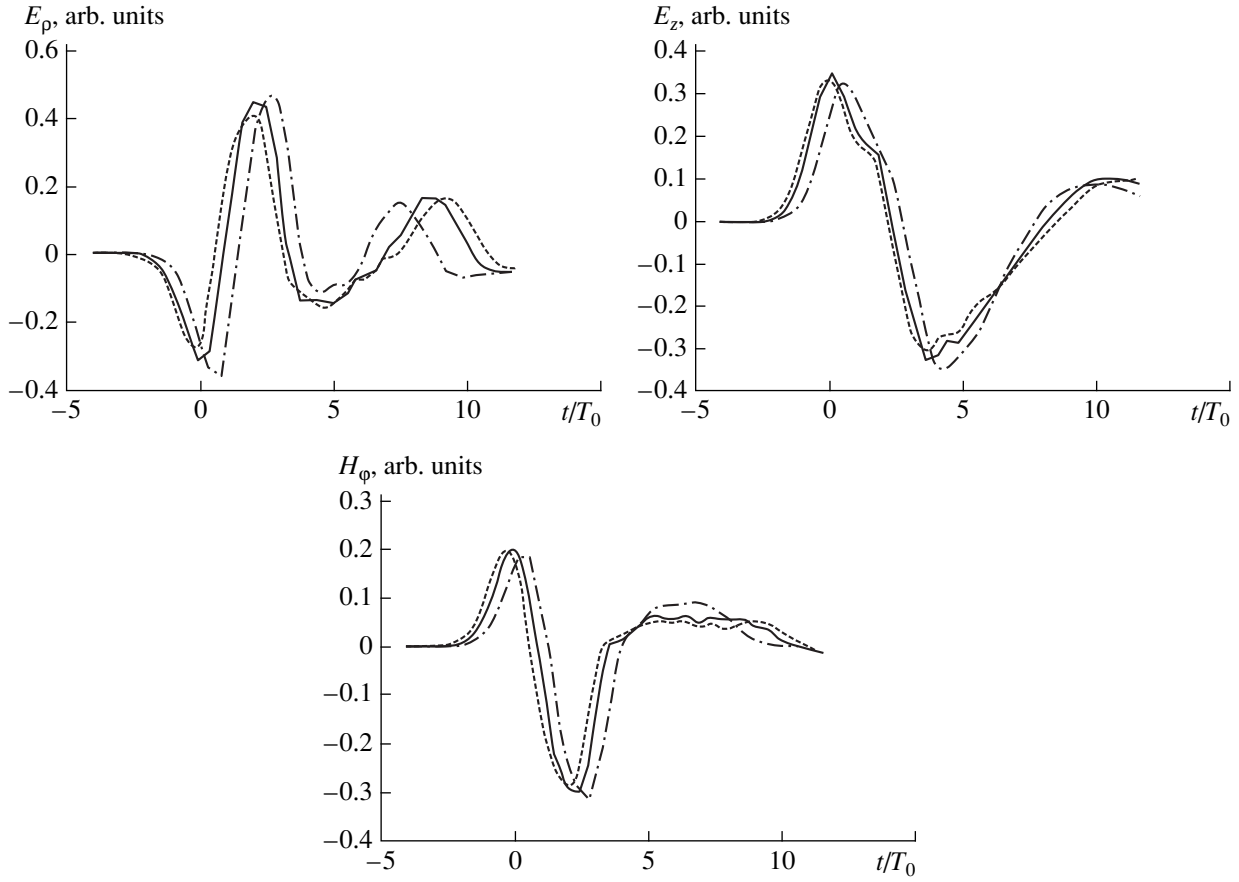

Fig. 9. Time dependence of the electromagnetic field components in the focal region: $\rho/\lambda = 0.666$; z/λ = (dashed line) 2.666, (solid line) 0, and (dash-and-dot line) 1.333.

following dimensions: $r_0 \approx 0.7$ m; length, 1.5 m; and maximum radius, ≈1.6 m.

RESULTS OF NUMERICAL CALCULATIONS

The computation of the space–time distribution of the electric field near the paraboloid focus was performed using a two-dimensional electromagnetic code. An FTL current pulse induced by radiation in an inner layer ($dl = 0.25$ cm) of the paraboloid ($z_p(\rho)$, $0 < z/r_0 < 0.9$, the focal distance $r_0 = 100$ cm) was simulated using the expression for electric current density

$$\mathbf{j}(t, z, \rho) = f\left(t - \frac{z_k - z}{c}\right)\delta(z_p(\rho))\mathbf{n},$$

$$\mathbf{n} = \frac{1}{\sqrt{1 + \left(\frac{\rho}{r_0}\right)^2}}\left\{-\frac{\rho}{r_0}; 1\right\}, \quad (41)$$

$$f(t) = \left(\frac{t}{T_0}\right)^2 e^{-\frac{t}{T_0}}\left(\frac{t}{T_0}\right), \quad T_0 = 0.5 \times 10^{-9}\ \text{s}, \quad (42)$$

where δ is the Dirac function.

The mesh size was taken to be $\Delta z/\lambda = \Delta x/\lambda = 0.166$.

Simulated results for the propagation of an electromagnetic wave induced by an FTL pulse on the paraboloid surface are presented at different time instants in Figs. 4–6. It can be seen that the amplitude of the localized electromagnetic pulse increases as the focus is approached. For comparison, an analytic curve for electric field intensity E_z is shown in Fig. 5.

Calculations showed that a strong electric field is generated in the focal region of size $\gtrsim\lambda$ (Figs. 7–9). The field direction remains invariable for the time interval $\cong 2T_0$, during which the field can be used for accelerating charged particles. It should be noted that the radial component of the electric field is much smaller than the longitudinal component and equals zero at the paraboloid axis. In addition, the magnetic field upon acceleration is directed so that the Lorentz force, acting on the electron beam, presses it against the paraboloid axis (i.e., the beam contracts). Thus, the accelerator can be expected to provide a small angular spread of accelerated particles.

CONCLUSION

The obtained results show that the use of FTL emission sources for accelerating charged particles is feasible. Accelerators based on FTL microwave sources are expected to accelerate charged particles to energies of several hundred or even several thousand MeV, while being significantly smaller in size than today's linear accelerators. The requirements for the performance of the accelerator components do not seem to be unique. Therefore, the production of such accelerators should present no problems if FTL microwave sources themselves are developed.

REFERENCES

1. Yu. N. Lazarev and P. V. Petrov, Pis'ma Zh. Éksp. Teor. Fiz. **60** (9), 625 (1994) [JETP Lett. **60**, 634 (1994)].

Translated by Chamorovskiĭ

Technical Physics, Vol. 45, No. 8, 2000, pp. 980–986. Translated from Zhurnal Tekhnicheskoĭ Fiziki, Vol. 70, No. 8, 2000, pp. 25–30.

Emission of Particles from a Magnetic Trap

Yu. G. Pavlenko

Advanced Education and Science Center, Moscow State University, Moscow, 121357 Russia

Received May 11, 1999

Abstract—Three types of magnetic traps that provide three-dimensional potential wells for neutral atoms and ferromagnetic particles are considered. The possibility of forming directed particle beams is discussed. © *2000 MAIK "Nauka/Interperiodica".*

INTRODUCTION

Ions that are cooled to ultralow temperatures and localized in electromagnetic traps open many possibilities for investigating quantum jumps, the quantum properties of photon statistics, optical bistability, and the problems standing in the way of constructing frequency standards. Experiments with ensembles of particles made it possible to observe the formation of ordered structures and phenomena similar to phase transitions [1, 2]. In connection with this, it becomes relevant to analyze the problems of the localization, accumulation, and confinement of neutral particles in magnetic traps [1, 3–5]. Another aspect of this area of research is associated with the possibility of emitting particles from a magnetic trap and implementing a device that was called an atomic laser [6]. The escape of particles can be driven by one or another triggering mechanism [7, 8].

The motion of particles with a nonzero magnetic moment is described by a set of six nonlinear equations for the coordinates of the center of mass and for the components of the magnetic moment. Here, we propose a new approach to investigating the dynamics of the magnetic moment of a particle in a magnetic field. The dynamic equations for the magnetic moment are represented in Hamiltonian form with the fundamental Poisson bracket of complex "coordinates" and "momenta." The solution obtained is a canonical transformation that drives the new Hamiltonian to zero. We consider several configurations of a constant axisymmetric nonuniform magnetic field that provide three-dimensional potential wells for trapping cooled particles in a bounded region. A resonant RF pulse triggers the spin-flip transition to the state of infinite particle motion. The question then arises of how to pass over to the state of semi-infinite motion. We show that an axisymmetric field configuration provides the possibility of emitting particles in the form of a directed beam. In order to implement this effect, three ring currents that produce a symmetric magnetic trap should be supplemented with an additional ring coil.

EQUATIONS FOR PARTICLE MOTION AND MAGNETIC MOMENT

The energy of the particle–magnetic-field interaction has the form $U(t, x) = -\boldsymbol{\mu}\mathbf{B}$, where $\boldsymbol{\mu} = g\mu_B\mathbf{S}$ is the mean magnetic-moment operator, $\mathbf{S}$ is the mean effective spin, g is the Landé factor, and $\mu_B = e\hbar/2m_e = 5.787 \times 10^{-5}$ eV/T is the Bohr magneton [9]. For a neutron and proton, we have $g\mu_B \longrightarrow g_{n,p}\mu_N$, where $g_n = -3.826$, $g_p = 5.586$, and $\mu_N = 3.15 \times 10^{-8}$ eV/T is the nuclear magneton. The magnetic moment of a ferromagnetic particle is equal to $\mu = MV$, where M is the volume density of the magnetic moment, V is the volume of a particle, and $M_{\max} \sim 10^7$ (J/T cm^3).

The equation of motion for the center of mass of an atom in a quasi-uniform magnetic field is a consequence of the Ehrenfest equation

$$md^2\mathbf{x}/dt^2 = g\mu_B S_n \partial B_n/\partial\mathbf{x} + m\mathbf{g}_0, \qquad (1)$$

where g_0 is the free-fall acceleration.

Equation (1) is also valid for a ferromagnetic particle [10]. The vector $\mathbf{S}$ satisfies the equation

$$d\mathbf{S}/dt = \boldsymbol{\Omega} \cdot \mathbf{S}, \qquad (2)$$

where $\boldsymbol{\Omega} = -\gamma\mathbf{B}$ and $\gamma = g\mu_B/\hbar$.

Equation (2) has an obvious first integral $\mathbf{S}^2(t) = S_0^2$. Note that, in electron systems, the cyclotron frequency is equal to ν [GHz] $= eB/(2\pi m_e) = 27.9922B$ [T].

We consider particle motion in a magnetic field that is a superposition of the constant axisymmetric field $\mathbf{B}_s(x)$, the constant uniform field $\mathbf{B}_0 = (0, 0, b_0)$, and the RF magnetic field

$$\mathbf{B}_\sim(t) = (b_p\cos\omega_t, -b_p\sin\omega t, 0)\,f(t), \qquad (3)$$

where we introduced the function $f(t) = 0$ for $t < t_0$ and $t > t_0 + \tau$ and $f(t) = 1$ for $t_0 \le t \le t_0 + \tau$.

The vector potential of the magnetic field, $A_s(\rho, \varphi, z) = (0, A_\varphi, 0)$, satisfies the conditions $\mathrm{div}\mathbf{B} = 0$ and

curl$\mathbf{B}$ = 0. In cylindrical coordinates, the component $A_\varphi = A(\rho, z)$ can be represented as a series [11]:

$$A(\rho, z) = \rho b_s(z)/2 - \rho^3 b_s''(z)/16 + \ldots(-1)^{n+1}1/[(n-1)!n!](\rho/2)^{2n-1}b_s^{(2n-2)}(z), \quad (4)$$

where $\rho = (x^2 + y^2)^{1/2}$ and $b_s(z)$ is an arbitrary function.

From (4), we find the constant nonuniform magnetic field:

$$\mathbf{B}_s(\mathbf{x}) \approx [-(x/2)(b_s' - b_s'''\rho^2/8), -(y/2)(b_s' - b_s'''\rho^2/8), b_s - (\rho^2/4)b_s'']. \quad (5)$$

The lines of the constant magnetic field $\mathbf{B}(\mathbf{x}) = \mathbf{B}_0 + \mathbf{B}_s(\mathbf{x})$ are described by $\rho[A(\rho, z) + \rho b_0/2] = \text{const}$. Let us consider some configurations of a nonuniform magnetic field.

(i) In a hyperbolic configuration, the magnetic field intrinsically vanishes at the z-axis and increases when away from it, so that we can set

$$b_s(z) = a_1 z + a_2 z^2/2 + a_3 z^3/6. \quad (6)$$

Here, the first term describes the quadrupole field and the second terms defines the mirror field.

(ii) A quasi-periodic magnetic field can be specified through the function $b_s(z) = b\cos kz$, where $k = 2\pi/\lambda$ with λ the spatial period, in which case we have

$$\mathbf{B}_s(x) \approx [(bkx/2)\sin kz, (bky/2)\sin kz, b(1 + k^2\rho^2/4)\cos kz]. \quad (7)$$

(iii) For a configuration produced by a ring current-carrying coil of radius a, centered at the z-axis and lying in the $z = h$ plane, we can set $b_s(z) = \mu_0 Ia/(2R^3)$, where $R^2 = a^2 + (z - h)^2$, I is the current magnitude, and $\mu_0 = 4\pi \times 10^{-7}$ H/A^2 is the permeability of the vacuum.

EQUATION OF PARTICLE MOTION IN A MAGNETIC TRAP

Equations (1) and (2) yield a law according to which the total energy of a particle changes as

$$dE/dt = -g\mu_B \mathbf{S}\partial\mathbf{B}_t/dt, \quad (8)$$

where $E = mv^2/2 - g\mu_B\mathbf{S}(t)\mathbf{B}_t(t, \mathbf{x}) - m\mathbf{g}_0\mathbf{x}$ and $\mathbf{B}_t(t, \mathbf{x}) = \mathbf{B}_0 + \mathbf{B}_s(x) + \mathbf{B}_\sim(t)$ is the total magnetic field.

We start by solving equations (1) and (2) in the time interval $0 \le t \le t_0$, assuming that $\mathbf{B}(\mathbf{x}) = \mathbf{B}_0 + \mathbf{B}_s(\mathbf{x})$. The spatial and spin variables change with the characteristic frequencies $\omega_a = (\mu B''/m)^{1/2}$ and $\Omega = \gamma B$, where $B'' \sim 200$ T/m^2 and $B \sim 1$ T. Since $\omega_a \ll \Omega$, we can neglect the contribution of the rapidly oscillating components of the vector $\mathbf{S}$ to equation (1) and switch to slowly varying spatial variables. This procedure is equivalent to the replacement of $\mathbf{S}$ by its mean value. In the Appendix, we solve equation (2) and show that the mean spin is equal to $\langle\mathbf{S}\rangle = C\mathbf{B}/B$ with $C = \mathbf{S}(0)\mathbf{B}/B$. The thermally equilibrium states are characterized by $C > 0$. As the temperature decreases, we have $C \longrightarrow S_0$. Moreover, if $C = S_0$, then $\mathbf{S}(t) = S_0\mathbf{B}/B$, in which case the total energy of a particle can be written as $E = mv^2/2 - \mu B(\mathbf{x}) - m\mathbf{g}_0\mathbf{x}$, where $\mu = g\mu_B S_0$.

Substituting $\mathbf{S} = C\mathbf{B}/B$ into (1) results in the equation

$$md^2\mathbf{x}/dt^2 = g\mu_B C\partial B/\partial\mathbf{x} + m\mathbf{g}_0. \quad (9)$$

Let the origin of the coordinates be at the axis of the magnetic configuration, and let this axis coincide with the z-axis directed vertically upward. In order to determine the conditions under which the particles move in a bounded spatial region ($|z| < L/2$, $\rho < L$), we introduce the function $b_z = b_0 + b_s(z)$ and assume that $|b_z| \gg |B_{s1}|$, $|B_{s2}|$, in which case we have $B(x) \approx b_z + (\rho^2/8)[(b_z')^2/b_z - 2b_z'']$. From (9), we obtain the set of equations

$$md^2z/dt^2 = g\mu_B C[b_z' + (\rho^2/4)(b_z'b_z''/b_z - b_z''')] - mg_0, \quad (10)$$

$$md^2x/dt^2 = (g\mu_B C/4)[(b_z')^2/b_z - 2b_z'']x, \quad (11)$$

$$md^2y/dt^2 = (g\mu_B C/4)[(b_z')^2/b_z - 2b_z'']y. \quad (12)$$

In the paraxial approximation $\rho \ll L$, such that the values of ρ satisfy the condition $\rho^2|b_z'b_z''/b_z - b_z'''| \ll 4|b_z'|$, equation (10) can be written as

$$md^2z/dt^2 = -\partial W(z)/\partial z, \quad (13)$$

where the function $W(z) = -g\mu_B C b_z(z) + mg_0 z$ plays the role of the potential energy.

Equation (13) has an obvious first integral

$$(dz/dt)^2 = G(z), \quad G(z) = (2/m)[E_3 - W(z)], \quad (14)$$

where E_3 is the total energy of the longitudinal particle motion. Under the condition $b_z'' > (b_z')^2/2b_z$, equations (11) and (12) describe a harmonic oscillator with a time-varying frequency.

EMISSION OF PARTICLES FROM A MAGNETIC TRAP

For cold particles moving in a magnetic trap, we have $C \longrightarrow S_0$, in which case the energy of the particle–magnetic-field interaction via the particle magnetic moment is $U(t, \mathbf{x}) \longrightarrow -\mu B$, where $\mu = g\mu_B S_0$. Let the RF magnetic field (3), which is rotating around the z-axis, be also present in the system, so that the total magnetic field is $\mathbf{B}_t(t, \mathbf{x}) = B_s(\mathbf{x}) + \mathbf{B}_0 + \mathbf{B}_\sim(t)$. We assume that the condition $b_0 \gg |b_s|$ holds. A resonant pulse of the RF magnetic field with the duration $\tau = \pi/\Omega_p$, where

$\Omega_p = \gamma b_p$, triggers the spin-flip transition $S_0 \longrightarrow -S_0$ at the frequency $\omega = \gamma b_0$ [12]. In fact, according to (A.14), the solution to the dynamic equations for the magnetic moment on the time scales $t > t_0 + \tau$ has the form $\mathbf{S}(t) = -S_0\mathbf{B}/B$, where $S_0 = \mathbf{S}(t_0)\mathbf{B}/B$. For a particle moving in an alternating electric field, law (8), according to which the total particle energy changes, reduces to $dE/dt = -g\mu_B\mathbf{S}d\mathbf{B}_\sim(t)/dt$, which yields the total energy $\Delta E = 2\mu b_0$ acquired by the particle over the time interval τ. On the time scales $t \geq t_0 + \tau$, the energy of a particle interacting with a constant magnetic field becomes $U_f(t, \mathbf{x}) = \mu B$. Under the action of the RF pulse, the conditions for the particle to move in a bounded region fail to hold and the particle escapes from the trapping region.

PARTICLE IN AN AXISYMMETRIC MAGNETIC TRAP

Localization of a Particle

In (6), we set $a_3 = -a_{30} < 0$ and $a_1 > 0$, in which case the potential energy of a particle is equal to $W(z) = -g\mu_B C(b_0 + a_1 z + a_2 z^2/2 - a_{30}z^3/6) + mg_0 z$. The equation $dW/dz = 0$ implies that the potential energy has two local extremes, a maximum and a minimum, at the points with the coordinates $e_{2,1} = [a_2 \pm (a_2^2 + 2a_{30}[a_1 - mg_0/g\mu_B C])^{1/2}]/a_{30}$, such that $W(e_1) > W(e_2)$. If E_3 is in the $W(e_2) < E_3 < W(e_1)$ range, then the particle oscillates in the potential well between two turning points z_2 and z_1, such that $e_1 < z_1 < e_2 < z_3$. In the well region, we have $G(z) \geq 0$. The zeros of the function $G(z)$ are such that $z_3 > z_2 > z_1$. Substituting the function $G(z)$ in the form $G(z) = -\sigma^2(z - z_1)(z - z_2)(z - z_3)$ with $\sigma^2 = g\mu_B C a_{30}/3m$ into (14), we obtain a solution to equation (10):

$$z(t) = z_3 - (z_3 - z_2)\mathrm{sn}^2[\omega_z(t + T)/2, \xi],$$

where $\mathrm{sn}[\omega_z(t + T)/2, \xi]$ is an elliptic sine, $\omega_z = \sigma(z_3 - z_1)^{1/2}$, $\xi^2 = (z_3 - z_2)/(z_3 - z_1)$, $z_3 - z(0) = (z_3 - z_2)\mathrm{sn}^2[\omega_z T/2, \xi]$, $z(t)$ is a periodic function with the period $4K/\omega_z$, and $K(\xi)$ is the complete elliptic integral.

Now, we analyze particle motion in the x- and y-directions by examining the simplest situation, when the inequalities $b_0 \gg |b_s|$ and $(b_z')^2/b_z - 2b_z'' \approx a_1^2/b_0 - 2a_2 < 0$ are assumed to be satisfied in the region where the particle moves along the z-axis. In this case, equations (11) and (12) reduce to

$$d^2x/dt^2 + \omega_{12}^2 x = 0, \quad d^2y/dt^2 + \omega_{12}^2 y = 0, \quad (15)$$

where $\omega_{12}^2 = (g\mu_B C/4m)[2a_2 - a_1^2/b_0]$.

The projection of the particle trajectory onto the (x, y) plane is an ellipse, so that the particle moves in a bounded spatial region. Note that, if the magnetic axis is horizontal, then the equilibrium vertical displacement of the particle away from the axis is equal to g_0/ω_{12}^2.

Emission of Particles from the Trap

After the interaction between a particle and a resonant RF pulse, the potential energy of the particle and its total energy are equal to $W(z) \longrightarrow W_f(z) = \mu b_z(z) + mg_0 z$ and $E_{3f} = E_3 + 2\mu b_0$. On the time scales $t \geq t_0 + \tau$, equation (14) takes the form

$$(dz/dt)^2 = G_f(z), \quad G_f(z) = (2/m)[E_{3f} - W_f(z)]. \quad (16)$$

Since the equation $G_f(z) = 0$ has the single real root $z = z_0$, there remains only one turning point, so that the z_0-particles moving in the z-direction leave the trap in the positive direction along the z-axis. The time at which the particles escape from the potential well can be estimated from (16) as follows:

$$t_{ax} \sim 2/\sigma_f D^{1/4},$$

where

$$\sigma_t^2 = \mu a_{30}/3m,$$

$$D^4 = 3[z_0^2 - 2a_2 z_0/a_{30} - (2/a_{30})(a_1 + mg_0/\mu)].$$

The characteristic time scale t_r on which the particle beam diverges in the radial direction can be estimated from equations (15) with the replacement $-g\mu_B C \longrightarrow \mu$: $t_r \sim 2[(\mu/m)(a_1^2/b_0 - 2a_2)]^{-1/2}$. If $t_{ax} \ll t_r$, the particles occupy the region stretched out along the z-axis, forming a beam extended in the positive direction along the z-axis.

PARTICLE IN A QUASIPERIODIC MAGNETIC TRAP

Inserting $b_z(z) = b_0 + b\cos kz$ into (10)–(12), we obtain the following equations in the paraxial approximation:

$$d^2kz/dt^2 + \omega_z^2 \sin kz = -kg_0, \quad (17)$$

$$d^2x/dt^2 - (\omega_z^2/2)[(b/2b_0)\sin^2 kz + \cos kz]x = 0, \quad (18)$$

$$d^2y/dt^2 - (\omega_z^2/2)[(b/2b_0)\sin^2 kz + \cos kz]y = 0, \quad (19)$$

where $\omega_z^2 = g\mu_B C k^2 b/m$.

We can draw an analogy between (17) and the equation of motion of a pendulum with a constant force moment. If $kg_0 < \omega_z^2$, the coordinates z_{eq} of the equilibrium points can be obtained from the equation $\omega_z^2 \sin kz_{eq} = -kg_0$ with $\cos kz_{eq} > 0$. The potential energy is equal to $W(z) = -g\mu_B C(b_0 + b\cos kz) + mg_0 z$. In the vicinity of an equilibrium point, we have $z = z_{eq} +$

$A\cos(\omega_0 t + \alpha)$. In other words, a particle oscillates with frequency ω_0 such that $\omega_0^2 = \omega_z^2 \cos kz_{eq}$. In this case, equations (18) and (19) belong to the class of Hill equations. If $kA \ll 1$, equations (18) and (19) reduce to the Mathieu equation $d^2u/ds^2 + (p + 2q\cos 2s)u = 0$, where $s = 2(\omega_0 t + \alpha)$ and

$$p = -(1/8)[1 + b\sin^2 kz_{eq}/(2b_0\cos kz_{eq})],$$

$$q = -(A/8)(-\tan kz_{eq} + b\sin kz_{eq}/b_0).$$

The theory of Mathieu functions implies that, in the parameter plane (p, q), there are regions in which the solutions are either bounded or unbounded [13, 14]. In the plane (p, q), the solutions to equations (18) and (19) are bounded in the first stability domain, which is located to the right of the curve $p_{c0}(q) = -q^2/2 + 7q^4/128 + \ldots$ and is bounded by the curve $p_{s1}(q) = 1 + q - q^2/8 + \ldots$ for $q < 0$ and by the curve $p_{c1}(q) = 1 - q - q^2/8 + \ldots$ for $q > 0$ [13].

PARTICLE IN A SPHERICAL SEXTUPOLE MAGNETIC TRAP

Localization of a Particle

The magnetic trap implemented experimentally by Paul and his collaborators [3] and aimed at confining neutrons was produced by the magnetic field of three ring current-carrying coils placed at the intersections of a spherical surface with the planes $z = \pm h$ and $z = 0$. The equatorial current was chosen to flow in the direction opposite to the polar currents, in which case the two points corresponding to the equilibrium states are those located symmetrically with respect to the equatorial plane ($z \neq 0$). This circumstance complicates the extraction of neutrons from the trap.

We consider the motion of particles in a magnetic field produced by three unidirectional ring currents. To do this, we treat (4) with

$$b_s(z) = -(\mu_0 Ia/2)[1/R_1^3 + 1/R_2^3] - \mu_0 I_0 a_0/2R_0^3, \quad (20)$$

where $R_1^2 = a^2 + (z + h)^2$, $R_2^2 = a^2 + (z - h)^2$, $h > a/2$, and $R_0^2 = a_0^2 + z^2$. Let the z-axis be directed horizontally, and let the x-axis be directed vertically downward. From (10)–(12), we obtain the following equations in the paraxial approximation:

$$md^2z/dt^2 = -dW/dz, \quad (21)$$

$$md^2x/dt^2 = (g\mu_B C/4)[(b_s')^2/b_0 - 2b_s'']x + mg_0, \quad (22)$$

$$md^2y/dt^2 = (g\mu_B C/4)[(b_s')^2/b_0 - 2b_s'']y, \quad (23)$$

where $W(z) = -g\mu_B C[b_0 + b_s(z)]$ and $b_0 \gg b_s$.

Equations (21)–(23) give the coordinates of the equilibrium point: $z_{eq} = 0$, $x_{eq} = 2mg_0/[g\mu_B C b_s''(0)]$, and $y_{eq} = 0$, $b_s''(0) = 3g\mu_B C[Ia(a^2 - 4h^2)(a^2 + h^2)^{7/2} + I_0/2a_0^4]$.

If the potential well is sufficiently deep, $|b_s(h)| \gg |b_s(0)|$, then the parameters of the magnetic system should satisfy the inequality

$$(I/a^2)[1 + (1 + 4h^2/a^2)^{-3/2} - 2(1 + h^2/a^2)^{-3/2}] \gg I_0/a_0^2[1 - (1 + h^2/a_0^2)^{-3/2}].$$

On the other hand, since $b_s'(0) = 0$, a particle will move in a bounded region in the vicinity of the plane $z = 0$ in the in the x- and y-directions only if the inequality $b_s''(0) > 0$ holds. Consequently, the particles can generally be localized if the function $b_s(z)$ satisfies the conditions $2b_s'' - (b_s')^2/b_0 > 0$ and $|b_s(h)| > |b_s(0)|$.

Emission of Particles from the Trap

In order to ensure the directed motion of the particles after the resonant pulse has come to an end, it suffices to switch on an additional coil, with current I_c and radius r, located in the plane $z = -H$ such that $H > h$. After the particle spin reverses direction, the potential energy of the particle becomes $W^{(c)}(z) = \mu(b_0 + b_s + b_c)$, where $b_c(z) = \mu_0 I_c r/(2R^3)$, $R^2 = r^2 + (z + H)^2$, and $b_s(z)$ is defined in (20). The magnetic field of the additional coil plays the role of a magnetic mirror that reflects particles in the positive direction along the z-axis. To make the beam radially nondivergent, the additional coil should satisfy the condition $2(b_s'' + b_c'') - (b_s' + b_c')^2/b_0 < 0$.

ACKNOWLEDGMENTS

This work was supported in part by the Russian Foundation for Basic Research, project no. 97-01-00957.

APPENDIX

Equation (2) is derived by averaging the Heisenberg equations of motion for the spin operator over the superposition of states of a quasiclassical wave packet. Consequently, equation (2) is neither Lagrangian nor Hamiltonian; it also cannot be derived variationally. But it can be made Hamiltonian with the help of the method that was developed by Schwinger, who found the relation between the spin operator and the conjugate "creation" and "annihilation" operators, which can be introduced when examining two harmonic oscillations [15].

We introduce a spinor-column Ψ with two complex elements a_1 and a_2, such that $\Psi^+ = (a_1^*, a_2^*)$. We denote the Pauli matrices by σ_k ($k = 1, 2, 3$) and define

the components $S_k = (1/2)\Psi^+\sigma_k\Psi$ of the vector **S** through the relationships

$$S_1 = (a_1^* a_2 + a_2^* a_1)/2, \quad S_2 = (a_1^* a_2 - a_2^* a_1)/2i, \quad S_3 = (a_1^* a_1 - a_2^* a_2)/2. \tag{A.1}$$

We also introduce the "coordinates" and "momenta" $q_k = a_k$ and $p_k = ia_k^*$ ($k = 1, 2$) with the fundamental Poisson bracket (PB) $[q_i, p_k] = \delta_{ik}$. The relationship $[S_1, S_2] = \varepsilon_{ijk}S_k$ for the PB puts equation (2) in Hamiltonian form $dS/dt = [S, H]$ with the Hamiltonian $H = \mathbf{\Omega S}$.

We consider the dynamic equations for the magnetic moment in a constant nonuniform magnetic field $\mathbf{B}_0 + \mathbf{B}_s(x)$. Along the phase trajectories of the system, we have $\mathbf{\Omega}(t) = -\gamma\mathbf{B}(t)$, where $\mathbf{B}(t) = \mathbf{B}_0 + \mathbf{B}_s(\mathbf{x}(t))$. In terms of canonical variables, the Hamiltonian has the form

$$H = (1/2)[a_1^* a_2\Omega_- + a_2^* a_1\Omega_+ + (a_1^* a_1 - a_2^* a_2)\Omega_3], \tag{A.2}$$

where $\Omega_\pm = \Omega_1 \pm i\Omega_2$.

The dynamic equations $da_k/dt = [a_k, H]$ ($k = 1, 2$) become

$$da_k/dt = -iH_{kn}a_n, \tag{A.3}$$

where $H_{11} = \Omega_3/2$, $H_{12} = \Omega_-/2$, $H_{21} = \Omega_+/2$, and $H_{22} = -\Omega_3/2$.

We begin by solving the eigenvalue problem $\lambda v_n = -H_{nk}v_k$. From the equation $\det(H + \lambda I) = 0$, we obtain the eigenvalues $\lambda_{1,2} = \pm\lambda_0$ and $\lambda_0 = \Omega/2$, where $\Omega = (\Omega_1^2 + \Omega_2^2 + \Omega_3^2)^{1/2}$. Substituting $\lambda = \lambda_{1,2}$ into the eigenvalue problem yields the orthonormal eigenvectors $v_{n(1)}$ and $v_{n(2)}$:

$$\begin{aligned} v_{1(1)} &= [(\Omega - \Omega_3)/2\Omega]^{1/2}, \\ v_{1(2)} &= \Omega_-/[2\Omega(\Omega - \Omega_3)]^{1/2}, \\ v_{2(1)} &= -\Omega_+/[2\Omega(\Omega - \Omega_3)]^{1/2}, \\ v_{2(2)} &= [(\Omega - \Omega_3)/2\Omega]^{1/2}. \end{aligned} \tag{A.4}$$

We can parameterize the eigenvectors by introducing the angles Θ and φ for the vector B in spherical coordinates through the relationships $B_1 = B_{12}\cos\varphi$ and $B_2 = B_{12}\sin\varphi$, where $B_{12} = B\sin\Theta$, and $B_3 = B\cos\Theta$, where $B_{12} = (B_1^2 + B_2^2)^{1/2}$.

We represent Hamiltonian (A.2) in terms of the coordinates and momenta $H = -iH_{mn}p_m q_n$ and make the canonical transformation (CT) $q_k = a_k$, $p_k = ia_k^* \longrightarrow q_k' = c_k$, $p_k' = ic_k^*$ generated by the function $F_2(q, p', t) = (\Lambda^+)_{\mu k}p_\mu' q_k$, which depends on the old coordinates and new momenta. Here, the columns of the unitary matrix $\Lambda_{m\mu} = [u_{m(\mu)}]$ are the eigenvectors of the matrix $\mathbf{B\sigma}/2B$, which coincide with (A.4) to within a phase factor [16]:

$$\begin{aligned} u_{1(1)} &= \cos(\Theta/2)\exp(-i\varphi/2), \\ u_{1(2)} &= -\sin(\Theta/2)\exp(-i\varphi/2), \\ u_{2(1)} &= \sin(\Theta/2)\exp(i\varphi/2), \\ u_{2(2)} &= \cos(\Theta/2)\exp(i\varphi/2). \end{aligned} \tag{A.5}$$

The CT generated by the function F_2 has the form $(q_\alpha' = \partial F_2/\partial p_\alpha', p_m = \partial F_2/\partial q_m) \longrightarrow (q_n = \Lambda_{n\alpha}q_\alpha', p_m = (\Lambda)_{\mu m}^+ p_\mu^+)$. Since $(\Lambda)_{\alpha k}^+ = [u_{k(\alpha)}]^*$, we have

$$q_n = u_{n(\alpha)}q_\alpha', \quad p_m = [u_{m(\mu)}]^* p_\mu'. \tag{A.6}$$

Consequently, in the new variables, the Hamiltonian $H'(q', p', t) = (H + \partial F_2/\partial t)$ is equal to $H' = H_0' + h'$ with

$$\begin{aligned} H_0'(q', p', t) &= -iH_{\mu\alpha}'p_\mu' q_\alpha'', \\ h'(q', p', t) &= \omega_{\mu\alpha}p_\mu' q_\alpha', \end{aligned} \tag{A.7}$$

where $H_{\mu\alpha}' = (\Lambda)_{\mu m}^+ H_{mn}\Lambda_{n\alpha} = -\lambda_\mu\delta_{\mu\alpha}$, $\omega_{\mu\alpha}(t) = \Lambda_{\mu k}^+\Lambda_{k\alpha}$. The CT puts the Hamiltonian $H_0'(q', p', t)$ in the diagonal form $H_0'(q', p', t) = -\lambda_n c_n^* c_n$ or

$$H_0' = -\Omega(|c_1|^2 - |c_2|^2)/2. \tag{A.8}$$

We assume that, along the phase trajectories of the system, the magnetic field satisfies the condition $|\omega_{\mu\alpha}| \ll \Omega$ ($\mu, \alpha = 1, 2$), in which case we have $H'(q', p', t) \approx -\lambda_n c_n^* c_n$. The solution to the equations generated by the Hamiltonian H' is a CT $c_k \longrightarrow b_k$ such that $c_1 = b_1\exp(i\eta/2)$ and $c_2 = b_2\exp(-i\eta/2)$ pass over to $b_1 = (S_0 + C)^{1/2}\exp(i\phi/2)$ and $b_2 = (S_0 - C)^{1/2}\exp(-i\phi/2)$, where $\eta(t) = \int\Omega(t)dt$ and C and ϕ are integration constants. The general solution to equations (A.3) has the form $a_n = \Lambda_{n\alpha}c_\alpha$. Inserting $a_n = \Lambda_{n\alpha}c_\alpha$ into (A.1) gives $S_n = R_{n(\alpha)}S_\alpha'$, where the real vectors $R_{n(\alpha)}$ ($\alpha = 1, 2, 3$) are defined as

$$\begin{aligned} &R_{1(1)} = B_1B_3/BB_{12}, \ R_{1(2)} = -B_2/B_{12}, \ R_{1(3)} = B_1/B, \\ &R_{2(1)} = B_2B_3/BB_{12}, \ R_{2(2)} = B_1/B_{12}, \ R_{2(3)} = B_2/B, \\ &R_{3(1)} = -B_{12}/B, \ R_{3(2)} = 0, \ R_{3(3)} = B_3/B. \end{aligned} \tag{A.9}$$

The components of the vector S_α' are determined by relationships (A.1) with the replacement $a_n \longrightarrow c_n$:

$$\begin{aligned} S_1' &= (S_0^2 - C^2)^{1/2}\cos(\eta + \phi), \\ S_2' &= -(S_0^2 - C^2)^{1/2}\sin(\eta + \phi), \quad S_3' = C. \end{aligned} \tag{A.10}$$

The relationship $\mathbf{BS} = BC$ implies that, in a quasi-uniform magnetic field, the projection $C = \mathbf{BS}/B$ of the vector $\mathbf{S}$ onto the tangent to a magnetic field line is an adiabatic invariant. The mean spin is equal to $\langle \mathbf{S} \rangle = \mathbf{R}_3 C = \mathbf{B}C/B$.

Note that the CT $a_k \longrightarrow c_k$ defines a transition to the new basis vectors $\mathbf{n}_k \longrightarrow \mathbf{n}'_k$ ($k = 1, 2, 3$), in which the magnetic field $\mathbf{B}$ is directed along the unit vector $\mathbf{n}'_3$. In fact, the matrix $E_{ik} = (R^{-1})_{ik}$ describes the operations of rotating by the Eulerian angles $\varphi_1 = \varphi$, $\varphi_2 = \Theta$, and $\varphi_3 = 0$ about the 3-2-3 axes, respectively [17]. With allowance for (A.9), we represent the solution to equation (2) as

$$\begin{aligned} S_1 &= (S'_1 \cos\Theta + S'_3 \sin\Theta)\cos\varphi - S'_2 \sin\varphi, \\ S_2 &= (S'_1 \cos\Theta + S'_3 \sin\Theta)\sin\varphi + S'_2 \cos\varphi, \\ S_3 &= -S'_1 \sin\Theta + S'_3 \cos\Theta. \end{aligned} \tag{A.11}$$

Now, we consider the dynamics of the magnetic moment of a particle in the magnetic field $\mathbf{B}_t = \mathbf{B}_0 + \mathbf{B}_s(\mathbf{x}) + \mathbf{B}_\sim(t)$. The total Hamiltonian of the dynamic equations for the magnetic moment has the form $H_t = H + h$, where the Hamiltonian H is defined in (A.2) and

$$h = -(1/2)[a_1^* a_2 \Omega_p \exp(i\omega t) + a_2^* a_1 \Omega_p \exp(-i\omega t)], \quad t \geq t_0, \tag{A.12}$$

with $\Omega_p = \gamma b_p$.

We set $b_0 \gg |b_s|$ and $\Omega \approx \Omega_0 = \gamma b_0$. Under the resonance condition $\omega = \Omega_0$, the CT $a_k \longrightarrow c_k \longrightarrow b_k$ converts the Hamiltonian to the form

$$H'_t = -(\Omega_p/2)(b_1^* b_2 + b_2^* b_1). \tag{A.13}$$

Taking into account (A.9) or (A.11), we obtain the components of the vector $\mathbf{S}(t)$:

$$\begin{aligned} S_1 &= \mathrm{Re}\, b_1^* b_2 \exp(-i\omega t), \\ S_2 &= \mathrm{Im}\, b_1^* b_2 \exp(-i\omega t), \\ S_3 &= (b_1^* b_1 - b_2^* b_2)/2. \end{aligned} \tag{A1a}$$

The equations generated by Hamiltonian (A.13) and supplemented with the boundary conditions $S_1(t_0) = 0$, $S_2(t_0) = 0$, and $S_3(t_0) = S_0$ have the solution

$$\begin{aligned} b_1 &= i(2S_0)^{1/2} \cos\Omega_p(t - t_0)/2, \\ b_2 &= -(2S_0)^{1/2} \sin\Omega_p(t - t_0)/2. \end{aligned}$$

Therefore, the components of the vector $\mathbf{S}(t)$ are equal to

$$\begin{aligned} S_1(t) &= S_0 \sin[\Omega_p(t - t_0)]\sin\omega t, \\ S_2(t) &= S_0 \sin[\Omega_p(t - t_0)]\cos\omega t, \\ S_3(t) &= S_0 \cos\Omega_p(t - t_0). \end{aligned} \tag{A.14}$$

If an RF field is nonzero over the time interval $t - t_0 = \tau$ such that $\Omega_p \tau = \pi$, then, on the time scales $t \geq t_0 + \tau$, we have $S_1(t) = 0$, $S_2(t) = 0$, and $S_3(t) = -S_0$. In other words, the resonant "π-pulse" reverses the direction of the magnetic moment. We conclude with the following two comments.

(i) We write equation (2) in tensor form, $dS_i/dt = A_{ik} S_k$, where $A_{ik} = \varepsilon_{ijk} \Omega_j(t)$ is an antisymmetric tensor with the elements $A_{21} = \Omega_3$, $A_{32} = \Omega_1$, and $A_{13} = \Omega_2$. In this case, the equation $\sigma V_i = A_{ij} V_j$ has the eigenvectors $\mathbf{V}_{(1)} = (\mathbf{R}_{(1)} + i\mathbf{R}_{(2)})/\sqrt{2}$, $\mathbf{V}_{(2)} = [\mathbf{V}_{(1)}]^*$, and $\mathbf{V}_{(3)} = \mathbf{R}_{(3)}$, which refer to the eigenvalues $\sigma_1 = -i\Omega$, $\sigma_2 = i\Omega$, and $\sigma_3 = 0$. The vectors $V_{(\alpha)}$ compose the orthogonal basis $[V_{(\alpha)}]^* V_{(\beta)} = \delta_{\alpha\beta}$ [8].

(ii) The functional

$$I = \int dt L(a_k^*, a_k, t)$$

satisfies the Euler–Lagrange equation

$$L(a_k^*, a_k) = (i/2)[a_n da_n^*/dt - a_n^* da_n/dt] + H(a_k^*, a_k, t),$$

which is in Hamiltonian form [18]. A significant advantage of the Hamiltonian formalism is the possibility of using new methods for integrating the canonical equations of motion [18–20]. Introducing the functional makes it possible to apply direct variational methods of the Bubnov–Galerkin type.

REFERENCES

1. P. É. Toshek, Usp. Fiz. Nauk **158**, 450 (1989).
2. K. N. Drabovich, Usp. Fiz. Nauk **158**, 499 (1989) [Sov. Phys. Usp. **32**, 622 (1989)].
3. W. Paul, Usp. Fiz. Nauk **160** (12), 109 (1990).
4. D. E. Pritchard, Phys. Rev. Lett. **51**, 1336 (1983).
5. W. Petrich, M. E. Anderson, J. R. Ensher, *et al.*, Phys. Rev. **74**, 3352 (1955).
6. M. Holland, K. Burnett, C. Gardiner, *et al.*, Phys. Rev. A **54**, 1757 (1996).
7. A. M. Gazman, M. Moore, and P. Meyste, Phys. Rev. A **54**, 977 (1996).
8. V. I. Yukalov, Laser Phys. **7**, 998 (1997).
9. B. W. Shore, *The Theory of Coherent Atomic Excitation* (Wiley, New York, 1990).
10. L. D. Landau and E. M. Lifshitz, *Electrodynamics of Continuous Media* (Nauka, Moscow, 1982; Pergamon, New York, 1984).

11. W. Glaser, *Grundlagen der Elektronenoptik* (Springer-Verlag, Vienna, 1952; Gostekhizdat, Moscow, 1957).
12. C. P. Slichter, *Principles of Magnetic Resonance* (Springer-Verlag, Berlin, 1990; Mir, Moscow, 1967).
13. N. W. McLachlan, *Theory and Application of Mathieu Functions* (Clarendon, Oxford, 1947; Inostrannaya Literatura, Moscow, 1953).
14. P. M. Morse and H. Feshbach, *Methods of Theoretical Physics* (McGraw-Hill, New York, 1953; Inostrannaya Literatura, Moscow, 1958), Vol. 1.
15. D. C. Mattis, *The Theory of Magnetism* (Harper and Row, New York, 1965; Mir, Moscow, 1967).
16. V. B. Berestetskii, E. M. Lifshitz, and L. P. Pitaevskii, *Quantum Electrodynamics* (Nauka, Moscow, 1980; Pergamon, Oxford, 1982).
17. J. Mathews and R. L. Walker, *Mathematical Methods of Physics* (Benjamin, Menlo Park, 1970; Atomizdat, Moscow, 1972).
18. Yu. G. Pavlenko, *Hamiltonian Methods in Electrodynamics and Quantum Mechanics* (Mosk. Gos. Univ., Moscow, 1988).
19. A. M. Perelomov, *Generalized Coherent States and Their Applications* (Nauka, Moscow, 1987; Springer-Verlag, New York, 1986).
20. A. M. Perelomov, *Integrable Systems of Classical Mechanics and Lie Algebra* (Nauka, Moscow, 1990).

Translated by G. V. Shepekina

Technical Physics, Vol. 45, No. 8, 2000, pp. 987–994. Translated from Zhurnal Tekhnicheskoĭ Fiziki, Vol. 70, No. 8, 2000, pp. 31–38.

Nonlinear Development of Capillary Waves in a Viscous Liquid Jet

Yu. G. Chesnokov

St. Petersburg State Institute of Technology (Technical University), St. Petersburg, 198013 Russia

Received March 9, 1999; in final form, September 14, 1999

Abstract—The one-dimensional approximate equations describing the dynamics of a Newtonian viscous fluid are used to analyze the nonlinear development of capillary waves in a jet. It is shown that the size of satellite droplets resulting from a nonuniform jet breakup decreases with the Reynolds number at a constant wavenumber. The satellite-droplet formation ceases at a certain value of the Reynolds number, which depends on the wavenumber and initial perturbation amplitude. © *2000 MAIK "Nauka/Interperiodica".*

INTRODUCTION

A liquid jet issuing out of a nozzle can break up into droplets as the amplitude of a perturbation is increased by capillary forces. The perturbation may appear on the jet surface or arise from fluctuations of pressure, flow rate, or physical characteristics of the fluid. This phenomenon is employed in a variety of technical devices, such as printers, chemical apparatus, etc. [1]. For this reason, capillary waves on the surface of a liquid jet have been studied over many years, both experimentally and theoretically. This subject has been discussed in a number of literature surveys [1, 2], and there is no need for reviewing it in detail here.

Lord Rayleigh established that a liquid jet is unstable with respect to a sinusoidal disturbance whose wavelength is longer than the circumference of the jet cross section. The instability is driven by capillary forces. When the jet radius locally decreases, capillary forces give rise to a corresponding local pressure increase. Vice versa, at the location where the jet radius increases, the pressure at the surface decreases. As a result, the liquid flows from the regions where the jet contracts to the regions where it expands, and the perturbation tends to increase with time elapsed. Solving the linearized equations of fluid mechanics, Rayleigh obtained an equation relating the growth rate of the perturbation amplitude to the perturbation wavelength. The time interval from the initial moment of perturbation to the moment when the jet breaks up into droplets predicted by the linear theory was found to be in fair agreement with experimental results.

The principal drawback of the linear theory lies in the fact that the linearized equations used in the theory become inapplicable as the perturbation amplitude grows. Accordingly, the results based on the theory are valid only for the relatively short interval where the perturbation amplitude remains small. Two different approaches can be used to allow for nonlinear interaction between disturbances. In one approach, the desired solution is represented as a series in a small perturbation amplitude. In the other, the equations of fluid mechanics supplemented with appropriate boundary conditions are integrated numerically.

A number of studies were focused on the problem of nonlinear perturbation development in a cylindrical inviscid jet [3–9]. In particular, it was shown that nonlinear interaction between perturbations can result in nonuniform breakup of a liquid jet into drops. Relatively small droplets, so-called satellites, can form between relatively large, so-called main, drops. Lafrance calculated the sizes of main drops and satellites as depending on the wavenumber and found that his results were in good agreement with experimental data [8].

Direct numerical simulations of liquid-jet breakup were reported in [10–16], where both inviscid [13, 14] and viscous [10–12, 15, 16] liquid jets were considered. In [15], a very detailed analysis of the effects of the Reynolds number, wavenumber, and initial perturbation amplitude on the process of jet breakup into droplets was presented. However, numerical integration of the equations of fluid mechanics is not a universal method. The high computational costs make it impossible to do without the assumption of longitudinally periodic flow or take into account the initial velocity profile. For this reason, many theoretical analyses of the capillary instability of a liquid jet are based on the one-dimensional approximate equations derived by assuming that the transverse length scale of the flow is much smaller than its longitudinal length scale.

This approach was developed, for example, in [17–26]. These studies include analyses based on perturbation methods [17–22] and numerical simulations [23–26]. Eggers obtained a self-similar solution to the one-dimensional equations describing the behavior of a liquid jet just before and after its breakup [27, 28]. The stability of this solution with respect to small perturbations was analyzed in [29]. In [30], it was shown that

1063-7842/00/4508-0987$20.00

there exists a countable set of self-similar solutions of this type, the Eggers solution being the most stable with respect to perturbations.

Different authors considered different variants of approximate one-dimensional equations. Systematic derivation of such equations was considered, for example, in [31, 32], where the results obtained by solving various approximate equations were compared with the exact solution to Rayleigh's problem. In [32], a procedure was developed for constructing approximate equations that are valid to an arbitrary order with respect to the small parameter defined as the ratio of the transverse and longitudinal length scales of the flow. It was shown that the equations derived therein can be used as a basis for constructing a solution to the stability problem for a cylindrical viscous liquid jet that is consistent with Rayleigh's solution up to terms proportional to the wavenumber squared.

In this paper, the approximate one-dimensional equations derived in [32] are used to solve the problem of nonlinear development of perturbations in a cylindrical jet of a viscous liquid. A solution to a similar problem that does not rely on approximate one-dimensional equations has been found only for the inviscid liquid jet. As in [32], the temporal stability of a liquid jet is analyzed. This means that an infinite jet is considered in a coordinate system moving with the liquid. The spatial stability of a viscous liquid jet, i.e., the stability of a semi-infinite jet under given initial conditions at the nozzle outlet cross section, was analyzed in [19–21] by invoking the so-called Cosserat equations. These equations, as well as other variants of approximate one-dimensional equations, can be employed under the assumption that the transverse length scale of the flow is small compared to its longitudinal length scale. This condition holds for long-wavelength perturbations when the corresponding wavenumber is small. It should be noted that the terms of leading order with respect to this parameter in the Cosserat equations, which contain the liquid viscosity, are not consistent with the exact equations [31]. This makes it impossible to analyze the effect of viscosity on the development of perturbations within the framework of these equations. An analysis of nonlinear interaction between capillary waves on the surface of a cylindrical jet of a viscous liquid based on the equations proposed in [32] can be used both to examine the effect of viscous friction forces on the development of capillary waves and to determine to what extent these equations are valid for describing the nonlinear interaction between perturbations. To accomplish the latter task, one should compare the results obtained in this study with solutions to the problem of nonlinear development of capillary waves in inviscid liquid jets that can be found in literature, as well as with the results obtained by solving a similar problem numerically for viscous liquid jets.

STATEMENT OF THE PROBLEM

In this paper, the capillary stability of a cylindrical jet of an incompressible Newtonian liquid is analyzed. Lord Rayleigh showed that the breakup of a jet into droplets is caused by the growth of axially symmetric perturbations. Therefore, perturbations of this particular form are considered in the present analysis. The fluid velocity in the jet is assumed to be sufficiently high, so that the effect of gravity on the breakup of a liquid jet driven by capillary forces is negligible.

It is convenient to seek a solution in terms of dimensionless variables. Denote the jet radius by a, the liquid density by ρ, its viscosity by μ, and the surface tension at the interface between the liquid jet and the ambient gas by σ. Then, the jet radius a can be used as a reference length; $t_0 = (\rho a^3/\sigma)^{1/2}$, as a reference time; $v_0 = (\sigma/\rho a)^{1/2}$, as a reference velocity; and $p_0 = \sigma/a$, as a reference pressure. Consider the cylindrical coordinate system (r, Θ, z) with z-axis aligned with the symmetry axis. Denote the axial and radial velocity components by u and v, respectively, and pressure by p. The governing equations for a liquid jet flow include the continuity equation

$$v_r + \frac{v}{r} + u_z = 0,$$

the axial Navier–Stokes equation

$$u_t + vu_r + uu_z = -p_z + \frac{1}{\mathrm{Re}}\left[\frac{1}{r}(ru_r)_r + u_{zz}\right],$$

and the radial Navier–Stokes equation

$$v_t + vv_r + uv_z = -p_r + \frac{1}{\mathrm{Re}}\left[\frac{1}{r}(rv_r)_r - \frac{v}{r^2} + v_{zz}\right].$$

Here, t is time and the Reynolds number Re is defined as

$$\mathrm{Re} = (\rho a\sigma)^{1/2}/\mu.$$

In these equations, the subscripts denote derivatives with respect to the corresponding variables: $v_r = \partial v/\partial r$, etc. The free surface of the jet is prescribed by the equation

$$r = \eta(z, t).$$

On the surface, a kinematic boundary condition

$$\eta_t + u\eta_z = v \quad \text{at} \quad r = \eta$$

and two dynamic boundary conditions are set. One of these dictates that the tangential component of viscous stress vanish on the jet surface:

$$2v_r\eta_z + (u_r + v_z)(1 - \eta_z^2) - 2u_z\eta_z = 0 \quad \text{at} \quad r = \eta.$$

By the other dynamic condition, the normal component of viscous stress has a jump equal to $\sigma(1/R_1 + 1/R_2)$ across the surface, where R_1 and R_2 are the longitudinal and transverse principal curvature radii of the

jet surface, respectively. In dimensionless form, it can be written as

$$p - \frac{1}{\mathrm{Re}}[2v_r - (u_r + v_z)\eta_z] = p_a + \frac{1}{R_1} + \frac{1}{R_2}.$$

Here, p_a is the ambient pressure, assumed to be constant. In the cylindrical coordinate system, the principal curvature radii are calculated as

$$\frac{1}{R_1} = \frac{1}{\eta(1+\eta_z^2)^{1/2}}, \quad \frac{1}{R_2} = -\frac{\eta_{zz}}{(1+\eta_z^2)^{3/2}}.$$

The problem formulated here has a solution of the form

$$u = v = 0, \quad \eta = 1, \quad p = p_a + 1. \qquad (1)$$

These formulas describe the motion of the liquid in a cylindrical jet in a coordinate system tied to the liquid. This solution is not valid in the near field of a jet, where viscous relaxation of the velocity profile of the nozzle flow takes place. According to some estimates (e.g., see [6]), the near-field length is small compared to the distance at which the capillary breakup of the jet occurs. For this reason, almost all studies of the capillary stability of liquid jets are focused on the analysis of the particular solution written out above with respect to small perturbations.

ONE-DIMENSIONAL EQUATIONS OF THE DYNAMICS OF A CAPILLARY JET

Calculation of nonlinear interactions between perturbations in a viscous liquid jet is associated with certain difficulties. When a solution is sought in the form of a series in powers of a small parameter (perturbation amplitude), it turns out that explicit analytical solutions of the equations describing the liquid motion in the jet cannot be obtained in the second approximation with respect to the small parameter. However, one can construct an approximate solution based on the assumption that the length scale of the longitudinal (axial) profiles of flow variables is much greater than the length scale of their cross-sectional profiles. Approximate one-dimensional equations that are valid under this condition have been considered by many authors. In [32], a technique was developed for constructing equations of this type that are valid to an arbitrary order with respect to the small parameter defined as the ratio of transverse to longitudinal length scale of the flow. Actually, these equations are quite accurate when the perturbation wavelength is sufficiently long; i.e., the corresponding wavenumber is small. Here, the derivation of the approximate equations is briefly outlined in order to introduce the notation and assumptions that underlie the theoretical analysis.

When the equations of fluid mechanics and boundary conditions are written in a dimensionless form, different reference lengths should be introduced for the transverse and longitudinal coordinates r and z. The resulting equations would then involve a small parameter δ equal to the ratio of the reference lengths. The dimensionless parameter Re is assumed to be a quantity on the order of unity (while $\delta \longrightarrow 0$). If the variables η, u, v, and p are sought in the form of series,

$$\eta = \sum_{m \geq 0} \delta^{2m} \eta^{(2m)}(z, t),$$

$$u = \sum_{n, m \geq 0} \delta^{2(n+m)} r^{2n} u^{n, 2m}(z, t),$$

$$v = \delta r \sum_{n, m \geq 0} \delta^{2(n+m)} r^{2n} v^{n, 2m}(z, t),$$

$$p - p_a = \sum_{n, m \geq 0} \delta^{2(n+m)} r^{2n} p^{n, 2m}(z, t),$$

then equations for the coefficients of these expansions can be obtained by substituting the series into the equations of fluid mechanics and boundary conditions and equating the coefficients of like powers of r and δ. In [32], equations of this kind were used to analyze the stability of the flow described by (1) in the linear approximation with respect to the initial perturbation amplitude. At the initial moment, a sinusoidal perturbation, e.g., the jet-surface perturbation

$$\eta = 1 + \varepsilon \cos(kz) + O(\varepsilon^2) \text{ at } t = 0,$$

was introduced, where ε is a small parameter and k is the wavenumber.

When the analysis is restricted to the leading terms of asymptotic expansions, i.e., to the equations for $\eta^{(0)}$ and $u^{0,0}$, a perturbation with an arbitrary wavenumber is found to be unstable. This is inconsistent with Rayleigh's exact results, which show that only the perturbations with $k < 1$ are unstable. In the second approximation with respect to δ, only long-wavelength perturbations are unstable. If the wavenumber k is greater than a certain value depending on Re, the flow is unstable. The approximate expression for the rate of perturbation growth agrees with Rayleigh's results up to terms of order k^2.

In this paper, a somewhat different approach is applied. Consider the new variables

$$\phi = \eta^{(0)} + \delta^2 \eta^{(2)} + O(\delta^4),$$
$$w = u^{0,0} + \delta^2 u^{0,2} + O(\delta^4).$$

The equations for the coefficients $\eta^{(0)}$, $\eta^{(2)}$, $u^{0,0}$, and $u^{0,2}$ in the expansions were written out in [32]. Multiplying the equations for $\eta^{(2)}$ and $u^{0,2}$ by δ^2; summing the resulting relations with the equations for $\eta^{(0)}$ and

$u^{0,0}$, respectively; and dropping the terms of order δ^4, one obtains the equations for ϕ and w:

$$\phi_t + \phi_z w + \frac{1}{2}\phi w_z + \frac{1}{16}[\phi^3 w_{zz} + 10\phi_z\phi^2 w_{zz} + 6(\phi_{zz}\phi^2 + 3\phi_z^2\phi)w_z] = 0, \tag{2}$$

$$w_t + ww_z = \frac{3}{8}(\phi^2 w_z w_{zz} + 2\phi\phi_z w_z^2) + \frac{3}{\mathrm{Re}}\left[w_{zz} + \frac{2\phi_z w_z}{\phi} + \frac{1}{8}\phi^2 w_{zzzz} + \frac{5}{4}\phi\phi_z w_{zzz} + \left(2\phi\phi_z + \frac{5}{2}\phi_z^2\right)w_{zz} + \left(\phi\phi_{zzz} + \frac{5}{2}\phi_z\phi_{zz} + \frac{1}{2}\frac{\phi_z^3}{\phi}\right)w_z\right] + \frac{\phi_z}{\phi^2} + \phi_{zzz} + \frac{3}{4}\frac{\phi_z\phi_{zz}}{\phi}. \tag{3}$$

These equations are obtained without introducing different reference lengths for r and z; i.e., $\delta \equiv 1$ here. This approach is advantageous in that the necessary algebra is somewhat simplified. The presentation below shows that, in contrast to [32], the boundary that separates the stable and unstable perturbations calculated in the linear approximation with respect to ε is identical with that predicted by Rayleigh's theory; i.e., the flow is unstable when $k < 1$.

APPROXIMATE EQUATIONS FOR PERTURBATION AMPLITUDES: THE FIRST APPROXIMATION

Assume that the jet surface is perturbed at the initial moment $t = 0$, while the flow velocity remains unperturbed. Then, equations (2) and (3) must be supplemented with the following initial conditions:

$$\phi = 1 + \varepsilon\cos(kz) - \frac{\varepsilon^2}{4} + O(\varepsilon^4), \tag{4}$$

$$\phi_t = 0 \text{ at } t = 0. \tag{5}$$

Here, ε is a small parameter (initial perturbation amplitude). A derivation of (4) can be found in [3]. It is based on the condition that the jet volume is conserved. A solution to the formulated problem is sought in the following form:

$$\phi = 1 + \varepsilon\phi_1 + \varepsilon^2\phi_2 + O(\varepsilon^3),$$
$$w = \varepsilon w_1 + \varepsilon^2 w_2 + O(\varepsilon^3).$$

Substituting these expansions into equations (2) and (3) and the initial conditions and collecting the coefficients of like powers of ε on both sides, one obtains the equations and initial conditions for the first and second approximations. In the linear approximation in ε,

$$\phi_{1t} + \frac{1}{2}w_{1z} + \frac{1}{16}w_{1zzzz} = 0, \tag{6}$$

$$w_{1t} = \frac{3}{\mathrm{Re}}\left[w_{1zz} + \frac{1}{8}w_{1zzzz}\right] + \phi_{1z} + \phi_{1zzz}, \tag{7}$$

$$\phi_1 = \cos(kz), \tag{8}$$

$$\phi_{1t} = 0 \text{ at } t = 0. \tag{9}$$

The equations for ϕ_2 and w_2 are

$$\phi_{2t} + \frac{1}{2}w_{2z} + \frac{1}{16}w_{2zzz} + \phi_{1z}w_1 + \frac{1}{2}\phi_1 w_{1z} + \frac{1}{16}(3\phi_1 w_{1zzz} + 10\phi_{1z}w_{1z} + 6\phi_{1zz}w_{1z}) = 0, \tag{10}$$

$$w_{2t} + w_1 w_{1z} = \frac{3}{8}w_{1z}w_{1zz} + \frac{3}{\mathrm{Re}}\left[w_{2zz} + \frac{1}{8}w_{2zzzz} + 2\phi_{1z}w_{1z} + \frac{1}{4}\phi_1 w_{1zzzz} + \frac{5}{4}\phi_{1z}w_{1zz} + 2\phi_{1zz}w_{1zz} + \phi_{1zzz}w_{1z}\right] + \phi_{2z} + \phi_{2zzz} - 2\phi_1\phi_{1z} + \frac{3}{4}\phi_{1z}\phi_{1zz}. \tag{11}$$

The initial conditions for these equations are

$$\phi_2 = -\frac{1}{4}, \tag{12}$$

$$\phi_{2t} = 0 \text{ at } t = 0. \tag{13}$$

A solution to equations (6) and (7) subject to initial conditions (8) and (9) can be sought in the form

$$\phi_1 = h_1(t)\cosh(ikz), \quad w_1 = if_1(t)\sinh(ikz).$$

Here, i is the imaginary unit. Define

$$A(k) = \frac{k}{2} - \frac{k^3}{16}.$$

For h_1 and f_1, one obtains the following expressions:

$$h_1(t) = \alpha_0 e^{\omega_1 t} + \beta_0 e^{\omega_2 t},$$
$$f_1(t) = \frac{1}{A}(\alpha_0\omega_1 e^{\omega_1 t} + \beta_0\omega_2 e^{\omega_2 t}).$$

Here, $\omega_1(k)$ and $\omega_2(k)$ are the roots of the quadratic equation

$$\omega^2 + \frac{6kA(k)}{\mathrm{Re}}\omega - k(1-k^2)A(k) = 0, \tag{14}$$

and the coefficients α_0 and β_0 are calculated as

$$\alpha_0 = \frac{\omega_2}{\omega_2 - \omega_1}, \quad \beta_0 = \frac{\omega_1}{\omega_1 - \omega_2}.$$

In the linear approximation, the exact solution to the problem of capillary stability of a viscous liquid jet was obtained by Rayleigh. It can be used to find a relation for calculating the perturbation growth rate ω. As shown in [32], this relation can be written as

$$\omega^2\frac{F(k)}{2} + \omega\frac{k^2(2F(k)-1)}{\mathrm{Re}} + \frac{2k^4}{\mathrm{Re}^2}(F(k)-F(k_1)) = \frac{1}{2}k^2(1-k^2), \quad (15)$$

where $k_1^2 = k^2 + \omega\mathrm{Re}$; $F(k) = kI_0(k)/I_1(k)$; and $I_0(k)$ and $I_1(k)$ are the first- and second-order modified Bessel functions of the first kind, respectively.

Representing $F(k)$ as a series in powers of k and retaining only the leading two terms, one obtains

$$F(k) = 2 + \frac{k^2}{4} + O(k^4).$$

By using this relation, the sum of the second and third terms on the left-hand side of (15) is transformed into

$$\omega\frac{k^2(2F(k)-1)}{\mathrm{Re}} + \frac{2k^4}{\mathrm{Re}^2}(F(k)-F(k_1)) = \frac{3k^2}{\mathrm{Re}}\omega + O(k^6).$$

On the other hand,

$$\frac{I_1(k)}{I_0(k)} = A(k) + O(k^5).$$

Thus, equation (4) for small k can be derived from (15) by neglecting terms of order k^6. Calculations show that the exact and approximate solutions are in good agreement, even at relatively large k. For example, at Re = 10 and k = 0.9, the exact and approximate values of ω are 0.17547 and 0.17555, respectively.

SECOND APPROXIMATION

In the second approximation, a solution to equations (10) and (11) subject to initial conditions (12) and (13) can be sought in the form

$$\phi_2 = h_2(t)\cosh(2ikz) + g_2(t),$$
$$w_2 = if_2(t)\sinh(2ikz).$$

To write formulas for h_2, g_2, and f_2 in a more compact form, the following notation is introduced:

$$\Omega_i = 4\omega_i^2 - 2(\omega_3-\omega_4)\omega_i + \omega_3\omega_4, \quad i = 1, 2;$$

$$\Omega_3 = (\omega_1+\omega_2)^2 - (\omega_3+\omega_4)(\omega_1+\omega_2) + \omega_3\omega_4;$$

$$B_1 = kA(2k)\left(1+\frac{3}{8}k^2\right);$$

$$B_2 = 3 - \frac{k^3}{A(k)}; \quad B_3 = \frac{6k^2}{\mathrm{Re}}\left(1-\frac{k^2}{16}\right)\frac{A(2k)}{A(k)}.$$

The expressions for g_2, h_2, and f_2 are

$$g_2 = -\frac{1}{4}h_1^2,$$

$$h_2 = c_1e^{2\omega_1 t} + c_2e^{2\omega_2 t} + c_3e^{(\omega_1+\omega_2)t} + c_4e^{\omega_3 t} + c_5e^{\omega_4 t},$$

$$f_2 = \frac{1}{A(2k)}\left[\omega_1\left(2c_1 - \frac{\alpha_0^2B_2}{2}\right)e^{2\omega_1 t} + \omega_2\left(2c_2 - \frac{\beta_0^2B_2}{2}\right)e^{2\omega_2 t} + (\omega_1+\omega_2)\left(c_3 - \frac{\alpha_0\beta_0B_2}{2}\right)e^{(\omega_1+\omega_2)t} + \omega_3c_4e^{\omega_3 t} + \omega_4c_5e^{\omega_4 t}\right].$$

Here, $\omega_3 = \omega_1(2k)$; $\omega_4 = \omega_2(2k)$; and the coefficients c_i (i = 1, …, 5) are calculated as

$$c_1 = \frac{\alpha_0^2}{\Omega_1}\left[B_1\left(\frac{\omega_1^2}{2A^2(k)} - 1\right) + B_2\omega_1^2 + B_3\omega_1\right],$$

$$c_2 = \frac{\beta_0^2}{\Omega_2}\left[B_1\left(\frac{\omega_2^2}{2A^2(k)} - 1\right) + B_2\omega_2^2 + B_3\omega_2\right],$$

$$c_3 = \frac{\alpha_0\beta_0}{\Omega_3}\left[2B_1\left(\frac{\omega_1\omega_2}{2A^2(k)} - 1\right) + \frac{1}{2}B_2(\omega_1+\omega_2)^2 + B_3(\omega_1+\omega_2)\right],$$

$$c_4 = \frac{(2\omega_1-\omega_4)c_1 + (2\omega_2-\omega_4)c_2 + (\omega_1+\omega_2-\omega_4)c_3}{\omega_4-\omega_3},$$

$$c_5 = \frac{(2\omega_1-\omega_3)c_1 + (2\omega_2-\omega_3)c_2 + (\omega_1+\omega_2-\omega_{3l})c_3}{\omega_3-\omega_4}.$$

The second approximation of the exact solution (i.e., the solution obtained without approximating the governing equations) is not known for a viscous liquid. However, the results obtained can be compared with the exact solution for an inviscid liquid. In this case, $\omega_2 = -\omega_1$, $\omega_4 = -\omega_3$ and the first two terms in the expansions of ω_i in powers of k are identical with the exact solution, so that the exact and approximate solutions differ

by a quantity on the order of k^6. The leading two terms in the expansion of c_3 in powers of k are given by

$$c_3 = \frac{1}{2} + \frac{63}{32}k^2 + O(k^4).$$

A comparison with the corresponding term obtained in [5] shows that this expansion agrees with the exact one up to terms of order k^2. However, in the expressions for Ω_i (i = 1, 2), which have the form

$$\Omega_i = 4\omega_i^2 - \omega_3^2$$

in the approximation considered, the leading terms in the expansions of the first and second terms in powers of k are mutually canceled. For this reason, only the leading terms turn out to be correct both in the expansions of Ω_i and in the expansions of c_i (i = 1, 2). Nonetheless, the results of calculations of the jet based on the exact and approximate relations are in good agreement.

EFFECTS OF WAVENUMBER AND REYNOLDS NUMBER ON THE DEVELOPMENT OF CAPILLARY WAVES

The relations obtained above can be used to examine the effect of viscosity on the evolution of perturbations. The strongest effect of fluid viscosity is on the duration of the interval from the initial moment of perturbation to the moment when the liquid jet breaks up into droplets. To find this quantity, the following method was applied. With the Reynolds number and the initial perturbation amplitude held constant, the coordinates of points of the liquid jet surface were calculated at various times. The moment at which the radial coordinate of one of the points vanishes was assumed to be the desired quantity. It should be pointed out here that, generally, the formulas obtained above are not applicable at such moments. At the moment of jet breakup, the neglected terms in the expansions in powers of the small parameter are of the same order as the retained terms. Nevertheless, the derived formulas can be used to obtain realistic estimates for the quantities of interest here. It is well known that the time to breakup of a liquid jet into droplets can be quite accurately predicted not only by the weakly nonlinear theory, but also by the linear theory. The geometry of the jet at the moment of its breakup can be quite accurately calculated by means of perturbation theory as well. This is demonstrated by comparing the results of a calculation of the size of the main and satellite droplets depending on the wavenumber with experimental results [8].

Figure 1 shows that, at each value of the Reynolds number, the time to jet breakup first decreases as the wavenumber is increased and then reaches a minimum and increases. As expected, the effect of the Reynolds number increases with wavenumber. This is explained by the increase in the spatial derivatives of fluid velocity toward shorter wavelengths, which enhances the effect of viscosity on the flow behavior. The location of the minimum of the time to jet breakup plotted versus wavenumber shifts leftwards with increasing Re. A similar trend is predicted by the linear theory. Calculations (not represented in this figure) show that the time to jet breakup strongly depends on the initial perturbation amplitude. The graphs shown here are plotted for the initial perturbation amplitude $\varepsilon = 0.01$.

Figure 2 shows that the Reynolds-number dependence of the time to breakup is weak in a wide range of Re. Only at relatively low Re does the time to breakup steeply increase. In this domain, the instability develops very slowly and can be described by the results obtained here even better.

The jet geometry at times close to the moment of breakup into droplets strongly depends on the wavenumber. The jet radius plotted versus longitudinal coordinate for long-wavelength perturbations has a second maximum, starting from a certain moment (see Fig. 3). This phenomenon is not observed for short-wavelength perturbations (Fig. 4). The appearance of the second maximum is an indication of satellite-droplet formation

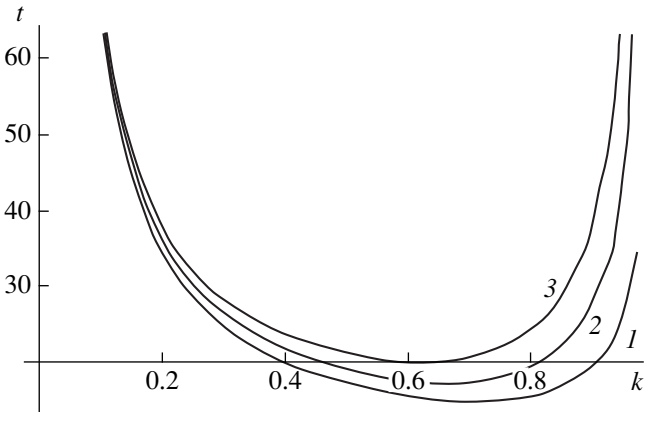

Fig. 1. Time to jet breakup versus wavenumber for various values of the Reynolds number: Re = (*1*) ∞; (*2*) 10; (*3*) 5.

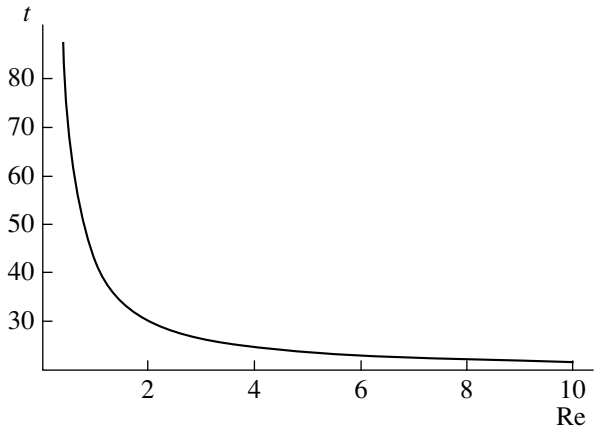

Fig. 2. Time to jet breakup versus Reynolds number for k = 0.4.

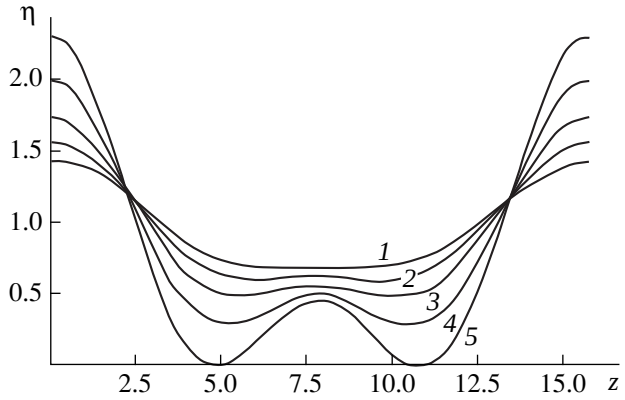

Fig. 3. Jet shape at Re = 10 and $k = 0.4$ for $t =$ (*1*) 18, (*2*) 19, (*3*) 20, (*4*) 21, and (*5*) 21.9305.

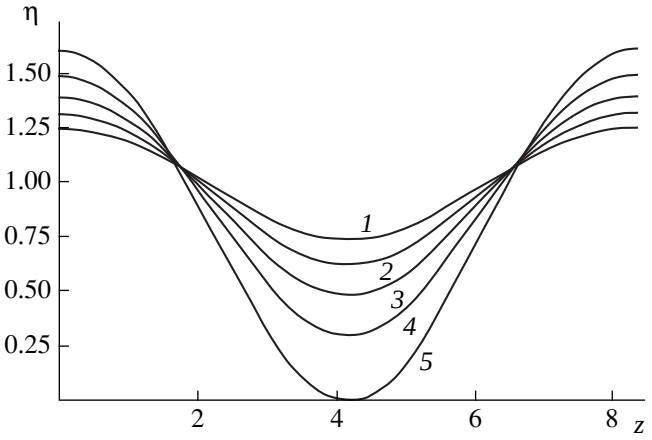

Fig. 4. Jet shape at Re = 10 and $k = 0.75$ for $t =$ (*1*) 14, (*2*) 15, (*3*) 16, (*4*) 17, and (*5*) 18.149.

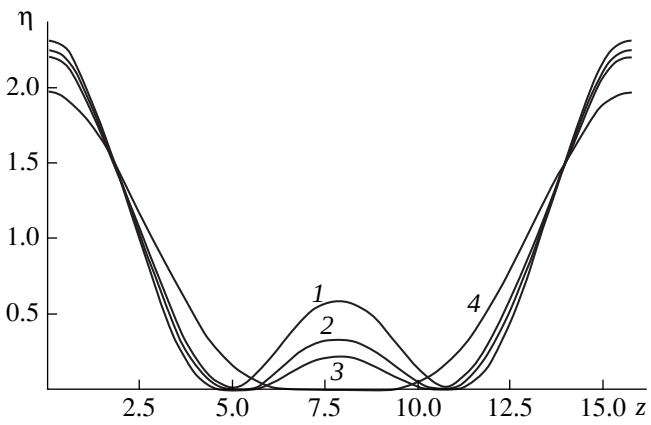

Fig. 5. Jet shape at the moment of breakup for $k = 0.4$ and Re = (*1*) 100, (*2*) 5, (*3*) 3, and (*4*) 0.3.

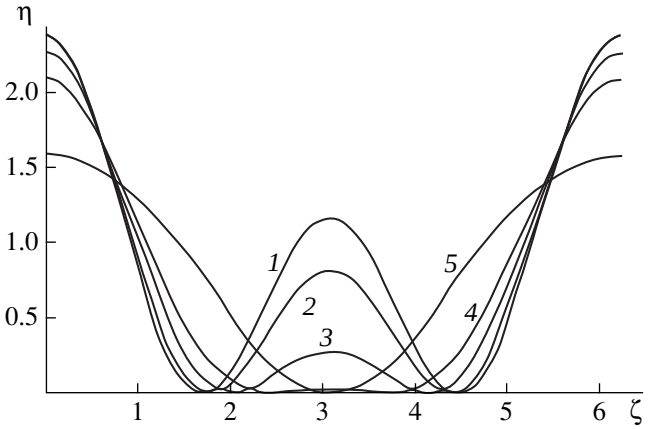

Fig. 6. Jet shape at the moment of breakup for Re = 10 and $k =$ (*1*) 0.1, (*2*) 0.3, (*3*) 0.45, (*4*) 0.525, and (*5*) 0.8.

between the main droplets. As the Reynolds number is increased, the magnitude of the second maximum in the graph of jet radius versus longitudinal coordinate at the moment of jet breakup decreases (Fig. 5), and the point where the jet radius vanishes shifts toward the midpoint of the segment bounded by the two principal maximums. At a certain value of Re, the second maximum disappears completely. This means that the size of satellite droplets decreases with increasing Re, and the jet breakup ceases at a certain Re. The fluid viscosity suppresses the development of the second harmonic, and satellite droplets do not form. Figure 6 shows the dependence of the jet radius on $\zeta = kz$ for various k. It demonstrates that, as the wavenumber increases, the point where the jet radius vanishes at the moment of jet breakup shifts toward the center, while the jet radius at the midpoint of the segment bounded by the two principal maximums decreases. Therefore, the size of satellite droplets decreases with the perturbation wavelength. Note that the results presented here are consistent with the numerical results reported in [15].

REFERENCES

1. *Monodispersion of Substances: Principles and Application*, Ed. by E. V. Ametistov, V. V. Blazhenkov, A. K. Gorodov, *et al.* (Énergoizdat, Moscow, 1991).
2. D. B. Bogy, Annu. Rev. Fluid Mech. **11**, 207 (1971).
3. M.-C. Yuen, J. Fluid Mech. **33**, 151 (1968).
4. D. P. Wang, J. Fluid Mech. **34**, 299 (1968).
5. A. H. Nayfeh, Phys. Fluids **13**, 841 (1970).
6. M. P. Markova and V. Ya. Shkadov, Izv. Akad. Nauk SSSR, Mekh. Zhidk. Gaza, No. 3, 30 (1972).
7. T. Kakutani, Y. Inoue, and T. Kan, J. Phys. Soc. Jpn. **38**, 529 (1974).
8. P. Lafrance, Phys. Fluids **18**, 428 (1975).
9. K. C. Chaudhary and L. G. Redekopp, J. Fluid Mech. **96**, 257 (1980).
10. J. E. Fromm, IBM J. Res. Dev. **28**, 322 (1984).

11. D. W. Bousfield, R. Keunings, G. Marrucci, and M. M. Denn, J. Non-Newtonian Fluid Mech. **21** (1), 79 (1986).
12. F. Shokoohi and H. G. Elrod, J. Comput. Phys. **71**, 324 (1987).
13. N. N. Mansour and T. S. Lundgren, Phys. Fluids A **2**, 1141 (1990).
14. V. V. Vladimirov and V. N. Gorshkov, Zh. Tekh. Fiz. **60** (11), 197 (1990) [Sov. Phys. Tech. Phys. **35**, 1349 (1990)].
15. N. Ashgriz and F. Mashayek, J. Fluid Mech. **291**, 163 (1995).
16. H. Huynh, N. Ashgriz, and F. Mashaek, J. Fluid Mech. **320**, 185 (1996).
17. H. C. Lee, IBM J. Res. Dev. **18**, 364 (1974).
18. W. Y. Pimbley, IBM J. Res. Dev. **20**, 148 (1976).
19. D. B. Bogy, Phys. Fluids **21**, 190 (1978).
20. D. B. Bogy, Trans. ASME, Ser. E **45**, 469 (1978).
21. D. B. Bogy, IBM J. Res. Dev. **23**, 87 (1979).
22. V. V. Blazhenkov, A. F. Ginevskiĭ, V. F. Gunbin, and A. S. Dmitriev, Izv. Akad. Nauk SSSR, Mekh. Zhidk. Gaza, No. 2, 53 (1988).
23. V. E. Epikhin and V. Ya. Shkadov, Izv. Akad. Nauk, Mekh. Zhidk. Gaza, No. 2, 12 (1993).
24. V. V. Blazhenkov, A. F. Ginevskiĭ, V. F. Gunbin, *et al.*, Izv. Akad. Nauk, Mekh. Zhidk. Gaza, No. 3, 54 (1993).
25. N. A. Razumovskiĭ, Zh. Tekh. Fiz. **63** (9), 26 (1993) [Tech. Phys. **38**, 752 (1993)].
26. J. Eggers and T. F. Dupont, J. Fluid Mech. **262**, 205 (1994).
27. J. Eggers, Phys. Rev. Lett. **71**, 3458 (1993).
28. J. Eggers, Phys. Fluids **7**, 941 (1995).
29. M. P. Brenner, X. D. Shi, and S. R. Nagel, Phys. Rev. Lett. **73**, 3391 (1994).
30. M. P. Brenner, J. R. Lister, and H. A. Stone, Phys. Fluids **8**, 2827 (1996).
31. F. J. García and A. Castellanos, Phys. Fluids **6**, 2676 (1994).
32. S. E. Bechtel, C. D. Carlson, and M. G. Forest, Phys. Fluids **7**, 2956 (1995).

Translated by A. S. Betev

Technical Physics, Vol. 45, No. 8, 2000, pp. 995–1000. Translated from Zhurnal Tekhnicheskoĭ Fiziki, Vol. 70, No. 8, 2000, pp. 39–44.

GASES AND LIQUIDS

On Capillary Motion of a Viscoelastic Liquid with a Charged Free Surface

S. O. Shiryaeva and O. A. Grigor'ev

Yaroslavl State University, Sovetskaya ul. 14, Yaroslavl, 150000 Russia

E-mail: rectorat@.uniyar.ac.ru

Received May 18, 1999; in final form, October 14, 1999.

Abstract—The structure of the capillary–relaxation motion spectrum in a liquid with a charged free surface has been investigated taking into account the viscosity relaxation effect. On the basis of numerical analysis of the dispersion equation for the wave motion in a viscoelastic incompressible liquid, it is shown that for a given wave number the range of characteristic relaxation times in which relaxation-type wave motion exists is limited and expands with increasing wave number. The growth rate of instability of the charged liquid surface markedly depends on the characteristic relaxation time and increases with its growth; in liquids with elastic properties, the energy dissipation rate of capillary motion is enhanced. At a surface charge density that is supercritical for the onset of Tonks–Frenkel instability, both purely gravitational waves and waves of a relaxational nature exist.

INTRODUCTION

The problem of capillary motion in a liquid exhibiting elastic properties is of interest in connection with numerous scientific and technological applications, and for this reason it has often been a focus of attention (see, for example, [1–7] and the references therein). Nevertheless, many issues remain unclear because of the known awkwardness of the theoretical solution, the variety of possible ways of choosing nondimensional parameters in the boundary problem, and the large number and complicated structure of nondimensional parameters arising in the final solution [1–7].

The essence of the problem is that under a sufficiently brief ($t \le 10^{-5}$ s) external impact even non-Newtonian liquids show elastic properties: they are first deformed elastically, and, after the impact ends, the residual shear stresses persists, relaxing in time $t \sim 10^{-5}$ s [8] and setting the liquid in motion. This effect manifests itself in capillary wave motion, because, at a wavelength of ~10 μm, the wave period is already comparable with the characteristic relaxation time of the elastic stress. As shown in [1–7], taking account of the elastic properties of a liquid leads to an appreciable complication of the capillary motion spectrum, resulting in limitation of the capillary wave spectrum and an increase in the wave energy dissipation rate due to the formation of high-frequency phonon-type wave motions.

In the consideration below, the entire analysis (in contrast to [3], where the dispersion equation for the wave motion of a viscoelastic liquid was derived in the framework of a microstructure approach and statistical mechanics methods) will be performed using a continuous medium model on the basis of hydrodynamics equations for a viscous liquid (as was done in [1–2, 4–7]), on the assumption that the viscoelastic properties of a liquid can be accounted for by introducing complex viscosity through the Maxwell formula [9]

$$\nu = \nu_0(1 - i\omega t_*)^{-1},$$

representing a Fourier image of the exponential variation of the viscosity of a viscoelastic liquid with time. In this expression, ν_0 is a coefficient of kinematic viscosity at zero frequency, ω is the complex frequency, t_* is the characteristic time of viscosity relaxation, and i is the imaginary unit.

The analysis in [1–7] of the influence of the viscosity relaxation effect on the relationships governing capillary motion in a liquid with a charged free surface is mainly qualitative, as it was performed either by asymptotic methods [1–5, 7] or by numerical methods capable of establishing only qualitative relationships [5, 6]. In the latter case, ways are sought of first deriving a nondimensional dispersion equation for use in numerical calculations. In the numerical analysis in [5, 6], the frequency and the enhancement and damping rates of capillary motion in a liquid were converted using either the wave motion frequency in an ideal liquid with a charged free surface or the characteristic damping rate of the capillary waves. In both cases, the objective was to diminish the number of nondimensional physical parameters describing the capillary motion of the liquid in the system considered. As a variable argument of the sought-for complex frequencies, a complex parameter was used, which depended on the wave number, the capillary pressure, and the pressure

1063-7842/00/4508-0995$20.00 © 2000 MAIK "Nauka/Interperiodica"

exerted by an electrostatic field on the free surface of the liquid, that is, ultimately, on the physical characteristics of the liquid, namely, its density, capillary constant, surface tension, coefficient of viscosity, and the surface density of the electrical charge. From this analysis, it is hard to find out just how the characteristics of capillary motion in a liquid depend on parameters such as wave number k or surface density κ of the electrical charge. Our purpose is to overcome this limitation.

1. The problem will be solved by calculating the spectrum of capillary waves on the charged flat surface of an ideally conductive liquid of infinite depth bordering a vacuum. The liquid, which has density ρ, viscosity ν, and surface tension coefficient σ, is exposed to gravitational field $\mathbf{g}$ and electrostatic field $\mathbf{E}_0$ (the surface density of the charge induced by field $\mathbf{E}_0$ on the unperturbed free surface of the liquid is connected to E_0 by the well-known relation $E_0 = 4\pi\kappa$. The strength of the electrostatic field E_0 near the liquid surface is determined by the potential difference between the free surface of the liquid with zero potential and a flat counterelectrode positioned parallel to the unperturbed flat surface of the liquid at distance b and with a potential $\Phi = V$.

Let us choose a Cartesian coordinate system with the z-axis directed vertically upward, $\mathbf{n}_z \| -\mathbf{g}$ ($\mathbf{n}_z$ is a unit vector of coordinate z), and x-axis along the propagation direction of a flat capillary wave ($\sim\exp(ikx - i\omega t)$). Let us also assume that the plane $z = 0$ coincides with the unperturbed free surface of the liquid. The function $\zeta(x, t) = \zeta_0\exp(ikx - i\omega t)$ describes a small perturbation of the equilibrium flat surface of the liquid caused by thermal capillary wave motion with a very small amplitude ($\zeta_0 \sim (kT/\sigma)^{1/2}$), where k is the Boltzmann constant, T is the absolute temperature, and $\boldsymbol{U}(\mathbf{r}, t)$ is the velocity field of the liquid motion caused by the free surface perturbation $\zeta(x, t)$ and having the same order of smallness [10].

Let us derive the spectrum of the capillary waves in a liquid for the given conditions. The mathematical formulation of the problem includes the linearized Navier–Stokes equation for an incompressible liquid; the incompressibility condition; the Laplace equation for the electrical field potential near the liquid surface; and the corresponding boundary conditions

$$\frac{\partial \mathbf{U}}{\partial t} = -\frac{1}{\rho}\nabla P(\mathbf{U}) + \nu\Delta\mathbf{U} + \mathbf{g}, \tag{1}$$

$$\operatorname{div}\mathbf{U} = 0, \tag{2}$$

$$\Delta\Phi = 0, \quad \mathbf{E} = -\nabla\Phi, \tag{3}$$

$$z = -\infty\colon\ \mathbf{U} = 0, \tag{4}$$

$$z = 0\colon\ -\frac{\partial\xi(x, t)}{\partial t} + U_z = 0, \tag{5}$$

$$\mathbf{n}(\boldsymbol{\tau}\nabla)\mathbf{U} + \boldsymbol{\tau}(\mathbf{n}\nabla)\mathbf{U} = 0, \tag{6}$$

$$-P(\mathbf{U}) + \rho g\zeta + 2\rho\nu\mathbf{n}(\mathbf{n}\nabla)\mathbf{U} - P_E(\zeta) + P_\sigma(\zeta) = 0, \tag{7}$$

$$\Phi = 0, \tag{8}$$

$$z = b\colon\ \Phi = V. \tag{9}$$

In the above expressions, $\mathbf{n}$ and $\boldsymbol{\tau}$ are the normal and tangential unit vectors relative to the free liquid surface, respectively; $P(\mathbf{U})$ is the pressure within the liquid due to the capillary motion of the liquid and is of the first order of smallness in ζ; and $P_E(\zeta)$ and $P_\sigma(\zeta)$ are additional pressures on the free liquid surface related to the electrical forces and the surface tension forces, respectively, both of them resulting from the perturbation $\zeta(x, t) = A\exp(ikx - i\omega t)$ of the equilibrium flat surface of the liquid caused by the capillary wave motion and of the first order of smallness in ζ [11, 12],

$$P_\sigma(\zeta) = -\sigma\frac{\partial^2\zeta}{\partial x^2}, \quad P_E(\zeta) = 4\pi\varepsilon^{-1}\kappa^2 k\zeta. \tag{10}$$

As the liquid is viscous, to describe the flows in it, we divide the velocity field $\mathbf{U} = \mathbf{U}(\mathbf{r}, t)$ into two components in accordance with the Helmholtz theorem: the potential component (with the velocity field potential $\psi(\mathbf{r}, t)$) and the vortex component (described by the stream function $\varphi(\mathbf{r}, t)$. Then the expression for pressure field $P(\mathbf{U})$ in the liquid can be written in the form

$$P(\mathbf{U}) = -\rho\frac{\partial\psi}{\partial t} - \rho g\zeta. \tag{11}$$

2. We will be seeking a solution of problem (1)–(6) in the following form [12]:

$$U_x(x, z, t) = (ikB\exp(-kz) - lC\exp(-lz)) \times \exp(ikx - i\omega t),$$

$$U_z(x, z, t) = (-kB\exp(-kz) + ikC\exp(-lz)) \times \exp(ikx - i\omega t),$$

$$l^2 = k^2 - i\omega\nu^{-1}.$$

Here A, B, and C are constants and l is the characteristic linear scale of the spatial variation of the vortex component of the velocity field.

We follow the reasoning in [12] and add an extra term to the dynamic boundary condition for the normal component of the stress tensor to take into account the electric field pressure. Then, expressing the viscosity as a function of frequency $\nu = \nu_0/(1 - i\omega t_*)$ in accordance with the Maxwell formula, we obtain the dispersion relationship characterizing the capillary motion of a

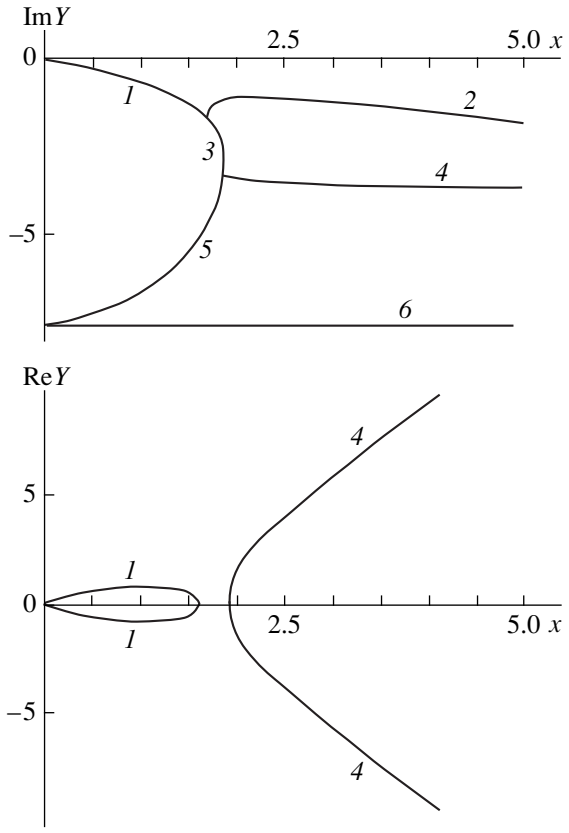

Fig. 1. Nondimensional real Re$Y(X)$ and imaginary Im$Y(X)$ frequency components as functions of the nondimensional wave number X calculated for $\beta = 1$, $W = 0$, and $\tau = 0.11$.

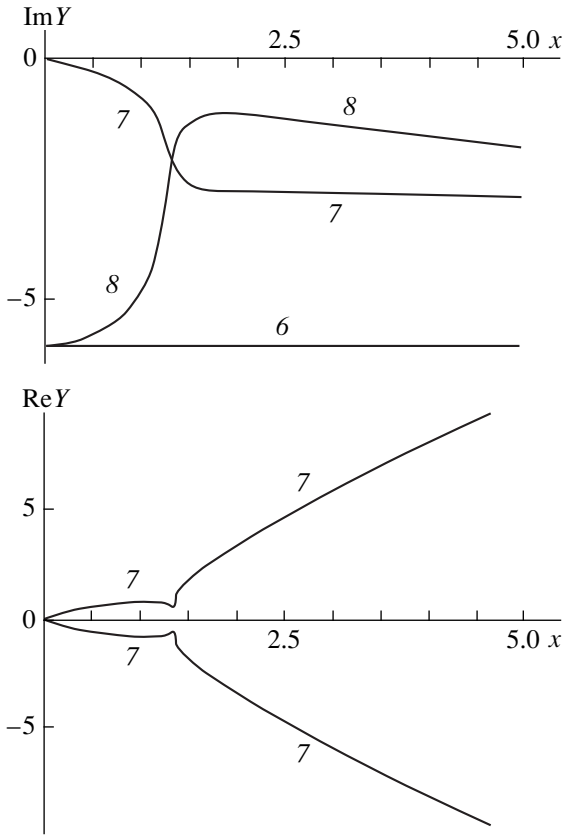

Fig. 2. Same as in Fig. 1 for $\tau = 0.17$ and $W = 0$.

viscoelastic liquid with a charged free surface in the dimensional form

$$\left(\omega + \frac{\nu_0 2ik^2}{(1 - i\omega t_*)}\right) + \frac{4\nu_0^2 k^4}{(1 - i\omega t_*)^2}\sqrt{1 - \frac{i\omega(1 - i\omega t_*)}{\nu k^2}}$$

$$= \frac{k}{\rho}(g\rho + \sigma k^2 - 4\pi\kappa^2 k).$$

Introducing the nondimensional variables

$$X = ka, \quad a = \sqrt{\sigma/\rho g}, \quad Y = \frac{\omega a^2}{\nu_0},$$

$$\tau = \frac{t_* \nu_0}{a^2}, \quad \beta = \frac{\sigma a}{\rho \nu_0^2}, \quad W = \frac{4\pi\kappa^2 a}{\sigma},$$

we obtain

$$[Y(1 - iY\tau) + 2iX^2]^2 + 4X^4\sqrt{1 - \frac{iY(1 - iY\tau)}{X^2}} \qquad (12)$$

$$= \beta X[1 + X^2 - WX](1 - iY\tau)^2,$$

where a is the capillary constant of the liquid; W is the Tonks–Frenkel parameter characterizing the free-surface stability of the liquid with respect to its own charge; and the capillary–gravitational wave with the wave number k at the liquid surface sustains instability at $W > (k + k^{-1})$ [13, 14].

3. Variations of the real ReY = Re$Y(X)$ and imaginary ImY = Im$Y(X)$ components of nondimensional frequency Y on nondimensional wave number X calculated numerically using Eq. (12) for various characteristic relaxation times τ and the Tonks–Frenkel parameter W are presented in Figs. 1–8.

The numerical calculations show (Figs. 1, 2) that at $W = 0$ (with no charge at the free surface of the liquid) the viscosity relaxation effect leads to the emergence of a periodic relaxation motion (branch *4*), as well as two aperiodic relaxation motions (branches *5*, *6*). Branches *1–3* correspond to the capillary–gravitational liquid motions arising in nonviscous liquids as well. When the parameter τ increases to 0.17 (Fig. 2), the aperiodic motion *3* vanishes and curves *1* and *4* combine into a single capillary–relaxation periodic motion *7*; an aperiodic motion *8* also arises as curves *2* and *5* combine. A further increase in τ does not change the general qualitative picture of the capillary motions; however, it

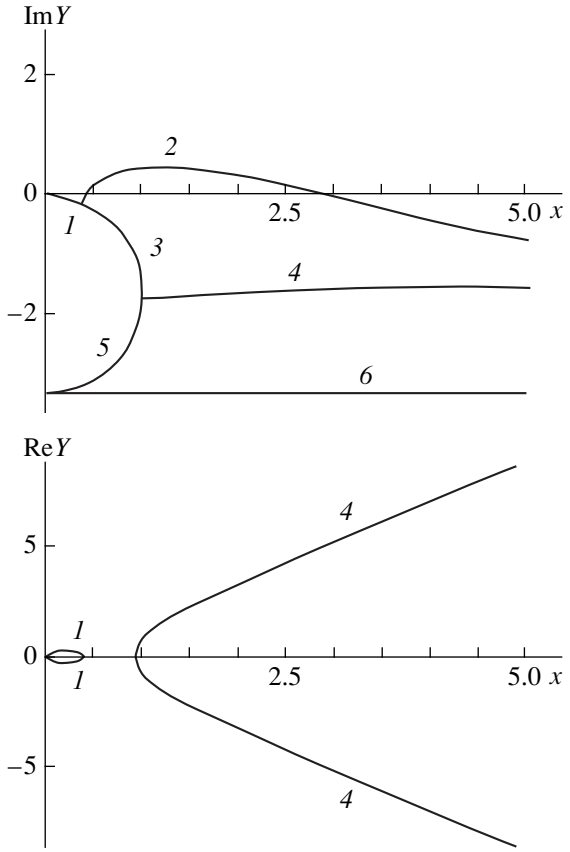

Fig. 3. Same as in Fig. 1 for $\tau = 0.3$ and $W = 3$.

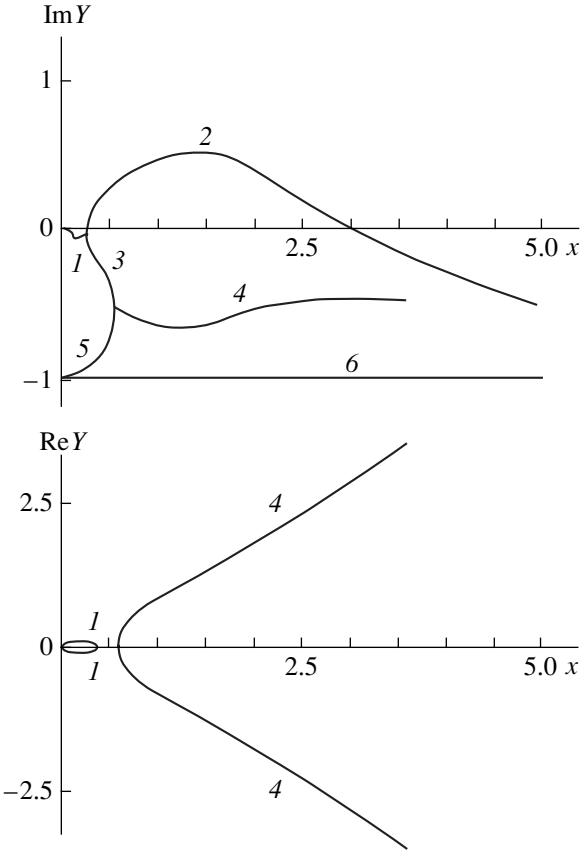

Fig. 4. Same as in Fig. 1 for $\tau = 1$ and $W = 3$.

decreases the frequency of the wave motions described by branch *7* and the damping rates of all branches.

The presence of an electrostatic field near a liquid surface (due to the surface charge) with subcritical strength in the sense of the Tonks–Frenkel instability ($W = 1$), while not affecting the frequency of the relaxation oscillations, decreases the capillary wave frequencies, and at larger τ ($\tau = 0.3$), branch *1* combines with *4* and branch *2* with *5*.

At a supercritical strength of the electrostatic field ($W = 3$, see Figs. 3, 4), the locus corresponding to curve *1* describing capillary–gravitational waves shrinks considerably and curve *2* corresponding to capillary–gravitational aperiodic motions penetrates into the half-plane $\mathrm{Im}Y > 0$, which is evidence of the onset of aperiodic instability of the surface perturbations in the corresponding range of wave numbers k.

Increasing the parameter τ does not change the spectrum of the waves, which became unstable because of supercritical charge; however, it causes an increase in the growth rates of unstable motions and decreases the damping rates of stable motions.

For a highly supercritical Tonks–Frenkel parameter $W = 6$ (Fig. 5), expansion of the spectrum of the waves experiencing instability is observed (branch *2*) both into region $X < 1$ of the gravitational waves and into region $X > 1$ of the capillary waves; in addition, the aperiodically damping motions *3* and *5* vanish.

Thus, when the parameter W is subcritical for the onset of Tonks–Frenkel instability, gravitational, capillary, and relaxation waves exist; at supercritical parameter W, the capillary waves are unstable in a limited range of wave numbers. At the same time, the gravitational waves ($k \ll 1$), as well as the relaxational waves, remain and the spectra of the wave numbers characterizing these wave motions are contiguous (Figs. 3–5).

Investigation of the dependence of the instability growth rates (the section of branch *2* at $\mathrm{Im}Y > 0$ in Figs. 3–5) on nondimensional wave number X for various values of characteristic relaxation time τ of the elastic stresses in a liquid was carried out in [13] using the same dimensionless parameters as in the present study. It was found that this dependence is very strong and that the growth rate increase reaches 100% of the growth rate value at $W = 6$ when τ varies from 0.11 to 1, in contrast to the conclusions based on qualitative investigations made in [5, 6], where even such a strong effect was obscured by the complicated form of the dimensionless parameters and arguments used.

The numerical investigation of the growth rate of unstable capillary motions in a liquid as a function of nondimensional characteristic time τ of the viscosity

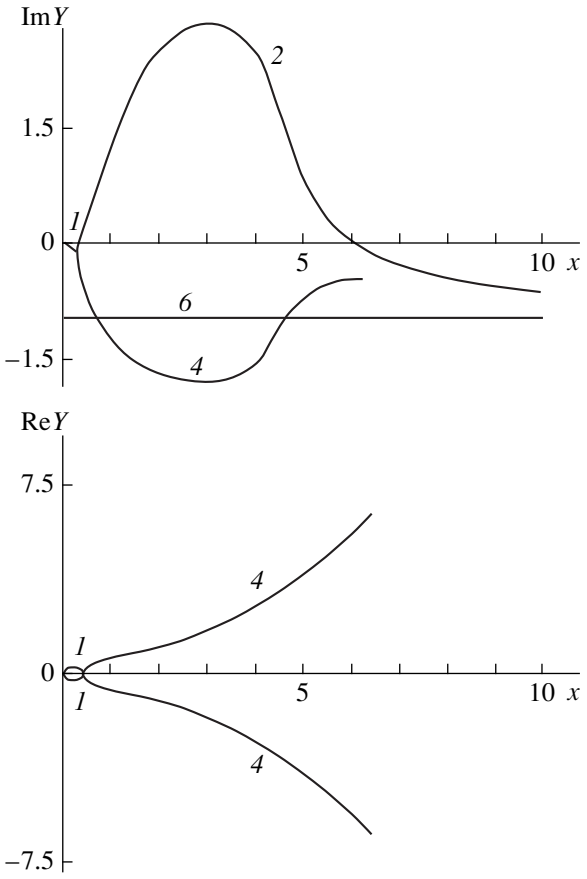

Fig. 5. Same as in Fig. 1 for $\tau = 1$ and $W = 6$.

relaxation carried out for various wave numbers X and various W show (Fig. 6) that the larger W and X are, the faster the growth rates increase with τ.

The dependence of the components $\mathrm{Re}Y = \mathrm{Re}Y(W)$ and $\mathrm{Im}Y = \mathrm{Im}Y(W)$ of the nondimensional frequency Y on the Tonks–Frenkel parameter W calculated for $X = 1$ and different values of τ shows that taking into account the viscosity relaxation effect with $\tau = 0.1$, in comparison with the purely gravitational–capillary wave motions described by branches *1–3*, leads to the onset of three aperiodic relaxation motions *4–6*, one of which (*4*) becomes periodic when τ is increased to 0.3 (Fig. 7).

A further increase in characteristic relaxation time τ leads to convergence of the relaxation (branch *4*) and capillary–gravitational (branch *1*) periodic motions, as well as of aperiodic motions *2* and *5*, accompanied by the formation of compound capillary–relaxation motions.

The real $\mathrm{Re}Y = \mathrm{Re}Y(\tau)$ and imaginary $\mathrm{Im}Y = \mathrm{Im}Y(\tau)$ components of nondimensional frequency Y as a function of nondimensional characteristic time τ of the viscosity relaxation calculated for $Y = 1$ and $W = 3$ are shown in Fig. 8. Branch *1* describes variation of the instability growth rate with τ: the growth rate slowly increases with increasing τ. Branch *2* describes the periodic relaxation motions existing, according to

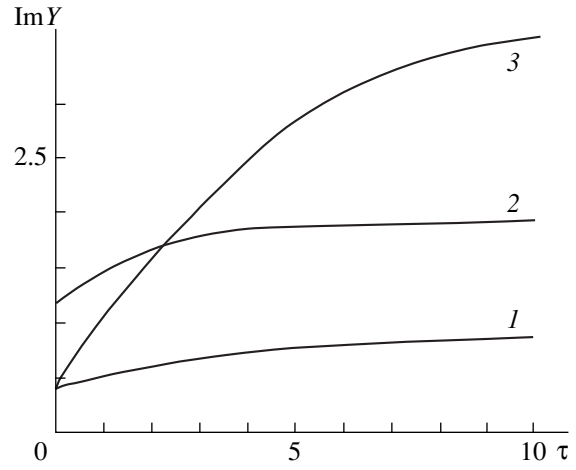

Fig. 6. Plot of the nondimensional growth rate of the instability vs. the nondimensional characteristic time τ of the viscosity relaxation. (*1*) $X = 1$ and $W = 3$; (*2*) $X = 1$ and $W = 6$; (*3*) $X = 5$ and $W = 6$.

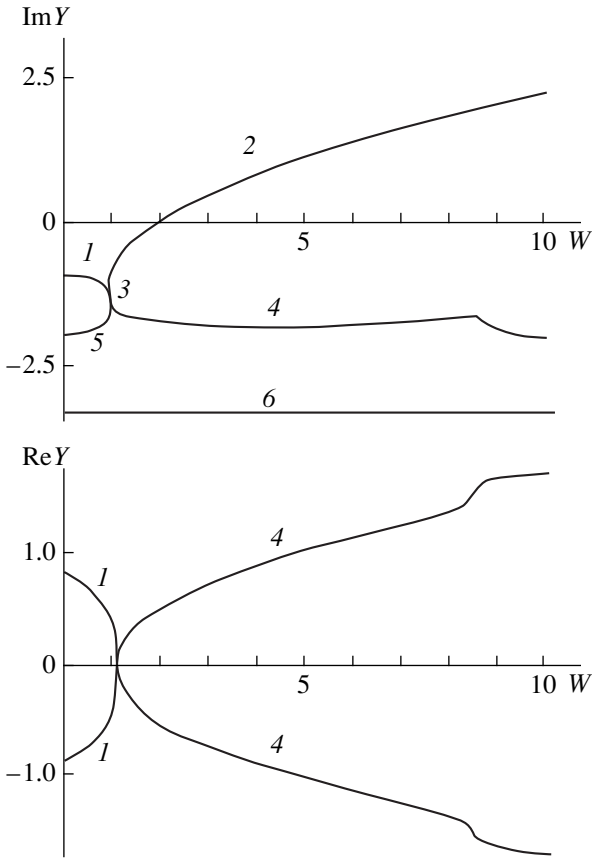

Fig. 7. Nondimensional real $\mathrm{Re}Y(W)$ and imaginary $\mathrm{Im}Y(W)$ frequency components as functions of the Tonks–Frenkel parameter W for $X = 1$ and $\tau = 0.3$.

Fig. 8, within a limited range of τ values. Branches *3–5* describe the aperiodic relaxation motions in a liquid. Fig. 8 and numerical calculations carried out for other values of W show that the periodic relaxation motions

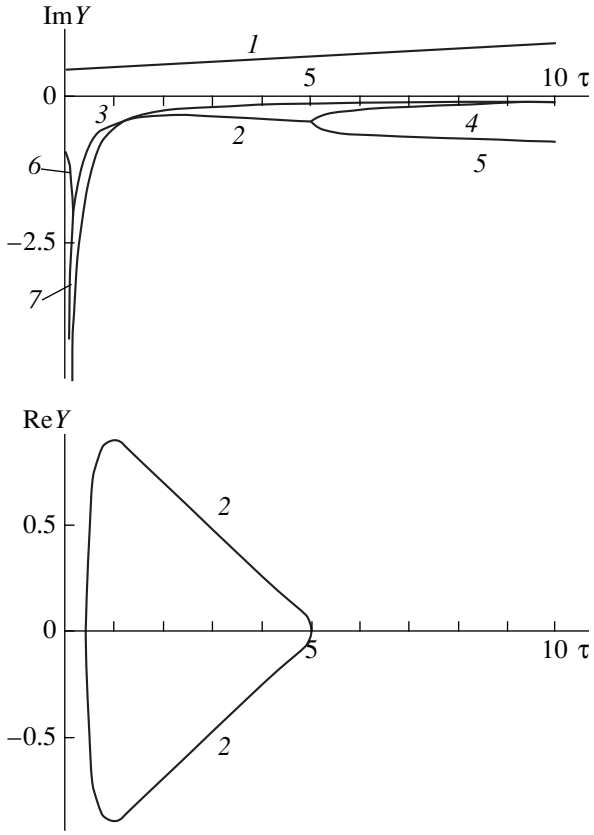

Fig. 8. Nondimensional real Re$Y(\tau)$ and imaginary Im$Y(\tau)$ frequency components as functions of the nondimensional characteristic time τ of the viscosity relaxation for $X = 1$ and $W = 3$.

exist within a limited interval of τ values whose extent is inversely proportional to the Tonks–Frenkel parameter W. As the wavelength increases, the range of τ in which the relaxation oscillations exist expands and the instability growth rate of the capillary waves increases.

CONCLUSIONS

In summarizing the above consideration of the viscosity relaxation influence on the relationships in the capillary motions of a liquid with a charged free surface, let us note the following:

The instability growth rate for the branch of capillary motions unstable with respect to the surface charge strongly depends on the characteristic time of viscosity relaxation and on the surface charge density. For sufficiently large surface charge densities (parameter W), the instability growth rate increases appreciably with an increase in the nondimensional characteristic relaxation time τ.

The range of wave numbers in which surface instability with respect to the surface charge is observed is governed only by the nondimensional Tonks–Frenkel parameter W and does not depend on the characteristic time of viscosity relaxation, although the wave number of the most unstable wave at $W = \text{const}$ slowly increases with increasing τ.

At a fixed value of the wave number $k = \text{const}$, the range of characteristic relaxation times τ in which periodic solutions exist is limited; however, it expands with increasing wave number k.

For large enough characteristic relaxation times τ, the branches of the capillary–gravitational and relaxation waves combine into a single compound motion existing at any wave number k, including those corresponding to purely gravitational waves ($k \longrightarrow 0$).

As the characteristic relaxation time τ decreases, the damping rates of relaxation-type capillary motions in the liquid rapidly increase.

REFERENCES

1. Yu. A. Bykovskiĭ, É. A. Manykin, P. P. Poluéktov, *et al.*, Zh. Tekh. Fiz. **46** (11), 2211 (1976) [Sov. Phys. Tech. Phys. **21**, 1302 (1976)].
2. G. A. Levachova, É. A. Manykin, and P. P. Poluéktov, Izv. Akad. Nauk SSSR, Mekh. Zhidk. Gaza, No. 2, 17 (1985).
3. C. F. Tejero and M. Baus, Mol. Phys. **54**, 1307 (1985).
4. I. N. Aliev, Magn. Gidrodin., No. 2, 78 (1987).
5. O. A. Grigor'ev and S. O. Shiryaeva, Izv. Akad. Nauk, Mekh. Zhidk. Gaza, No. 1, 98 (1996).
6. S. O. Shiryaeva, O. A. Grigor'ev, M. I. Munichev, and A. I. Grigor'ev, Zh. Tekh. Fiz. **66** (10), 47 (1996) [Tech. Phys. **41**, 997 (1996)].
7. S. I. Bastrukov and I. V. Molodtsova, Dokl. Akad. Nauk **350**, 321 (1996) [Phys. Dokl. **41**, 388 (1996)].
8. B. B. Badmaev, Ch. S. Laĭdabon, B. V. Deryagin, and U. V. Bazaron, Dokl. Akad. Nauk SSSR **322**, 307 (1992).
9. J. Frenkel, *Kinetic Theory of Liquids* (Nauka, Leningrad, 1975; Clarendon, Oxford, 1946).
10. Ya. I. Frenkel', Zh. Éksp. Teor. Fiz. **6**, 348 (1936).
11. L. D. Landau and E. M. Lifshitz, *Course of Theoretical Physics*, Vol. 8: *Electrodynamics of Continuous Media* (Nauka, Moscow, 1982; Pergamon, New York, 1984).
12. V. G. Levich, *Physicochemical Hydrodynamics* (Fizmatgiz, Moscow, 1959).
13. S. O. Shiryaeva and O. A. Grigor'ev, Pis'ma Zh. Tekh. Fiz. **25** (2), 1 (1999) [Tech. Phys. Lett. **25**, 41 (1999)].
14. A. I. Grigor'ev, S. O. Shiryaeva, V. A. Koromyslov, and D. F. Belonozhko, Zh. Tekh. Fiz. **67** (8), 27 (1997) [Tech. Phys. **42**, 877 (1997)].

Translated by N. Mende